First differential measurements of tZq production and luminosity determination using Z boson rates at the LHC

Dissertation

zur Erlangung des Doktorgrades

an der Fakultät für Mathematik, Informatik und Naturwissenschaften

Fachbereich Physik

der Universität Hamburg

vorgelegt von

David Ludwig Walter

aus Offenburg, Deutschland

Hamburg

September 2022

Eidesstattliche Erklärung / Declaration on oath

Hiermit versichere ich an Eides statt, dass ich die vorliegende Dissertation selbst verfasst und keine anderen als die angegebenen Quellen und Hilfsmittel benutzt habe. |

I hereby declare upon oath that I have written the present dissertation independently and have not used further resources and aids than those stated in the dissertation.

Hamburg, den September 19, 2022.

Unterschrift des Doktoranden

Gutachterinnen der Dissertation:	Dr. Abideh Jafari Prof. Dr. Elisabetta Gallo Prof. Dr. Antonio Onofre
Zusammensetzung der Prüfungskommission:	Dr. Abideh Jafari Prof. Dr. Elisabetta Gallo PD Dr. Andreas Meyer Prof. Dr. Peter Schleper Prof. Dr. Sven-Olaf Moch
Vorsitzender des Prüfungsausschusses:	Prof. Dr. Sven-Olaf Moch
Datum der Disputation:	09. September 2022
Vorsitzender des Fach-Promotionsausschusses PHYSIK:	Prof. Dr. Wolfgang J. Parak
Leiter des Fachbereichs PHYSIK:	Prof. Dr. Günter H. W. Sigl
Dekan der Fakultät MIN:	Prof. Dr. Norbert Ritter

Abstract

In this thesis, measurements are presented using proton-proton collision data at $\sqrt{s} = 13\,\text{TeV}$ collected by the CMS experiment in the years 2016, 2017, and 2018, corresponding to an integrated luminosity of $138\,\text{fb}^{-1}$.

New results on single top quark production in association with a Z boson (tZq) are presented. The inclusive cross section is measured with unprecedented accuracy. Differential cross sections are presented for the first time, measuring 11 kinematic observables that are sensitive to modeling aspects and possible effects of new physics. Absolute and normalized distributions are obtained for experiment independent parton- and particle-level definitions. The spin asymmetry of the top quark, a measure of its polarization, is measured for the first time in the tZq process. The results are obtained utilizing binned maximum likelihood fits which directly account for backgrounds and systematic uncertainties. The results are compared to theory predictions with different modeling assumptions on the parton content of the proton. No significant deviations from standard model predictions are observed.

Using the same data, the measurement of Z boson production is presented as a means to determine the integrated luminosity. It is demonstrated that the measurement of Z boson rates constitutes a precise and complementary method to monitor and transfer the luminosity between data sets and that the method leads to an improved measurement of the integrated luminosity.

Zusammenfassung

In dieser Arbeit werden Messungen an Proton-Proton-Kollisionensdaten präsentiert. Die Daten wurden vom CMS-Experiment am LHC in den Jahren 2016, 2017 und 2018 bei einer Schwerpunktsenergie von 13 TeV gesammelt und entsprechen einer integrierten Luminosität von 138 fb^{-1}.

Es werden neue Ergebnisse zur Produktion einzelner Top-Quarks in assoziation mit Z-Bosonen vorgestellt. Der totale Wirkungsquerschnitt wird mit einer noch nie dagewesenen Genauigkeit von etwa 11% gemessen. Zum ersten Mal werden differentielle Wirkungsquerschnitte in Abhängigkeit von elf kinematischen Größen gemessen, mit denen Modellierungsaspekte und mögliche Effekte der neuen Physik untersucht werden können. Dabei werden Detektor- und Hadronisierungseffekte korrigiert und absolute sowie normierte Verteilungen gezeigt. Die Spin-Asymmetrie des Top-Quarks, ein Maß für seine Polarisation und beeinflusst von möglicher neuer Physik, wird zum ersten Mal im tZq-Prozess gemessen. Die Ergebnisse werden mit Hilfe von gebinnten Maximum-Likelihood-Anpassungen erzielt, die Untergründe und systematische Unsicherheiten direkt berücksichtigen. Theoretische Vorhersagen unter verschiedenen Modellannahmen zur Partondichtefunktion des Protons werden mit den Resultaten verglichen. Keine signifikanten Abweichungen von den Vorhersagen des Standardmodells sind beobachtet.

Unter Verwendung der gleichen Daten wird die Messung der Produktion von Z-Bosonen als Mittel zur Bestimmung der integrierten Luminosität vorgestellt. Die Rate von Z-Bosonen, die in zwei Myonen zerfallen, wird in kurzen Zeitintervallen von etwa 30 min gemessen. Messungen der Trigger-, Identifizierungs- und Rekonstruktions-Effizienz der beiden Myonen werden in situ an der gleichen Ereignisprobe durchgeführt. Restkorrekturen und systematische Unsicherheiten werden im Detail untersucht. Aus den bei niedriger Strahlintensität aufgezeichneten Daten wird eine absolute Skala für die Luminosität aus der Anzahl der Z-Bosonen abgeleitet. Es wird gezeigt, dass die Messung der Z-Bosonenraten eine präzise und ergänzende Methode zur Überwachung und Übertragung der Luminosität zwischen Datensätzen darstellt und dass die Methode zu einer verbesserten Messung der integrierten Luminosität führt.

Contents

Introduction

The standard model of particle physics (SM) is the achievement of decades of research of the fundamental laws at the smallest scales. As a quantum field theory, the SM describes all fundamental particles known today in a self-consistent way. It also describes the strong, weak, and electromagnetic interactions between the particles. Only gravitation is not part of the SM but is negligible at a microscopic level. Many predictions of the SM have been confirmed by particle physics experiments. In particular, the SM was remarkably able to predict a number of elementary particles, the existence of which was later confirmed by experiments. A theoretical overview of the SM in the context of this thesis is given in Chapter 1. The vast majority of measured properties of the particles agree very well with the predictions. However, the SM misses the description of gravitation, dark matter, and dark energy. Tensions have been discovered by direct measurements, such as for the anomalous magnetic dipole moment of the muon, lepton flavor universality, or, most recently, the W boson mass [1–3]. Nowadays, it is widely assumed that the SM is only one aspect of a broader, as yet unknown theory.

Particle collisions are analyzed to test the scope of the SM and to find more manifestations of physics beyond the SM (BSM). The highest ever reached energy in collisions of fundamental particles is obtained by the Large Hadron Collider (LHC). This thesis documents measurements using data from proton-proton (pp) collisions recorded at the Compact Muon Solenoid (CMS) experiment in the years 2016, 2017, and 2018. The LHC apparatus and CMS experiment are discussed in Chapter 2.

One challenge to perform precision measurements of quantities predicted by the SM or BSM models is the understanding of the total rate of pp collisions — the luminosity. The LHC started pp collisions in 2009 and since then steadily increased the instantaneous luminosity and energy to provide more data. This allows to investigate more rare processes and achieve measurements with higher statistical precision. In the upcoming years, the beam intensity will be further increased. It will reach its peak during the operation of the High-Luminosity LHC (HL-LHC) expected to start in 2029, where up to 200 pp collisions every 25 ns are targeted. Further developments in the methods to measure the luminosity precisely in such extreme conditions are required.

A novel method is discussed in this thesis: the determination of luminosity from the Z boson production rate. The method has unique features and completely different systematic uncertainties with respect to conventional ways of measuring luminosity. This allows to perform stringent cross-checks but also to combine the different estimates. Unlike conventional methods, the same Z boson events used to determine the luminosity from their production rate, can also be used to monitor the detector response. A summary of the studies is presented in Chapter 3.

The large amount of data recorded in the years 2016–2018 and the unprecedented center-of-mass energy of 13 TeV give the prime opportunity to study rare physics processes

in more detail. One of these rare processes is the production of single top quarks in association with Z bosons (tZq). The top quark is the heaviest particle of the SM and expected to play a special role with respect to possible physics beyond the standard model. Unlike any other quarks, the top quark decays before forming hadrons and provides the unique possibility to test the properties of a bare quark, such as its charge or spin. In pp collisions at the LHC, top quarks are mainly produced in pairs via the strong interaction. More rarely, they can also be produced singly via the weak force through the vertex with a b quark and W boson (W-t-b). This channel allows to study the chiral structure of the SM in detail. Single top quarks are expected to be produced with a high level of polarization which can be modified by anomalous couplings. A deviation from SM predictions is a strong hint of BSM physics. A theoretical overview of top quark physics, with the focus on single production, is given is Section 1.3. The tZq process offers sensitivity to the electroweak couplings of the top quark to the Z boson and between three vector bosons. Additionally, through the necessity of a b quark in the initial state, and through the asymmetry of top quark and antiquark production in pp collisions, the process is prone to many modeling assumptions which, in turn, are tested by this measurement. Discussions about the theoretical aspects and arguments for this analysis are given in Section 1.4.

In this thesis, many aspects of the tZq process are studied in detail as documented in Chapter 4. Events with three leptons, either electrons or muons, are utilized as they give the cleanest signature. The reconstruction of the Z boson and top quark candidates and the identification of the associated jet are investigated. Various sources of background are investigated and estimated using simulated samples. Special care is taken of background that contributes through misidentified leptons. As simulated samples do not provide a satisfactory description, this kind of background is estimated from control samples in data. To enhance the sensitivity of the measurements, a multiclass neural network is designed to separate signal from background events. Calibrations on simulated samples are applied and systematic uncertainties are studied. Binned maximum likelihood fits are performed to extract the desired quantities from the data. Systematic uncertainties are included as nuisance parameters and constrained in the fit. Among the measured quantities is the inclusive cross section of tZq, from which an estimate on the CKM-matrix element V_{tb} is derived. Several differential cross sections are measured as functions of kinematic observables that are sensitive to modeling assumptions in SM predictions or to BSM effects. Parton- and particle-level definitions are used to correct for detector and hadronization effects and to obtain experiment-independent results. Finally, the top quark spin asymmetry, which is proportional to the top quark spin polarization, is measured. The results are discussed and compared to SM predictions with different assumptions on the parton distribution functions (PDFs).

1. Theoretical foundations of single top quark physics at the LHC

The standard model of particle physics (SM) is the undisputed theory to describe all fundamental particles known to date. It also describes their interaction through the strong, electromagnetic, and weak forces. A summary of the most important aspects is given in Section 1.1, more detailed descriptions are given for example in Refs. [4–6]. The SM is also known to be incomplete; for example, the gravitation, dark matter, or dark energy are not addressed by this model. This means that at a high, hitherto unknown, energy scale the SM no longer accurately describes the observations, and physics beyond the standard model (BSM) must be found. Rigorous tests of the SM are performed in particle collision experiments through deep inelastic scatterings. At the forefront are proton-proton (pp) collisions, where data in the highest energy regime ever reached by particle colliders are produced. Such data are investigated in the analyses presented in this thesis. A theoretical overview about pp collisions is given in Section 1.2. Among those data are events from rare processes containing multiple heavy particles that have never been studied in great detail before. Events containing the heaviest known particle, the top quark, are of particular interest: the associated top quark production with other heavy particles such as the Z boson can reveal possible new phenomena in the interactions between those. Here, the electroweak production of top quarks (single top) is even more interesting since new interactions in top quark electroweak couplings are the least constrained. In the context of this thesis, a theoretical overview about top quark production is given in Section 1.3. Subsequently, a detailed discussion of the single top quark production in association with a Z boson is given in Section 1.4.

1.1. The standard model of particle physics

The SM is based on quantum field theory (QFT) which obeys the laws of quantum mechanics and special relativity. For each particle, a separate quantum field exists characterized by its quantum numbers such as charge and spin. A particle can be interpreted as an excited state of its underlying quantum field. The structure of the SM is understood by its underlying symmetries. Compliance with special relativity implies that the theory has to be invariant under Lorentz transformations, which are rotations and boosts of the coordinate system. The behavior of a quantum field under Lorentz transformation is characterized by its spin. It classifies particles into fermions (half integer spin) and bosons (integer spin). The particles of the SM together with their electric charge, spin, and mass are summarized in Fig. 1.1. They are explained in the following.

Fermions follow the Fermi–Dirac statistics which states, that according to Pauli's exclusion principle, two particles with the same quantum numbers can not exist at the same

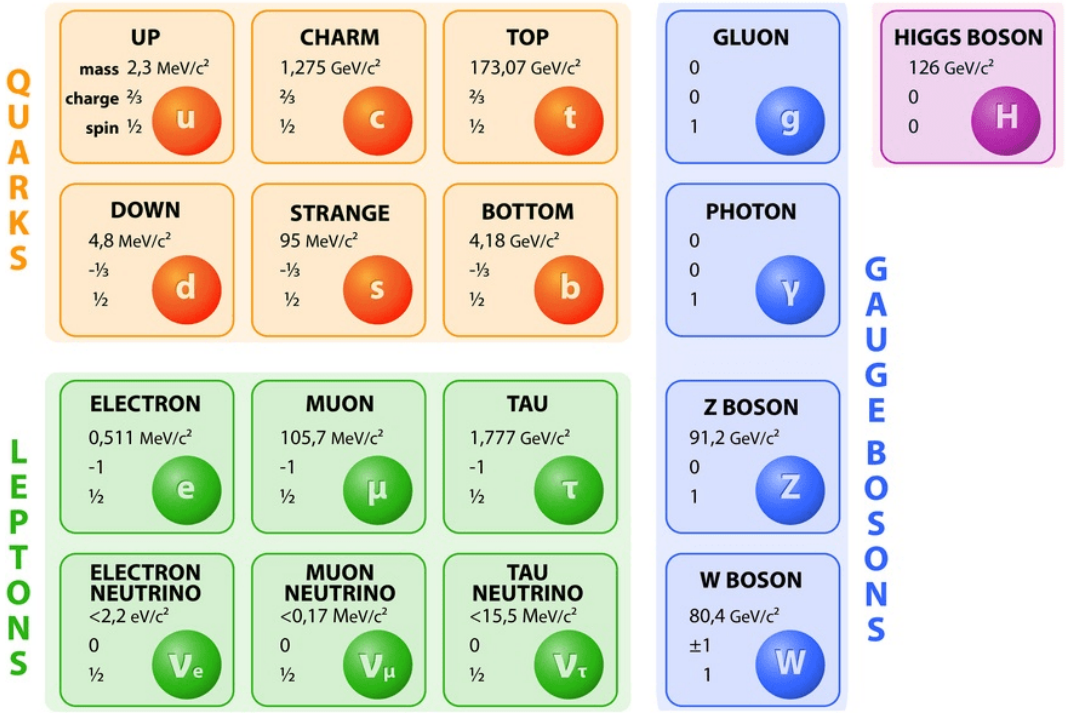

Fig. 1.1.: Summary of all known elementary particles. The three generations of quarks (yellow) and leptons (green) are shown in the first three columns. The fourth column shows the force carrier of the SM (blue) while the Higgs boson (purple) is shown on the right as the only spin 0 particle of the SM. From Ref. [7]

point in space and time. Fermions with the same quantum number must therefore be separated from each other and form thus the known matter of the universe. The elementary fermions that we know today are the quarks which are subject to all fundamental forces, the charged leptons which are affected by all but the strong interaction, and the neutral leptons, neutrinos, which are assumed to be massless in the SM and only interact via the weak force.

The quarks and leptons exist in three generations. The particles of the second and third generation are identical copies of the particles of the first generation, with the exception of their mass. Two types of quarks exist in each generation, known as up-type and down-type. The up-type quarks of the first to third generation are the up (u), charm (c), and top (t) quarks. Corresponding down-type quarks are in order the down (d), strange (s), and bottom (b) quarks. The three generations of charged leptons are electrons (e), muons (μ), and tau leptons (τ). Neutrinos are named correspondingly as electron (ν_e), muon (ν_μ), and tau (ν_τ) neutrinos. The six different kinds of quarks and leptons are often referred to as the six quark and lepton "flavors". For each fermion, an antiparticle exists that has the opposite sign of all quantum numbers but the same mass.

The other type of particles in the SM are the bosons that obey the Bose–Einstein statistics where two bosons can take the same quantum state. Bosons with spin 1 behave like a vector under Lorentz transformation and are thus called vector bosons. They are force carriers in the SM, including gluons (g) for the strong force, electroweak ($W^\pm$ and Z) bosons for the weak force, and the photon (γ) for the electromagnetic interaction. Bosons with spin 0 behave like a scalar, which means they are invariant under Lorentz

transformation. The only elementary scalar boson in the SM that we know today is the Higgs (H) boson. The strength of the Higgs boson interaction with SM particles is governed by their masses.

The fact that there are exactly three fermion generations in the SM has not yet been fundamentally understood. Experiments however have shown no evidence for particles of a fourth generation. For example, measurements of the Z boson width from experiments at the CERN LEP can exclude a fourth neutrino generation in a wide mass range [8].

Gauge theory

The equation of motion for a field Φ is obtained from the principle of the least action

$$\frac{\partial \mathcal{S}[\Phi]}{\partial \Phi} = 0 \,, \tag{1.1}$$

where $\mathcal{S}$ is a functional that depends on the field and can be written as

$$\mathcal{S}[\phi] = \int \mathcal{L}(\Phi(x_\mu), \partial_\mu \Phi(x_\mu), x_\mu) dx_\mu \,. \tag{1.2}$$

Here, the Lagrangian density $\mathcal{L}$ contains the full information of the system. It is needed to make predictions of deep inelastic scatterings and particle decays.

The SM interactions are described through local internal symmetries of $\mathcal{L}$. As detailed later, the `SU(3)` symmetry represents the strong interaction. At large energy scale, the `SU(2)` $\times$ `U(1)` symmetry represents the electroweak interaction, while at low energy, the `SU(2)` symmetry is broken which leads into the split into electromagnetic and weak interactions. An internal symmetry (also known as gauge symmetry) corresponds to a transformation that acts on the quantum field itself and leaves physical observables unchanged. Local means that the transformation depends on the space time, which is necessary to fulfill the causality principle. The force carriers of the SM, the bosons, are required to restore the symmetry after a transformation of the fermion fields. Hence, they are often called gauge bosons. Noether's theorem states, that each symmetry of $\mathcal{L}$ is related to a conserved quantity [9]. These conserved quantities are identified with charges to which the gauge bosons couple and represent further quantum numbers.

1.1.1. Free fermion fields

Under the Lorentz transformation, fermions are represented by two-component fields called spinors. Spinors can be distinguished into two different states, depending on the orientation of their spin: right chirality with spin $+1/2$ and left chirality with spin $-1/2$. Under the parity transformation, which mirrors the space and turns a right handed coordinate system into a left handed one, right chiral spinors transform into left chiral ones. Since quantum electrodynamic (QED) was found to be invariant under parity transformation, fermions are described as having right and left chiral components. The two chirality states of the fermion can be put together in a bispinor:

$$\Psi = \begin{pmatrix} \psi_\mathrm{L} \\ \psi_\mathrm{R} \end{pmatrix} \,, \tag{1.3}$$

which is a four component field. The Lagrangian of a free fermion field can be written as

$$\mathcal{L}_{\text{Dirac}} = -m\bar{\Psi}\Psi + i\bar{\Psi}\gamma^{\mu}\partial_{\mu}\Psi \ , \tag{1.4}$$

which is invariant under parity transformation. The Dirac adjoint $\bar{\Psi} = \Psi^{\dagger}\gamma^{0}$ and the 4×4 Dirac gamma matrices γ^{μ} facilitate a Lorentz invariant notation of the Lagrangian. Greek indices (μ, ν) hereby denote the four spacetime indices and take on the values $0, 1, 2, 3$.

1.1.2. Quantum chromodynamics

The strong interaction is described in the theory of quantum chromodynamics (QCD). The underlying symmetry is given by the SU(3) group, connected to a conserved quantity called color charge. Fermions interacting via the strong force, i.e. quarks, carry one color charge. The charges are labeled with red (r), green (g), and blue (b), chosen as analogy to the additive color mixing model: three quarks with different colors can form a color-neutral bound state, called baryon. Antiquarks carry anticolor, hence a color-neutral bound state can also exist as a quark-antiquark pair, called meson. Mesons and baryons are collectively denoted as hadrons.

Under SU(3) transformations, quarks are organized in a color triplets $Q = \left(\mathrm{q_r}, \mathrm{q_g}, \mathrm{q_b}\right)^{\mathrm{T}}$, where q_i is a fermion field for a quark with color i, represented, for example, by a bispinor. Leptons do not interact via the strong force and are described as color singlets, which means they do not carry a color charge. For the Lagrangian to be invariant under SU(3) transformations, the existence of vector boson fields, the gluon fields G_{μ}^{A}, is assumed. Capital Roman indices (A, B, C) take values from 1 to 8 here and in the following. The Lagrangian then becomes invariant under the simultaneous transformation of the quark triplet and gluon fields,

$$Q \to \mathrm{e}^{ig_s T^A \alpha^A(x)} Q \ , \qquad G_{\mu}^{A} \to G_{\mu}^{A} + \partial_{\mu}\alpha^{A}(x) \ , \tag{1.5}$$

where g_s is the coupling constant that indicates how strong gluons couple to quarks, $\alpha^{A}(x)$ are phase factors describing the transformation, and T^{A} are the eight generators of the SU(3) group. Since there are eight generators, eight gluon fields exist. They carry each one color and one anticolor charge. Vividly, a SU(3) transformation means that quarks are interchanged within a triplet with simultaneous switching the colors of the gluon fields. Physical observables are thereby unaltered, hence the SU(3) symmetry is not broken. The QCD Lagrangian is given by

$$\mathcal{L}_{\text{QCD}} = \sum \bar{Q}\left(i\gamma^{\mu}D_{\mu} - m\right)Q - \frac{1}{4}G_{\mu\nu}^{A}G_{A}^{\mu\nu} \ , \tag{1.6}$$

$$D_{\mu} = \partial_{\mu} - ig_s T^{A} G_{\mu}^{A} \ , \tag{1.7}$$

$$G_{\mu\nu}^{A} = \partial_{\mu}G_{\nu}^{A} - \partial_{\nu}G_{\mu}^{A} + g_s f^{ABC} G_{\mu}^{B} G_{\nu}^{C} \ , \tag{1.8}$$

where the sum goes over all six quark flavors. The covariant derivative D_{μ} provides the kinematic term of the quark fields and their interaction with the gluon fields. The field strength tensor $G_{\mu\nu}^{A}$ describes the kinematics of the gluon fields, where f^{ABC} is the structure constant defined by $\left[T^{A}, T^{B}\right] = if^{ABC}T^{C}$. The fact that the generators do not

commute classifies the SU(3) group as nonabelian. This leads to the gluon self-couplings. Resulting couplings between three and four gluon can be illustrated as

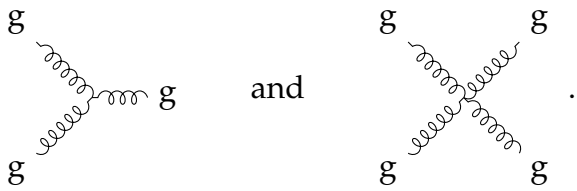

(1.9)

The diagrams are shown in the Feynman representation where time reads horizontally from left to right and space separation reads vertically. It is commonly used to describe interactions since it directly allows to translate the elements of the diagrams (vertices and lines) into a formula to ultimately calculate the probability amplitude of a process. Depending on the type, interacting particles may be shown by straight (fermions), curly (gluons), wavy (electroweak bosons), or dashed (Higgs boson) lines. Every vertex represents the interaction between the attached particles and brings a coupling strength coefficient to the calculation. If the coupling strength is smaller than 1, processes with more vertices are less likely to happen. This means, a perturbative approach is justified in the calculation.

The effective coupling strength of the QCD interaction depends on the energy scale k and is given by

$$\alpha_S(k^2) = \frac{g_s^2(k^2)}{4\pi} \approx \frac{\alpha_S({\mu_R}^2)}{1 + \beta_0 \alpha_S({\mu_R}^2) \ln\left(\frac{k^2}{{\mu_R}^2}\right)} , \tag{1.10}$$

where $\alpha_S({\mu_R}^2)$ is the coupling constant at a given energy scale, μ_R, and β_0 is a dimensionless constant. It is defined as $\beta_0 = {}^{33-2n_f}/_{12\pi}$ with n_f being the number of quark flavors that can be considered massless at the energy scale μ_R. The energy scale μ_R is the renormalization scale. It needs to be introduced in a procedure called renormalization to absorb ultraviolet divergent terms arising from large momenta in internal loops of so-called "virtual" particles such as

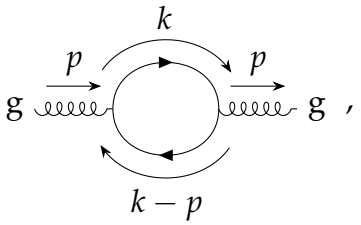

(1.11)

where p is the momentum of the incoming and outgoing gluon and k is the unconstrained momentum carried by the virtual particle. According to Eq. (1.10), once $\alpha_S({\mu_R}^2)$ is determined from the experimental data, the coupling strength can be evaluated at any other energy scale. This feature is generally known as the "running" of a Lagrangian parameter, here the coupling constant, with energy. At the energy scale corresponding to the Z boson mass, $m_Z = 91.188\,\text{GeV}$, the α_S constant is determined to be 0.1181 ± 0.0011 [10]. Towards higher energies, α_S decreases logarithmically. Since higher energies are in this respect equivalent to smaller distances between interacting particles, this means that quarks and

gluons can move practically freely at small distances. This effect is called "asymptotic freedom". Conversely, α_S becomes larger for small energies and large distances. In a given process, the growth in the coupling strength at low energies leads to an increase of the size of terms with multiple interaction vertices. As a consequence, the expansion of the probability amplitude in powers of the coupling strength will not converge anymore. The calculations are therefore based on nonperturbative phenomenological approaches. The energy at which QCD becomes nonperturbative is given by the QCD scale Λ_{QCD}. Its exact value depends on the theory choice and is in the order of 200–300 MeV [11]. The phenomenon is called "confinement" as the stronger interaction between quarks and gluons at lower energies confines them together. When for example two quarks are pulled apart, the QCD potential energy of the system increases linearly [12]. Since the time to form hadrons is in the order of about $1/\Lambda_{QCD} \approx 3 \cdot 10^{-24}$ s, no bare quarks or gluons but only color-neutral objects can be observed directly. The top quark is special in this respect because it has a decay time of about $5 \cdot 10^{-25}$ s that is shorter than the hadronization time and can therefore be considered as free particle [10]. Although it cannot be measured directly, it passes on its properties such as spin and charge to the decay products. Thus, the top quark is the only quark that allows studies of the bare quark characteristics.

1.1.3. Electroweak theory

The Wu experiment from 1956 found that the weak interaction is, unlike QED, not invariant under parity transformation (P-violation) [13]. This was contrary to widespread assumptions at the time. Later it was found that the P-violation is maximal for the weak interaction, meaning that only fermions with left chirality take part in the weak interaction while those with right chirality do not. Eventually, the weak interaction was found to be together with the electromagnetism a manifestation of a more general force, the electroweak (EW) interaction. The theory of EW unification was developed by Glashow [14], Salam [15], and Weinberg [16] who were awarded with the physics Nobel prize in 1979. Below an energy of about 246 GeV, the underlying symmetry spontaneously breaks and the EW interaction disintegrates in the two forms. The symmetry breaking is described by the Higgs mechanism as outlined later in this section.

Before symmetry breaking

Before symmetry breaking, the EW theory has a $\mathtt{SU(2)} \times \mathtt{U(1)}$ symmetry. The charges of the $\mathtt{U(1)}$ and $\mathtt{SU(2)}$ symmetries are the hypercharge Y_W and the third component of the weak isospin T_3. The electromagnetic charge is given by the Gell-Mann–Nishijima equation [17, 18]:

$$Q = \frac{Y_W}{2} + T_3 \,. \tag{1.12}$$

To describe the P-violating nature of the weak interaction, the $\mathtt{SU(2)}$ transformation only acts on fermions with left chirality. Therefore, left chiral fermions are organized in isospin doublets L. Fermions with right chirality do not transform under the $\mathtt{SU(2)}$ group and are considered as weak isospin singlets r. The fermion fields of the SM and their charges with regard to the EW theory are summarized in Table 1.1. Since neutrinos are considered

as massless and only interact via the weak interaction, they only occur with left chirality in the SM.

Table 1.1.: The fermion fields of the SM and their EW charges are listed. Quarks and leptons with left chirality are organized in isospin doublets, or with right chirality in isospin singlets. Under the assumption that the neutrino mass is zero, there is no right handed neutrino in the SM. For each fermion, an antifermion exists with an opposite charge and chirality.

Fermions	Generation 1	Generation 2	Generation 3	Weak hypercharge Y_W	3rd comp. of isospin T_3	Electric charge Q
Quarks	$\begin{pmatrix} u_L \\ d_L \end{pmatrix}$	$\begin{pmatrix} c_L \\ s_L \end{pmatrix}$	$\begin{pmatrix} t_L \\ b_L \end{pmatrix}$	$+1/3$	$+1/2$	$+2/3$
				$+1/3$	$-1/2$	$-1/3$
	u_R	c_R	t_R	$+4/3$	0	$+2/3$
	d_R	s_R	b_R	$-2/3$	0	$-1/3$
Leptons	$\begin{pmatrix} \nu_{e\,L} \\ e_L \end{pmatrix}$	$\begin{pmatrix} \nu_{\mu\,L} \\ \mu_L \end{pmatrix}$	$\begin{pmatrix} \nu_{\tau\,L} \\ \tau_L \end{pmatrix}$	-1	$+1/2$	0
				-1	$-1/2$	-1
	e_R	μ_R	τ_R	-2	0	-1

The U(1) and SU(2) transformations act on fermion and vector boson fields similar to the SU(3) transformation in QCD. The difference is given by the generators of the symmetry groups. Since there are three generators of the SU(2) group, also three gauge boson fields W_μ^a exist. Here and in the following, small Roman indices (a, b, c) take on the values $1, 2, 3$. The U(1) group has just one generator leading to only one gauge boson field B_μ. The U(1) transformation is essentially a phase shift of the fermion field with an arbitrary angle, which gets absorbed by B_μ. The SU(2) symmetry means that physics are unchanged under rotation and exchange of two particles in an isospin doublet with simultaneous interchanging of the W_μ^a. The kinematic term of the EW Lagrangian for fermions is given by

$$\mathcal{L}_{\mathrm{EW,f}} = \sum \bar{L} i\gamma^\mu D_\mu L + \sum \bar{r} i\gamma^\mu D_\mu r \,, \tag{1.13}$$

$$D_\mu = \partial_\mu - i\frac{g'}{2}\hat{Y}_W B_\mu - ig\hat{T}^a W_\mu^a \,, \tag{1.14}$$

where the two sums include all isospin doublets and singlets, respectively. The g and g' are dimensionless coupling parameters. The $\hat{Y}_W$ and $\hat{T}$ are the hypercharge and weak isospin operators, which are the generators of the U(1) and SU(2) group, respectively. The covariant derivative D_μ incorporates the interaction between the fermion and gauge boson fields. The kinematic term for the gauge bosons is given by

$$\mathcal{L}_{\mathrm{EW,g}} = -\frac{1}{4} B^{\mu\nu} B_{\mu\nu} - \frac{1}{4} W_a^{\mu\nu} W^a_{\mu\nu} \,, \tag{1.15}$$

$$B^{\mu\nu} = \partial_\mu B_\nu - \partial_\nu B_\mu \,, \tag{1.16}$$

$$W_a^{\mu\nu} = \partial_\mu W_\nu^a - \partial_\nu W_\mu^a + g f^{abc} W_\mu^b W_\nu^c \,, \tag{1.17}$$

with f^{abc} being the structure constant of the generators of the SU(2). Similar to the SU(3), also the SU(2) is a nonabelian group, leading to the self-interaction between the gauge boson fields W_ν^a. The U(1) on the other hand is abelian and no self-interaction of B_μ appears.

The Higgs mechanism

Under SU(2) symmetry, no mass term for vector boson fields is allowed, and only equal masses for fermions within an isospin doublet are allowed. From experiments it is known that this is not the case and the symmetry has to be broken at low energies. An explanation of spontaneous symmetry breaking and the generation of mass terms for the vector bosons is given by the Higgs–Brout–Englert mechanism [19, 20]. After the discovery of the Higgs boson in 2012 by the CMS and ATLAS Collaborations [21, 22], Peter Higgs and Francois Englert were awarded the 2013 Nobel prize in physics.

An isospin doublet of two complex scalar fields $\Phi = \left(\Phi^+, \Phi^0\right)^{\mathrm{T}}$ with positive and neutral electric charge can be included in the Lagrangian without breaking the symmetry. The Lagrangian of the Higgs field can be written as

$$\mathcal{L}_{\mathrm{H}} = (D_\mu \Phi^\dagger)(D^\mu \Phi) - V(\Phi) \,, \tag{1.18}$$

$$V(\Phi) = -\rho^2 \Phi^\dagger \Phi + \lambda \left(\Phi^\dagger \Phi\right)^2 \,, \tag{1.19}$$

with $V(\Phi)$ being the Higgs potential. The real parameter λ is the Higgs quartic coupling and has to be positive to ensure that the EW vacuum is not unstable [23]. The parameter ρ^2 defines the minimum of $V(\Phi)$ for a given positive value of λ as illustrated in Fig. 1.2. At very large energy ρ^2 is negative and $V(\Phi)$ has exactly one minimum at $\Phi_{\mathrm{min}} = (0,0)^{\mathrm{T}}$.

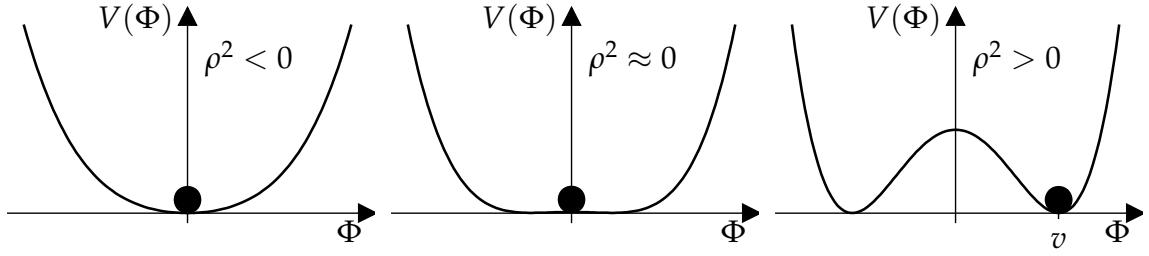

Fig. 1.2.: 1D profile of the Higgs potential before symmetry breaking (left) at a critical energy (middle) and after symmetry breaking (right).

As the universe cools down, the values for λ and ρ^2 change. At the point where ρ^2 gets positive, an infinite number of minima arise given by $\Phi_{\mathrm{min}} = \mathrm{e}^{i\phi} \left(0, \sqrt{\rho^2/2\lambda}\right)^{\mathrm{T}}$ for every real value of ϕ. In reality, one of the minima is spontaneously chosen which breaks the SU(2) symmetry. As physics does not depend on which exact minima is developed, the choice of $\Phi_{\mathrm{min}} = (0, v/\sqrt{2})^{\mathrm{T}}$ can be made with the vacuum expectation value $v = \sqrt{\rho^2/\lambda}$. To learn about the physical properties of the Higgs doublet, an expansion can be made around the new minimum, which can be written as

$$\Phi = \mathrm{e}^{i\Theta_i \frac{\sigma_i}{2}} \begin{pmatrix} 0 \\ \frac{v+H}{\sqrt{2}} \end{pmatrix} \quad \rightarrow \quad \begin{pmatrix} 0 \\ \frac{v+H}{\sqrt{2}} \end{pmatrix} \,. \tag{1.20}$$

The pre factor in this equation is in the form of an SU(2) transformation analogous to Eq. (1.5). A particular transformation, the unitary gauge, is chosen to absorb the three free parameters Θ_i. One Higgs field H remains. Using the new Φ in Eq. (1.18) introduces a non-diagonal mass matrix for the vector boson fields. The gauge boson fields of the experimentally observable mediator particles result from the mass eigenstates of the original fields. The new mass eigenstates are given by

$$\begin{pmatrix} W_\mu^+ \\ W_\mu^- \end{pmatrix} = \begin{pmatrix} 1/\sqrt{2} & -1/\sqrt{2} \\ 1/\sqrt{2} & 1/\sqrt{2} \end{pmatrix} \begin{pmatrix} W_\mu^1 \\ W_\mu^2 \end{pmatrix} \tag{1.21}$$

and

$$\begin{pmatrix} A_\mu \\ Z_\mu \end{pmatrix} = \begin{pmatrix} \cos\Theta_W & +\sin\Theta_W \\ -\sin\Theta_W & \cos\Theta_W \end{pmatrix} \begin{pmatrix} B_\mu \\ W_\mu^3 \end{pmatrix} , \tag{1.22}$$

where Θ_W is the Weinberg angle, also known as the weak mixing angle since it mixes the fields of the U(1) and SU(2) groups. This mixing is reflected in the different masses of the Z and W bosons given by $m_Z = {}^{m_W}/_{\cos\Theta_W}$. The Θ_W is a free parameter of the SM and relates also the coupling constants g and g' to the electromagnetic charge e as $e = g\sin\Theta_W = g'\cos\Theta_W$. The massive Z_μ and $W_\mu^\pm$ boson fields mediate the neutral and charged current interactions through the Z and $W^\pm$ bosons. Their masses are given by

$$m_Z = \frac{1}{2} v \sqrt{g^2 + g'^2} , \tag{1.23}$$

$$m_W = \frac{1}{2} v g , \tag{1.24}$$

while the mass of the Higgs boson is given by

$$m_H = \sqrt{2\lambda v^2} . \tag{1.25}$$

The large masses of the Z and W bosons are responsible for the short range interaction as it translates to short lifetimes of less than 10^{-24} s [10]. The weak interaction at energies well below the masses of its mediators is approximated by a point-like interaction with an effective coupling strength of $G_F \approx 10^{-5}\,\mathrm{GeV}^{-2}$, known as the Fermi constant [10].

The Z and W bosons decay to all three generations of leptons and all quarks except the top quark. The so-called on-shell branching ratios of the Z and W bosons are shown in Fig. 1.3 where the fraction to quarks is the largest, since they exist in three different colors. In the SM for the limit that the masses of the decay products can be neglected over the mass of the gauge boson (e.g. $m_W \gg m_\tau$, where m_τ is the mass of the τ lepton), the gauge bosons couple to all charged leptons with the same strength, a property called lepton universality. However, evidence for lepton universality violation was measured in B^+ mesons decaying into K^+ mesons in association with lepton pairs [2]. For the ratio of decays into electrons and muons, a tension of 3.1 standard deviations away from the SM prediction was observed. It remains to be seen if this is an effect of BSM physics.

The A_μ field in Eq. (1.22) is responsible for the electromagnetic interaction mediated by photons which remain massless. The coupling strength of the electromagnetic interaction is given by the fine-structure constant α_{EM} which converges to a value of about $1/137$ at zero energy and increases with higher energy. At the energy scale investigated in this thesis, the electromagnetic interaction is stronger than the weak interaction but much weaker than α_S.

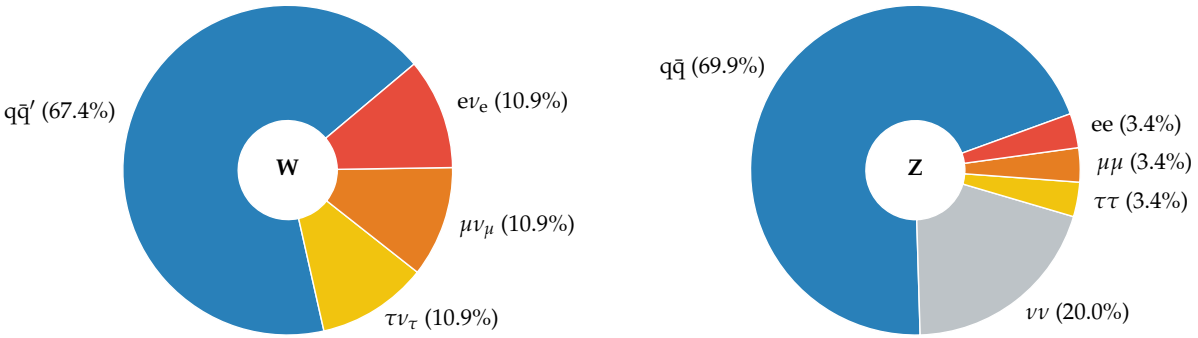

Fig. 1.3.: Fractions of the different decay modes of the W boson (left) and Z boson (right). Numbers are taken from Ref. [10].

Fermion masses

Coupling terms of the Higgs field with fermion fields can be included in the Lagrangian without breaking the SU(2) symmetry. This is described by the Yukawa interaction, originally developed to explain the attractive strong force via the exchange of spin 0 bosons like pions [16]. The Higgs-fermion coupling terms are in the form of

$$\mathcal{L}_{\text{Yukawa},f} = -\lambda_f \left(\bar{L}\Phi r + h.c.\right) \ , \tag{1.26}$$

where λ_f is a coupling constant and $h.c.$ denotes the hermitian conjugate. After symmetry breaking the Higgs field develops a new vacuum and in the case of electrons Eq. (1.26) becomes:

$$\mathcal{L}_{\text{Yukawa,e}} = -\frac{\lambda_e}{\sqrt{2}}\left((\bar{\nu}_{e\,L}, \bar{e}_L)\begin{pmatrix} 0 \\ v+H \end{pmatrix} e_R + h.c.\right) \tag{1.27}$$

$$= -\frac{\lambda_e v}{\sqrt{2}}\bar{e}_L e_R - \frac{\lambda_e H}{\sqrt{2}}\bar{e}_L e_R + h.c. \ , \tag{1.28}$$

where the first term acts as a mass of the electron and the second term describes the Yukawa coupling of the Higgs field, H, to the electron field. As λ_e appears in both terms, the Higgs–Yukawa coupling has a linear relation to the fermion masses; the heavier a fermion is, the stronger it couples to the Higgs field.

Quark flavor mixing

The quarks in Table 1.1 are presented in their EW eigenstates where flavor changing charged currents through W bosons lead to a transition of two quarks in a doublet, but not between two generations. It is, however, well known that transitions between two quark generations appear. Additionally, similar to P violation, observations have shown that the simultaneous transformation of charge conjugation, i.e. transforming a particle in its antiparticle, and parity (CP) is not conserved in the quark sector of EW interactions [24]. Both can be explained as mass eigenstates of the quarks, q, are a mixture of their EW

eigenstates q', formulated as:

$$\begin{pmatrix} \mathrm{d}' \\ \mathrm{s}' \\ \mathrm{b}' \end{pmatrix} = V \begin{pmatrix} \mathrm{d} \\ \mathrm{s} \\ \mathrm{b} \end{pmatrix} = \begin{pmatrix} V_{\mathrm{ud}} & V_{\mathrm{us}} & V_{\mathrm{ub}} \\ V_{\mathrm{cd}} & V_{\mathrm{cs}} & V_{\mathrm{cb}} \\ V_{\mathrm{td}} & V_{\mathrm{ts}} & V_{\mathrm{tb}} \end{pmatrix} \begin{pmatrix} \mathrm{d} \\ \mathrm{s} \\ \mathrm{b} \end{pmatrix} . \tag{1.29}$$

The 3×3 matrix V is the Cabibbo–Kobayashi–Maskawa (CKM) matrix [25, 26] where the quadrature of each element gives the probability of a transition. The matrix needs to be unitary where five of the nine free parameters are unphysical and absorbed as phases of the quark fields. Thus, V has four free parameters: three mixing angles and one phase responsible for CP violation. A violation of unitarity would be a clear sign of new physics. A variety of different experiment probe the properties of the CKM matrix [10]. Such a sign might be present as independent measurements show that $|V_{\mathrm{ud}}|^2 + |V_{\mathrm{us}}|^2 + |V_{\mathrm{ub}}|^2 = 0.998 \pm 0.0005$, which is 3 standard deviations away from unity. Using unitarity constraints, the best known values of the matrix elements are extracted from a combined fit to measurements as:

$$|V| = \begin{pmatrix} 0.97401 \pm 0.00011 & 0.22650 \pm 0.00048 & 0.00361^{+0.00011}_{-0.00009} \\ 0.22636 \pm 0.00048 & 0.97320 \pm 0.00011 & 0.04053^{+0.00083}_{-0.00061} \\ 0.00854^{+0.00023}_{-0.00016} & 0.03978^{+0.00082}_{-0.00060} & 0.999172^{+0.000024}_{-0.000035} \end{pmatrix} . \tag{1.30}$$

Due to small off-diagonal values of V, transition between different generations are largely suppressed. This results in a long lifetime of b hadrons in the order of 1.5 ps [10]. Thus, b hadrons with an energy in the order of a few GeV travel in average a few mm to cm before they decay.

Neutrino masses

Assuming neutrinos to be massless in the SM, neutrinos with right chirality do not exist. Observations of neutrino oscillations, however, contradicts this assumption [27–29]. Such oscillations can be explained through an analogon of the CKM matrix for neutrinos, the Pontecorvo–Maki–Nakagawa–Sakata (PMNS) matrix [30, 31], which requires the neutrinos to have masses. The most straight forward approach to describe this in the SM would be to include neutrinos with right chirality. This would allow to add a so-called Dirac mass term in the form of Eq. 1.28. The existence of the so-called "sterile" neutrinos, which do not interact via any of the fundamental forces in the SM, would be extremely difficult to verify experimentally. To date, experiments have only been able to put an upper limit on the masses of neutrinos. The most stringent limit on the mass of ν_{e} from direct measurements was reported by the KATRIN experiment and is $m_{\nu_{\mathrm{e}}} < 0.8\,\mathrm{eV}$ at 90% confidence level [32]. Measurements with the KATRIN experiment are still ongoing and expected to push the limit down to 0.2 eV.

1.2. Proton proton collisions

Scattering experiments have a great history of success in physics. They are the most important instrument with which experimental physicists established particle physics and

brought it to its present state. One of the most widely known scattering experiments is the Rutherford experiment performed in 1911 [33]. In this experiment, charged particles were shot onto a gold foil where an elastic scattering in the electromagnetic potential of the gold atoms occurred. The measured quantity was the differential cross section $\mathrm{d}\sigma/\mathrm{d}\Omega$. It is defined as the number of particles scattered into a solid angle per time unit divided by the incident flux. Or, in other words, the probability for one single particle to be scattered in a given phase space region. Ultimately, the experiment led to the development of the Bohr atomic model, where the atom has a very small nuclei and electrons are considered as moving around it in orbits. Nowadays, deep inelastic scatterings are performed at much higher energies and the SM has been developed to describe the observations. However, the basis of a vast majority of studies continue to measure inclusive or differential cross sections of different processes. So are the results presented in this thesis.

In proton-proton (pp) collisions the main interaction, known as hard scattering, is carried out by two constituents of the proton, quarks or gluons, together denoted as partons. In pp collisions at the LHC, a wide range of processes are governed by the QCD interaction, meaning that the probability amplitude of the process can be expanded in powers of α_S. As discussed earlier, at the high-energy regime of the LHC, α_S becomes small and the perturbative expansion of the hard scattering can converge. The full picture of pp collisions is however more complicated as it contains the probability of partons inside protons to contribute to the hard scattering. Besides this, particles that are produced in a hard scattering undergo a chain of decay, radiation, and hadronization. Since every part of the collision proceeds at a different energy regime, a factorization ansatz is often employed, dealing with every part separately.

The appearance of a specific parton α inside a proton that carries the fraction of the total proton momentum, x_α, is given by the parton distribution function (PDF) $F_\alpha(x_\alpha;\mu_F)$. The PDF depends on the energy scale μ_F, usually denoted as factorization scale, and is explained in Section 1.2.2. The differential cross section of pp scattering at a center of mass energy $\sqrt{s}$ is then given by

$$\mathrm{d}\sigma\left(\mathrm{pp}\to\{f\};s\right)=\sum_{\alpha,\beta}\int \mathrm{d}x_\alpha \mathrm{d}x_\beta F_\alpha(x_\alpha;\mu_F)F_\beta(x_\beta;\mu_F)\mathrm{d}\hat{\sigma}\left(\alpha\beta\to\{f\};s\right)\ , \tag{1.31}$$

where $\hat{\sigma}\left(\alpha\beta\to\{f\};s\right)$ is the cross section of the two initial partons α and β to produce a set of final-state particles $\{f\}$. The sum in Eq. (1.31) takes into account different partons in all possible initial states (such as spin) that contribute to the final state.

Effects of the proton remnants and the parton shower that describes the emission of gauge bosons or gluon splitting of the initial- or final-state particles are nonperturbative. Further, the formation of quark bound states known as hadronization has to be described by other means. To model collision events, as much theory inputs as practically possible are used and supplemented by phenomenological models. The individual steps that occur in a pp collision are illustrated in Fig. 1.4 and described in the following.

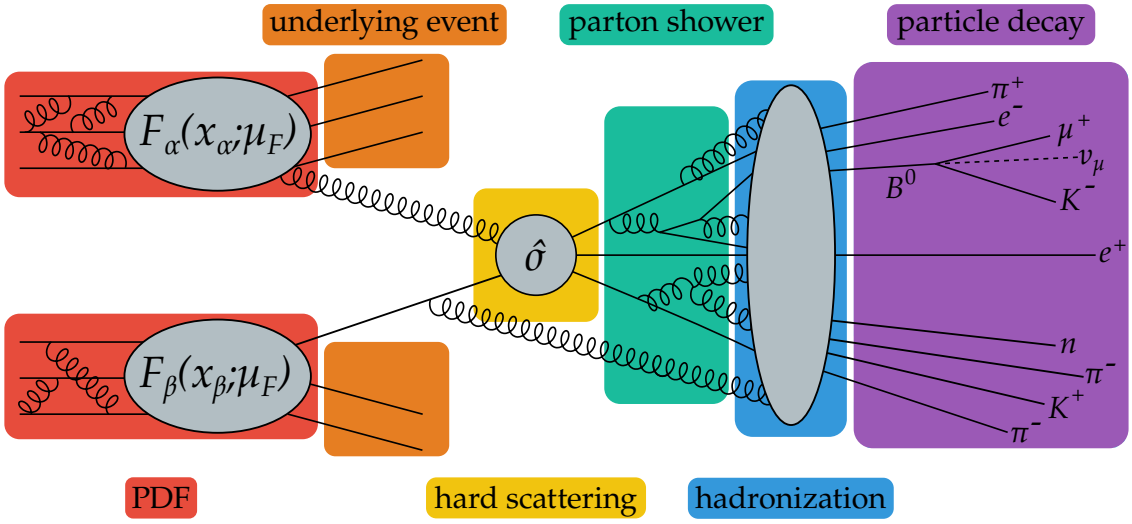

Fig. 1.4.: Illustration of a pp interaction. The incoming partons are described by the proton PDFs $F_\alpha(x_\alpha;\mu_F)$ (red) where usually two partons undergo the hard interaction (yellow) with the associated constituent cross section $\hat{\sigma}$. The proton remnants form the underlying event (orange). The parton shower (green) models additional initial- and final-state radiation and the further evolution of the emerging particles before hadronization (blue) takes over. Isolated leptons or Jets of particles arise from the hadronization. Long lived particles can decay subsequently (purple).

1.2.1. The hard scattering process

In a process where two initial partons α and β scatter at a center-of-mass energy s and produce a set of final-state particles $\{f\}$, the differential cross section can be written as

$$\mathrm{d}\hat{\sigma}\left(\alpha\beta \to \{f\}; s\right) = (2\pi)^4 \delta^{(4)}\left(\boldsymbol{P}_{\{f\}} - \boldsymbol{p}_\alpha - \boldsymbol{p}_\beta\right) \frac{1}{4E_\alpha E_\beta} \prod_{f\in\{f\}} \frac{\mathrm{d}^3\vec{p}_f}{2E_f\,(2\pi)^3} |\mathcal{M}_{\alpha\beta\to\{f\}}(s)|^2 \,, \tag{1.32}$$

where the $\delta^{(4)}$ is the Kronecker delta that ensures the conservation of energy between incoming and outgoing particles. The sum of four momenta of all final-state particles is denoted as $\boldsymbol{P}_{\{f\}}$, and $\boldsymbol{p}_\alpha$ and $\boldsymbol{p}_\beta$ are the four momenta of the two initial state particles. The vector $\vec{p}_f$ is the momentum of the final-state particle f in the three dimensional space, while E stands for the energy of the indexed particle. The invariant matrix element $\mathcal{M}$ quantifies the transition amplitude of the scattering process and its precise determination can be a major challenge for theorists. To extract the inclusive cross section, the integration over the phase space of the final-state particles in Eq. (1.32) needs to be performed. Since $\mathcal{M}$ is part of the integral and depends on the kinematics and states of incoming and outgoing particles, it needs to be computed first.

For the calculation, all possible ways of how the initial state partons can scatter and produce the set of final particles have to be summed up. This can be illustrated with the Feynman representation, e.g. in EW theory for the scattering of two fermions in the initial

and final state, as:

$i\mathcal{M} =$ 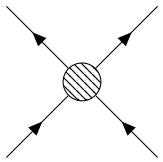 (1.33)

$=$ 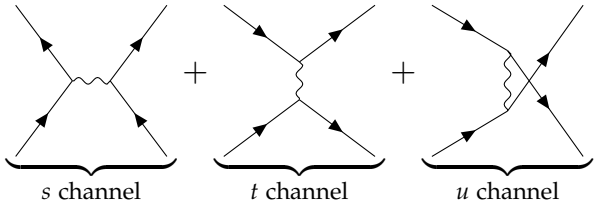
 (1.34)

$+$ 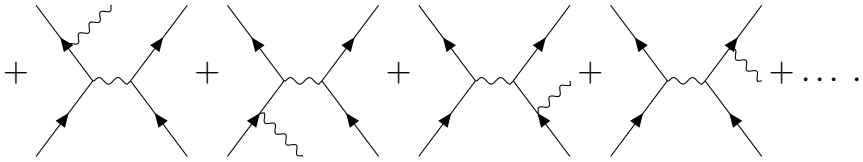 $+ \ldots$. (1.35)

In the illustrated example, Eq. (1.34) is representing the leading-order (LO) diagrams with two interaction vertices. Higher-order terms with more interaction vertices as shown in Eq. (1.35) are denoted as next-to-LO (NLO) and give further contributions to get a more accurate picture of experimental observations. Eq. (1.34) differentiates production mechanisms following the Mandelstam notation [34]. In the t- and u-channel processes, the exchange particle is space-like, each incoming particle radiates/absorbs the exchange particle and becomes a final-state particles. The s channel describes the scattering through a resonance. Both incoming particles annihilate and create a time-like exchange particle that eventually splits into the final-state particles. The four momenta of the exchange particle in each channel are given by the Mandelstam variables [34]

$$s = (\boldsymbol{p}_1 + \boldsymbol{p}_2)^2 = (\boldsymbol{p}_3 + \boldsymbol{p}_4)^2 \,, \tag{1.36}$$

$$t = (\boldsymbol{p}_1 - \boldsymbol{p}_3)^2 = (\boldsymbol{p}_4 - \boldsymbol{p}_2)^2 \,, \tag{1.37}$$

$$\text{and} \quad u = (\boldsymbol{p}_1 - \boldsymbol{p}_4)^2 = (\boldsymbol{p}_3 - \boldsymbol{p}_2)^2 \,, \tag{1.38}$$

where the four momenta $\boldsymbol{p}_1$ and $\boldsymbol{p}_2$ correspond to the incoming and $\boldsymbol{p}_3$ and $\boldsymbol{p}_4$ to the outgoing particles. The s-channel is especially interesting since s is the invariant mass of the exchange particle that can be calculated from the kinematics of the final-state particles. This is a powerful tool to discover new unstable particles using only the measured kinematics of the products from the detector. By considering the s-channel production of a massive particle R under neglection of NLO terms, the differential cross section as function of the invariant mass can be found from the propagator term of the exchange particle as

$$\frac{\mathrm{d}\hat{\sigma}}{\mathrm{d}s} \approx \left| \frac{\sqrt{k}}{(s - m_R^2) + i m_R \Gamma_R} \right|^2 = \frac{k}{(s - m_R^2)^2 + m_R^2 \Gamma_R^2} \,, \tag{1.39}$$

with

$$k = \frac{2\sqrt{2} m_R \Gamma_R \gamma}{\pi \sqrt{m_R^2 + \gamma}} \qquad \text{and} \qquad \gamma = \sqrt{m_R^2 (m_R^2 + \Gamma_R^2)} \,, \tag{1.40}$$

which is a Breit–Wigner function as illustrated in Fig. 1.5. The m_R and Γ_R are the mass and decay width of the resonant particle, respectively. The width depends on the number of final-state particles to which the resonance can decay and determines the lifetime of the resonant particle as $\tau_R = 1/\Gamma_R$.

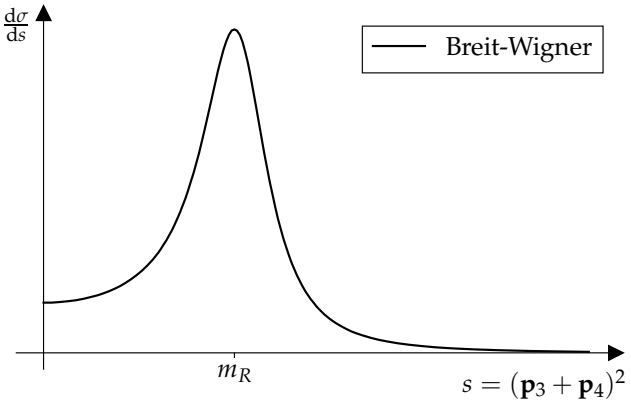

Fig. 1.5.: The Breit–Wigner function describing the differential cross section spectrum of a $2 \to R \to 2$ scattering process through the resonant production and decay of a particle R with mass m_R as function of the invariant mass s of the final-state particles.

The first step in the computation of the hard scattering process is to calculate the invariant matrix element $\mathcal{M}$. For each set of distinguishable final-state particles, $\mathcal{M}$ can be calculated separately. Since $\mathcal{M}$ goes as squared in the differential cross section $d\hat{\sigma}$, all Feynman diagrams that contribute to such a final state interfere and have to be taken into account at once. This also includes higher-order terms of the perturbation series corresponding to Feynman diagrams with additional vertices. The calculation of higher-order terms becomes increasingly difficult and the simulation becomes computationally intensive. In pp collider experiments, the calculation is typically performed only at LO for the EW interaction, which is often sufficient since the coupling strengths are much smaller than one. Higher-order terms of QCD interactions on the other hand usually lead to large corrections in the perturbation series and should be considered. Once $\mathcal{M}$ has been calculated it can be evaluated for a given set of kinematic properties and quantum number of the incoming and outgoing matrix element particles. Heavy particles such as Z, W, or Higgs bosons, or top quarks can be treated as resonances because interference effects with other processes that lead to the same final states can be considered small for invariant masses close to the mass of the resonant particles. Their decay can be described subsequent to the actual hard process. This reduces the number of outgoing matrix element particles and thus the complexity of the calculation. For invariant masses further away from the mass of the resonant particle, interference effects, e.g. between the Z boson and the photon or a dilepton pair, have to be considered for a accurate description.

To account for missing higher-order terms in the calculation of $\mathcal{M}$, and to model nonperturbative effects, initial-state radiation (ISR) and final-state radiation (FSR) of gluons or photons are described by parton shower (PS) models. Although they only give an approximate description, they allow in principle any number of soft (i.e. low p_T) and collinear emissions to be simulated. The PS also models the further development of particles from ISR, FSR, or the matrix element, e.g. the splitting of gluons or photons into quark-antiquark pairs or lepton-antilepton pairs, respectively. These processes are described by the Altarelli–Parisi splitting functions, which describe the vertices between quarks and gluons and have to be calculated in QCD via perturbation theory. These

calculations are performed with up to next-to-NLO (NNLO) precision [35, 36].

1.2.2. Parton distribution functions

Protons consist of three valence quarks (uud), which determine its quantum numbers. At short distances, these valence quarks exchange gluons, which in turn can split into quark-antiquark pairs of different flavors. This makes it possible to find antiquarks or heavier quarks like s, c, or b quarks in the so-called "proton sea". As already mentioned, one usually defines a fixed energy scale, the factorization scale μ_F, below which nonperturbative QCD effects are described by the PDF.

As PDFs describe the nonperturbative regime of QCD, they can not be predicted from first principles. Their estimation is based on data from electron-proton scattering, fixed target experiments, and hadron colliders [37]. Measurements from the different experiments are used to extract information about PDFs. Usually, the data are taken at different energies. The Dokshitzer–Gribov–Lipatov–Altarelli–Parisi (DGLAP) equation [38–40] can be used to evolve PDFs to the desired μ_F. The evolution depends on the Altarelli–Parisi splitting functions as already mentioned in the PS discussion. The data are finally combined using global fits. Classical approaches parameterize the PDFs using a polynomial ansatz [41]. The PDFs for simulated events used in this thesis are the NNPDF3.0 and NNPDF3.1 sets and use a more modern approach based on a three-layer feed forward neural network [37, 42]. They also include EW corrections. Uncertainties are provided in a Hessian set of orthogonal eigenvectors to take them into account correctly in the analysis. NNPDF3.1 PDFs are shown in Fig. 1.6 at two different values for μ_F. As shown in the plots, the valence quarks carry large fractions of the proton momentum, x, while sea quarks and gluons occur with smaller values of x. The frequency of sea quarks and especially gluons increases at higher energy scales. This leads to a decrease in the occurrence of valence quarks, and the part of momentum each one carries.

1.2.3. Hadronization and color reconnection

Color-charged partons emerge from the PS. The transition of those partons into color neutral hadrons is a process called hadronization. This process occurs in the energy regime of confinement and is described by phenomenological models like the Lund string model [43]. With the analogy to the electromagnetism, gluons are treated as field lines between two quarks. Self-interaction between gluons lead to the formation of narrow tubes, called strings. When the two quarks are getting separated, and the potential energy of the system is high enough, the string breaks and a new quark-antiquark pair is produced in order to form color neutral objects. This procedure can repeat itself several times until the kinematic energy of the quarks is small enough to form bound states. The outcome of the process is a shower of hadrons.

In a pp collision two constituents take part in the main interaction. The remnants of each proton emerge and in some cases multiple partonic interactions (MPIs) can occur. The particles arising from those effects are collectively denoted as underlying event and interfere with the outgoing particles from the main interaction. A multitude of color-charged particles escape the collision point which are represented by color lines. Different

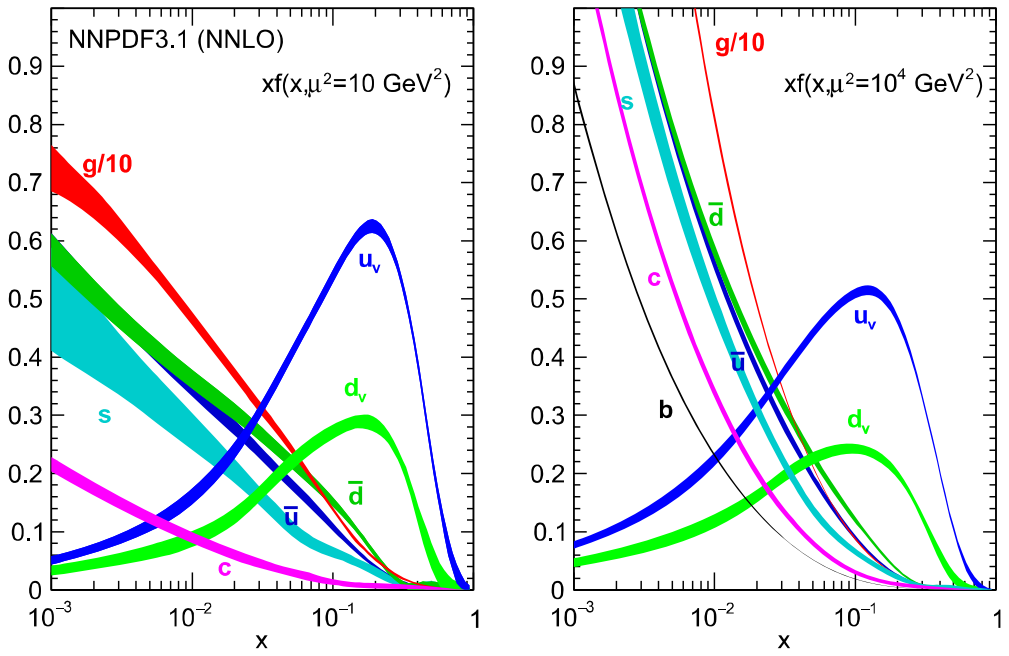

Fig. 1.6.: Shown are the neural network parton distribution functions (NNPDFs) calculated using the DGLAP equations at NNLO precision [37]. The probability density functions for a gluon, valence quark (indexed with v), or sea quark, in the proton are plotted in dependence on the fraction x of the proton momentum. At lower values of the factorization scale (left) the valence quarks carry the largest portion of momentum while for higher values of μ_F (right) the contribution from gluons is dominating.

so-called color reconnection models exist to take into account their color interference. In this work, the MPI-based model was used as default choice [44]. The model first identifies groups of color lines that are reconnected. The identification is based on a probability that is larger for color lines with low p_T, while those from MPI systems with high p_T more likely escape the collision point without reconnection to other color lines. For each identified group, the color lines are connected through strings in a way that the total string length is minimal. Alternative models are currently being tested in CMS [45]. Two of them are studied in the work presented in this thesis and their impacts on the results are estimated. The so-called QCD-inspired model [46] extends the MPI-based model by demanding certain QCD color rules and adds the possibility to form junctions of strings. It thus has a higher emphasis on the baryon production through Y-shaped connections of three strings. The gluon-move model [47] allows to move gluons between different color lines if it minimizes the total string length. It also allows the creation of junctions and the reconnection of two different strings.

1.3. The top quark of the standard model

The top quark was first predicted in 1973 by Makoto Kobayashi and Toshihide Maskawa to explain CP violation in the quark sector [26]. It took over two decades until finally the top quark was discovered in 1995 at the Tevatron accelerator analyzing proton-antiproton collision data at $\sqrt{s} = 1.8\,\text{TeV}$ with the CDF and D0 experiments [48, 49]. The

discovery took many years due to the high mass of the top quark. With a pole mass of $172.76 \pm 0.30\,\text{GeV}$ [10] the top quark is the heaviest particle of the SM and is the only quark with a mass of the same order as the EW symmetry breaking scale of about 246 GeV. This makes it a very interesting object of study and a potential portal to new physics. The large mass implies a strong coupling to the Higgs boson and affects the Higgs boson mass, as well as the vacuum expectation value of the Higgs potential. Measurements of the top quark mass provide therefore strong insight in the EW sector of the SM [23].

As discussed earlier, the top quark has a lifetime that is about 20 times shorter than the hadronization time. It is thus the only quark that decays before it forms bound states. This represents one of the few cases where the weak interaction occurs faster than the strong one and allows to perform unique studies on the properties of an unconfined quark. For example, it is possible to measure its charge in the search for exotic particles [50]. One type of such exotic particles are heavy vector-like quarks that could decay into the SM top quarks under the emission of Z bosons. A search for such events has just recently been performed by the CMS Collaboration [51].

The dominant production mechanism in pp colliders is in quark-antiquark pairs ($t\bar{t}$) via the strong interaction, either via gluon fusion in the s or t channel or quark-antiquark induced in the s channel. Measurements of $t\bar{t}$ production cross sections can for example be used as input to global fits in the determination of the gluon PDF at large values of the proton momentum fraction [52].

1.3.1. Single top quark production

It is also possible to produce top quarks singly through the EW interaction. This complementary production mechanism can occur in the s channel via the production and decay of a virtual time-like W boson, in the t channel via the exchange of a space-like W boson, or via the production in association with a W boson:

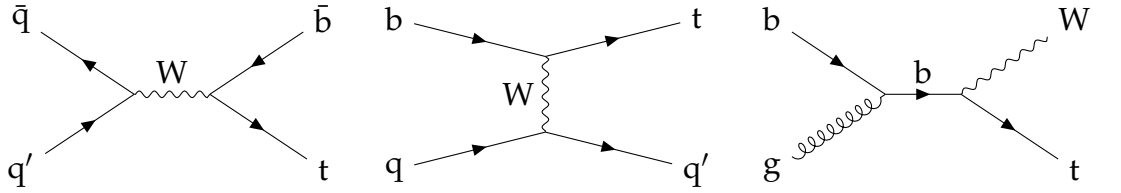

(1.41)

Unlike $t\bar{t}$ production, the final states of the three production mechanisms differ in the accompanied particles and hence can be distinguished in measurements. With the use of multivariate analysis techniques the observation of singly produced top quarks was accomplished in 2009 independently with the CDF and D0 experiments [53, 54]. Each experiment performed a combined analysis of events from t- and s-channel production. The predicted cross sections of single top quark production mechanisms for different values of $\sqrt{s}$ together with previous measurements of of the CDF, D0, and CMS Collaborations are shown in Figure 1.7. With the increasing center-of-mass energy and amount of data collected at the LHC, more rare single top quark production mechanisms are explored as shown in Fig. 1.7. Those are the t-channel production in association with a photon ($t\gamma q$) or in association with a Z boson (tZq). The latter is the main subject for the work presented in this thesis. A more detailed description will be given in Section 1.4.

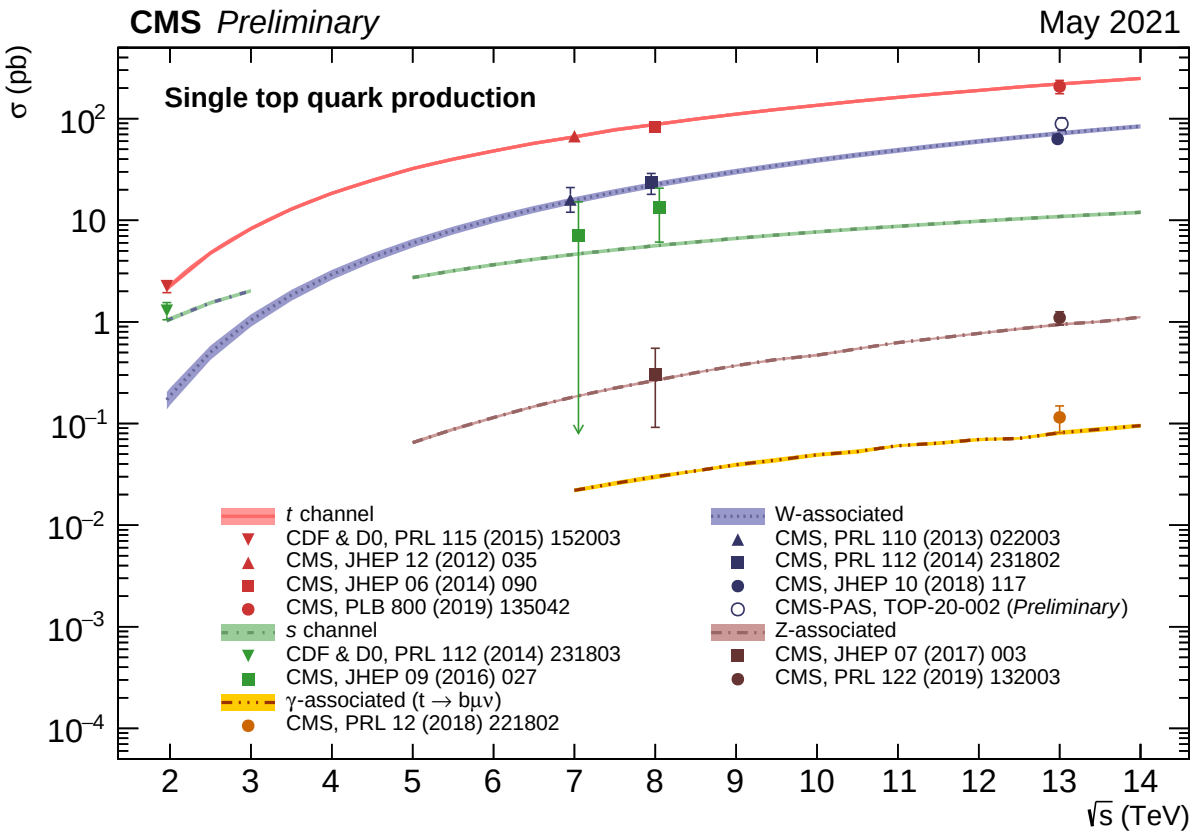

Fig. 1.7.: Overview of measured and predicted production cross sections as a function of the center-of-mass energy for different single top quark production mechanisms. The t channel (red) and s channel (green) were first measured in experiments at the Tevatron accelerator. The associated production with a W boson (blue), Z boson (brown), or photon (yellow) has been first measured at the LHC experiments. From Ref. [55].

In pp collisions the single top quark production mechanism with the largest cross section is through the t channel. As the proton consists of two up and one down valence quarks, the cross section of top quarks is about 1.7 times larger than the one of top antiquarks. Thus, measurements of the ratio between top quarks and antiquarks are sensitive to the proton PDFs [56].

The single top quark process is directly sensitive to modifications in the W-t-b interaction [57]. The production and decay of single top quarks proceeds through flavor changing charged currents and thus depends on the CKM-matrix element V_{tb}. Under the assumption that $|V_{td}|^2 + |V_{ts}|^2 \ll |V_{tb}|^2$, diagrams where the W-t-d or W-t-s vertices appear in the production can be neglected. For the same reason, the branching fraction of a top quark into a W boson and a b quark can be assumed to be 100% as can be seen from:

$$\mathcal{B}(t \to Wb) = \frac{|V_{tb}|^2}{|V_{td}|^2 + |V_{ts}|^2 + |V_{tb}|^2} = \frac{1}{\underbrace{\frac{|V_{td}|^2 + |V_{ts}|^2}{|V_{tb}|^2}}_{\approx 0} + 1} \approx 1 \,. \tag{1.42}$$

Using signal generated with $V_{tb} = 1$ both in the production and decay, $|V_{tb}|$ can be determined as

$$|f_{LV} V_{tb}| = \sqrt{\frac{\sigma_{meas}}{\sigma_{theo}(V_{tb} = 1)}} \,, \tag{1.43}$$

where f_{LV} is a real number that parameterized possible BSM effects. It is 1 in the SM and can be modified from anomalous left chiral vector couplings. This way, a combination of $|f_{LV} V_{tb}|$ from single top quark cross section measurements at $\sqrt{s} = 7$ and 8 TeV from the CMS and ATLAS experiments was performed as shown in Figure 1.8. Also included in this figure are previous measurements from CMS and ATLAS at $\sqrt{s} = 13$ TeV. In a more advanced and dedicated measurement in the single top quark t channel, a precise result of $V_{tb} = 0.988 \pm 0.024$ was presented without assuming $|V_{td}|^2 + |V_{ts}|^2 \ll |V_{tb}|^2$ [58]. The single top quark production represents the only case where the CKM-matrix element V_{tb} is accessed by a direct measurement with minimal assumptions. In particular, the measurement does not depend on the number of quark generations or unitarity of the CKM matrix.

1.3.2. Top quark polarization

The top quark almost exclusively decays into a W boson and a b quark and is characterized by the decay of the W boson. If the W boson decays into a lepton and neutrino the top quark is labeled as leptonic, otherwise it is labeled as hadronic. Properties like the spin of the top quark are passed on to the W boson and can be measured if it decays leptonically from the kinematic variables of the final-state particles. In top quark-antiquark pair production, the top quarks are produced unpolarized in LO and higher-order corrections introduce only a small polarization of $<1\%$. The spins between the top quark-antiquark pair are thereby strongly correlated. Observables sensitive to this effect have been measured in dileptonic $t\bar{t}$ decays by CMS [60].

A different situation applies to the single top quark production, where in the SM the top quark is produced EW via the W-t-b vertex. Hence, the top quark is produced with

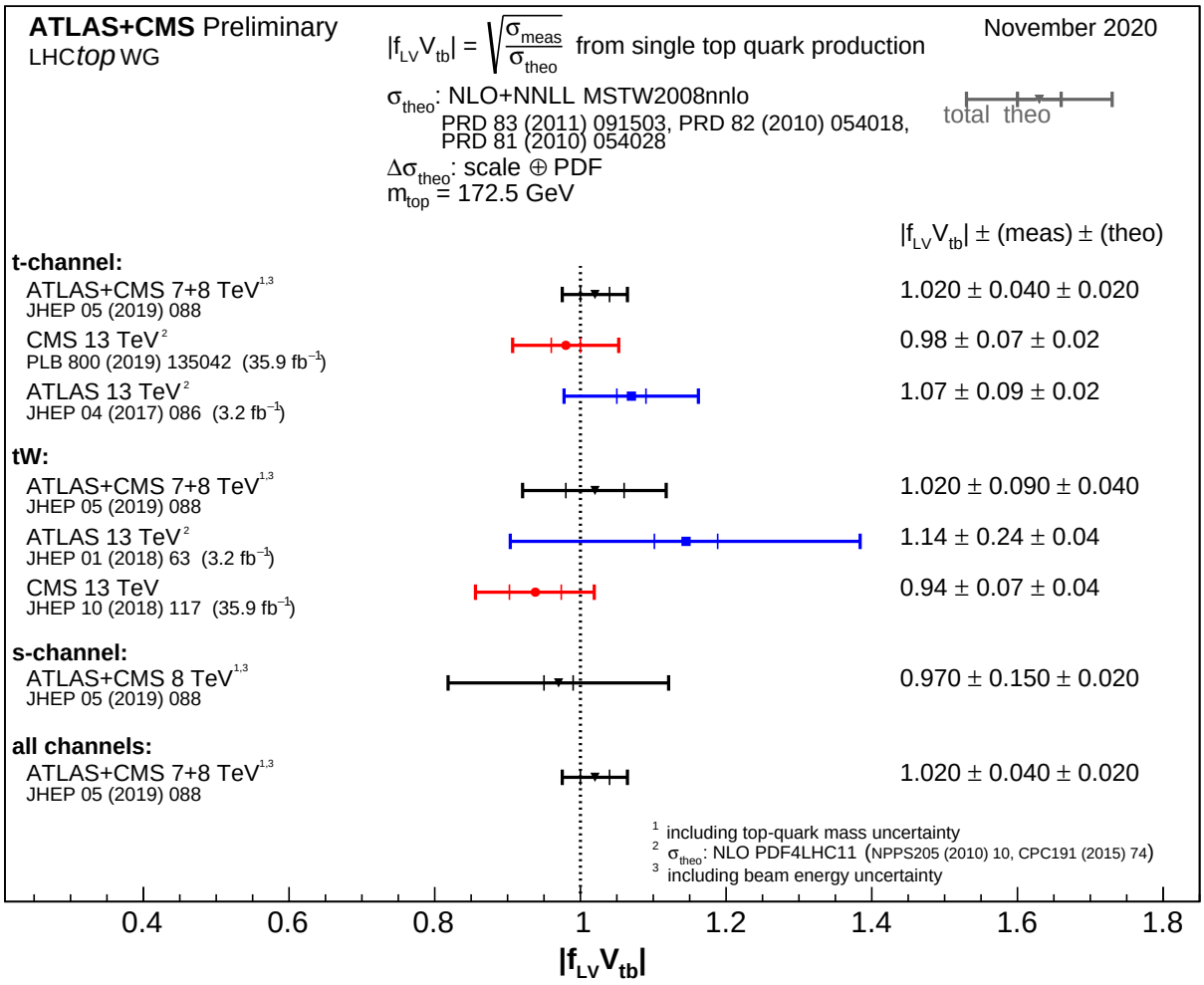

Fig. 1.8.: Determination of $|f_{LV}V_{tb}|$ from different single top quark production cross section measurements from CMS (red) and ATLAS (blue). A combination on the $\sqrt{s} = 7$ and 8 TeV measurements has been performed (black). From Ref. [59].

left chirality and is polarized to a much higher degree. New particles with right chiral interactions could change the top quark polarization. A deviation from SM predictions would thus be a strong indication of BSM physics. The top quark polarization is measured in the analysis presented in this thesis in terms of the associated spin asymmetry. The mathematical framework used in the measurement is discussed in the following.

Neglecting the mass of the b quark with respect to the top quark mass, the W boson is either longitudinal polarized with

$$f_0 = \frac{m_t^2}{2M_W^2 + m_t^2} \approx 70\% \,, \tag{1.44}$$

or left-handed polarized with $1 - f_0 \approx 30\%$ [61]. The kinematic effect of this is illustrated in Fig. 1.9. The illustrations show the b quark and W boson in the top quark rest frame which move in opposite directions. In the case that the top quark decays into a longitudinally polarized W boson, both the lepton and neutrino of the decay prefer to travel in the direction of the W boson and thus along the direction of the top quark spin. In case the W boson polarization is left handed, the neutrino is forced to be left handed and the lepton prefers to travel against the direction of the W boson, which is again along the direction of the top quark spin. For top antiquarks the situation is just the opposite, the lepton prefers to travel against the direction of the top antiquark spin.

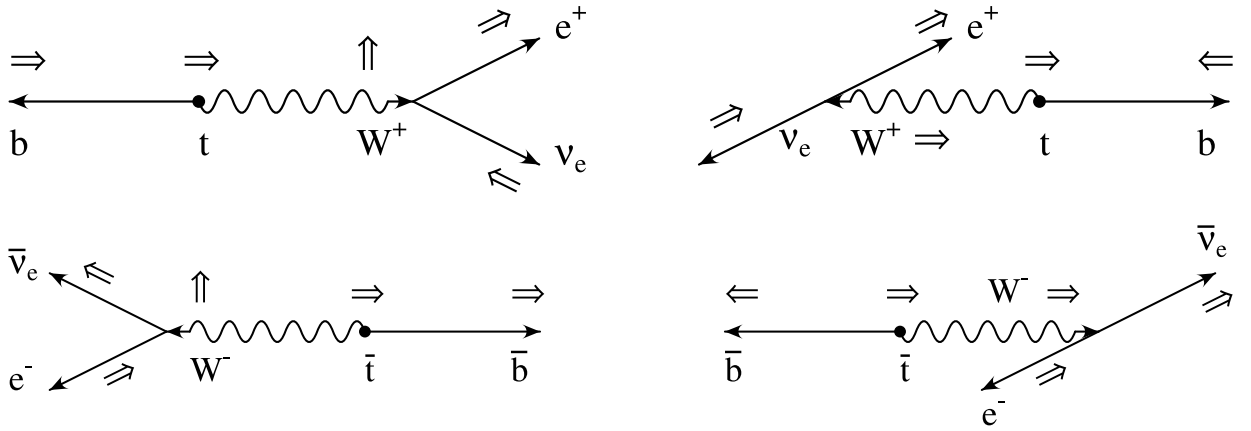

Fig. 1.9.: Illustration of the top quark decay in its center of mass frame. The small arrows at the end of each line illustrate the direction of motion while the double dashed arrows show the direction of the spin. The upper and lower sketches show the top quark and antiquark, respectively. The left and right side shows the cases for a longitudinal and left-handed polarized W bosons, respectively. In both polarizations, the electron moves preferably along the direction of the top quark spin, while the positron moves preferentially in the opposite direction to the top antiquark spin [61].

To measure the polarization, a reference axis has to be chosen. In the so-called helicity basis, the top quark spin is measured along its axis of motion in the center-of-mass frame. This scheme can be chosen in any process with a top quark, but it is subject to large higher-order corrections in α_S due to additional gluon radiations [62].

A better choice can be made for the single top quark t-channel production. In this process, a quark appears from the exchange of the time-like W boson, denoted as q' and shown in the middle Feynman diagram of Eq. (1.41). Since it recoils against the W boson, the q' prefers to travel in the opposite direction to the top quark. In the optimized

basis the momentum of q′ in the top quark rest frame is taken as the axis to measure the top quark polarization. This choice has a similar degree of polarization as the helicity basis but has the advantage that higher-order QCD effects have no large impact on the polarization and a theory prediction is much more reliable [62].

Often, the spin asymmetry is measured instead of the polarization. It is defined as $A_\ell = 1/2Pa_\ell$ with polarization P and a_ℓ being the spin analyzing power of the lepton which indicates how much the spin of the top quark is correlated to the spin of the lepton. For LO calculations a_ℓ is equal to unity [63]. Small corrections from NLO calculations lead to $a_\ell \approx 0.998$ [64]. The spin asymmetry can be related to the differential cross section

$$\frac{\mathrm{d}\sigma}{\mathrm{d}\cos(\theta^\star_{\mathrm{pol}})} = \sigma\left(\frac{1}{2} + A_\ell \cos(\theta^\star_{\mathrm{pol}})\right) , \tag{1.45}$$

where $\cos(\theta^\star_{\mathrm{pol}})$ is the angle in which the polarization is being measured. In the optimized basis it is the angle between the lepton from the top quark and the direction of motion of q′, defined as

$$\cos(\theta^\star_{\mathrm{pol}}) = \frac{\vec{p}(\mathrm{q}'^\star) \cdot \vec{p}(\ell^\star_{\mathrm{t}})}{|\vec{p}(\mathrm{q}'^\star)||\vec{p}(\ell^\star_{\mathrm{t}})|} , \tag{1.46}$$

where the asterisk indicates that the three momenta $\vec{p}$ of the particles are evaluated in the top quark rest frame.

Using this relation, the spin asymmetry was measured in a previous single top quark t-channel analysis of CMS to be $A_\ell = 0.440 \pm 0.070$ which is well in agreement with the SM expectations [65]. It is also possible to measure the top quark polarization separately for top quarks and antiquarks and to measure the three components of the polarization vector. Such a measurement was published quite recently by the ATLAS Collaboration [66].

1.4. Single top quark production in association with a Z boson

The main study in this thesis is the rare production of top quarks in association with a Z boson, tZq. It contains the t-Z coupling already in LO Feynman diagrams as shown in Fig. 1.10 and offers therefore tests to the SM in a unique way. This provides sensitivity to new phenomena in the top quark electroweak interaction with the Z boson [67]. In the diagrams, interference effects of the Z boson with the photon (Z/γ^* interference), and nonresonant dilepton production have to be considered to correctly describe observations. For simplicity the class of processes is denoted as tZq and also includes the production of top antiquarks, if not stated otherwise. Another process of single top quark production in association with a Z boson is the W boson associated production, tWZ. It has more particles in the final state and thus requires a larger momentum transfer in the collision. The cross section is about six times smaller than tZq and tWZ is considered as minor background in this thesis. The s-channel production is completely negligible.

The t-Z coupling can also be studied in the QCD induced top quark-antiquark pair production in association with a Z boson, $\mathrm{t\bar{t}Z}$. In pp collisions at $\sqrt{s} = 13\,\mathrm{TeV}$ the tZq and $\mathrm{t\bar{t}Z}$ production have cross sections in the same order of magnitude as shown in

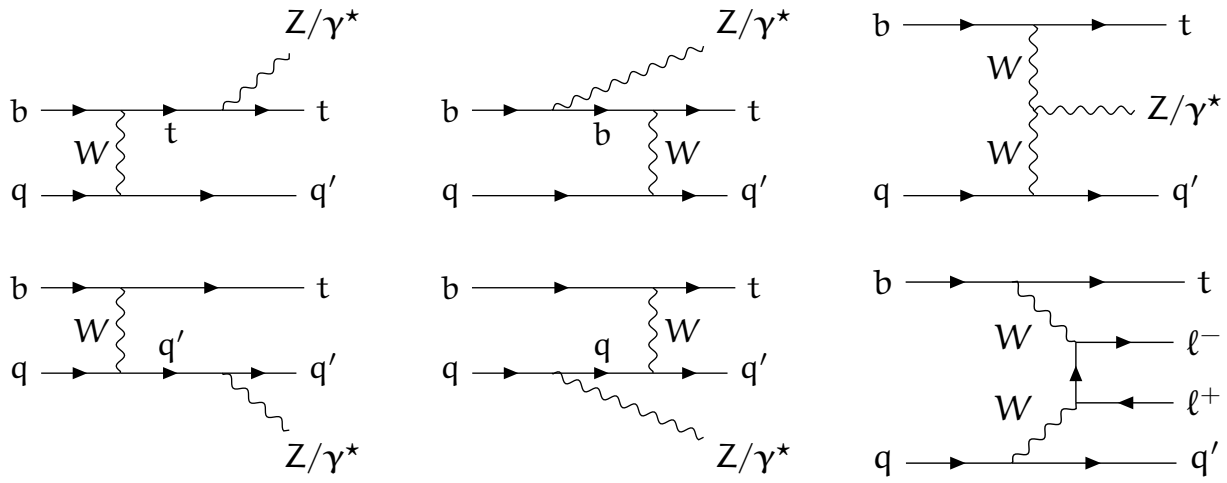

Fig. 1.10.: LO Feynman diagrams for the tZq production process. The production via triple gauge boson coupling (WWZ) is shown on the upper right. The nonresonant dilepton production in the lower right has to be included to correctly account for interference effects. The Z/γ^* interference also has to be considered to correctly describe observations.

Fig. 1.11. It results from the much heavier final state of $t\bar{t}Z$ that requires more energy and a larger momentum transfer in the production. This is in contrast to the case without an additional Z boson, where the $t\bar{t}$ production dominates over single top quark production. In terms of potential statistical accuracy, a study of tZq is thus very competitive to one of $t\bar{t}Z$, and beyond that offers a variety of unique features. Unlike $t\bar{t}Z$ production, the tZq production additionally contains the W-t-b vertex. BSM theories affecting the EW sector may modify both W-t-b and t-Z vertices simultaneously, further increasing the sensitivity of the tZq production [57].

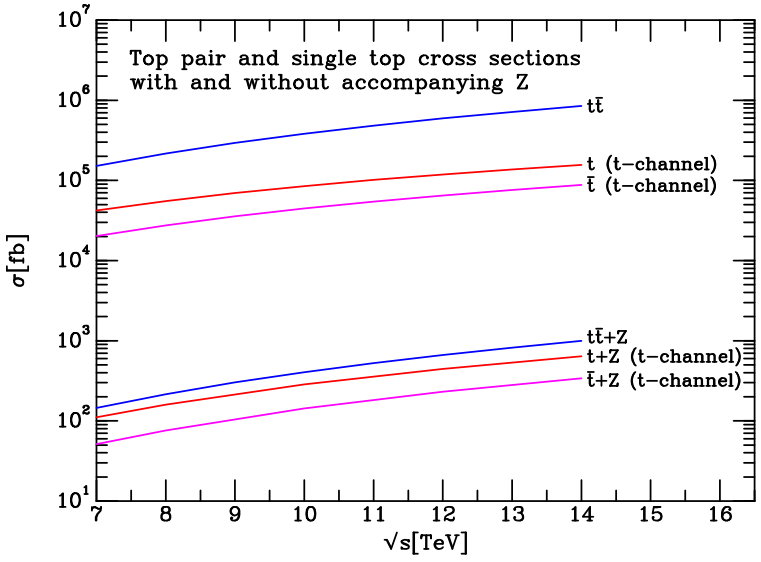

Fig. 1.11.: Inclusive cross sections of single top quark and $t\bar{t}$ production solely and in association with a Z boson in pp collisions as a function of the center-of-mass energy $\sqrt{s}$. The production cross sections for single top quarks and antiquarks is shown separately [68]

In theory, most aspects that motivate a single top quark measurement also count for an analysis of tZq production. This includes the sensitivity to PDFs from the ratio of top quark to antiquark production. As systematic uncertainties largely cancel in ratio

measurements, the statistical precision is more decisive. The tZq production is much more rare and much larger amount of data is required to obtain competitive results. However, through the presence of the Z boson more particles are present in the final state which allows for a cleaner signal selection. Once enough data has been collected, measurements of single top t-channel production with and without associated Z bosons could be combined to reduce the overall systematic uncertainty. More compatible results with the already available amount of data can be expected on the CKM-matrix element $|V_{tb}|$, which depends on the square root of the measured cross section, as seen from Eq. (1.43). Although not as precisely as from single top quark t-channel measurements, the determination of $|V_{tb}|$ from tZq events can give valuable input in a combination of $|V_{tb}|$ as events from a different phase space are used where statistic and systematic uncertainties are largely uncorrelated. Deeply interesting is the polarization of the top quark, that can be measured in tZq as discussed in Section 1.3.2. A measurement in tZq events is complementary to existing measurements in the single top quark t channel since different event topologies are explored. For example, anomalous couplings could occur from non SM Z boson interactions and modify the degree of polarization. A deviation from SM predictions would thus be a strong hint to BSM effects. In the results presented in this thesis the top quark spin asymmetry, proportional to the top quark polarization, is measured for the first time in tZq events.

An experimental analysis of tZq can further be used to validate and improve the theoretical description of this process. In this context, much of the experience gained from tZq can also be used for the single top quark production in association with a Higgs boson (tHq) which is predicted with a much smaller cross section in the SM. While tHq is very interesting for a complementary set of physics questions, both processes are affected in the same way by most of their theoretical uncertainties and face the same modeling challenges. At LO, the tZq production is a pure EW process and independent of α_S, as visible in Fig. 1.10. From this consideration, QCD corrections and uncertainties are expected to be small. However, including NLO terms introduces a dependence on α_S and thus leads to challenges for an accurate description. Moreover, tZq production depends on a b quark in the initial state. The b quark can be included in the description of the proton PDFs by using a PDF set in the five-flavor scheme (5FS). When using a PDF set that does not include b quarks, i.e. using the four-flavor scheme (4FS), the b quark has to be simulated in the hard interaction via the gluon-splitting process. The diagrams shown in Fig. 1.10 are shown in the 5FS, while two examples of Feynman diagrams at LO and NLO in the 4FS are shown in Fig. 1.12. In the 5FS, large terms are absorbed in the b quark PDF and the scheme is expected to give a more precise estimate for the inclusive cross section of tZq. The 4FS prediction on the other hand depends on α_S already at LO, while the NLO prediction adds one more QCD coupling and also allows gluon-gluon (gg) and quark-antiquark ($q\bar{q}$) initiated processes. It is thus expected to give a more realistic modeling of kinematic distributions of the outgoing particles [69]. The difference between the 4FS and 5FS predictions can be seen as an additional uncertainty due to missing higher-order terms of α_S [69]. The different modeling assumptions seemingly impact the predicted differential cross section distributions of the η and p_T of the additional jet in the tZq process as shown in Fig. 1.12. A measurement of these quantities is thus of utmost interest.

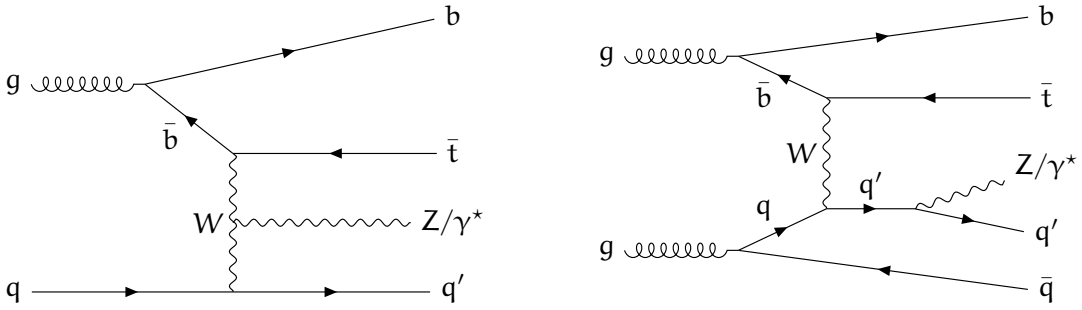

Fig. 1.12.: Example of LO (left) and NLO (right) Feynman diagrams for the tZq production process in the 4FS and in the final state with three leptons. The Z/γ^* interference is included in the simulation. At NLO in α_S, gluon-gluon (gg) and quark-antiquark ($q\bar{q}$) initiated processes are possible and an additional quark or gluon is present in the final state.

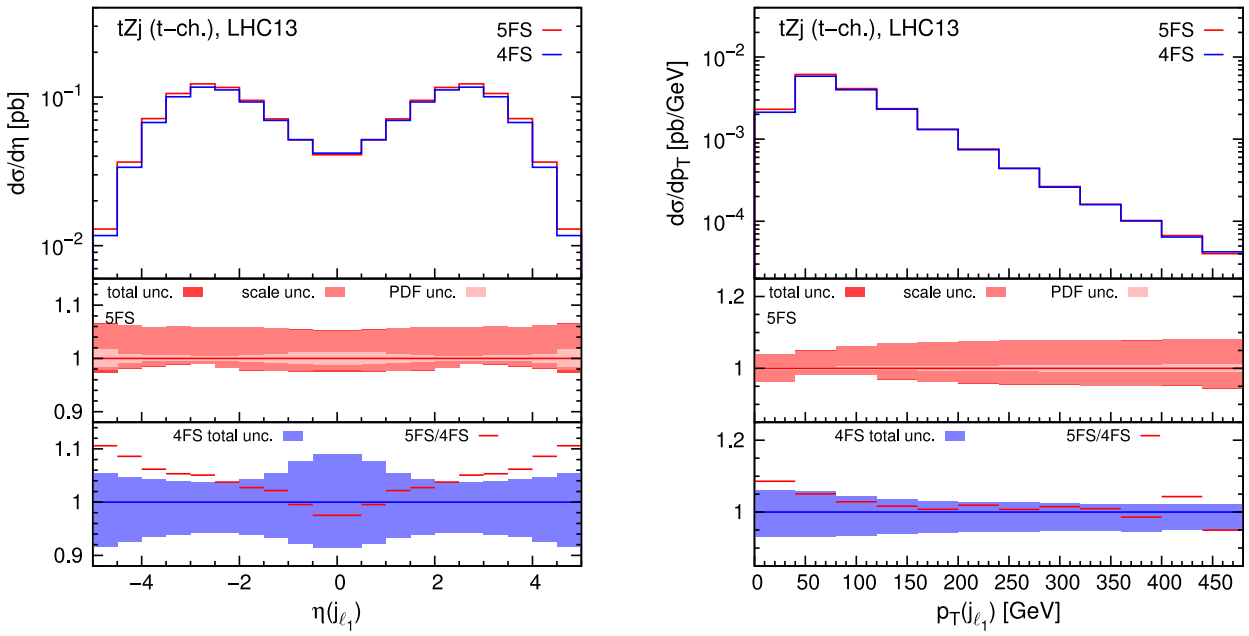

Fig. 1.13.: Comparisons between the simulation with 4FS (blue) and 5FS (red) assumptions. The upper panels shows the differential cross section distributions of η (left) and p_T (right) of the additional jet produced in tZq events. The middle panels show the uncertainty for the 5FS prediction from the QCD scale (red) and the PDFs (light red). The lower panels show the uncertainty related to the 4FS prediction (blue) and the ratio of the 5FS prediction to the 4FS predictions. From Ref. [69]

Reference [69] shows calculations for tZq in NLO in the strong as well as the EW coupling. The paper stresses that NLO EW calculations are only possible for a joint consideration of the t-channel, s-channel, and W boson associated production, at least for cases where the W boson decays into quarks. The presented inclusive cross sections are listed in Table 1.2 and are calculated with a dynamic QCD scale choice of $\mu_R = \mu_F = H_T/6$. For this choice, the difference between the 4FS and 5FS is minimal. The H_T is hereby given by the scalar sum of the transverse masses of the top quark, dilepton pair, and b quark if present in the final state. The transverse mass of a particle is defined as $m_T^2 = m^2 + p_x^2 + p_y^2$, where m is its invariant mass and p_x and p_y are its momenta transverse to the beam axis in collider experiments. NLO EW terms have a mild impact on the inclusive cross section and lead to a reduction of <5%, which is smaller than the scale uncertainty of QCD at NLO. The case is different for differential cross sections, e.g. for the p_T of the two leptons associated to the Z boson, $p_T(\ell, \ell')$, or the p_T of the top quark, $p_T(t)$. In the tails at high values, a larger reduction can be observed when including NLO EW terms. For a $p_T(\ell, \ell') > 400\,\text{GeV}$ this effect is at the level of 15% and is understood by soft and collinear EW corrections that do not cancel out, called Sudakov logarithms. Strong impacts are also visible in the $m_{\ell\ell'}$ distribution, where below 90 GeV the increase of the differential cross section reaches up to 50%. This effect originates from the final-state radiation of a photon and is largely described by including QED terms in the parton shower. Since a joint consideration of all channels requires more work in the understanding also of the overlap between tWZ and $t\bar{t}Z$, and the impact of NLO EW corrections is comparatively small, the work presented in this thesis still treats the t channel separately. However, in future analyses with more data and higher precision, a combined treatment of all channels might be preferable.

Table 1.2.: Cross section predictions for the single top quark production in association with a Z boson. Values are shown for the t channel using the 4FS and 5FS with NLO precision in α_S and for all channels combined (t-channel, s-channel, and W boson associated production in cases where the W decays into quarks). In the combined case the 5FS with NLO precision in the QCD coupling solely and in both, QCD and EW couplings are presented. The uncertainties correspond to scale and PDF variations. [69]

Accuracy	Channel	4FS [fb]	5FS [fb]
NLO QCD	t channel	$80.2^{+3.7}_{-5.0} \pm 0.3$	$84.0^{+4.7}_{-0.9} \pm 0.3$
NLO QCD	all	$93.7^{+4.9}_{-1.7} \pm 0.4$	—
NLO QCD+EW	all	$89.6^{+5.1}_{-1.7} \pm 0.4$	—

An understanding of tZq production is important also in searching for flavor changing neutral currents (FCNC), where for example a top quark decays into a c or u quark under emission of a Z boson. This process is heavily suppressed in the SM with a branching ratio of $\mathcal{B}(t \to qZ) < 10^{-12}$ [10]. Several BSM theories can introduce FCNC processes that lead to much higher branching ratios and similar final states as tZq as illustrated in Fig. 1.14. Dedicated searches in the decay of $t\bar{t}$ events that can probe $\mathcal{B}(t \to uZ) \leq 1.3 \cdot 10^{-4}$ and $\mathcal{B}(t \to cZ) \leq 4.2 \cdot 10^{-4}$ at $\sqrt{s} = 14\,\text{TeV}$ and an integrated luminosity of $100\,\text{fb}^{-1}$ are outlined in Ref. [70].

The SM effective field theory (SMEFT) framework can be used as a more general approach in the search of new physics. It assumes possible new physics at an energy scale

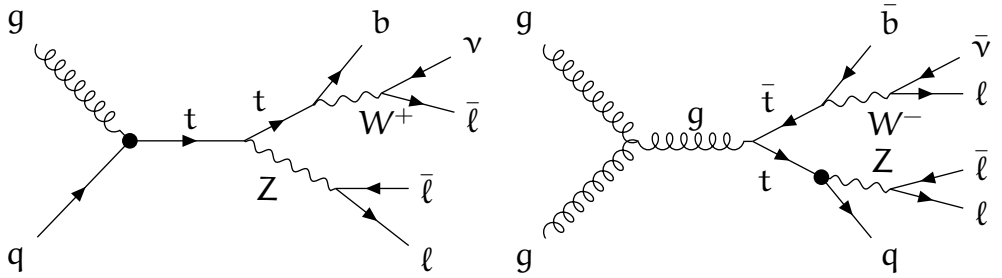

Fig. 1.14.: Flavor changing neutral current interactions of the top quark in the production through the coupling to a gluon (left) and decay through the emission of a Z boson (right), illustrated with dots, respectively. The quark that is labeled with q corresponds to a c or u quark

that lies above our currently well-understood regime while making minimal assumptions about the nature of the new physics model. At this scale, any kind of new physics is parameterized in terms of a perturbation series of an effective field theory (EFT), where each term describes a non SM operator, multiplied by a coefficient, the so-called Wilson coefficient, that defines the magnitude of the operator. The tZq process plays a crucial role in the global effort to constrain the largest possible number of Wilson coefficients. As discussed in Refs. [67, 71–73] and shown in Fig. 1.16, tZq production is affected by a variety of SMEFT operators from the top quark sector, diboson production, and vector boson fusion. For example the $\mathcal{O}_{\mathrm{tW}}$ and $\mathcal{O}_{\phi\mathrm{tb}}$ operators describe modified left- and right-chiral W-t-b couplings, respectively. Another example is the $\mathcal{O}_{\mathrm{tB}}$ operator that modifies the t-Z coupling. The process is also sensitive to $\mathcal{O}^{(3)}_{\phi\mathrm{Q}}$ which allows unitarity violation. This means when interpreting the transition amplitude $|\mathcal{M}^2|$ as a probability, this probability is not conserved. The four operators have in common that they show a good growth with energy in the tZq process. The effect of possible new physics parameterized by these operators have thus a strong impact on the shape of differential cross section distributions as can be seen in Fig. 1.16.

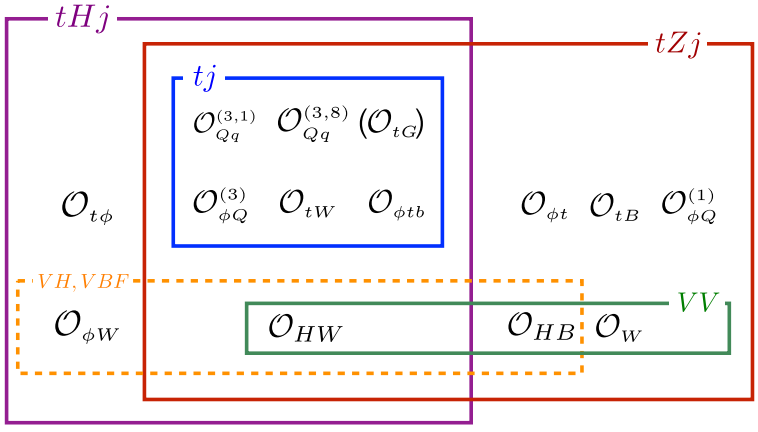

Fig. 1.15.: Different SMEFT operators that affect tZq (red) or tHq (purple) production. Operators that mutually also affect single top quark production (blue), diboson production (green), or vector boson fusion and the production of a Higgs boson in association with a vector boson (yellow) are shown. From Ref. [71]

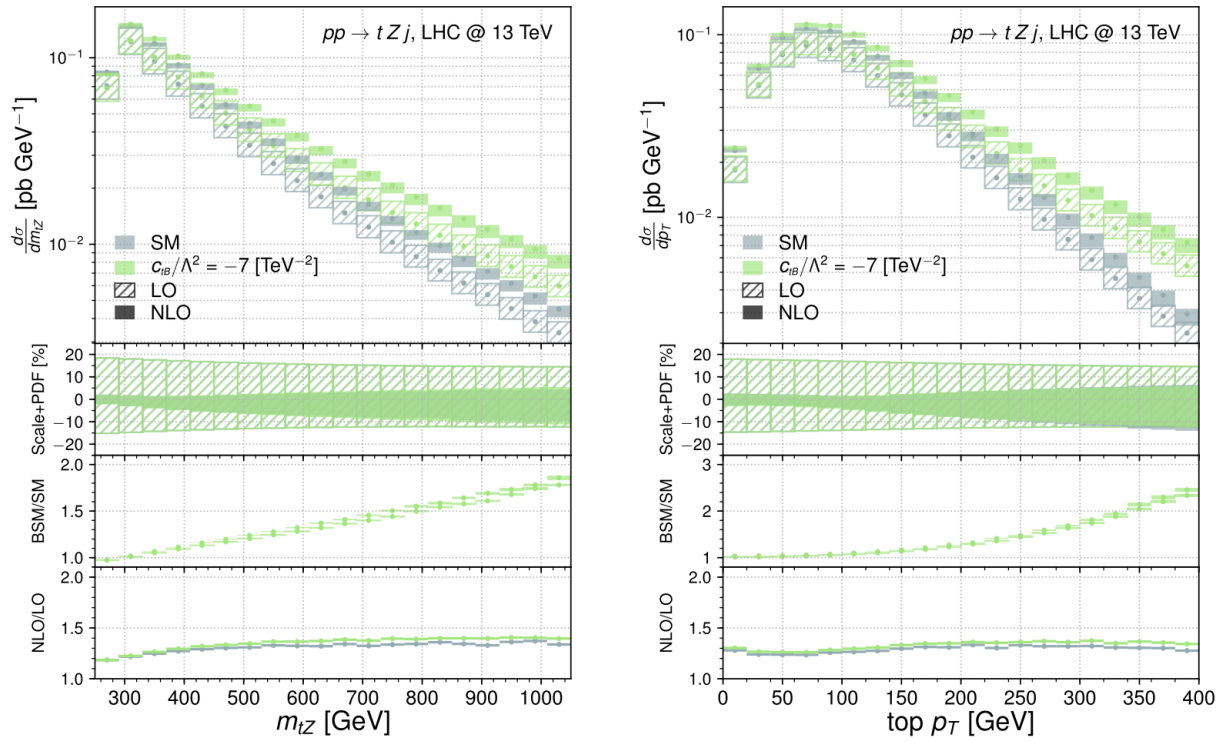

Fig. 1.16.: The upper panel of the plots show the differential cross sections as function of the invariant mass of the top-Z system, $m(\mathrm{t},\mathrm{Z})$ (left) and the p_T of the top quark, $p_\mathrm{T}(\mathrm{t})$ (right). The SM prediction is shown in gray boxes where the shaded boxes show the LO prediction and the filled ones include NLO terms in α_S. The green boxes show the LO and NLO prediction in the EFT scenario where the Wilson coefficient c_tB, associated to the $\mathcal{O}_\mathrm{tB}$ operator, is varied from zero. The lower panels show the relative uncertainties, the ratio of the cross sections in the EFT scenario divided by the SM expectation, and the ratio of NLO to LO predictions. From Ref. [71]

2. The CMS experiment at the LHC

For the work presented in this thesis, proton-proton (pp) collision data were studied at the highest center-of-mass energy achieved to date. Section 2.1 provides an overview of the Large Hadron Collider (LHC), the machine used to accelerate and collide the protons. The data was recorded by the Compact Muon Solenoid (CMS) experiment that is centered around one of the collision points at the LHC. The different components of the CMS detector are explained in Section 2.2. Simulated data are part of the toolkit of every modern particle physicist and also an integral item for the measurements described in this document. Generated events are propagated through different steps of pp collisions and the interactions of the collision product with the CMS detector are emulated as described in Section 2.3. The recorded information in the various layers of the CMS detector of both data and simulation is used to reconstruct particles that emerged from the pp collision as discussed in Section 2.4. These represent the building block on which the analysis performed for this thesis is based.

2.1. The LHC facility

For particle physics experiments, a high center-of-mass energy $\sqrt{s}$ in collisions is necessary for the production of rare SM processes and to find or exclude potential new BSM physics. To meet this requirement, the LHC [74] at the CERN laboratory in Geneva was built between 1998 and 2008. It is a circular particle accelerator that brings protons, xenon ions, and lead ions into head-on collisions. With a circumference of 27 km it is the largest and most powerful particle accelerator that ever existed. As the analyses discussed in this thesis use data from pp collisions, the following discussions will refer exclusively to the case with protons, unless stated otherwise. In head-on pp collisions $\sqrt{s}$ is given by twice the beam energy and a value of $\sqrt{s} = 14\,\text{TeV}$ was initially targeted for the LHC.

Another important quantity in collider experiments is the average number of events of a specific process, N, that are produced in a given time interval. It is given by

$$N = \sigma\mathcal{L} = \sigma \int \mathcal{L}(t)\mathrm{d}t \,, \tag{2.1}$$

with the production cross section σ of the process as discussed in Section 1.2, and the instantaneous and integrated luminosity $\mathcal{L}(t)$ and $\mathcal{L}$, respectively. The instantaneous luminosity is a characteristic of the particle collider and determines the frequency of event production. It has to be as large as possible to achieve a high statistical significance in physics analysis. Targeting an unprecedented value of $\mathcal{L}(t) = 10^{34}\,\text{cm}^{-2}\,\text{s}^{-1}$ the LHC has optimized parameters affecting $\mathcal{L}(t)$,

$$\mathcal{L}(t) = \frac{N_\text{b} n_1 n_2 f}{A_\text{eff}} \,. \tag{2.2}$$

Two separate beams containing bunches of charged particles are circulated in opposite directions. In Eq. (2.2), N_b is the number of bunches per beam, n_1 and n_2 are the number of protons per bunch in either of the beams, f the circulation frequency, and A_{eff} is the overlap area between the two bunches in the collision. Highly focused beams lead to a smaller A_{eff} and hence a larger instantaneous luminosity. Moreover, the n_1 and n_2 are tuned to increase $\mathcal{L}(t)$. A precise measurement of $\mathcal{L}(t)$ is indispensable for precision measurements at the LHC, as can be seen from Eq. (2.1). A summary of how this is done within the CMS experiment is given in Section 2.5. The increase of instantaneous luminosity leads to an increase of simultaneous pp interactions called pileup (PU). Only one interaction among all is of physics interest while others lead to unwanted contributions. The mitigation of PU effects in measured data is a challenging task. In the CMS experiment this is achieved thanks to high resolution detectors and advanced reconstruction techniques as discussed in Sections 2.2 and 2.4, respectively.

At the LHC, cutting-edge technology is used to reach the ambitious goals set on the beam energy and intensity. For the two beams, two separate beam pipes are used. In each pipe, eight superconducting cavities cooled down to 4.5 K generate electromagnetic potential with a frequency of 400 MHz and an accelerating power of 5 MV m^{-1} to accelerate and tighten the bunches. Dipole magnets with magnetic field strengths of 7.74 T are installed to bend the particles to a circular path. Superconducting quadrupole magnets cooled down to 1.9 K with superfluid helium 4 focus the beam. To mitigate unwanted collisions with gas atoms in the beam pipe, a vacuum pressure as low as 10^{-13} atm is ensured.

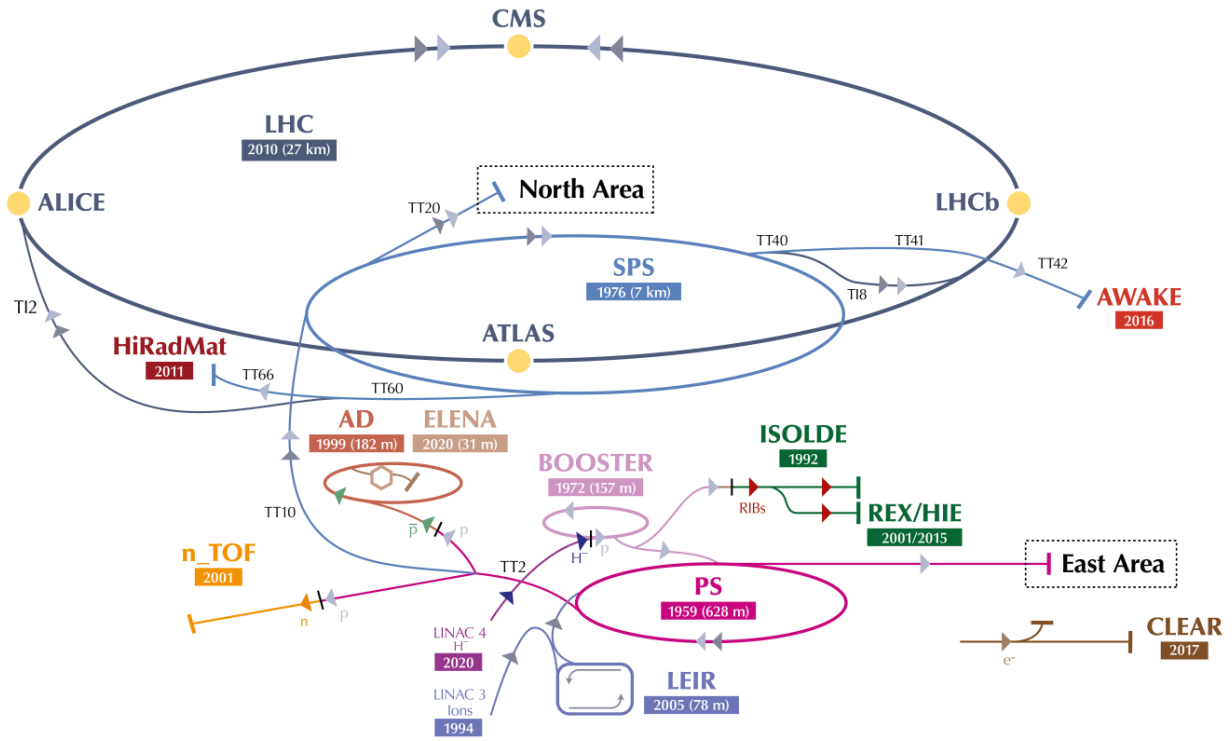

Fig. 2.1.: Sketch of the CERN accelerator complex [75].

A complex accelerator system is needed to fuel the LHC as illustrated in Fig. 2.1. To

create proton beams, hydrogen atoms with an additional electron (H^-) are first accelerated with the linear accelerator LINAC4 to an energy of 160 MeV. The two electrons from H^- are then stripped off in the injection to the proton synchrotron booster (BOOSTER). The thereby obtained protons are accelerated in the BOOSTER to 2 GeV, then in the proton synchrotron (PS) to 26 GeV, and further in the super proton synchrotron (SPS) to 450 GeV. Finally, they are injected into the LHC ring and accelerated to their final collision energy. The two particle beams moving in opposite directions are brought into collision in four interaction points illustrated with the yellow dots of Fig. 2.1. The LHC is designed to be filled with 2808 bunches per beam with each bunch having $1.2 \cdot 10^{11}$ protons and a bunch spacing of 25 ns from each other. Collisions can be provided for a period of ten hours or longer until the beam is diluted. The beam remnant is then dumped in a water-cooled graphite block and the LHC has to be refilled again.

At the four main interaction points mentioned above, four particle detectors are placed. The ALICE [76] detector is designed to primarily investigate heavy-ion collisions. In these collisions, extremely high temperatures are created and among others, direct signs of a quark-gluon plasma are measured, a state that was present in the very beginning of the universe [77]. The LHCb [78] detector is an asymmetric detector with the focus on precision measurements of b hadron properties. One remarkable result that was already mentioned in Section 1.1.3 is the evidence of lepton universality violation in B^+ meson decays with a significance of 3.1 standard deviations [2]. Noteworthy is also the precise measurement of the W boson mass with an uncertainty of 32 MeV [79]. Due to the forward geometry of the LHCb experiment, this result is obtained from different kind of events and has complementary information with respect to measurements that can be performed by the other two main detectors at the LHC: the ATLAS [80] and CMS [81] detectors. The ATLAS [80] and CMS [81] experiments are general-purpose experiments and designed to investigate a wide range of particle physics. They follow a similar physics program, which allows cross-checks and combinations of results. The most famous mutual achievement by the ATLAS and CMS experiments was the discovery of the Higgs boson with a mass of about 125 GeV in 2012 [21, 22]. Since then, the properties of the Higgs boson like its mass, CP structure, or Yukawa coupling to the top quark have been studied in great detail [82–84].

The first pp collisions at the LHC were performed in the years 2010 to 2012 at $\sqrt{s} = 7$ and 8 TeV, denoted as Run 1. During these years, the data were collected that led to the discovery of the Higgs boson. It corresponds to about $\mathcal{L} = 29.4\,\text{fb}^{-1}$ delivered for each, the CMS and ATLAS experiment. The luminosity that was recorded by the CMS experiment and is available for physics analyses is a bit lower due to deadtime in the readout electronics and amounts to about $\mathcal{L} = 27.3\,\text{fb}^{-1}$. After Run 1, the LHC went into the first long shutdown where maintenance and upgrades on the LHC machine were performed to prepare for an increase in instantaneous luminosity and beam energy. Parts of the detectors like active material or readout electronics were replaced and upgraded to cope with the higher data rates and radiation exposures, but also to improve the overall performance. The Run 2 of data taking started in 2015 and lasted until the end of 2018 where protons collided at an unprecedented energy of $\sqrt{s} = 13$ TeV. Peak luminosities were continuously increased and reached values of up to $\mathcal{L}(t) = 2 \cdot 10^{34}\,\text{cm}^{-2}\,\text{s}^{-1}$ in 2018, i.e., twice the target value [85]. This was mainly achieved by squeezing the beams at the

interaction points and thus reducing A_{eff}. The integrated luminosity delivered for the CMS experiment for each year is illustrated on the left-hand side of Fig. 2.2 and amounts to a total value of $\mathcal{L} = 164\,\text{fb}^{-1}$. The Run 2 data was analyzed for the work presented in this thesis, excluding the small amount of data taken in 2015. This corresponds to a recorded luminosity of $\mathcal{L} = 138\,\text{fb}^{-1}$. The distribution of the number of PU interactions (N_{PU}) for each year in Run 2 is drawn on the right-hand side of this figure and has an average value of $\langle N_{\text{PU}} \rangle = 34$ in the full data set.

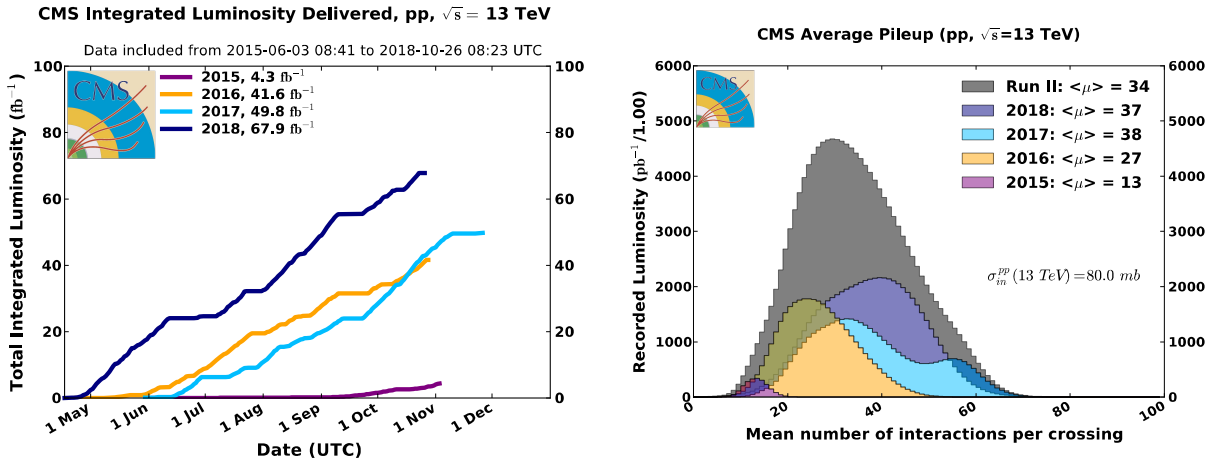

Fig. 2.2.: The left plot shows the integrated luminosity as a function of months in each year of the Run 2 data taking [86]. On the right, the spectrum of PU interactions in each year and in the full Run 2 data set is drawn [86].

During Run 1 and Run 2, also collisions with lead ions (lead-lead and proton-lead) were performed and the use of xenon ions was tested. Moreover, collisions at lower energies with $\sqrt{s} = 2.67\,\text{TeV}$ and $\sqrt{s} = 5.02\,\text{TeV}$ were performed, serving a wider range of physics programs. A second long shutdown followed Run 2 for further upgrades on the LHC facility and detectors. While this thesis is being written In early 2022, while this thesis is being written, pp collisions are about to start again. The further course of the year will mark the beginning of Run 3 with about $\sqrt{s} = 13.6\,\text{TeV}$. For a period of four years, an integrated luminosity of about $300\,\text{fb}^{-1}$ is expected to be recorded. After Run 3, a longer shutdown is planned to prepare for the high luminosity LHC (HL-LHC) [87]. As of now, the HL-LHC is planned to start in 2029 and last until 2038 or even 2041. An instantaneous luminosity of $5 \cdot 10^{34}\,\text{cm}^{-2}\,\text{s}^{-1}$ is targeted to increase the amount of data by a factor of 10, i.e., to $\mathcal{L} = 3\,000\,\text{fb}^{-1}$.

2.2. The CMS detector

The CMS detector is a multi-purpose experiment located in a cavern at Cessy in France at the interaction point 5 (IP5) of the CERN LHC to study pp collisions at center-of-mass energies of 0.9–14 TeV. The requirements for such a multi-purpose detector are the ability to measure and distinguish all possible particles that are created in a pp collision with the best possible spatial and momentum resolution. This also means that the detector

encloses the interaction point as much as possible. Beyond that, the detector has to be robust and resilient against radiation to operate for several years. The CMS detector is built according to a cylindrical concept with multiple barrel layers around the beam pipe, centered at the pp interaction point. Layers of endcap disks at both ends of the barrel layers complete the design and increase the coverage at low angles down to 0.77° with respect to the beam pipe. Each detector layer gives complementary information to allow the detection of the different types of particles that are produced. Of all known particles solely neutrinos leave the CMS experiment without direct detection. The inner detector layers are enclosed by a strong solenoid magnet to bend electromagnetically charged particles to curved trajectories. This allows to distinguish them from neutral particles and to determine their momentum from the curvature of the particle track. The solenoid has a diameter of 6 m, a length of 12.5 m, and produces a magnetic field strength as high as 3.8 T in the inner detector layers. An iron yoke surrounds the solenoid and guides the magnetic field with a strength of 2 T through the outer detector layers. Due to the design choice of the detector, which places many detector layers inside the strong solenoid magnet, the length and diameter of CMS are 21 m and 15 m, relatively. This is a compact and small detector, in comparison with e.g. the ATLAS experiment. The weight of the CMS detector is about 14 000 tons. A sketch of a the CMS detector is shown in Fig. 2.3.

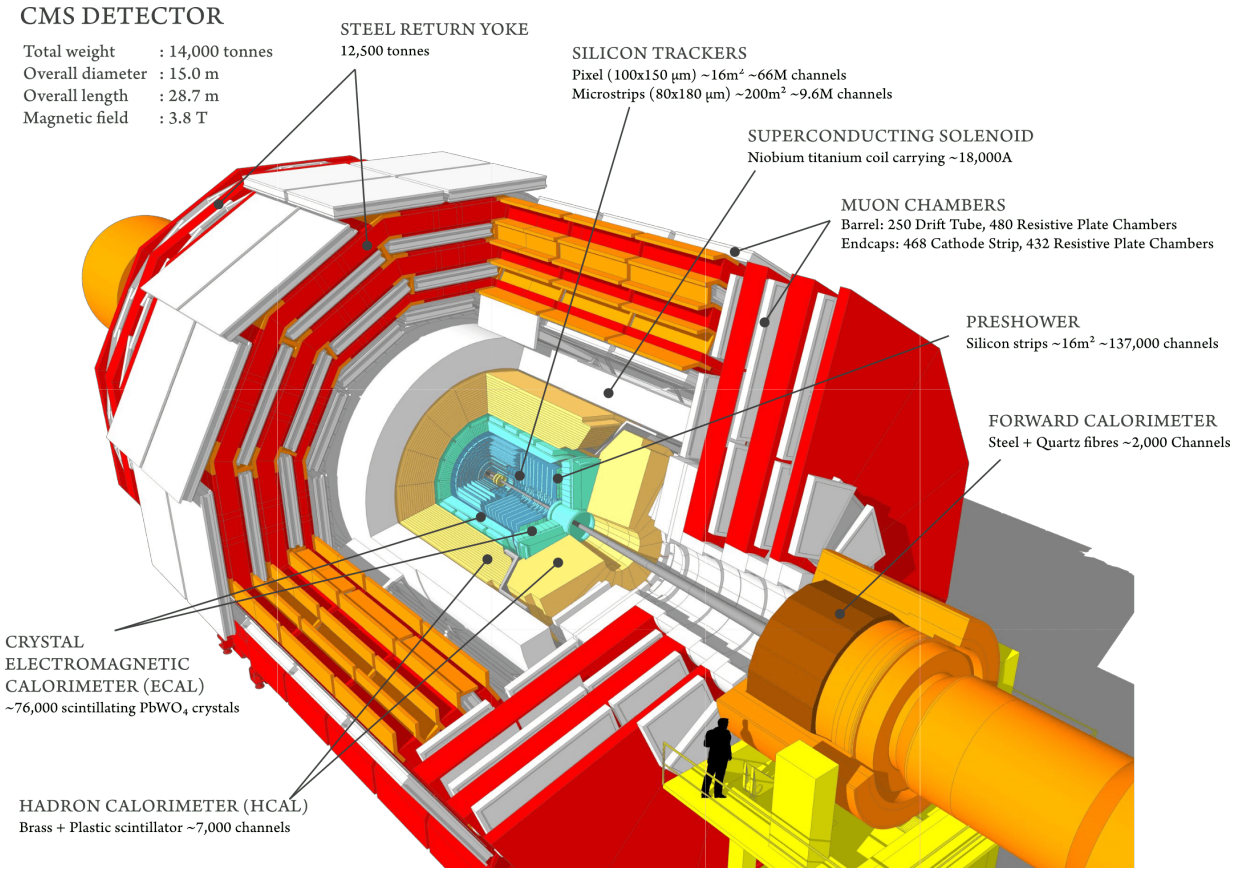

Fig. 2.3.: Illustration of the CMS detector [88].

2.2.1. Coordinate system

The origin of coordinates in CMS is defined at the nominal interaction point. The x-axis is chosen to point to the center of the collider ring, the y-axis points upwards perpendicular to the collider plane, and the z-axis is chosen in the direction of the beam pipe such that a right-handed coordinate system is obtained. To account for the azimuthal symmetry of the detector, spherical coordinates are usually used with the azimuthal angle ϕ defined in the x-y plane, starting from the y-axis. The polar angle θ is used in the y-z plane measured from the z axis.

In pp collisions, the momentum in direction of the z-axis (p_z) is usually different for the two initial state partons and is unknown. For this reason, the p_z and θ of the final-state particles are often not expressive. More useful in this sense is the rapidity

$$v = \frac{1}{2} \ln \frac{E + p_z c}{E - p_z c} \,, \tag{2.3}$$

which depends on the energy E of the particle and is a measure of its velocity perpendicular to the z-axis. It has the benefit that differences in v are invariant under Lorentz boosts in the beam direction. This means for instance that the Δv between two final-state particles is independent of the initial state p_z. Further, one can just add up rapidities instead of using the relativistic velocity-addition formula. A related angular variable is the pseudorapidity

$$\eta = -\ln \left[\tan \left(\frac{\theta}{2} \right) \right] \,. \tag{2.4}$$

In the relativistic limit where the mass of the particle is negligible over its energy, η is equivalent to v and has the same properties. Furthermore, it features that in each fixed η-interval, the flux of particles is constant. For these reasons, η is usually preferred over θ.

The energy and momentum is conserved in the transverse plane for the sum of all final-state particles in the event. It is defined as

$$\vec{p}_T = \begin{pmatrix} p_x \\ p_y \end{pmatrix} \quad \text{and} \quad E_T = \sqrt{E_x^2 + E_y^2} \,, \tag{2.5}$$

A value that defers from zero is usually attributed to the undetectable neutrinos in the event. Therefore, the missing transverse momentum $\vec{p}_T^{\,\text{miss}}$, with magnitude E_T^{miss}, is defined from the negative sum of the momenta of all measured particles.

2.2.2. Silicon tracker

The tracker is the innermost part of the detector, located at a distance down to 30 mm around the beam pipe. The measurement of hits from charged particles in the tracker allows to precisely reconstruct tracks. From the curvature of the tracks in the magnetic field, the momentum of the particle is determined. Tracks can be associated with the primary vertex (PV) of the hard interaction in pp collisions or secondary vertices (SVs) from decays of heavy particles. The reconstruction of the PV allows to identify and reject PU interactions while SVs can be used to select events with τ leptons, b hadrons, or other long-lived particles.

Multiple requirements are placed on the tracker material. For example, in 80 mm distance a flux of around 10 million particles per square centimeter per second are expected [89]. Hence, the material has to be radiation resistive for the operation of many years. The tracker must have a good spatial resolution to keep apart the hits of different particles. Since interactions happen every 25 ns, an excellent time resolution is also required. Furthermore, the tracker material can not be too dense since this would lead to multiple scatterings of incoming particles that pass through. It would also cause photons to convert into electron-positron pairs in the detector material.

To meet these requirements, the full tracker is based on silicon technology. Multiple barrel and endcap layers are installed to cover a range up to $|\eta| < 2.5$ [90]. When a charged particle travels through these layers it knocks out electrons in the detector material, which move in an electric field and create a small electric pulse. The pulse gets amplified and detected in readout electronics. Two different types of silicon detectors are used, namely: pixel and strip elements.

The pixel elements consist of small segments with the size of $100\,\mu\text{m} \times 150\,\mu\text{m}$ [91]. In this way, a single hit resolution of about $10\,\mu$m (transverse) and 20–40 μm (longitudinal) is achieved [92]. During Run 1 and until the end of 2016 three barrel layers and two endcap discs of pixel elements were mounted. To handle higher instantaneous luminosities, the pixel detector was replaced with a new one at the beginning of 2017 [93]. Upgraded digital readout chips were installed with a higher rate capability. The elements were cooled down to -20° C (compared to 4° C before) to further reduce disorder in the silicon. Four barrel layers and on each side three endcap discs were placed in a distance of $29\,\text{mm} < r < 160\,\text{mm}$ and $291\,\text{mm} < |z| < 516\,\text{mm}$, respectively. The extension by one layer ensures particles transit through four layers, creating further redundancies to allow more accurate measurements. Despite additional layers, it was possible to reduce the material budget using carbon fiber and graphite compounds.

Ten barrel layers of silicon strip elements are placed around the pixel detector up to a distance of 1.1 m. In the endcaps, three small and nine large discs are located on each side. The increased distance from the collision point means a lower flux of particles. This allows to use bigger segments and fewer readout electronics with respect to the pixel detectors. The size of the strip segments for the innermost layers to the outer ones range from $10\,\text{cm} \times 80\,\mu\text{m}$ to $25\,\text{cm} \times 205\,\mu\text{m}$ in length (η) and width (ϕ) [90, 92].

2.2.3. Electromagnetic calorimeters

One particular emphasis on the CMS design was the measurement of $\text{H} \to \gamma\gamma$ and $\text{H} \to \text{ZZ}^*$. Hence, good identification and energy resolution of photons and electrons were pursued. This is mainly achieved with the electromagnetic calorimeter (ECAL) that measures the energy of electromagnetically interacting particles [81, 94].

The ECAL is made of a barrel ($|\eta| < 1.479$) and two endcap ($1.479 < |\eta| < 3.0$) segments. Each segment consists of a single layer of homogeneously distributed small lead tungstate (PbWO_4) crystals. These act as absorber and scintillator material at the same time. When charged particles hit the material it acts as an absorber and photons get radiated via bremsstrahlung. Photons in turn undergo the so-called conversion and produce electron-positron pairs. These processes create an electromagnetic shower of

photons, electrons, and positrons. When the energy of electrons falls below a certain level, they mainly excite atoms in the ECAL material, which emit photons in a process called scintillation. The scintillation light is detected with photodiodes. The measured intensity is proportional to the energy deposited. Since the photon permeability of the $PbWO_4$ crystals is not high enough, photomultipliers are installed to amplify the signal.

The choice of $PbWO_4$ is based on multiple criteria. With its fast response and recovery about 80% of the light is collected in the time span between two bunch crossings (25 ns). Further, the Molière radius of 2.2 cm, describing the width of the electromagnetic shower, is small enough to have a good separation between different particles. Finally, the high atomic number (207.2 for Pb) leads to a small radiation length of $X_0 = 0.89$ cm. This length is defined as the distance after which high-energy electrons have reduced their energy to $1/e$ of the initial value while photons undergo a conversion on average after $7/9\, X_0$. With a thickness of 23 cm in the barrel and 22 cm in the endcap, the ECAL provides lengths of $26\, X_0$ and $25\, X_0$, respectively. Thereby, 98% of the energy for electrons and photons below 1 TeV is absorbed in the ECAL. The ECAL has a nuclear interaction length of $\lambda_I \approx 1$, meaning that traversing hadrons undergo on average about one inelastic nuclear interaction. Hence, they also lose part of their energy.

To improve the identification of neutral pions that decay into a pair of photons, and to distinguish them from photons of the hard interaction, a preshower calorimeter is placed after the tracker and before the main ECAL calorimeter in the forward region of the detector ($1.653 < |\eta| < 2.6$). It consists of two layers of lead absorbers with $2\, X_0$ and $1\, X_0$ thicknesses, and silicon strip sensors after each layer.

2.2.4. Hadronic calorimeters

Hadrons usually retain most of their energy when leaving the ECAL. Therefore, the ECAL is hermetically surrounded by a hadronic calorimeter system (HCAL) [81]. The HCAL allows to precisely measure the energy of hadronic jets. This is also important to measure the total energy of the system and determine the missing transverse energy originating from neutrinos or particles produced in BSM processes.

The HCAL consists of sampling calorimeters, meaning that each calorimeter consists of alternating layers of absorber and scintillator material. Flat brass absorber plates are sandwiched by plastic scintillator material. Additional steel plates provide further absorption material and serve to stabilize the structure. Similar to the ECAL, particles create hadronic showers when interacting with the absorber material. In the scintillator material, light gets emitted that is then transported via fiber and optical cables to photodiodes where it gets read out.

A barrel calorimeter (HB) covers the central region up to $|\eta| < 1.3$ while two endcap calorimeters (HE) cover $1.3 < |\eta| < 3.0$. Both the HB and HE are placed inside the magnetic coil which limits their available space for material. While the HE provides a thickness corresponding to about $10\, \lambda_I$, the HB provides only $5.82\, \lambda_I$ at its thinnest point ($|\eta| = 0$), meaning that many hadrons escape the HB. Therefore, an outer barrel calorimeter (HO) provides additional material outside of the magnetic coil. The HO contains an additional iron plate centered around $|\eta| = 0$ and is called the tail catcher. This leads to a thickness of the total calorimeter system, including the magnetic coil,

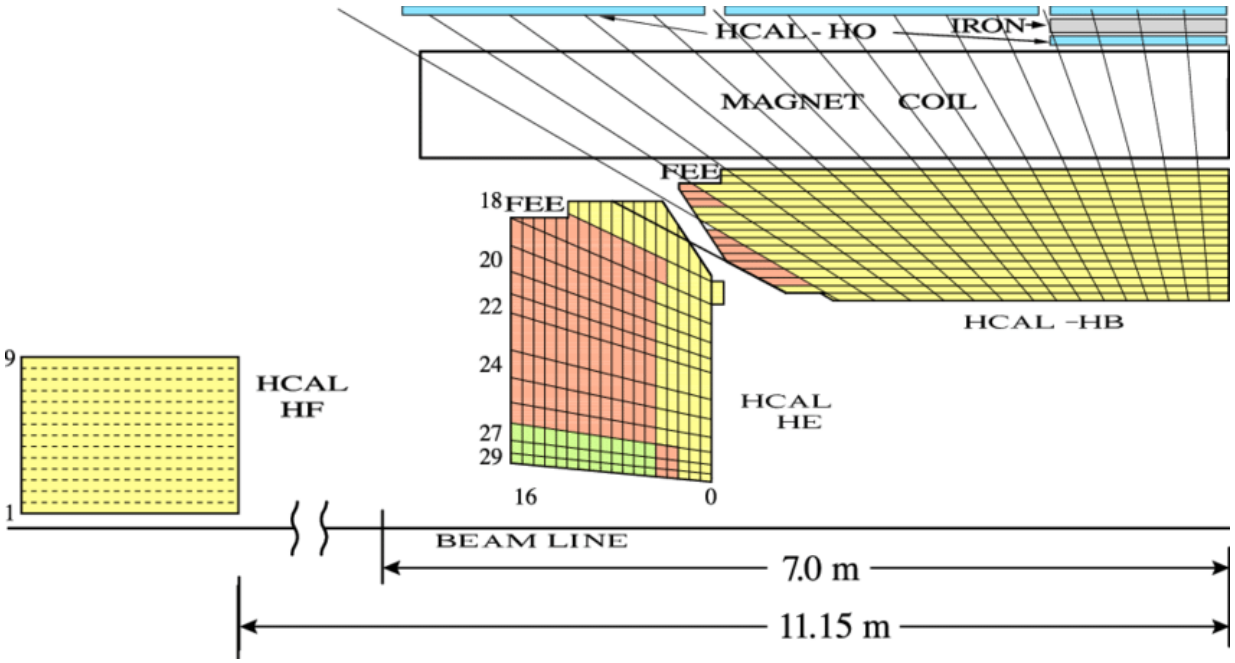

Fig. 2.4.: Profile of the HCAL system [95].

corresponding to $11.8\,\lambda_I$ at the thinnest point.

Two forward calorimeters (HF) are placed in $z = \pm 11.2\,\text{m}$ distance to the nominal interaction point. They ensure a coverage up to $|\eta| < 5.2$ such that also jets in the forward region can be detected as well. For the HF segment, the dose of radiation is much higher and a Cherenkov detector is used instead of scintillators. When charged particles hit the active material, Cherenkov light is generated and transported to the read-out system. Quartz fiber is used as active material because it shows a higher level of radiation hardness. It is arranged in tubes parallel to the beam pipe and enclosed by a steel structure that acts as the absorber material. The profile of the HCAL system is illustrated in Fig. 2.4.

2.2.5. Muon system

Muons are only weakly interacting in the tracker and calorimeter system and have a lifetime ($2.2\,\mu$s [10]) long enough to penetrate through them without losing much energy. The muon detector system is the outermost part of the CMS detector and is located outside the solenoid magnet. It is placed in between layers of the iron return yoke and covers the range up to $|\eta| < 2.4$. Three different types of gas detectors are used. A cross-sectional view of the muon system is shown in Fig. 2.5.

Four barrel stations of drift tubes (DTs) are placed in the region of $|\eta| < 1.2$. Each DT is 4 cm wide, filled with gas, and contains a positively charged wire in the center such that an electric field is generated. When a muon passes through, it can knock electrons out of the gas atoms. The free electrons move to the wire, creating a signal that is measured. Multiple layers of DTs are arranged perpendicular to each other to determine time and position. Through the curved trajectory of the muon in the magnetic field beaconed by

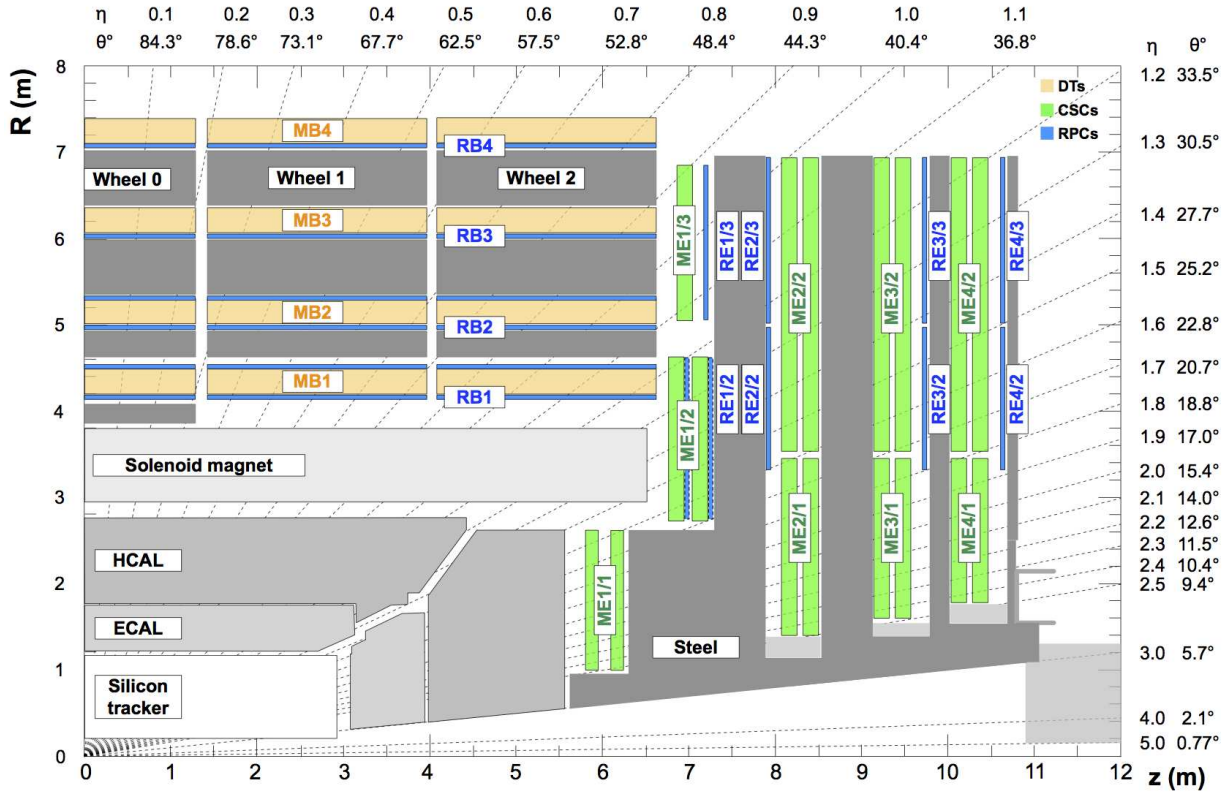

Fig. 2.5.: Profile of the CMS detector highlighted on the muon system [96].

the iron return yoke, also their momentum is measured.

In the endcap region, for $0.9 < |\eta| < 2.4$, cathode strip chambers (CSCs) are used. In the CSCs, positively charged wires are crossed by negatively charged copper strips. Free electrons moving to the wires create an avalanche of electrons, while the ionized gas atoms are creating a signal at the strips. The information is combined to measure the position of the muon. The CSCs are characterized by their good radiation hardness and fast response.

As a complementary detector, resistive plate chambers (RPCs) are used for $|\eta| < 1.9$. Each RPC is a gas volume enclosed by two flat plates to which a voltage is applied. Muons that pass through the gas create an avalanche of electrons. The muon momentum is measured based on the pattern of the signal. Combined with the short time resolution of about 1 ns, the RPCs are used in the trigger system which is explained in the next section. For future data taking, additional RPCs will be placed in the very forward region of the detector to cover angles down to $|\eta| < 2.4$.

Further redundancy will be obtained by complementing the muon system with gas electron multiplier (GEM) detectors improving the reconstruction and trigger efficiency, and the muon momentum resolution [97]. The technology has proven to be reliable already in other experiments like LHCb [78] and is particularly well suited to cope with the increased particle flux in the forward region and future LHC runs. Three stations of GEM detectors will range from $|\eta| > 1.6$ to $|\eta| < 2.8$, extending the previous coverage. Chambers with a size of 1–2 m^2 are filled with an argon CO_2 gas mixture. Incoming muons ionize the gas and are thereby detected. The first parts are already installed and

operational for Run 3 while further parts are planned to be added during technical stops. The upgrade will be finalized in the long shutdown after Run 3 such that the complete system will be ready for the HL-LHC data taking starting in 2027.

2.2.6. Trigger system

During Run 2 the proton bunches in the LHC were collided with a rate of up to 40 MHz at the CMS detector [98]. The amount of data generated by this enormous number of collisions is by far too large to store permanently. Moreover, most collisions lead to QCD interactions of lesser interest. A two-tiered trigger system is employed to select rarer events, interesting for physics analysis, and reduce the data to a feasible amount [99].

The first level (L1) is implemented in hardware and makes a decision in less than 4 μs whether an event is processed further or rejected [98]. Thus the rate is reduced to 100 kHz. L1 triggers are connected to the various calorimeter elements and muon detectors to access information of each individual system. The data from the calorimeters are combined to identify detector signals compatible with the hypothesis of an electron, photon, τ lepton, hadronic jet, or missing transverse energy. Similarly, potential muon candidates are identified by combining the information from the muon detectors. A global trigger combines the output of the calorimeters and muon system and allows to select events with an analysis-specific target.

On the second level, software-based high level triggers (HLTs) are used [98, 99]. These reduce the rate to about 1 kHz for offline storage. To select events, they undergo a more elaborate and resource-intensive reconstruction, which now also includes track reconstruction. Algorithms close to the ones used in the offline reconstruction are used, as explained in Section 2.4.

Both L1s and HLTs can be prescaled to comply with the maximum possible rate. If a trigger has a prescale p, only the fraction of $1/p$ events that are selected by this trigger are actually stored. The prescale is typically adjusted to the instantaneous rate during data taking and allows to collect events from processes with large cross sections. These are of great value for detector calibration, for example, or the development and validation of certain algorithms.

2.2.7. Data sets and computing

Selected events are distributed to different primary data sets. Depending on which HLT the event has passed, it ends up in one or the other. Events accepted by a single muon trigger are for example stored in the single muon primary data set while those selected by an electron or photon trigger are stored in the e/γ primary data set. If an event is accepted by multiple HLTs with different associated data sets, it will be stored in multiple primary data sets.

During data taking, the data are organized in different periods containing data from a certain amount of LHC fills with similar conditions. The data of each LHC fill are split into multiple runs; A new run starts whenever there is a change in the settings related to the data taking. Each run is further split into so-called luminosity blocks, where each luminosity block lasts 23.3 s.

The raw data, which have the full information on detector hits and energy depositions, is then further processed in an offline reconstruction chain as discussed in Section 2.4. For a possible later reconstruction with updated detector calibrations, the raw data is written on tape for permanent storage.

The processing of the data is performed on the decentralized worldwide LHC computing grid [100]. It consists of multiple data centers, classified into four levels, known as Tiers. The central hub, Tier 0, is located at CERN and provides a bit less than 20% of the total computing power of the network. From there, the data is distributed to 13 Tier 1 data centers that are connected via optical fibers, allowing for data transfer rates of 10 GB/s. The tier 1 centers have large storage capacity, performance power, and maintenance 24 hours a day is guaranteed. The CMS grid has 155 Tier 2 data centers that vary a lot in size and are hosted by various universities and institutes around the globe. Finally, smaller clusters or even individual computers are connected to the network as Tier 3 nodes. The network includes 42 countries with in total 900 000 computer cores. It is running more than two million tasks per day from over 12 000 scientists.

2.3. Event simulation at the CMS experiment

2.3.1. Simulation of pp collision data

The simulation of events from pp scattering is an integral part for the CMS experiment. Simulated samples are used to model the efficiency and acceptance effects. They are further utilized to develop and validate algorithms for the reconstruction and identification of particles. In the context of this thesis, simulated samples are deployed to design the analysis and extract physical quantities from data.

Different tools are used at different steps of simulation. One commonly used matrix element generator is the MadGraph 5 that calculates $\mathcal{M}$ at LO in perturbative QCD with up to four non collinear high-p_T partons [101]. The MadEvent package [102] is used to generate events following the Monte Carlo (MC) method [103], which is basically a numerical integration of the desired phase space. For this reason, simulated events are often called MC events. An extension is the MadGraph5_aMC@NLO package which allows to include terms at NLO in α_S [104]. Subsequently, the final-state matrix element particles must be passed through a separate PS program. The PS simulation can lead to contributions that are already covered by the matrix element simulation if events are simulated with additional partons or at NLO precision in α_S. Hence, a careful matching procedure has to be applied to avoid double counting of the phase space. For the MadGraph 5 generator, the MLM scheme is used [105]. In the more complicated case of MadGraph5_aMC@NLO, overlapping contributions are subtracted by the FxFx [104] merging. Practically this is accounted for by events with negative weights.

Another matrix-element generator that includes Feynman diagrams up to NLO in α_S is POWHEG [106–108]. POWHEG uses a different, process specific, procedure where the radiation of the particle with the highest p_T is generated first. The PS program can then add further emissions with lower p_T. In this approach, no events with negative weights are produced.

PYTHIA is a multi purpose toolbox that allows the simulation of the hard process, parton

shower, hadronization, color reconnection and particle decay [109]. Even if the hard process can be produced at LO precision, PYTHIA is typically used to only simulate the subsequent processes. It offers interfaces to matrix element simulations from MADGRAPH 5, MADGRAPH5_aMC@NLO, or POWHEG. To simulate the underlying event, PYTHIA uses a set of adjustable parameters, the so called underlying event tune — or simply tune. These tunes have to be determined using data. Previously, the CUETP8M1, CUETP8M2, and CUETP8M2T4 tunes have been used in analyses within the CMS experiment [110–112]. For the results shown in this document, most samples are simulated with the newer CP5 tune, for which also a variation of parameters has been made to estimate the associated uncertainties [113].

2.3.2. Detector simulation

A full simulation of the CMS detector is performed for simulated pp collisions data. All detector materials, including dead materials from for example the scaffold system, are modeled with GEANT4 [114] toolkit. Emerging particles from simulated events, so-called "generator-level" particles, are propagated through this simulation where the effects of the magnetic field, bremsstrahlung, photon conversions, or multiple scatterings are accounted for. The generated signatures like energy deposits and hits in the active detector elements are taken as input for the emulation of the readout electronics and the trigger system. Simulated events are then treated in the same manner as data with respect to the event reconstruction as it will be explained in Section 2.4. The objects thus obtained are denoted as "detector-level" particles. Simulated samples also include events coming from PU. In practice, the main interaction is overlayed with pp collisions simulated according to elastic or inelastic pp scatterings. The PU spectrum is based on a distribution expected in data.

2.4. Event reconstruction the the CMS experiment

In this section, the reconstruction software that is commonly used in the CMS experiment is described. Based on the measured energy deposits (hits) in various detector layers, all particles in an event are tried to be reconstructed. A slice of the CMS detector is shown in Fig. 2.6, illustrating the expected path and interaction of the different kinds of particles. In the first reconstruction step, particle trajectories (tracks) and their points of origin (vertices) are determined. The momenta of charged particles are determined from the curvature of the track. The energy deposits in the ECAL and HCAL are grouped into clusters and complement the determination of energy and direction of charged particles. The combination of tracks and calorimeter clusters is essential in the case of high p_{T} or low-quality tracks. Moreover, the contributions of charged and neutral particles are separated. Subsequent algorithms aim to identify particles that penetrate the detector such as electrons, photons, muons, and hadrons. These represent the building blocks that are combined with the particle flow algorithm [115] where a refined identification and reconstruction is performed. Under a specific hypothesis, dedicated fits and calibrations are performed. The resulting particles are then clustered into jets. Finally, a set of higher-

level algorithms are described to identify analysis-specific objects, such as b jets and prompt leptons.

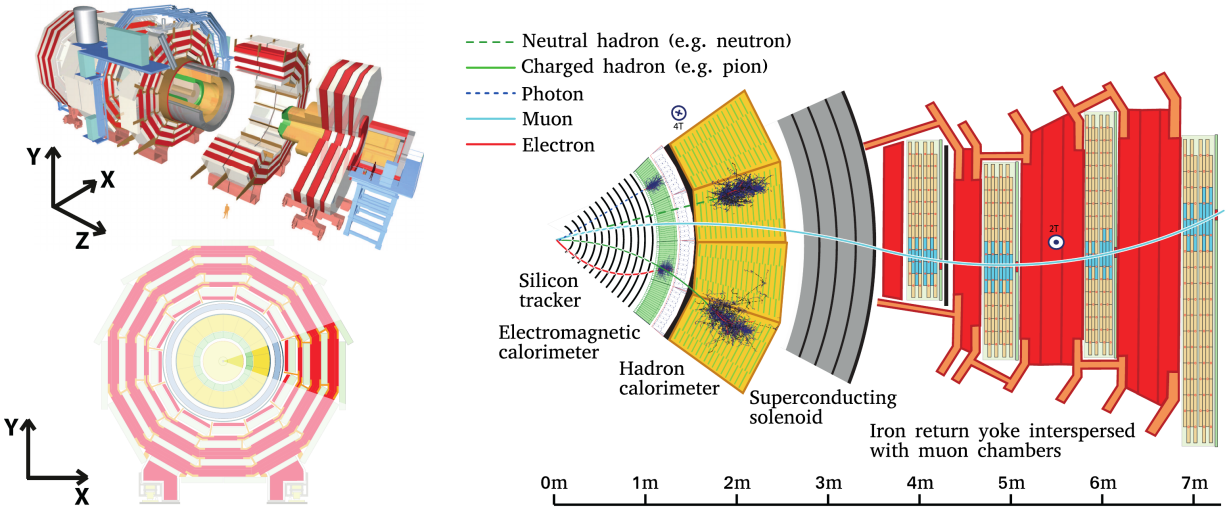

Fig. 2.6.: In the upper left a sketch of the CMS detector in different pieces is drawn. The lower left shows a profile of the CMS detector in the x-y plane where a slice is highlighted and shown on the right with the paths of interacting particles. Adapted from Ref. [116].

2.4.1. Particle identification and reconstruction

Tracks To find tracks of charged particles in the silicon tracker (inner tracks), a Kalman filter algorithm is used [117]. The procedure starts with hits in the layers (seeds) from which a first estimate on the track parameters is made. The track is stepwise propagated through all surrounding layers and combined with the hits found there. In each step, the track parameters are updated and multiple track hypotheses are made. Finally, ambiguities are resolved for tracks that share at least half of their hits by discarding the track with the lower number of hits. A global fit is performed that yields the direction and momentum of the track. To recover high efficiencies, the procedure is repeated for up to ten iterations, starting with tight quality criteria on the seeds and the final track. After each iteration, the energy deposits assigned to the found tracks are removed from the hit collection and the quality requirements are relaxed for the next iteration. The last iterations are seeded by tracks from the muon chambers (discussed later in this section) to increase the efficiency of reconstructing muon tracks in the silicon tracker [115]. The track reconstruction efficiency is studied in simulation [92]. For isolated muons within $|\eta| < 2.4$ and with $1 < p_{\mathrm{T}} < 100\,\mathrm{GeV}$, it is found to be above 99% and largely independent of p_{T} and η. The fake rate, defined as the fraction of tracks not generated by charged particles (e.g. from the detector noise), was found to be negligible for those tracks. Isolated charged hadrons and electrons show some dependency on η where the efficiency is above 95% in the central region and goes down to 80% in the forward region of the detector. Fake rates for those particles are below 2% in the central region while they reach values above 10% in the transition region of the barrel and endcaps.

Primary vertices The interaction vertex of one particular inelastic pp scattering is denoted as primary vertex (PV). Because of PU, multiple pp interactions occur in each bunch crossing as shown in Fig. 2.7. This gives rise to many PVs. The PV reconstruction is a highly nontrivial problem and can only be solved by considering all PVs together. To find these PVs, high-quality inner tracks are extrapolated to their closest point on the beamline and an uncertainty is assigned to this position. Multiple tracks have to be associated with every yet unknown PV. To find the global minimum in this high dimensional space, the deterministic annealing algorithm [118] is utilized, which is based on problems of statistical mechanics. A function similar to the energy of a thermodynamic system is formulated with the inputs of the positions and uncertainties of PVs and tracks, and probabilities for each track-PV pair, that the track originates from the regarded vertex. The function is minimized following an iterative procedure that is analogous to the reduction of the temperature of a thermodynamic system [92]. The procedure results in the determination of PV positions with a resolution of about 20 μm [92]. A reconstruction efficiency of essentially 100% was found for PVs with at least three associated tracks and above 98% for PVs where only two tracks are associated [92]. This makes the number of reconstructed primary vertices (N_{PV}) a good proxy for the number of PU events (N_{PU}). No direct PU dependency on the efficiency of the PV reconstruction was found, but a dependence occurs indirectly via the limited tracking efficiency. On the other hand, the correct identification of the PV of the interaction with the largest energy transfer, which is typically used in physics analyses, is increasingly challenging under higher PU conditions. It is chosen at a later point of the reconstruction chain as the one with the highest sum of p_{T}^2 of associated physics objects. The physics objects considered here are the $E_{\mathrm{T}}^{\mathrm{miss}}$ and jets, reconstructed via the particle flow algorithm, as described in Section 2.4.2.

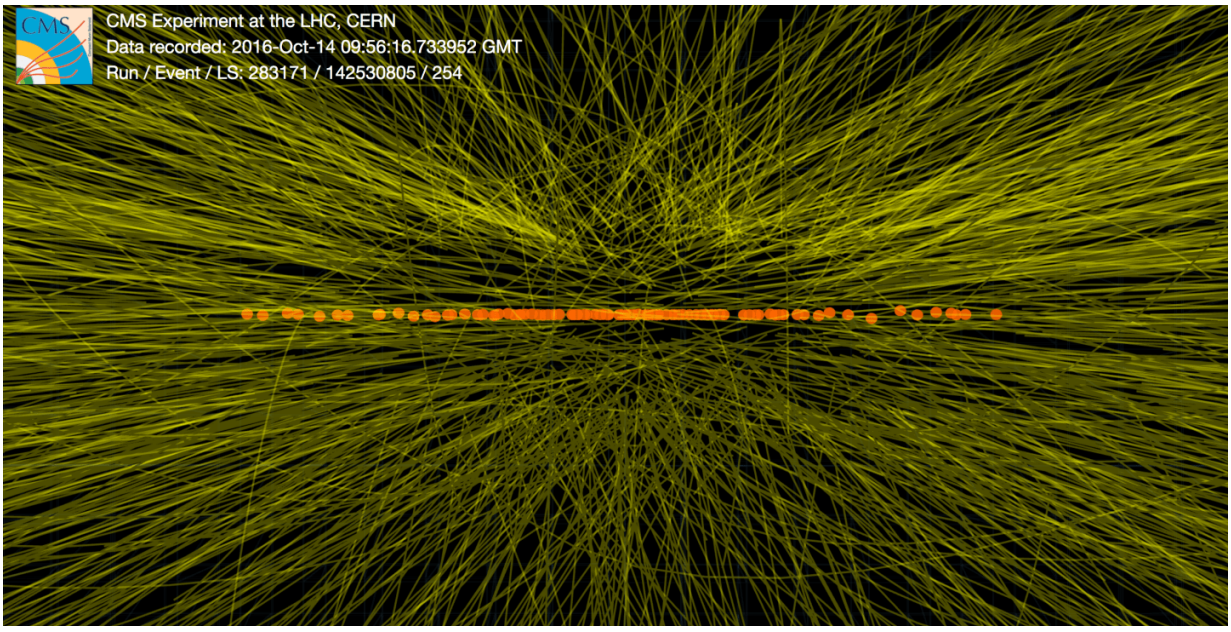

Fig. 2.7.: Illustration of a side view of the nominal interaction point of the CMS experiment in a pp bunch crossing at high PU in 2016. Each pp interaction is illustrated with an orange point and yellow lines illustrate emerging particles. From Ref. [119].

The distance of the closest approach of a track to the PV is called impact parameter

(IP) which is calculated in one (longitudinal, d_z), two (transversal, d_{xy}), or three spatial dimensions. Beyond that, the significance of the impact parameter (SIP_x) in x dimensions is calculated as the IP value divided by its uncertainty. These quantities can be used, for instance, as quality criteria to select particles coming from one particular PV and reject those from others.

Muon tracks Muon tracks are reconstructed in the muon system by first clustering hits of different segments and then performing a fit. These so-called standalone muons are then matched with inner tracks if possible. If a match is found, a combined fit is made, resulting in a global muon. Additionally, each inner track with a large enough p_T is extrapolated to the muon system. If it can be matched with the hits there, it is identified as tracker muon. Considering all types of reconstructed muons, an efficiency of about 99% is achieved for finding a muon that is produced inside the acceptance of the muon system. Global muon tracks have an excellent p_T resolution of 1% for muons with $p_T < 100\,\text{GeV}$ [96]. Identified muon candidates are contaminated by punch-through hadrons, where a highly energetic hadron reaches the muon system. Through additional quality requirements, like lepton isolation (explained in Section 2.4.3), most of those punch-through hadrons can be rejected. Furthermore, incident cosmic muons that coincide with a bunch crossing are sometimes identified as standalone muons [115]. They usually have large impact parameter values and can thus be sorted out easily.

Calorimeter clustering In the calorimeters, locally adjacent energy deposits in the calorimeter systems are grouped in so-called clusters. Energy deposits in the subdetectors, the preshower, ECAL barrel, each ECAL endcap, as well as the HCAL barrel and endcaps are clustered separately. Starting from a cell with a regional maximum in measured energy, neighboring cells with measured energy above a certain threshold are connected to the cluster. An iterative fit with a Gaussian-mixture model is performed to extract the cluster parameters. Depending on the particle producing the energy deposits, specific assumptions are made to refine and calibrate the clustering. This procedure and the necessary identification steps are explained in the following.

Electrons Electrons typically produce an inner track, an ECAL cluster, but no HCAL cluster. Therefore, tracks are matched to ECAL clusters and vice versa. The characteristic pattern produced by electrons is exploited to distinguish them from neutral hadrons. Electrons with high p_T often generate bremsstrahlung photons in the silicon tracker, leading to a more widespread ECAL cluster. Under this hypothesis, multiple ECAL clusters are combined into a so-called supercluster. Furthermore, the ratio of the measured momentum of the inner track to the measured energy of the ECAL cluster can be exploited. Also, a more adapted fit with a Gaussian-sum filter (GSF) [120] is performed to extract the track parameters under an electron hypothesis. A multivariate analysis (MVA) makes use of a boosted decision tree (BDT) that combines the characteristic signatures of the electron and the properties of the resulting GSF track to construct a variable that discriminates electrons from other particles like hadrons or photons [121]. A cut on this discriminator variable can be defined (working point) as an additional quality requirement on the electrons.

Photons and hadrons An ECAL cluster that can not be matched to an inner track or HCAL cluster is considered an isolated photon. To further identify photons and hadrons, the ECAL and HCAL clusters are merged and refit together. The energy and position of the combined cluster are compared to the momentum of inner tracks. If a match is found, a combined fit is performed and the resulting track qualifies as charged hadron. In case no match is found, several scenarios for neutral hadrons or photons are considered.

Particle flow reconstruction The aforementioned predefined tracks and clusters represent the building blocks for the particle flow (PF) algorithm [115]. Starting with muon candidates, a dedicated PF reconstruction and identification is performed linking several of those elements. The linked building blocks of PF muons are removed from the collection, reducing the complexity of the identification of other particles. In the PF reconstruction chain, electrons, isolated photons, charged hadrons, non-isolated photons, and neutral hadrons are processed in order. The reconstruction of muons is revisited in the end to correct for residuals in the calorimeter system. Finally, the PF algorithm is used to compute the missing transverse momentum $\vec{p}_{\mathrm{T}}^{\,\mathrm{miss}}$ as the negative $\vec{p}_{\mathrm{T}}$ sum of all PF candidates.

2.4.2. Jets

In the CMS experiment, particles are combined into jets using the anti-k_{T} jet clustering algorithm [122, 123]. The algorithm is chosen due to its relatively fast computation and its collinear and infrared save properties. That means that the same jets are found for arbitrary soft and collinear gluon emissions, and collinear gluon splitting. For the combination of particles into jets, a distance parameter $d_{i,j}$ between two particles i and j is defined as

$$d_{i,j} = \min\left(p_{\mathrm{T},i}^{-2}, p_{\mathrm{T},j}^{-2}\right) \frac{\Delta_{ij}^2}{R^2}\,, \tag{2.6}$$

with $\Delta_{ij}^2 = \left(v_i - v_j\right)^2 + \left(\phi_i - \phi_j\right)^2$ and the radius parameter R that controls the size of the jet. The standard choice in CMS is $R = 0.4$. A distance measure between a particle and the beam axis is defined as $d_{i,\mathrm{B}} = p_{\mathrm{T},i}^{-2}$. The values for $d_{i,j}$ and $d_{i,\mathrm{B}}$ are evaluated for all possible combinations. If the smallest $d_{i,j}$ is smaller than any $d_{k,\mathrm{B}}$, the two particles i and j are combined into a new pseudo particle. Otherwise, the (pseudo) particle k with the smallest $d_{k,\mathrm{B}}$ is defined as a jet and removed from the clustering process. This process is repeated until all (pseudo) particles are clustered into jets. In this way, the hardest particles (the ones with the highest p_{T}) are combined with nearby soft particles (the ones with low p_{T}). If two hard particles have a distance of $R < \Delta_{ij} < 2R$, they split the softest particles in between among them and create two separate jets. The result of this clustering process for a typical event is shown in the v-ϕ plane in Fig. 2.9.

The momentum of a jet is calculated from the vectorial sum of momenta of the PF candidates clustered into the jet. To mitigate the effect of PU interactions, charged PF candidates identified as coming from PU vertices are removed before the clustering process [124]. Additionally, an offset correction is applied to account for neutral particles.

The very forward region of the detector ($\eta > 2.5$) is not covered by the tracker and jets coming from PU are more likely to be associated with the PV of the main interaction.

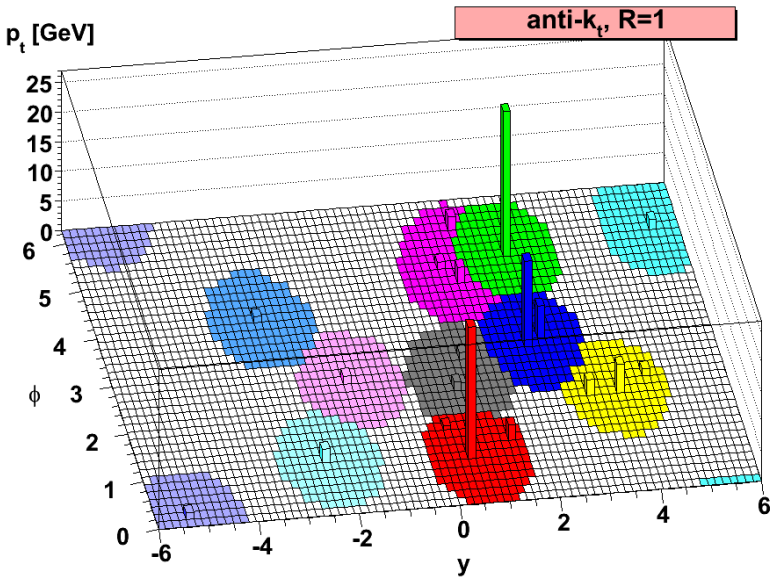

Fig. 2.8.: Example result of jets clustered using the anti-k_T clustering algorithm with a radius parameter of $R = 1.0$ [122].

Therefore, an MVA based on a BDT classification algorithm has been developed, known as PU jet ID [125]. The algorithm combines information of the jet shape and the particle multiplicity to identify jets coming from PU. Scale factors to correct the difference in the selection efficiency are measured for three different working points. For the selection efficiency of 95%, 90%, and 80% for quark jets from the hard interaction, about 20%, 40%, and 50% of jets coming from PU are rejected, respectively.

Corrections for the jet energy in data and differences between data and simulation are applied depending on the p_T and η of the jet. Following a factorization ansatz, PU offset corrections are applied in a first step. These are estimated from QCD dijet samples that are simulated with and without PU interactions. Next, corrections for data-to-simulation differences are estimated using data selected via a trigger that randomly picks events. These data typically do not contain events from hard interactions and are therefore pure in jets from PU interactions. Further corrections are estimated from simulation to mitigate differences in the detector response between data and simulation. The aging of the detector leads to a time dependency in the detector response, with more and more data the calorimeter crystals become less transparent, especially in the forward region of the detector. Hence, residual time-dependent data-to-simulation corrections are derived from studies of γ+jet and Z+jet events and applied to the data [126].

Identification of heavy flavor jets

Jets that originate from b or c quarks are called heavy flavor jets while those originating from u, b, or s quarks are denoted as light flavor. The ability to identify heavy flavor jets, especially jets originating from b quarks (b jets), has become an indispensable tool for top quark or H $\rightarrow$ bb analyses, and many BSM searches. A variety of unique features

allow to distinguish b jets from gluon jets or light flavor jets. Hadrons containing b or c quarks have a lifetime in the order of picoseconds. Depending on their momentum, they can travel distances of several millimeters up to centimeters in the CMS detector before they decay [127]. When they decay, their daughter particles create displaced tracks and a secondary vertex (SV) can be reconstructed. The displaced tracks have on average high IP values. Since b quarks usually decay into c quarks, and these in turn decay into s quarks, several SVs may be reconstructed in one jet. The reconstruction of SVs is done using the inclusive vertex finding (IVF) algorithm [128]. Quality tracks with an upper and lower threshold on their IP values are clustered and fit to find the SV position. After tracks with bad compatibility to the SV are removed, the fit is repeated, followed by a further cleaning. SVs are characterized by their flight distance, which is the 3D spatial distance between the PV and SV positions. Another feature of hadrons containing heavy flavor quarks is that they often decay semileptonically and leptons are among the daughter particles. The relatively high mass of the hadron can be measured in the mass of the reconstructed SVs and leads to daughter particles having relatively high momentum perpendicular to the jet axis. All these features are combined in an MVA to construct a classification algorithm.

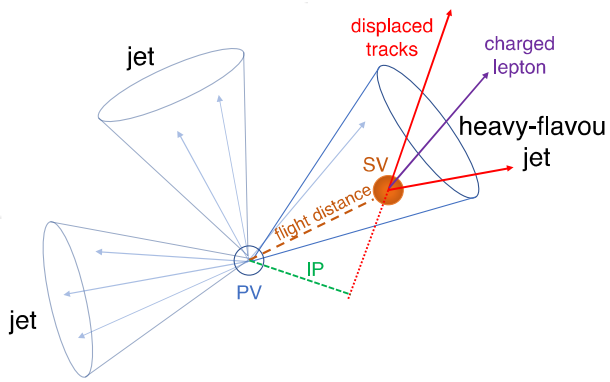

Fig. 2.9.: Illustration of unique features of heavy flavor jets [127].

The MVA classifier to identify b jets in the tZq measurement described in this thesis is the deep neural network (DNN) based DeepJet [129, 130] algorithm. Instead of constructing high-level variables according to the unique features of heavy flavor jets, the DeepJet algorithm uses the full information of all PF candidates clustered in the jet together with the SVs. Various input features of each element are first connected to convolutional neural network layers [131] to preprocess and compute abstract high-level variables. The nodes are then connected to long short-term memory (LSTM) units [132], sequentially for each element. Finally, they are connected to multiple fully connected feed-forward layers and the output in six nodes using the softmax activation function. The output nodes correspond to six exclusive groups for jets with at least two b hadrons, one b hadron that decays leptonically, one b hadron that does not decay leptonically, no b hadron but a c hadron, no b or c hadron but a light flavor quark, or a gluon. The three nodes for b hadrons are added up and used as the score for identifying b jets.

2.4.3. Prompt lepton identification

Reconstructed leptons (e and μ) can be divided into two classes, "prompt" and "nonprompt" leptons. Prompt leptons come from either the hard interaction, leptonic top quark decays, or from the decay of τ leptons, photons, or W, Z, or H bosons from the hard interaction. On the other hand, nonprompt leptons are either misidentified hadrons, misidentified photons not from the hard interaction, or produced in semileptonic hadron decays. In analyses with multiple leptons in the final state, and thus in the tZq analysis shown in this thesis, an efficient identification of prompt leptons with simultaneous rejection of nonprompt ones is a key ingredient. Similar to the identification of heavy flavor jets, unique features of the two leptons classes, as illustrated in Fig 2.10 are exploited. Prompt leptons usually have small IP values while the presence of a close-by b jet indicates a nonprompt lepton. Another indicator for prompt leptons is how well they are isolated from other particles.

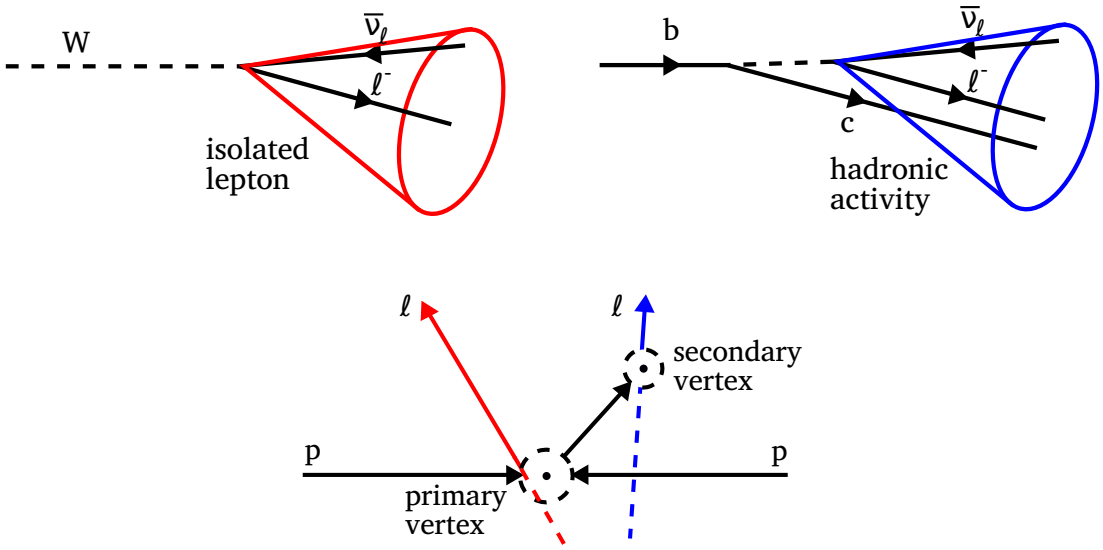

Fig. 2.10.: Illustration of characteristic features of prompt (red) and nonprompt (blue) leptons. Prompt leptons are usually isolated and have no other reconstructed particles in their surroundings while nonprompt leptons, e.g. from semileptonic b hadron decays, are often accompanied by other hadronic activity as shown in the upper plots. Prompt leptons also tend to have smaller distances to the PV of the main interaction, as shown in the lower plot.

Lepton isolation

The quantity to describe the presence of other particles around a lepton is called lepton isolation. In order to evaluate the lepton isolation, all particles inside a cone with the size $\Delta R = \sqrt{\Delta\eta^2 + \Delta\phi^2}$ around the lepton are considered. The cone size can be chosen to be constant where $\Delta R = 0.3$ is a typical choice. The lepton isolation can be calculated using tracks from the inner tracker (tracker based) or PF elements (PF based).

Prompt leptons with high p_T are often collimated with other particles, e.g. the b jet and lepton from semileptonic decays of boosted top quarks could overlap [133]. From this

perspective a cone size that is reduced for increasing lepton p_T is often defined as

$$\Delta R\left(p_T(\ell)\right) = \frac{10\,\text{GeV}}{\min\left(\max[p_T(\ell), 50\,\text{GeV}], 200\,\text{GeV}\right)}\,, \tag{2.7}$$

where $p_T(\ell)$ is the p_T of the lepton. This definition is known as mini isolation. The lepton isolation is defined as

$$I_\ell = \sum_{\text{charged}} p_T + \max\left(0, \sum_{\text{neutrals}} p_T - \rho\mathcal{A}\left[\frac{\Delta R}{0.3}\right]^2\right)\,, \tag{2.8}$$

where the first term is the scalar p_T sum of all charged particles associated with the PV. The second term estimates the contribution of neutral particles and includes the scalar p_T sum of all neutral particles associated with the PV. The negative term is known as effective area correction which is used to mitigate the impact of PU interactions [134, 135]. The parameter ρ is the energy density of neutral particles reconstructed within the geometric acceptance of the tracker. The effective area $\mathcal{A}$ measures the area in the η-ϕ plane and depends on the $|\eta|$ of the lepton. A relative isolation is obtained by dividing Eq. (2.8) by $p_T(\ell)$. It can be used to reject nonprompt leptons, or as an input variable for a more elaborate algorithm to identify prompt leptons, as discussed next.

Multivariate prompt lepton identification

The identification of prompt leptons for the tZq analysis of this thesis is ultimately done by the TOP LeptonMVA combining 13 variables via a BDT-based algorithm. The TOP LeptonMVA is an update to the discriminator used for the observation of tZq [136]. In addition to the lepton isolation, also the p_T, $|\eta|$, and IP variables, as well as variables related to the closest jet are used. Variables based on the closest jet to the lepton, as long as a jet is found within $\Delta R < 0.4$, include the number of charged particles in the jet, its DeepJet score, the momentum of the lepton perpendicular to the jet, and the p_T ratio of the lepton to the jet. For electrons, also the BDT score used in the electron reconstruction (discussed in Section 2.4.1) is used. A variable that quantifies the compatibility of the muon track with the muon hypothesis is used for muons instead. The TOP LeptonMVA is trained on prompt leptons from simulated tZq, $\mathrm{t\bar{t}Z}$, and $\mathrm{t\bar{t}W}$ samples, while $\mathrm{t\bar{t}}$ is used for the nonprompt ones. Only leptons are considered that pass the preselection criteria listed in Table 2.1.

The performance of the TOP LeptonMVA is illustrated in Fig. 2.11 by means of a receiver operator characteristic (ROC) curve that shows the efficiency to select prompt leptons from the tZq sample against the efficiency to select nonprompt leptons from Z/γ^* and $\mathrm{t\bar{t}}$ simulated samples. A comparison is shown to a similar algorithm that was used in the context of the CMS $\mathrm{t\bar{t}H}$ analysis in the multilepton final state (denoted as $\mathrm{t\bar{t}H}$ LeptonMVA) [84]. The $\mathrm{t\bar{t}H}$ LeptonMVA was trained on a slightly different set of simulated samples and is therefore slightly less performant. Beyond that, the TOP LeptonMVA has looser criteria on the lepton selection. For example, electrons with missing hit in one tracker layer are considered for the TOP LeptonMVA while they are not for the $\mathrm{t\bar{t}H}$ LeptonMVA. This allows a higher efficiency to select prompt leptons. As

Table 2.1.: Preselection criteria for the TOP LeptonMVA discriminator for electrons and muons. Including impact parameter cuts (d_{xy}, d_z, and SIP_3) and a cut on mini isolation divided by the lepton p_T (I_ℓ^{Mini}/p_T). Muons additionally have to fulfill a set of basic quality requirements on the muon track denoted as Medium ID.

Electrons	Muons
$p_T > 10\,GeV$	$p_T > 10\,GeV$
$\|\eta\| < 2.5$	$\|\eta\| < 2.4$
$d_{xy} < 0.05$	$d_{xy} < 0.05$
$d_z < 0.1$	$d_z < 0.1$
$SIP_3 < 8$	$SIP_3 < 8$
$I_\ell^{Mini}/p_T < 0.4$	$I_\ell^{Mini}/p_T < 0.4$
Has GSF track	Is PF muon
Missing inner hits <2	Is tracker muon or has global track
	Medium ID

illustrated in the plots, the working point of the $t\bar{t}H$ LeptonMVA is way tighter than those of the TOP LeptonMVA, resulting in a larger rejection of nonprompt leptons. This was the main target of the $t\bar{t}H$ analysis as documented in Ref. [84]. The tighter working point however leads to a lower selection efficiency of prompt leptons. For the TOP LeptonMVA looser working points were considered. Although the nonprompt lepton rejection is worse, the amount of prompt leptons that are kept is much larger, helping retrieve the rare signal for a precise analysis. The uncertainties arising from nonprompt leptons are constrained in the design of the final tZq analysis as explained in Section 4.

2.5. Luminosity measurement at the CMS experiment

For almost any precision measurement, it is crucial to determine the integrated luminosity precisely. Various analyses, such as the cross section measurements of the Z boson or $t\bar{t}$ production, are limited by the uncertainty of the luminosity [137, 138]. A target precision of 1% is set for future LHC data taking periods [139]. In fact, this goal has almost been reached with the latest CMS measurement of the luminosity for 2016 pp collision data at $\sqrt{s} = 13\,TeV$, where a precision of 1.2% was obtained [140].

From Eq. (2.1), the instantaneous luminosity can be in principle inferred from the rate $R(t) = dN/dt$ of any process that is the result of collisions,

$$\mathcal{L}(t) = \frac{1}{\sigma}\frac{dN}{dt} = \frac{1}{\sigma}R(t)\,. \tag{2.9}$$

Luminosity detectors often referred to as "luminometers" usually measure $R(t)$ of hits, tracks, or clusters. The cross section of such a signature incorporates acceptance and efficiency effects and is therefore denoted as visible cross section σ_{vis}. Typically it is not well known from first principles. To get the absolute scale of the luminosity, σ_{vis} needs to be estimated in a calibration procedure.

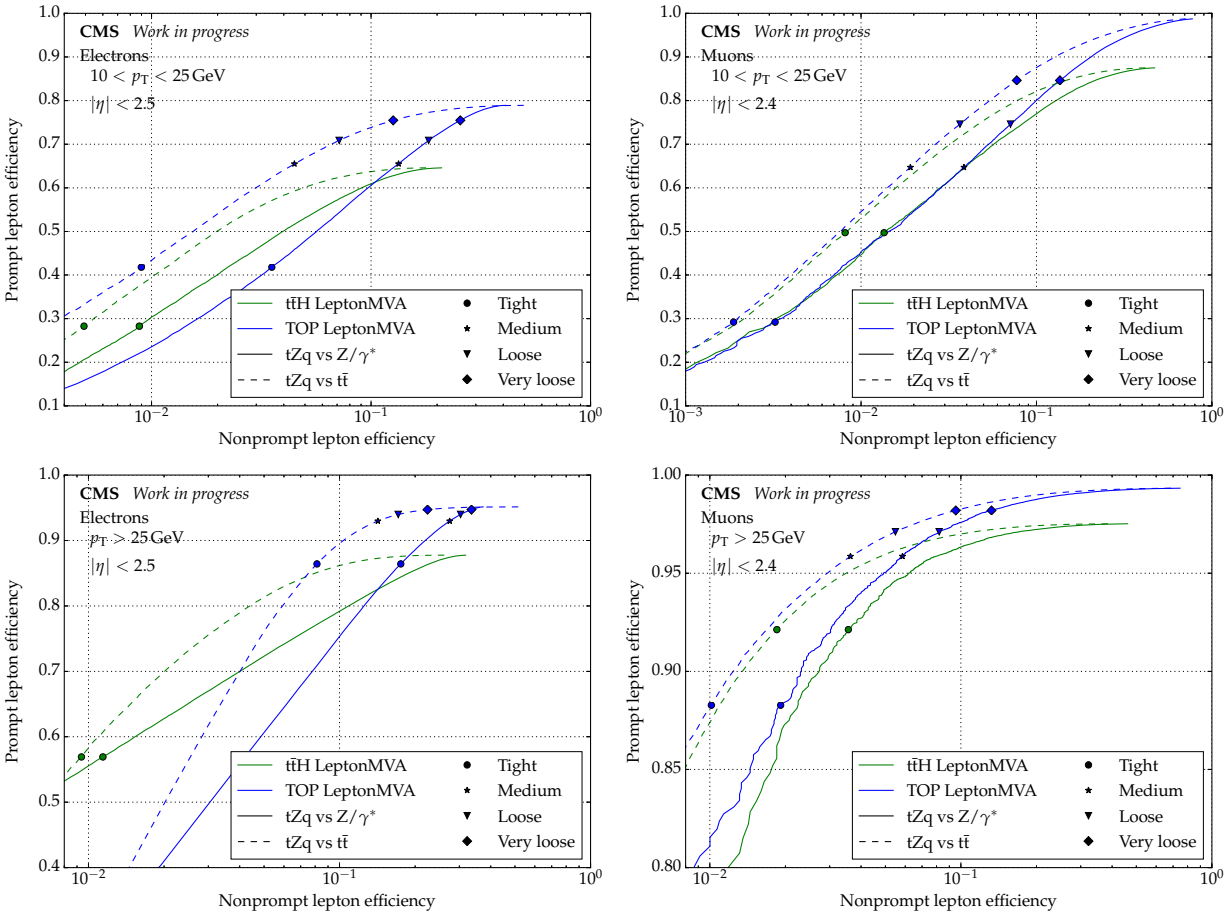

Fig. 2.11.: ROC curves for different LeptonMVA algorithms discussed in the text. The one in green was developed in the effort for the tt̄H analysis [84] while the one in blue is an update to the discriminator used for the observation of tZq [136]. The efficiency to select prompt leptons from the tZq sample is drawn against the efficiency to select nonprompt leptons from Z/γ^* (solid line) and tt̄ (dashed line) simulated samples. The markers highlight different working points for which the efficiency in data was studied in more detail and simulation-to-data correction factors were determined. Plots on the left show electrons while those on the right show muons. The p_T range for the leptons is between 10–25 GeV in the upper plots and above 25 GeV in the lower ones.

2.5.1. Luminosity detectors at the CMS experiment

In the CMS experiment, the luminosity is measured using several luminometers. This allows to combine redundant information and reduce systematic uncertainties. The following requirements are placed on the luminometer: A high rate is required to minimize the statistical uncertainty, to allow a precise calibration of the luminometer, and to measure the luminosity in short time intervals. Ideally, the $R(t)$ is high enough to measure the luminosity for single bunch crossings. Additionally, $R(t)$ should be proportional to $\mathcal{L}(t)$ also for collisions with a high number of PU interactions; a property called linearity. Nonlinearity may arise, for example, from particles produced in preceding bunches affecting rate measurements in later bunches due to radioactivity or back scattering (afterglow). Another important property is long-term stability. The luminometer should maintain its σ_{vis} during one data-taking period which typically amounts to a little less than one year. Instability could be caused for example by radiation damage or failing parts of the luminometer. Luminometers can be classified into online devices that provide luminosity instantaneously and offline devices where the luminosity is calculated delayed.

One offline luminometer is the pixel cluster counting (PCC) [141]. It is based on the pixel detectors in the inner silicon tracker. A set of pixel elements are grouped into clusters, the number of pixel clusters that are hit by charged particles is then proportional to the $\mathcal{L}(t)$ and used as $R(t)$. Because of its fine granularity, the probability that two charged particles hit the same pixel cluster is negligibly small. This fact ensures good linearity, also for collisions with a high number of PU interactions. To ensure good stability, pixel clusters in which problems occurred during the data-taking period are retrospectively removed from the luminosity determination. The PCC is the luminometer that is used to determine the luminosity in the majority of luminosity blocks in 2016.

The HF of the hadronic calorimeter is exploited as an online and offline luminometer [142]. The occupancy method (HFOC) is used where the rate is chosen as the fraction of channels that measure a signal above a certain energy level. It was chosen as the main luminometer for 2017. Another method is computing the sum of transverse energy in the HF (HFET). This was chosen in 2018 as the main method for luminosity determination.

The pixel luminosity telescope (PLT) [143] is a stand-alone detector, specifically designed to measure the online luminosity. It is placed on the end of the pixel endcaps and consists of in total 48 silicon pixel sensors. In contrast to the rate measuring luminometers, the PLT measures the fraction of events where no track signature is found. This resolves the problem of occupancy (e.g. overlapping tracks) and leads to good stability. At the same place in CMS is also the fast beam condition monitor (BCM1F) which is a detector dedicated to measure the online luminosity [144]. It features a fast time resolution of 6.25 ns that allows to separate signal from the actual bunch crossing from other sources. This allows studying systematic effects related to backgrounds in unique ways.

2.5.2. Absolute luminosity calibration

All these luminometers are calibrated to provide luminosity at an absolute scale. Using the intrinsic definition of $\mathcal{L}(t)$ given in Eq. (2.2), the visible cross section can be written as

$$\sigma_{\text{vis}} = \frac{A_{\text{eff}}}{N_{\text{b}} n_1 n_2 f} R(t) \ . \tag{2.10}$$

The challenge in measuring σ_{vis} lies in the determination of A_{eff}. This is done via the van der Meer (vdM) method [145, 146]. By assuming the bunch density as uncorrelated in x and y, the effective area can be written as $A_{\text{eff}} = 2\pi\Sigma_x\Sigma_y$, with the effective width (Σ_x) and height (Σ_y) of the bunches.

To measure the values for Σ_i, fills with a special beam setup are performed where the two beams are separated and gradually moved across each other. A sketch of these so-called vdM scans is shown in the left plot of Fig. 2.12. During this vdM scan, the $R(t)$ is measured, an example is shown for the PCC luminometer on the right plot of Fig. 2.12. From the Gaussian models that are used to describe the data, the Σ_i can be calculated using an analytic function.

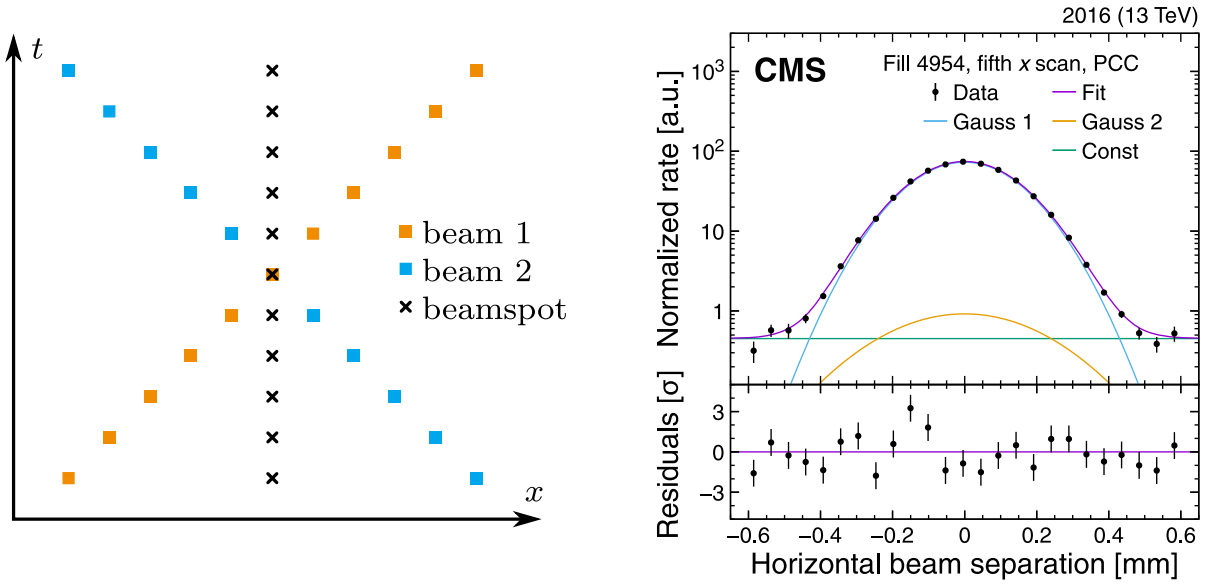

Fig. 2.12.: Left: Illustration of the beam position in a vdM scan [147]. Right: Example of the measured rate at the PCC luminometer during a horizontal vdM scan. The data is fit with a double-Gaussian function (purple), made of two Gaussian components (blue and yellow) and a constant contribution (green) [140].

Several systematic effects influence the measurement of σ_{vis}, such as the factorization bias of A_{eff} (x-y factorization), the measurement of the beam separation during a vdM scan (length scale), variations between different scans (scan to scan variations), or background subtraction. Protons outside of the actual bunch (ghosts) or trailing ones (satellites) constitute another source of uncertainty. Corrections are applied for beam current calibrations, the electromagnetic interaction between two colliding bunches (beam-beam effects), and

the time-dependent beam positions (orbit drift) [140, 142, 148]. The different sources of uncertainty on the luminosity measured during Run 2 with the CMS experiment are summarized in Table 2.2. They are divided into two groups, the normalization uncertainties mainly related to the calibration, and the integration uncertainties related to the luminometers used during data taking. The integration uncertainty depends largely on the PU conditions and the linearity of the corresponding detector. In the upcoming years, LHC will deliver higher instantaneous luminosities with about $\langle N_{\mathrm{PU}} \rangle \approx 50$ for Run 3 and up to $\langle N_{\mathrm{PU}} \rangle \approx 200$ during HL-LHC. The integration uncertainty will therefore become more and more important and most likely the dominant part of the uncertainty. New luminometers and methods have to be developed to cope with the challenging conditions and achieve the target precision of 1%.

Table 2.2.: Uncertainties of the luminosity measured by the CMS experiment during Run 2. The first group are normalization uncertainties and the second group integration uncertainties. Correlated uncertainties are marked with a check (✓) while uncorrelated ones have a dashed line (—). [140, 142, 148]

source	correlated	2016	2017	2018
x-*y* factorization	✓	0.5	0.8	2.0
Length scale	✓	0.3	0.3	0.2
Orbit drift syst.	✓	0.5	—	—
Orbit drift rand.	—	0.1	0.2	0.1
Beam-beam effects 2016	✓	0.5	—	—
Beam-beam effects 2017/2018	✓	—	0.6	0.2
Beam current calibration	✓	0.2	0.3	0.2
Ghosts and satellites	✓	0.1	0.1	0.1
Scan to scan variation	—	0.2	0.9	0.3
Bunch to bunch variation	—	—	0.1	0.1
Cross-detector consistency	—	—	0.6	0.5
Background subtraction	—	—	—	0.1
PCC afterglow type 1	✓	0.3	—	—
PCC afterglow type 2	✓	0.3	—	—
HF afterglow type 1	—	—	0.2	0.1
HF afterglow type 2	—	—	0.3	0.4
Cross-detector stability	—	0.5	0.5	0.6
PCC linearity	✓	0.3	—	—
HF linearity	—	—	1.5	1.1
CMS deadtime	—	0.1	0.5	0.1

2.5.3. Luminosity determination using physics processes

Physics processes were used in previous experiments to measure the luminosity. At electron-positron colliders Blabha scattering, $e^+e^- \to e^+e^-$, was used as such. Due to its very clean signature, events of this process are easily identified and can be well understood. The cross section is well known from perturbative QED calculations. Thus, at the CERN LEP, an uncertainty of 0.05% on the luminosity measured in 1994 was

achieved [149]. For the Belle II experiment at the SuperKEKB accelerator in Japan, an uncertainty of 0.6% was achieved using the same method including events with two photons [150]. While the experiment is still ongoing and more precise results can be expected in the future, the largest single source of systematic uncertainty at present is the knowledge of the center-of-mass energy.

In pp collisions, the cross section from theory is typically not known with well enough precision. As an example, the most precise theory prediction of Drell–Yan (DY) production at pp colliders with $\sqrt{s} = 13\,\text{TeV}$ is known to N^3LO accuracy in perturbative QCD calculation [151]. The uncertainty estimated from μ_R and μ_F scale variations is at the level of 0.8% while the PDF uncertainty amounts to 2.5%. For this reason, cross section predictions have hardly played a role in the luminosity determination at CMS so far.

However, it is still possible to use the production rate of physics processes as a relative measure for the luminosity. There is a variety of advantages over the conventional methods discussed in Section 2.5.1. As part of this thesis, the determination of the luminosity from the measurement of the $\text{Z} \to \mu\mu$ production rate has been studied as documented in the following chapter. The strengths and weaknesses of this approach have been identified for the first time in great detail within the CMS experiment. Also, a method for the estimation of the absolute luminosity, using a low PU data set as a reference point, is explored for the first time and yields competitive results.

3. Luminosity determination using Z boson production

This chapter describes the high precision determination of the luminosity in pp collision data taken at $\sqrt{s} = 13\,\text{TeV}$ in the years 2016–2018. Using Z boson events in the final state with two muons, the luminosity can be determined using

$$\mathcal{L} = \frac{N^{\text{Z}}_{\text{reco}}}{\sigma^{\text{Z}}_{\text{fid}} \epsilon^{\text{Z}}_{\text{ID}}} \,, \tag{3.1}$$

where $N^{\text{Z}}_{\text{reco}}$ is the background subtracted number of reconstructed Z bosons and $\epsilon^{\text{Z}}_{\text{ID}}$ its associated reconstruction efficiency. The fiducial cross section $\sigma^{\text{Z}}_{\text{fid}} = A\sigma^{\text{Z}}\mathcal{B}(\text{Z} \to \mu\mu)$ depends on the inclusive Z boson production cross section σ^{Z}, the branching fraction of Z events to decay into two muons $\mathcal{B}(\text{Z} \to \mu\mu)$, and the acceptance factor A for the two muons in the detector. The production of Z bosons that decay into pairs of muons is especially well suited for the measurement of the luminosity, for a number of reasons:

- Its decay into two muons has a remarkably clean signature, $\text{Z} \to \mu\mu$ events can be easily identified and reconstructed within the CMS detector.
- Due to the relatively large effective cross section, the number of Z bosons in about 30 min of data taking can be calculated with a statistical accuracy of $<$1%.
- The reconstructed invariant mass spectrum of both decay particles peaks at values of the Z boson mass of about 91 GeV. Background processes with two muons (or other particles wrongly identified as muons) usually have a nonresonant spectrum. This property can be used to subtract the number of background events.
- The efficiency to reconstruct a Z boson is given by the trigger, identification, and reconstruction efficiencies of the two muons. The efficiencies of the muons can be determined in situ, using the exact same event sample as for the Z boson rate measurement itself. No biases or uncertainties arise from assumptions on the calibration transfer between event samples. Only the correlation between the two muons of the Z boson decay and the correlation between the track components of each muon require residual corrections.

In this chapter, an in-depth study of Z boson production for the measurement of the relative and absolute luminosity is presented. In Section 3.1, an overview of the state of the art and the analysis strategy taken in this work is given. Samples used for the measurement are described in Section 3.2. To extract the signal contribution, binned maximum likelihood fits of signal and background shapes to the data are performed. The statistical treatment is introduced in Section 3.3. Section 3.4 describes the selection criteria of muons and Z candidates. A simultaneous extraction of the number of reconstructed Z

bosons and the single muon trigger efficiency is performed. The correlation in the trigger efficiencies of the two muons is investigated in detail. The dependency of the correlation on pileup (PU) is studied, both in data and in simulation. Subsequently, the measurements of the identification and reconstruction efficiencies of the muon track components are explained in Section 3.5. A tag-and-probe (T&P) method is used. A clean sample of Z events is selected by requiring that one muon fulfills tight quality requirements. The muon efficiency is then determined as the fraction of events in which the second muon fulfills given criteria. Fits are performed on the dimuon mass spectrum to subtract the background contribution. Included are simulation-based studies on the correlation between the track components of the muon and a closure test to show the self-consistency of the method. Results on the relative and absolute luminosity determined using Z bosons are given in Sections 3.6 and 3.7, respectively. Finally, systematic uncertainties are studied in detail in Section 3.8.

At the time of writing, a publication is in preparation and preapproved within the CMS Collaboration. The publication is expected to be completed in the upcoming months [152].

3.1. Introduction

The production of Z bosons is already used for their well-known properties as a "standard candle" in a variety of basic measurements. To name just a few: from the Z mass and width, the energy scale and momentum of muons and electrons are calibrated [96, 153]. The use of Z boson production for the precise measurement of the LHC luminosity has been discussed early on, e.g. in Ref. [154]. For Z bosons produced in pp collisions at 13 TeV, and decaying into two muons, the total inclusive cross section times branching ratio, $\sigma^{Z}\mathcal{B}(Z \to \mu\mu)$, has been measured to be $1.977 \pm 0.009\,(\text{stat}) \pm 0.041\,(\text{syst}) \pm 0.042\,(\text{lumi})$ nb [155]. Typically, about one-third of the total number of produced Z boson events are also reconstructed in the fiducial volume of the detector [137]. The current uncertainty in the prediction of the fiducial cross section originates from limited knowledge of proton PDFs and higher-order corrections and is about 3% [151]. Within this uncertainty, the integrated luminosity can be determined directly from the measured Z boson rate. However, the Z boson rate can also be used to measure the relative and absolute luminosity without the use of a theory cross section.

3.1.1. Relative luminosity determination using Z boson production

The measurement of the Z bosons is affected by completely different systematic uncertainties as the conventional ways of measuring luminosity (discussed in Section 2.5). The Z boson rate as a means to determine the relative luminosity is therefore valuable for cross-checks. It has already been proven a useful and complementary method to LHC machines and experiments to monitor the relative instantaneous luminosity and stability delivered to ATLAS and CMS experiments [156]. Since summer 2017, the ratio of the efficiency-corrected number of Z bosons, N^{Z}, from ATLAS and CMS experiments was monitored regularly. The ratio of N^{Z} can be directly compared to the luminosity ratio

recorded by both experiments as

$$\frac{\mathcal{L}^{(\mathrm{ATLAS})}}{\mathcal{L}^{(\mathrm{CMS})}} = \frac{N^{\mathrm{Z(ATLAS)}}}{N^{\mathrm{Z(CMS)}}}. \tag{3.2}$$

For the same fiducial phase space, the fiducial cross section $\sigma^{\mathrm{Z}}_{\mathrm{fid}}$ from Eq. (3.1) cancels out in the luminosity ratio. As shown in Fig. 3.1, the N^{Z} ratio is in good agreement with unity, indicating that both experiments recorded about the same luminosity.

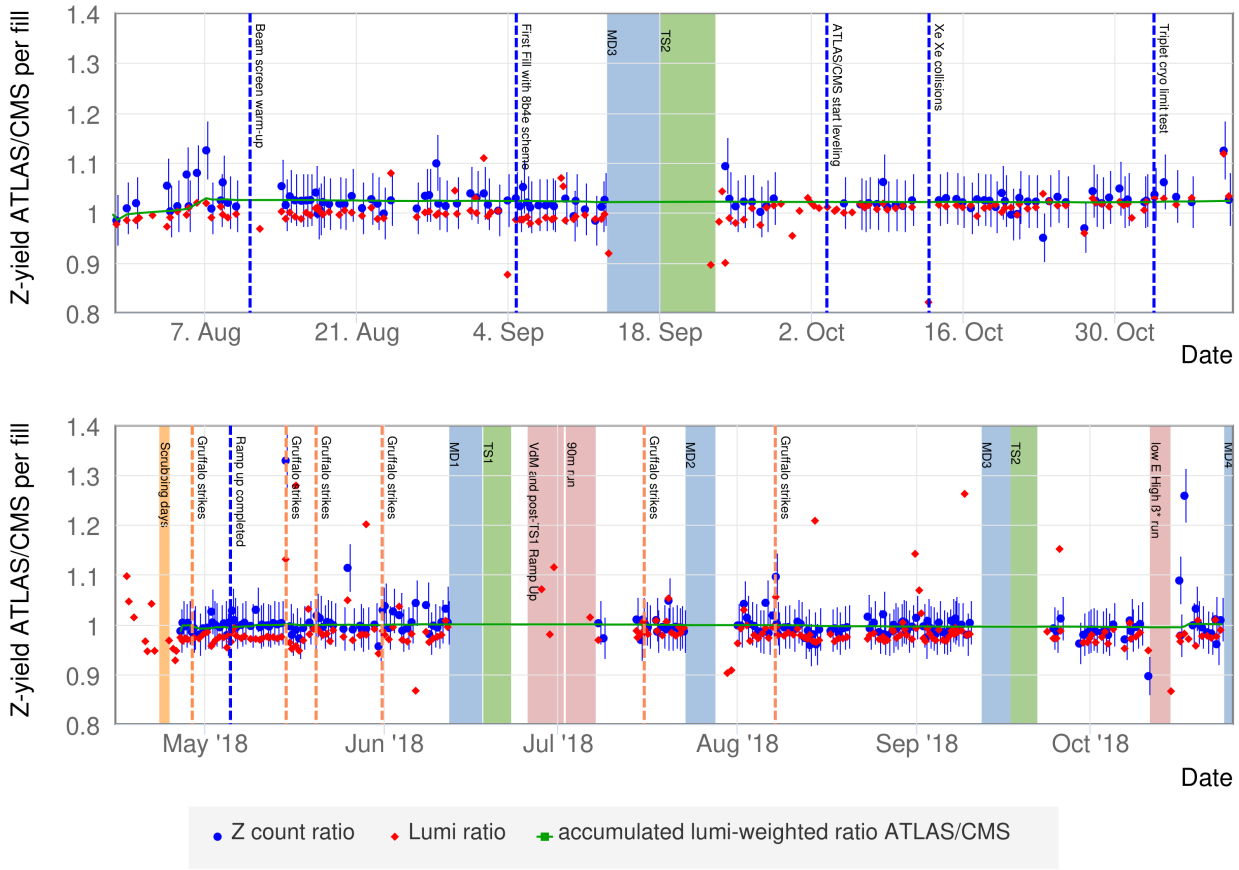

Fig. 3.1.: The plot shows data from 2017 (upper) and 2018 (lower) with the x-axis indicating the days when the data was taken. Blue dots show the efficiency-corrected numbers of Z bosons measured in the ATLAS experiment divided by the ones measured at the CMS experiment. The red dots show the ratio of the recorded luminosity of the two experiments. The green line shows the over-time accumulated ratio of the Z yields weighted with the collected luminosity. The dashed blue lines indicate changes in the beam settings. The dashed orange lines show the times when the so-called Gruffalo appeared, an effect where electron clouds formed in the beam pipe, making the proton beam unstable. The colored areas indicate other phases like technical stops (green), machine developments (blue), and operations with different beam optics (red). [156]

The use of Z boson production as a measure of the relative luminosity has also been explored by the ATLAS experiment as documented in Ref. [157]. It includes the measurement of Z bosons decaying into muons as well as electrons. Cross-checks between the two lepton flavor categories have been performed and show a consistent picture. Corrections as a function of N_{PU} have been applied based on an imperfect agreement in closure tests

performed in simulation. Results show good long-term stability in comparison with the reference luminosity for the full Run 2 data-taking period from 2015 to 2018.

3.1.2. Absolute luminosity determination using Z boson production

In this thesis, a method discussed in Ref. [158] is carried out for the first time. The measurement of the Z boson rate is used as an alternative and complementary approach for the determination of the integrated luminosity. The method makes use of the fact that σ^{Z}_{fid} is identical for all pp collision data at a given center-of-mass energy. The ratio of N^{Z} between data sets can be used to transfer the luminosity calibration from one data set to another. A theory prediction or precise knowledge on σ^{Z}_{fid} is not needed. For the work presented in this thesis, a low PU data set is used to determine the luminosity calibration with good precision. Based on this, the luminosity of data sets at high PU is then derived using the relation

$$\mathcal{L}_{\text{highPU}} = \frac{N^{Z}_{\text{highPU}}}{N^{Z}_{\text{lowPU}}} \mathcal{L}^{\text{Ref.}}_{\text{lowPU}} \,. \tag{3.3}$$

In general, the reference luminosity measured in low PU conditions, $\mathcal{L}^{\text{Ref.}}_{\text{lowPU}}$, is particularly well known. In the ratio of the efficiency-corrected numbers of Z bosons at high PU (N^{Z}_{highPU}) and low PU (N^{Z}_{lowPU}), all correlated uncertainties cancel out. For all data sets, the individual trigger and selection efficiencies are determined in situ, in intervals of $20\,\text{pb}^{-1}$, thus enhancing the sensitivity to possible variations due to changes in beam conditions or detector response as a function of time. The challenge in this measurement thus lies in the understanding of the uncertainties that are different between data sets, in particular uncertainties that depend on PU.

3.2. Data sets and simulated samples

3.2.1. Data sets

Data collected during Run 2 in 2016, 2017, and 2018 are used for the work presented in this chapter. Only luminosity blocks are considered for which it is known that the CMS detector was fully operational.

In 2016, a technical issue affected data recorded in the first half of the year. The pre-amplifiers of readout chips in the silicon strip tracker showed, contrary to expectations, a strong dependency on the operating temperature. A slower discharge under high occupancy conditions, i.e. high instantaneous luminosity and PU, was apparent. This led to increased noise and saturation effects causing a loss of hit efficiency for charged particles traversing the detector. In the summer of 2016, a voltage bias on the pre-amplifier (VFP) was set to allow for a faster discharge and recovery. Data corresponding to an integrated luminosity of $19.5\,\text{fb}^{-1}$ and $16.8\,\text{fb}^{-1}$ were recorded without and with the VFP setting, respectively. The two data-taking periods are denoted in the following as 2016 preVFP and 2016 postVFP [159, 160].

In 2016 data, events are selected which passed the `HLT_IsoMu24` or `HLT_IsoTkMu24` trigger. Both triggers have a requirement of $p_{\text{T}} > 24\,\text{GeV}$ and use isolation criteria. While

the first one is PF based, the latter one uses a tracker-based computation. For the years 2017 and 2018, events were selected that fired the HLT_IsoMu24 trigger. Events from the single muon primary data set are taken, where the considered single muon trigger was active. This was the case for 2016 and 2018, as well as for the majority of the 2017 data-taking period. In 2017, the trigger was prescaled in a small amount of data. This has been taken into account by scaling down the recorded luminosity used as a reference in the relevant luminosity blocks.

The low pileup data-taking period in 2017

To demonstrate the possibility to measure the absolute luminosity using Eq. (3.3), the low PU data-taking period from 2017 is exploited. The corresponding PU distribution is shown in Fig. 3.2. On average three interactions per bunch crossing occurred. The recorded luminosity is calculated by requiring the single muon trigger HLT_HIMu17 to be active during data taking. The recorded luminosity amounts to $\mathcal{L}^{\text{Ref.}}_{\text{lowPU}} = 199.3\,\text{pb}^{-1}$ using the latest luminosity calibration and only luminosity blocks for which it is verified that the CMS detector was fully operational.

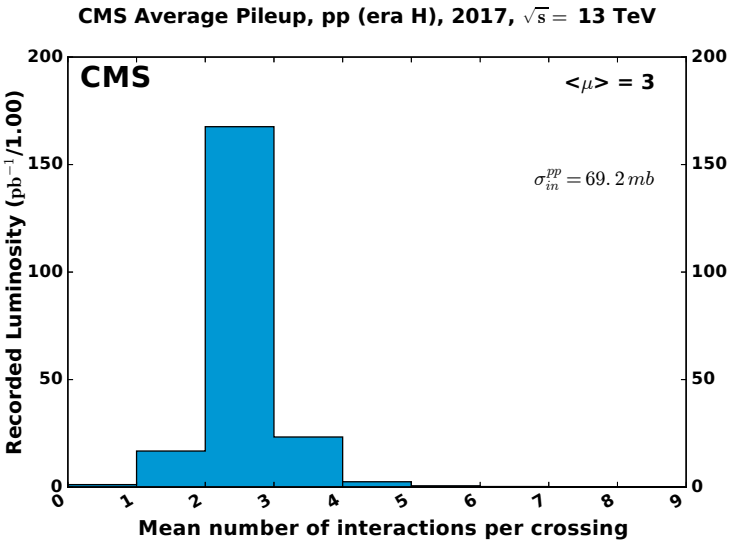

Fig. 3.2.: The PU distribution of the low PU data-taking period in 2017. To estimate these distributions, a total inelastic pp cross section of 69.2 mb is assumed. [86]

Unfortunately, the single muon trigger that is used in the high PU data was not active in the low PU data. To remove the difference in the trigger between the low PU and high PU data, the HLT_IsoMu24 was emulated afterwards. Emulation on the raw data was possible since the L1 trigger decisions were stored not only for the active trigger (HLT_HIMu17 in the low PU data) but also with the increased p_{T} thresholds needed for the HLT_IsoMu24 trigger.

3.2.2. Simulated samples

The measurement is almost completely independent of simulated events. Simulated DY samples are used for two purposes only: to produce the expected shape of the Z boson signal measured in the CMS detector for the signal extraction, and to determine residual

PU-dependent corrections to the efficiency measurements. Simulated events are produced at LO in perturbative QCD and EW with the MadGraph 5 (v2.6.5) [101] event generator, using the NNPDF3.1 [37] PDFs. Higher-order corrections are modeled with the parton shower using pythia (v8.24) [109] with the CP5 tune [113]. The effects of PU are simulated with pythia as well using a flat PU profile reaching from $N_{\mathrm{PU}} = 0$–75 to study the PU dependency of these events in detail. The detector simulation was performed using the Geant4 [114] toolkit as described in Section 2.3. Two sets of samples are used for 2016 corresponding to the conditions in the 2016 preVFP and 2016 postVFP data [159].

For the studies in this analysis, simulated events are selected in which the generated Z boson decays directly into a pair of muons. The detector-level muons are matched to the generator-level muons from the Z boson decay. A spatial requirement of $\Delta R = \sqrt{\Delta\eta^2 + \Delta\phi^2} < 0.05$ between the reconstructed muon and generated muon from the Z boson decay is applied. This is necessary to identify the signal signature since also hadronic jets or PU events can lead to reconstructed muons. Muons that are only reconstructed in the muon chamber but not in the inner silicon tracker have worse spatial resolution and are measured after possible scattering processes in the detector material which leads to deflections. These muons are matched within $\Delta R < 0.6$ to the generated ones.

The event kinematics for $\mathrm{Z} \to \mu\mu$ events are studied in simulation from reconstructed muons that are identified as signal as illustrated in Fig. 3.3. It can be seen that the peak momentum for the muons in $\mathrm{Z} \to \mu\mu$ events is at about $m_{\mathrm{Z}}/2 \approx 45\,\mathrm{GeV}$ and drops steeply after that point. Since most Z bosons are generated with low transverse momentum and almost all the energy of the Z boson is transferred to the muons' kinetic energy, they are emitted back-to-back in ϕ and are well separated from each other.

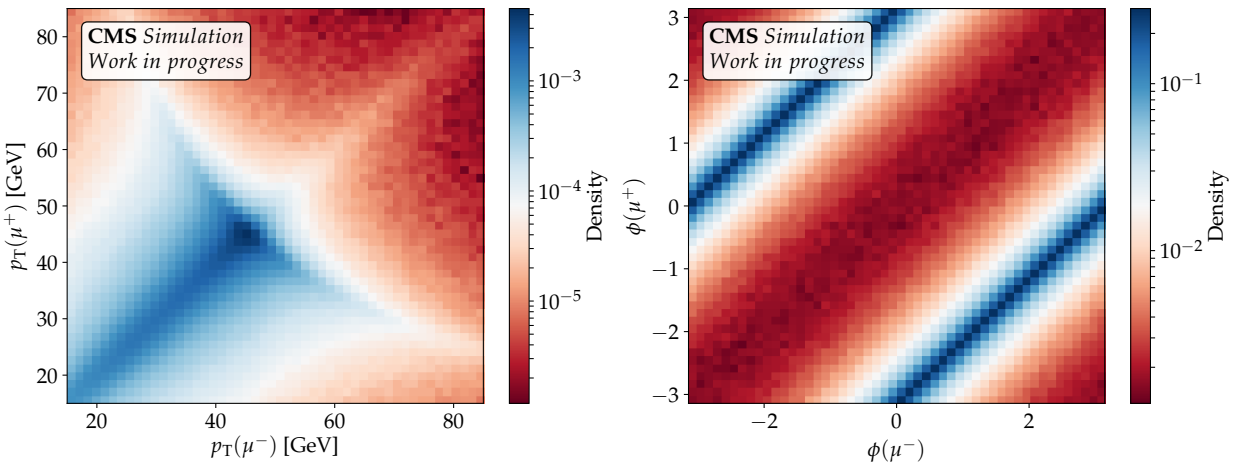

Fig. 3.3.: The distribution of the p_{T} (left) and ϕ (right) of simulated $\mathrm{Z} \to \mu\mu$ events is shown for the muon (x-axis) and the anti muon (y-axis). Muons are produced with a p_{T} spectrum that peaks at about $m_{\mathrm{Z}}/2 \approx 45\,\mathrm{GeV}$. The two muons are produced mainly back-to-back, as can be seen on the ϕ distribution.

3.3. Statistical model

The number of reconstructed Z bosons, muon trigger, identification, and reconstruction efficiencies are extracted using maximum likelihood fits to subtract the background contribution. In each case, the data are binned as a function of the invariant mass of dimuon candidates, $m_{\mu\mu}$.

3.3.1. Binned maximum likelihood fit

The probability to find k entries in a bin in which $\lambda(\boldsymbol{\omega})$ entries are predicted is given by the Poisson probability,

$$P(k;\boldsymbol{\omega}) = \frac{\lambda(\boldsymbol{\omega})^k \, \mathrm{e}^{-\lambda(\boldsymbol{\omega})}}{k!} \,, \tag{3.4}$$

where $\boldsymbol{\omega} = (\omega_1, \omega_2, \ldots \omega_P)$ is a list of parameters to describe the prediction. The likelihood is given by the product of the probabilities in all bins,

$$L(\boldsymbol{k};\boldsymbol{\omega}) = \prod_{i=1}^{B} \frac{\lambda_i(\boldsymbol{\omega})^{k_i} \, \mathrm{e}^{-\lambda_i(\boldsymbol{\omega})}}{k_i!} \,, \tag{3.5}$$

where B is the number of bins. The parameters that best describe the data, including the parameters of interest, are found by maximizing the likelihood. In practice, the negative log-likelihood (NLL) is used, as it is computationally easier to calculate sums, and to optimize for the minimum.

$$-\ln L(\boldsymbol{k};\boldsymbol{\omega}) = -\sum_{i=1}^{B} \left[\ln\left(\frac{\lambda_i(\boldsymbol{\omega})^{k_i}}{k_i!} \right) - \lambda_i(\boldsymbol{\omega}) \right] \,. \tag{3.6}$$

The number of expected Z candidates are described by two separate probability density functions $f_\mathrm{s}(x;\boldsymbol{\Theta})$ and $f_\mathrm{b}(x;\boldsymbol{\Theta})$ for the signal and background contributions, respectively, where $\boldsymbol{\Theta}$ corresponds to a set of internal parameters. The parameters $\boldsymbol{\Theta}$ are considered "nuisance" parameters as they are not of immediate interest, but must nevertheless be taken into account. The entries in each bin are given by:

$$\lambda_i(\boldsymbol{\omega} = (s, b, \boldsymbol{\Theta})) = s \int_{x_i^\mathrm{low}}^{x_i^\mathrm{hi}} f_\mathrm{s}(x;\boldsymbol{\Theta})\mathrm{d}x + b \int_{x_i^\mathrm{low}}^{x_i^\mathrm{hi}} f_\mathrm{b}(x;\boldsymbol{\Theta})\mathrm{d}x \,, \tag{3.7}$$

where x_i^low and x_i^hi are the bin edges of the variable x that is fit, while s and b are the number of the signal and background entries, respectively.

The fits are performed using the RooFit toolkit [161] via the numerical minimization library MINUIT [162] to minimize the NLL. Symmetric uncertainties on the parameters of interest are estimated from the Hesse matrix.

3.3.2. Signal modeling

For the probability density function (in the following referred to as "model") to describe the signal, $f_\mathrm{s}(x;\boldsymbol{\Theta})$, a histogram template convolved with a Gaussian resolution function

is used (MC×Gauss). The histogram template is produced using the same selection for simulated $Z \to \mu\mu$ events as for data. To extract the signal-only contribution, muons are additionally required to be matched to generator-level muons. The signal template for simulated events with different numbers of primary vertices, N_{PV}, was studied. No significant dependency on N_{PV} was found. Hence, the same template is used within each data-taking period.

An alternative shape to describe the signal is used to estimate the associated uncertainty. A Breit–Wigner function, defined in Eq. (1.39), is convolved with a Crystal Ball function (BW×CB) [163]. The parameters of the Breit–Wigner function are fixed to the mass and width of the Z boson ($m_R = m_Z = 91.188\,\text{GeV}$ and $\Gamma_R = \Gamma_Z = 2.495\,\text{GeV}$ [10]).

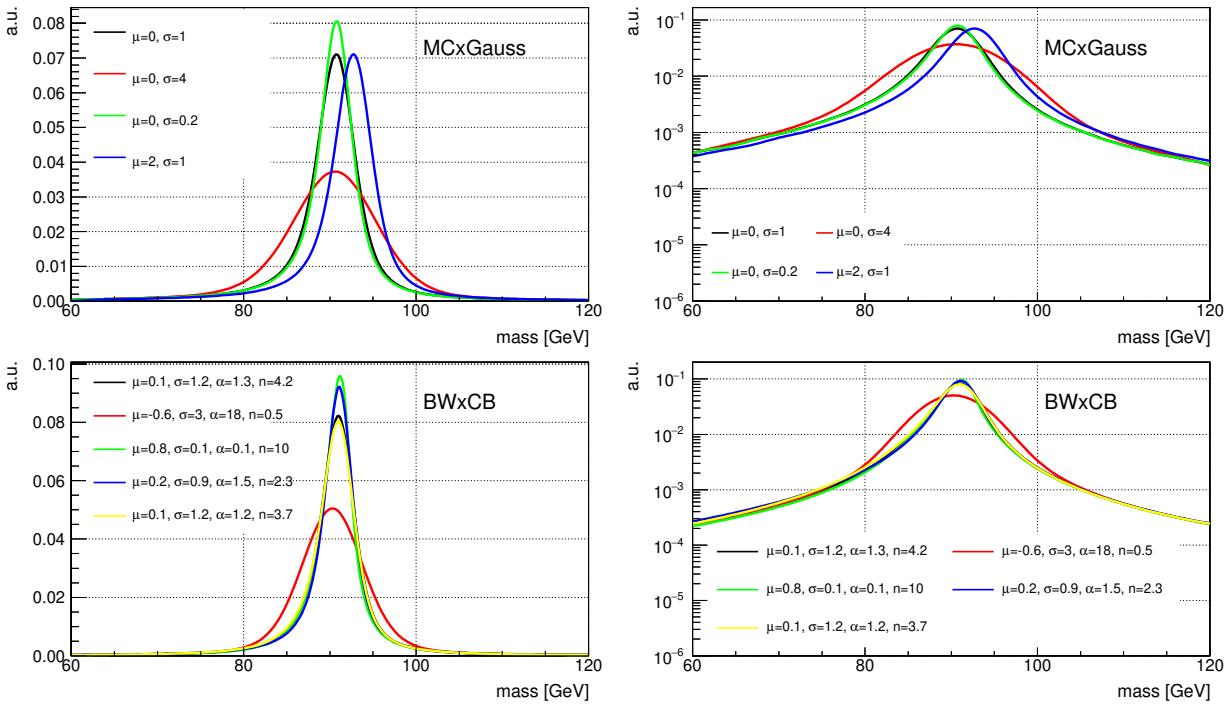

Fig. 3.4.: The two different signal models MC×Gauss (upper) and BW×CB (lower) with different parameterizations as function of $m_{\mu\mu}$, normalized to a unit area. The functions are displayed in a linear (left) and logarithmic (right) y-axis scale.

The two signal models for different choices for the free parameters are shown in Fig. 3.4. As visible in these figures, the Crystal Ball and Gauss functions allow to shift and smear the resonance peak around the Z boson mass. Both models show similar distributions and flexibility. Small differences are apparent in the tails of the distribution at $|m_{\mu\mu} - m_Z| > 20\,\text{GeV}$ where MC×Gauss has a larger contribution than BW×CB. The Breit–Wigner function describes only the resonant part of the signal, while the template also includes FSR effects, nonresonant production of γ^*, and Z/γ^* interference. For this reason, a lower signal contribution is expected when using BW×CB as alternative signal model.

3.3.3. Background modeling

The background contribution is modeled using the CMSSHAPE function

$$\text{CMSSHAPE}\,(x;\alpha,\beta,\gamma) = (1-\text{erf}(\alpha-x)\beta)\,\mathrm{e}^{-(x-m_Z)\gamma}\,, \tag{3.8}$$

where $m_Z = 91.188\,\text{GeV}$ is the pole mass of the Z boson [10]. The CMSSHAPE consists of a decaying exponential component to model the low-energy fakes and an error function to create a peaking structure of the background introduced by the combinatorial background.

An alternative background shape to study related systematic uncertainties is the so-called DAS function [164]:

$$\text{DAS}\,(x;\mu,\sigma,k_\text{l},k_\text{h}) = \begin{cases} \mathrm{e}^{\frac{k_\text{l}^2}{2}+k_\text{l}t} & \text{if} \quad t < -k_\text{l}\,, \\ \mathrm{e}^{\frac{k_\text{h}^2}{2}-k_\text{h}t} & \text{if} \quad t > k_\text{h}\,, \\ \mathrm{e}^{-\frac{1}{2}t^2} & \text{if} \quad -k_\text{l} < t < k_\text{h}\,, \end{cases} \tag{3.9}$$

with $t = {}^{x-\mu}/_{\sigma}$. It is a linear combination of a decaying exponential and a wide Gaussian with exponential tails. The two different background models with different parameterizations are illustrated in Fig. 3.5.

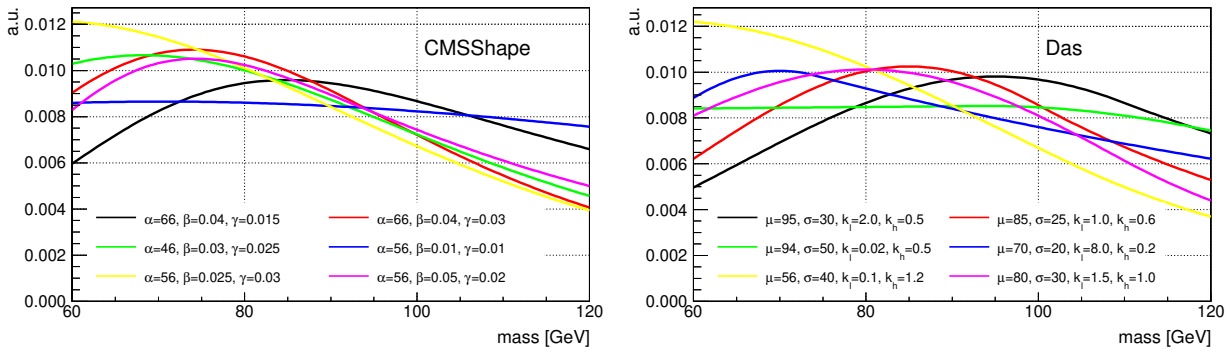

Fig. 3.5.: The CMSSHAPE (left) and DAS (right) function with different parameterizations as function of $m_{\mu\mu}$, normalized to a unit area.

More free parameters (4) are used in the DAS function, compared to the CMSSHAPE (3). For this reason, the CMSSHAPE is expected to be a bit more robust and is, therefore, the nominal choice in the measurement. Due to the higher number of free parameters, the DAS function can better describe possible characteristic features of the background. It can for example create a kink at the peak of the spectrum. Also, the falling parts are described by a smoother curve. The DAS function is therefore well suited as an alternative background model.

3.4. Selection of muons and extraction of reconstructed Z bosons

3.4.1. Muon identification

Muon candidates are selected within a pseudorapidity of $|\eta| < 2.4$ to ensure full coverage by the inner tracker and muon systems. Muons are required to have a $p_T > 25\,\text{GeV}$ such that the muons are well reconstructed and identified, and to ensure a plateau-level trigger efficiency. To keep the T&P efficiency measurement of the muons as simple as possible, symmetric cuts on both muons are used. Each muon has to be reconstructed in the muon system with an outer track, denoted as "standalone" muon, and with an inner track reconstructed in the silicon detector. The outer track is required to have signals in at least two muon stations. The inner track must have at least one valid hit in the silicon pixel detector and hits in more than five strip tracker layers. The muon candidate has to be a global muon, with additional quality criteria on the global muon track. It further has to be successfully reconstructed with the PF algorithm [115]. Details about the muon reconstruction are given in Section 2.4.1.

Impact parameters and isolation

Further criteria on the muon isolation or impact parameters (distance of closest approach of the lepton track to the identified primary vertex) can help to suppress backgrounds with misidentified or nonprompt muons as discussed in Section 2.4.3. However, requirements on this lead to complications in the measurement of the muon efficiency through the interplay of two effects. First, impact parameters depend on the reconstruction and correct identification of the associated primary vertex, which introduces a PU dependency. And second, the true vertex position is the same for both muons of the Z boson decay, which means the impact parameters of the two muons are highly correlated. The correlation in the transverse (d_{xy}) and longitudinal (d_z) impact parameters between the two muons in the event has been studied in simulation and the result is shown in Fig. 3.6. A large correlation coefficient is extracted for d_z, while for d_{xy} only a minor correlation is present. Because the measurement of the efficiency assumes the presence of one muon and is determined based on the presence of a second muon, a correlation between the two muons leads to a bias. Hence, no requirements are imposed on the impact parameters.

The use of muon isolation criteria has been studied for tracker- and PF-based isolation. The isolation criterion is estimated from charged particles that are associated with the same primary vertex as the muons. It thus has an indirect dependency on the reconstruction and identification efficiency of the primary vertex. A small correlation between the two muons is observed which leads again to a bias in the measurement. A second effect that appears when using isolation is a bias in the p_T spectrum between the two muons of the event. In a configuration where one decay muon is oriented in the direction of the Z boson momentum, the other decay muon tends to have a smaller momentum and often overlaps with jets coming from the ISR of the $Z \to \mu\mu$ event, the so-called "bosonic recoil". Isolation criteria are thus reducing the efficiency of this muon and indirectly introduce a bias. For these reasons, the requirement of isolation is omitted in the offline selection of

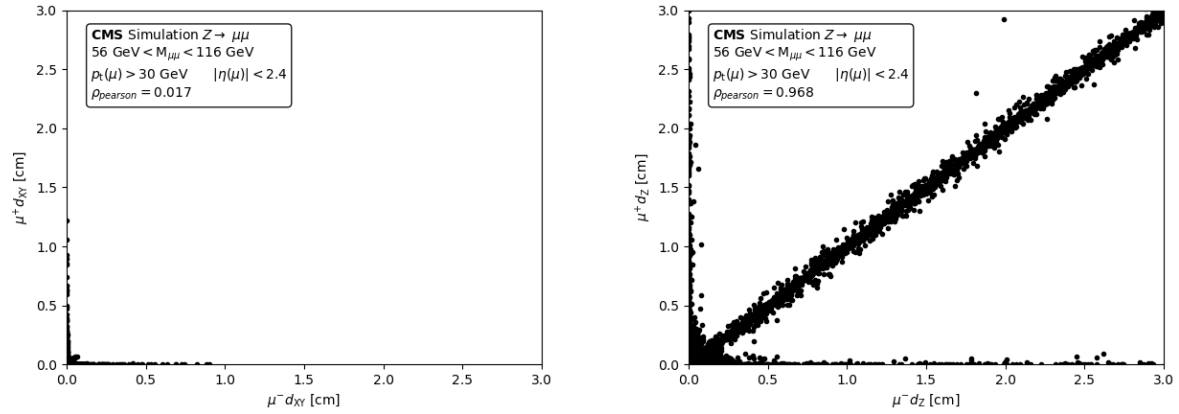

Fig. 3.6.: Scatter plot where each dot represents a $Z \to \mu\mu$ event. Shown are the IP values in the transversal (left) and longitudinal (right) direction for the muon on the x-axis and the anti muon on the y-axis. The values of the Pearson correlation coefficient are shown in each case.

muons.

3.4.2. Extraction of reconstructed Z bosons and the trigger efficiency

A Z candidate is reconstructed from two selected muons of opposite electric charge and with an invariant mass of $60\,\text{GeV} < m_{\mu\mu} < 120\,\text{GeV}$. At least one of the two muon candidates is required to be matched within $\Delta R < 0.1$ with a muon reconstructed at trigger level that fired the chosen single muon trigger. To avoid that the two selected muons are associated with the same trigger-level muon or that detector signals of the two muons overlap, an angular distance between the muons is required of $\Delta R > 0.8$.

The number of Z bosons with two selected muons ($N^{\text{Z}}_{\text{reco}}$) and the single muon HLT efficiency ($\epsilon^{\mu}_{\text{HLT}}$) are measured simultaneously using events in which only one (N_1) or both (N_2) muons have fired the trigger:

$$N_1 = 2 \cdot \epsilon^{\mu}_{\text{HLT}} \left(1 - C_{\text{HLT}} \cdot \epsilon^{\mu}_{\text{HLT}} \cdot\right) N^{\text{Z}}_{\text{reco}} + N_1^{\text{bkg}} \,, \tag{3.10}$$

$$N_2 = C_{\text{HLT}} \cdot \left(\epsilon^{\mu}_{\text{HLT}}\right)^2 \cdot N^{\text{Z}}_{\text{reco}} + N_2^{\text{bkg}} \,, \tag{3.11}$$

where C_{HLT} is a correlation factor for the modified probability that a second muon is passing the HLT if a first one has already passed it, and N_1^{bkg} and N_2^{bkg} account for backgrounds.

Two histograms are fit simultaneously to extract $N^{\text{Z}}_{\text{reco}}$ and $\epsilon^{\mu}_{\text{HLT}}$ at the same time. This has the advantage that each Z candidate is only used once, which is the correct statistical treatment. For the first histogram, Z candidates in which exactly one muon passes the HLT selection are fit, scaling the signal and background functions according to the two terms in Eq. (3.10), respectively. Those Z candidates in which both muons pass the HLT selection are filled into the second histogram and scaled according to Eq. (3.11). The parameters $\epsilon^{\mu}_{\text{HLT}}$ and $N^{\text{Z}}_{\text{reco}}$ are freely floating in the fit, while C_{HLT} is a constant taken from simulation as explained in the following section. Example fit results are shown in Fig. 3.7. The pulls of the distribution are plotted, defined as the difference between the

data and the fit model in each bin, divided by the statistical uncertainty estimated from the expected number of entries given by the model.

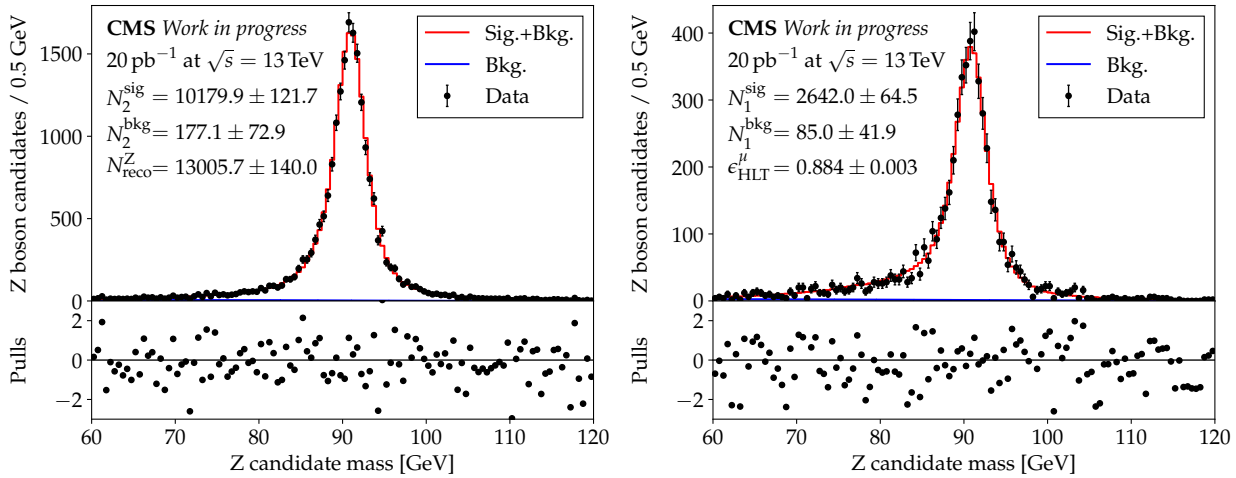

Fig. 3.7.: The upper panels show the reconstructed invariant mass distributions of Z candidates for 20 pb^{-1} of data for events where two (left) or one (right) muons pass the single muon trigger selection. The blue curves show the fitted background contribution, while the red curves illustrate the modeled signal plus background contribution. The numbers of signal and background candidates are given by $N_i^{sig} = N_i - N_i^{bkg}$ and N_i^{bkg}, respectively. The error bars indicate the statistical uncertainties. The lower panels show the pulls of the distribution.

3.4.3. Dimuon correlation at trigger selection

A correlation between the two muons coming from the trigger selection arises from the online isolation criteria which are part of the trigger selection and can thus not be eliminated. This was verified by the investigation of a single muon trigger path that does not have any isolation criteria. The chosen `HLT_Mu27` trigger shows no sign of correlation in simulation, but since this trigger is heavily prescaled in data, it can not be used for this analysis. The effect is known and was for example taken into account in the m_W measurement of the LHCb experiment [79].

The dimuon correlation factor C_{HLT} is estimated from simulation by re-arranging Eqs. (3.10) and (3.11):

$$C_{HLT} = \frac{4 \cdot N_{reco}^{Z} \cdot N_2^{sig}}{\left(N_1^{sig} + 2 \cdot N_2^{sig}\right)^2}, \tag{3.12}$$

where N_1^{sig} and N_2^{sig} are the signal-only numbers corresponding to N_1 and N_2. The dependence of C_{HLT} as a function of N_{PV} is shown in Fig. 3.8, separately for the different data-taking periods. Values on the order of 0.1–0.2% above unity are observed in simulation with a moderate dependency on N_{PV}. Overall, the trend in each year is similar.

Validation in data

To validate the correlation factors C_{HLT} in data, events are selected that pass an $E_{\text{T}}^{\text{miss}}$ trigger. The trigger `HLT_PFMETNoMu120_PFMHTNoMu120_IDTight` selects events with high $E_{\text{T}}^{\text{miss}}$ and high missing hadronic transverse energy calculated with the PF algorithm but excluding muons. This way, a large number of events containing muons is recorded without selecting on muons themselves. It was found in simulation that events passing the chosen $E_{\text{T}}^{\text{miss}}$ trigger leave C_{HLT} unbiased and can thus be used to measure it. Other $E_{\text{T}}^{\text{miss}}$, jet, and b-tag triggers were studied and found to either not contribute to a large number of events or introduce a strong bias on C_{HLT}, according to simulation.

The data obtained using the `HLT_PFMETNoMu120_PFMHTNoMu120_IDTight` trigger allow to access candidates where two muons pass the identification but none of them fires the single muon trigger as

$$N_0 = \left(1 - 2 \cdot \epsilon^{\mu}_{\text{HLT}} + C_{\text{HLT}} \cdot \left(\epsilon^{\mu}_{\text{HLT}}\right)^2\right) \cdot N^{\text{Z}}_{\text{reco}} + N_0^{\text{bkg}} \,. \tag{3.13}$$

Together with N_1 and N_2 in Equations (3.10) and (3.11), the correlation factor can be measured in data. The three histograms binned in $m_{\mu\mu}$ corresponding to N_0, N_1, and N_2 are fit simultaneously where $N^{\text{Z}}_{\text{reco}}$, $\epsilon^{\mu}_{\text{HLT}}$, and C_{HLT} are left free-floating in the fit.

The available sample size in data allows to perform the measurement only in a few bins of N_{PV} with rather large statistical uncertainty. The results are compared to simulation and shown in Fig. 3.8. Good agreement is observed within a 50% variation of the simulation in most of the bins.

3.5. Measurement of the Z boson reconstruction efficiency

The number of reconstructed Z bosons, extracted from the fit, $N^{\text{Z}}_{\text{reco}}$, is corrected with the Z reconstruction efficiency $\epsilon^{\text{Z}}_{\text{ID}}$. The efficiency $\epsilon^{\text{Z}}_{\text{ID}}$ comprises the reconstruction and identification efficiency $\epsilon^{\mu}_{\text{ID}}$ of the two muons, and their correlation. The muon identification was chosen such that the two muons are completely uncorrelated. For example, as explained above, the dependence on the primary vertex has been avoided. Simulated data are used to verify that there is no significant dimuon correlation for $\epsilon^{\mu}_{\text{ID}}$, as shown in Fig. 3.9.

For this reason, the efficiency to reconstruct Z bosons is given by the efficiency to reconstruct and identify the two muons $\epsilon^{\text{Z}}_{\text{ID}} = \left(\epsilon^{\mu}_{\text{ID}}\right)^2$. The efficiency-corrected number of Z bosons is

$$N^{\text{Z}} = \frac{N^{\text{Z}}_{\text{reco}}}{\epsilon^{\text{Z}}_{\text{ID}}} = \frac{N^{\text{Z}}_{\text{reco}}}{\left(\epsilon^{\mu}_{\text{ID}}\right)^2} \,. \tag{3.14}$$

The muon identification efficiency itself is factorized into three parts:

$$\epsilon^{\mu}_{\text{ID}} = \epsilon^{\mu}_{\text{ID|Glo}} \cdot \epsilon^{\mu}_{\text{Glo|Sta}} \cdot \epsilon^{\mu}_{\text{Sta|Trk}} \cdot c^{-1}_{\text{i|o}} \,, \tag{3.15}$$

where $\epsilon^{\mu}_{\text{ID|Glo}}$ is the identification efficiency under the condition that a global muon is reconstructed. This includes the efficiency of several quality criteria as discussed in Section 3.4.1. The quantity $\epsilon^{\mu}_{\text{Glo|Sta}}$ is the efficiency of a standalone muon to be reconstructed

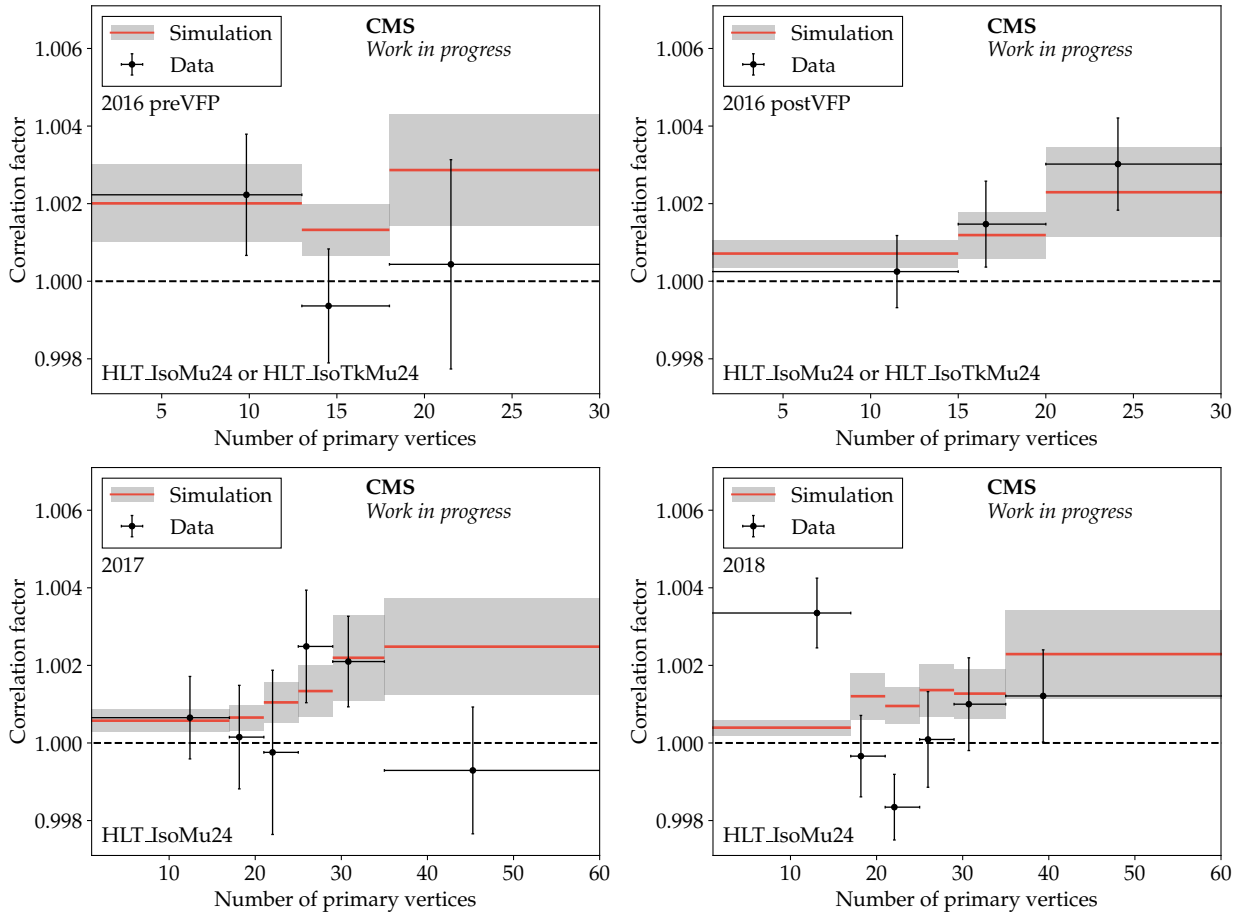

Fig. 3.8.: Dimuon correlation factor C_{HLT} for the muon trigger efficiency as a function of the number of reconstructed primary vertices, N_{PV}, in the simulation (red line) and the data (points). The data points are drawn at the mean value of N_{PV} in each bin of the measurement. The horizontal error bars on the points show the bin width, and the vertical error bars show the statistical uncertainty. The grey areas indicate an assumed uncertainty of 50% on the simulation.

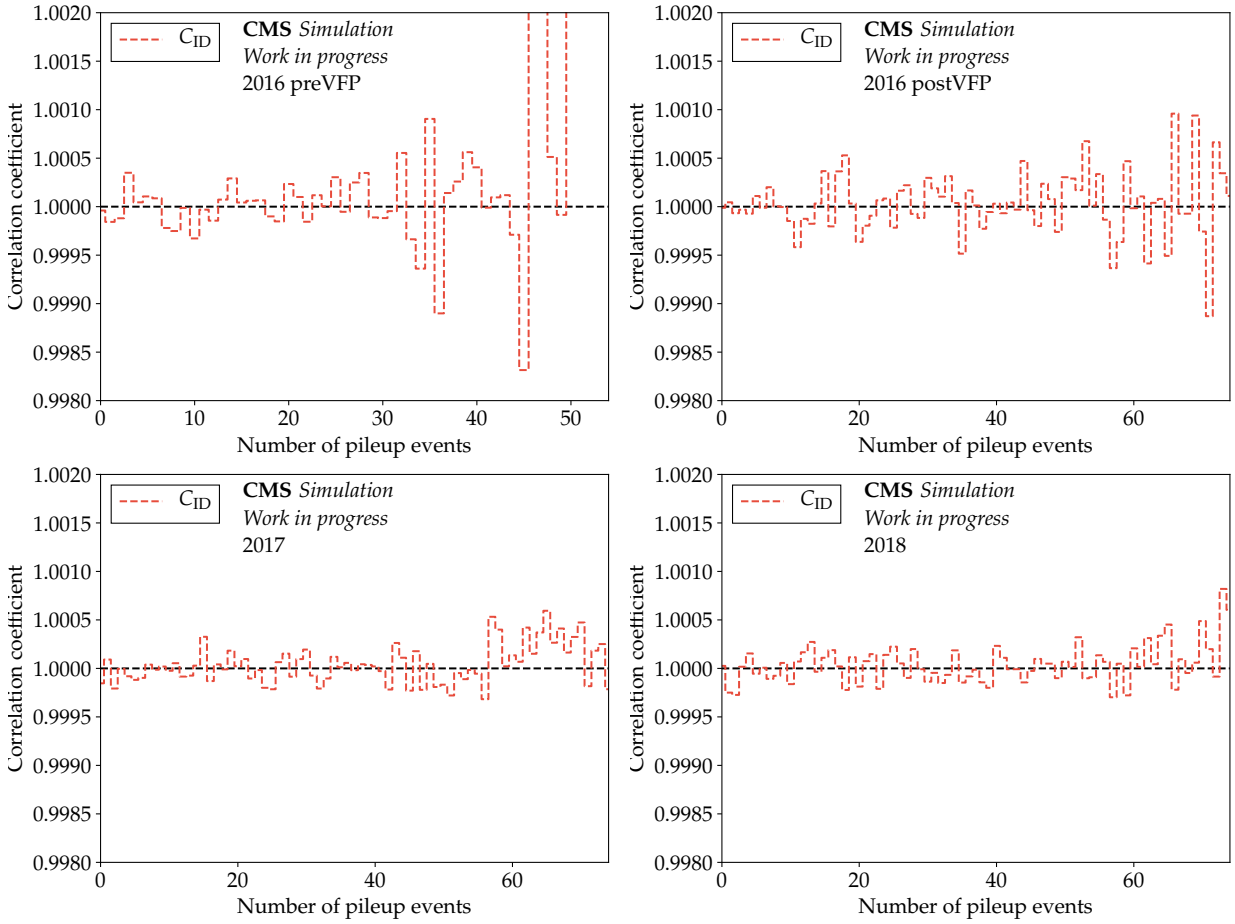

Fig. 3.9.: Dimuon correlation factors C_{ID} when applying the reconstruction and identification selection as functions of the N_{PU} for the 2016 preVFP (upper left), 2016 postVFP (upper right), 2017 (lower left), and 2018 (lower right) data-taking period. Simulated $Z \to \mu\mu$ events have been used.

as a global muon. It incorporates the efficiency to reconstruct the inner track and link it to the outer track to obtain a valid global track. The quantity $\epsilon^{\mu}_{\text{Sta|Trk}}$ is the efficiency of reconstructing a standalone muon, among all the muons that have a valid track in the inner tracker of the CMS detector — hence it measures the outer-track efficiency. A summary of the requirements for the different steps in the calculation of the muon efficiency is shown in Table 3.1. By only considering the product of the different muon efficiencies in Eq. 3.15, a correlation between the inner- and outer-track efficiencies would lead to an overestimation of $\epsilon^{\mu}_{\text{ID}}$. The quantity $c_{\text{i|o}}$ is the corresponding correlation factor and Eq. (3.15) needs to be divided by $c_{\text{i|o}}$ to correct for this effect. The correlation is further discussed in Section 3.5.2.

Table 3.1.: Requirements on the inner track (Trk), outer track (Sta), global muon (Glo), identified muon (ID), and trigger muon (HLT).

Requirement	Trk	Sta	Glo	ID	HLT
$p_{\text{T}} > 25\,\text{GeV}$	✓	✓	✓	✓	✓
$\lvert\eta\rvert < 2.4$	✓	✓	✓	✓	✓
Has inner track	✓	—	✓	✓	✓
Muon seed veto	✓	—	—	—	—
Number of tracker layer hits >5	✓	—	—	✓	✓
Number of pixel hits >0	✓	—	—	✓	✓
Has outer track	—	✓	✓	✓	✓
Has global track	—	—	✓	✓	✓
Is PF muon	—	—	—	✓	✓
Global track $\chi^2/ndf < 10$	—	—	—	✓	✓
Global track hits >0	—	—	—	✓	✓
Number of matched stations >1	—	—	—	✓	✓
HLT object (`HLT_IsoMu24`)	—	—	—	—	✓

3.5.1. Tag and probe measurement

Each part of the muon reconstruction and identification efficiency is measured via the tag-and-probe (T&P) approach as also documented in Ref. [96, 153, 165, 166]. In each event, muons are selected that fulfill a so-called "tag" requirement. In the case of this measurement, a tag muon is an identified muon that passes the single muon trigger. For each tag muon, "probe" muons are selected that form together with the tag muon a T&P pair. The T&P pair is considered if the two muons have opposite electric charge, an invariant mass of $60\,\text{GeV} < m_{\mu\mu} < 120\,\text{GeV}$, and are spatially separated by $\Delta R > 0.8$. The probe muons are further divided into two classes. Depending on whether the probe passes or fails the selection requirement, it is considered as passing or failing probe. The muon efficiency is then given by

$$\epsilon^{\mu} = \frac{n_{\text{p}}^{\text{sig}}}{n_{\text{p}}^{\text{sig}} + n_{\text{f}}^{\text{sig}}}\,, \tag{3.16}$$

where $n_{\mathrm{p}}^{\mathrm{sig}}$ and $n_{\mathrm{f}}^{\mathrm{sig}}$ correspond to the background subtracted numbers of passing and failing probes, respectively. For each event, multiple tag muons are allowed and each tag muon can form T&P pairs with multiple probe muons. This ensures that the T&P pair from the Z boson is among all selected T&P pairs, given that the necessary track component is reconstructed.

The track quality of the best available track is on average better for the passing probes compared to the failing ones. For example, for the passing probes in the measurement of $\epsilon^{\mu}_{\mathrm{Glo|Sta}}$, the best track parameters are determined from the inner track in most of the cases, while the failing probes often do not have an inner track and hence rely solely on the outer track, which has a significantly worse resolution. This can lead to different fractions of passing and failing probes that satisfy the acceptance cuts. To have an unbiased measurement, the track parameters are taken from the track available in all probes. In the case of $\epsilon^{\mu}_{\mathrm{Glo|Sta}}$, the parameters are taken from the outer track for both passing and failing probes.

Similar to the extraction of $N^{\mathrm{Z}}_{\mathrm{reco}}$ and $\epsilon^{\mu}_{\mathrm{HLT}}$, a maximum likelihood fit is performed in the $m_{\mu\mu}$ distribution simultaneously in two histograms for the passing and failing probes, respectively. The same shapes for the signal and background contributions as discussed in Sections 3.3.2 and 3.3.3 are used for each histogram. Signal templates generated from simulation are again produced using the individual probe selection with an additional match to the generator-level muons from the Z boson. In the signal extraction, ϵ^{μ} and n^{sig} are used as free parameters where the signal shape is scaled in the passing histogram with $\epsilon^{\mu} \cdot n^{\mathrm{sig}}$ and in the failing histogram with $(1-\epsilon^{\mu}) \cdot n^{\mathrm{sig}}$. The normalizations of the background shapes are freely floating independently in the passing and failing histograms.

Example fits for the measurement of the three parts of the muon identification and reconstruction efficiency defined in Eq. (3.17) are shown in Fig. 3.10. The worse resolution of the outer track used in the determination of $\epsilon^{\mu}_{\mathrm{Glo|Sta}}$ leads to a broader signal spectrum, as can be seen in the middle plots of Fig. 3.10. The inner track used for the T&P pairs to measure $\epsilon^{\mu}_{\mathrm{Sta|Trk}}$ has a much more accurate determination of the muon momentum, leading to a narrow peak at the Z boson mass as can be seen in the lower plots of Fig. 3.10.

3.5.2. Correlation between the inner and outer track

The values for $c_{\mathrm{i|o}}$ are extracted in simulated $\mathrm{Z} \to \mu\mu$ events from the ratio of the measured efficiencies using the factorization approach relative to the true efficiency $\epsilon^{\mu\,(\mathrm{true})}_{\mathrm{Glo}}$, as extracted from the simulation:

$$c_{\mathrm{i|o}} = \frac{\epsilon^{\mu}_{\mathrm{Glo|Sta}} \cdot \epsilon^{\mu}_{\mathrm{Sta|Trk}}}{\epsilon^{\mu\,(\mathrm{true})}_{\mathrm{Glo}}} \,. \tag{3.17}$$

The values for $c_{\mathrm{i|o}}$ as a function of N_{PU} are shown in Fig. 3.11. A PU-dependent correlation is observed that is largest for the 2016 preVFP data. In the regime where most of the events were recorded ($N_{\mathrm{PU}} \approx 30$), the correlation factor is on the order of 1% above unity.

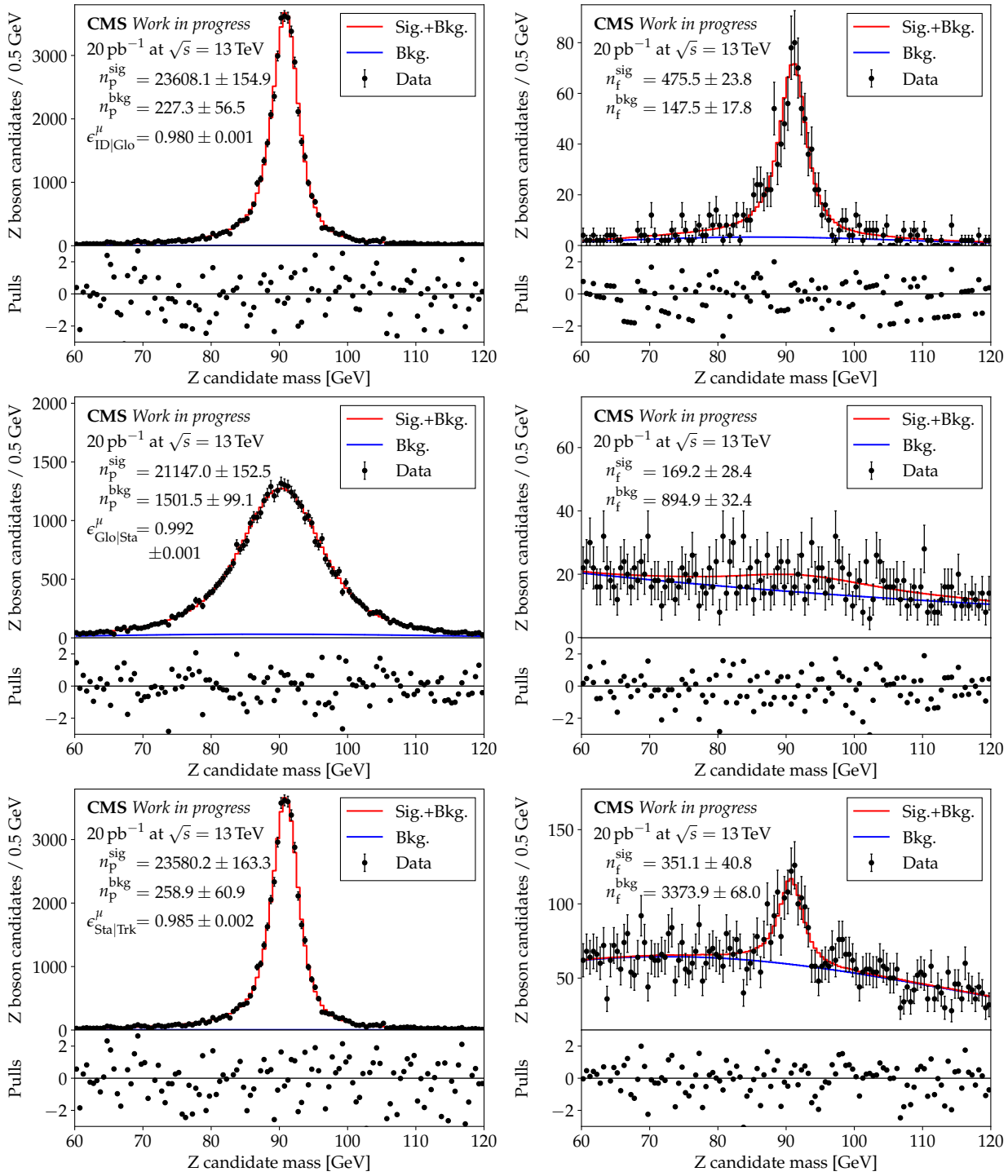

Fig. 3.10.: Results of the fits in the passing (left) and failing (right) histograms for the measurements of $\epsilon^{\mu}_{\mathrm{ID|Glo}}$ (upper), $\epsilon^{\mu}_{\mathrm{Glo|Sta}}$ (middle), and $\epsilon^{\mu}_{\mathrm{Sta|Trk}}$ (lower). The upper panels show the reconstructed invariant mass distributions of T&P pairs for 20 pb^{-1} of data. The blue curves show the fitted background contribution, while the red curves illustrate the modeled signal plus background contribution. The numbers of background and signal candidates are given by n_i^{bkg} and n_i^{sig}, respectively. The error bars indicate the statistical uncertainties. The lower panels show the pulls of each distribution.

In 2016 postVFP, due to the improved settings during data taking, the correlation at this point is mitigated to a level of 0.2%. For 2017 and 2018, $c_{\mathrm{i|o}}$ is less than 0.2% above unity where the bulk of events was taken ($N_{\mathrm{PU}} \approx 40$).

The reason for this correlation has not yet been completely understood and is the subject of current investigations. A part comes most likely from the current treatment of so-called "muon-seeded" tracks. In the track reconstruction chain, the outer track is used as a seed for the fitting of inner tracks. This improves the quality of existing inner tracks or creates new tracks that have not been found without muon seed. To mitigate the effect, those tracks are excluded from the measurement of $\epsilon^{\mu}_{\mathrm{Sta|Trk}}$. Ideally one would use a collection of tracks before they get updated using outer-track information. This collection is however not available in the processed data and one would need to reproduce the full data reconstruction on the raw data set. This was not carried out due to the immense computing capacities that would be required for this purpose.

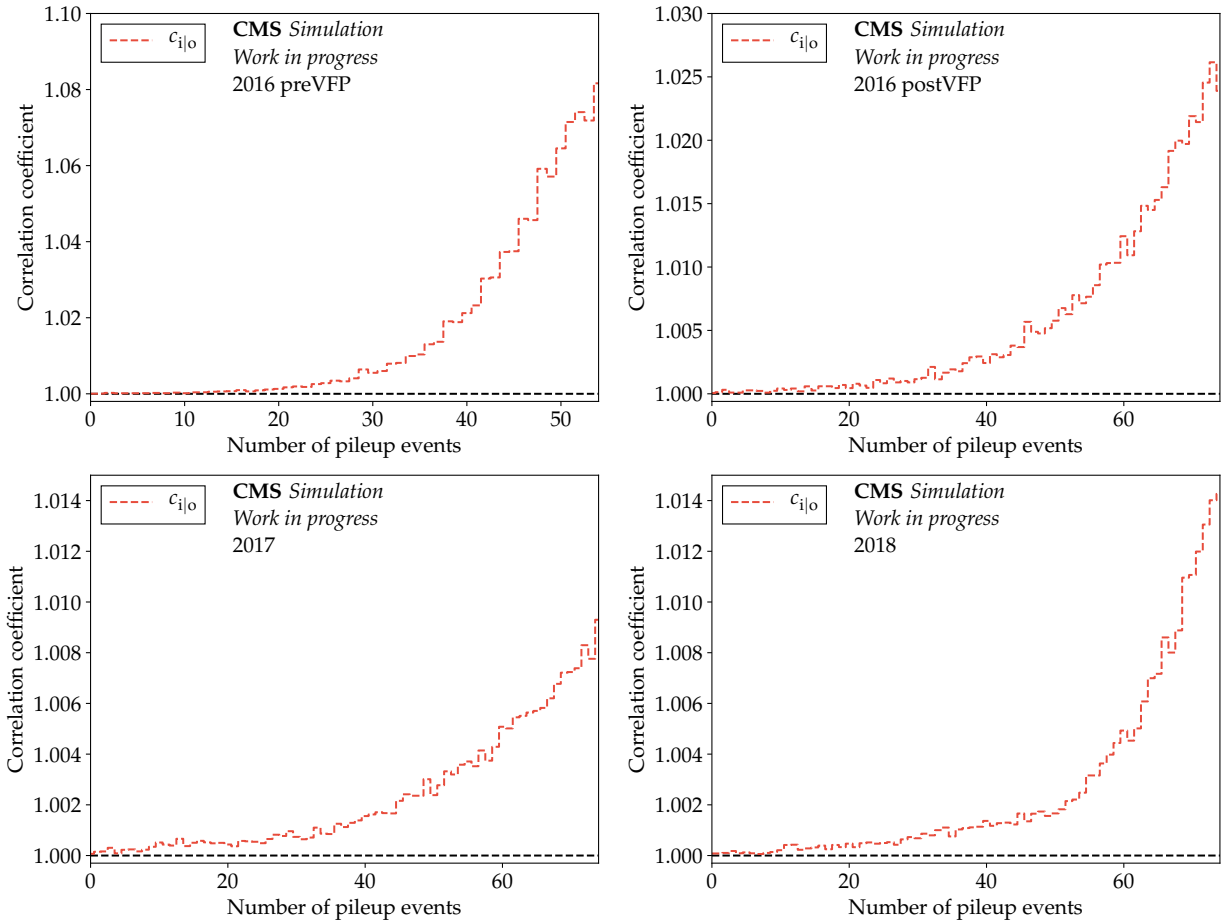

Fig. 3.11.: Correlation factors $c_{\mathrm{i|o}}$ for the inner- and outer-track efficiencies as a function of the N_{PU} for the 2016 preVFP (upper left), 2016 postVFP (upper right), 2017 (lower left), and 2018 (lower right) data-taking period using simulated $\mathrm{Z} \to \mu\mu$ events.

Like in the case of C_{HLT}, it would be desirable to validate $c_{\mathrm{i|o}}$ from data to gain confidence that the simulation describes the correlation correctly. One possibility would be to select $\mathrm{Z} \to \mu\mu$ events where one muon is identified and selected by the single muon trigger while the other muon has neither a reconstructed outer nor an inner track. Using

such events, $c_{\mathrm{i|o}}$ could be determined. However, only the information of the muon, and possibly $E_{\mathrm{T}}^{\mathrm{miss}}$, can be used. Since no information for the second muon is available to reconstruct $m_{\mu\mu}$, the challenge would be to determine and subtract the large background from W boson production.

3.5.3. L1 muon and ECAL prefiring corrections

The term "prefiring" describes the effect that a trigger decision is assigned to a bunch crossing preceding the one in which the collision actually took place. In CMS, the triggering and readout of more than one event in three subsequent bunch crossings are technically prohibited in the trigger logic. However, due to the limited time resolution of the muon system, the assignment of bunch crossings can be wrong in a fraction of cases. This leads to a loss of otherwise selected events, i.e. a trigger inefficiency. Since the T&P efficiency measurement is insensitive to this effect, the inefficiency due to prefiring is measured in dedicated analyses [98]. During Run 2 data taking, measurable prefiring occurred at nonnegligible rates for the L1 muon triggers. In 2016 and 2017, also the ECAL triggers prefired events [98]. For the L1 muon trigger, a PU independent correction for trigger inefficiency of 2.5% was found for 2016 preVFP and early runs in 2016 postVFP data taking. In the late runs of 2016 postVFP, the trigger timing was improved in the endcap region of the muon detector which lowered the effect to 1.4%. In 2017 and 2018 the time resolution was further improved by including redundant information in the barrel region of the muon system leading to a correction of 0.6%. In contrast, losses due to prefiring of the ECAL were found to require a PU-dependent correction of 0.05–0.2% for the PU range 0–50. The impact on the low PU data was found to be somewhat larger due to the lower trigger thresholds, and for the low PU data, a correction of 0.6% is applied.

3.5.4. Closure test in simulation

To verify the consistency of the method, a full closure test in simulation is performed treating simulation as closely as possible to data. The closure test also includes acceptance cuts on the reconstructed muon and Z candidates. The main objective of the closure test is to check the relative PU dependency. Generator-level muons are matched to reconstructed muons to decide whether a Z candidate counts as signal or background. Furthermore, an acceptance factor A defined in the definition of the fiducial cross section $\sigma_{\mathrm{fid}}^{\mathrm{Z}} = A\sigma^{\mathrm{Z}}\mathcal{B}(\mathrm{Z} \to \mu\mu)$ is calculated from generator-level muons as $A = 0.37$. The uncertainty or exact value of A is not needed since A is only used to check the absolute differences between the years.

The efficiency-corrected number of extracted Z bosons is measured in bins of N_{PU} and divided by the true number of Z bosons in simulated $\mathrm{Z} \to \mu\mu$ events. The results are shown in Fig. 3.12. The figures show the ratio without any correction (blue), with C_{HLT} for the dimuon correlation from trigger selection (red), and with $c_{\mathrm{i|o}}$ for the correlation between the inner and outer tracks (green). Good agreement with unity is found when applying both corrections in the 2016 postVFP, 2017, and 2018 data-taking periods. The closure in 2016 preVFP data is also largely improved. A significant nonclosure remains at

$N_{PU} > 40$ but is unproblematic for this analysis as almost no events were taken in this regime in the 2016 preVFP period.

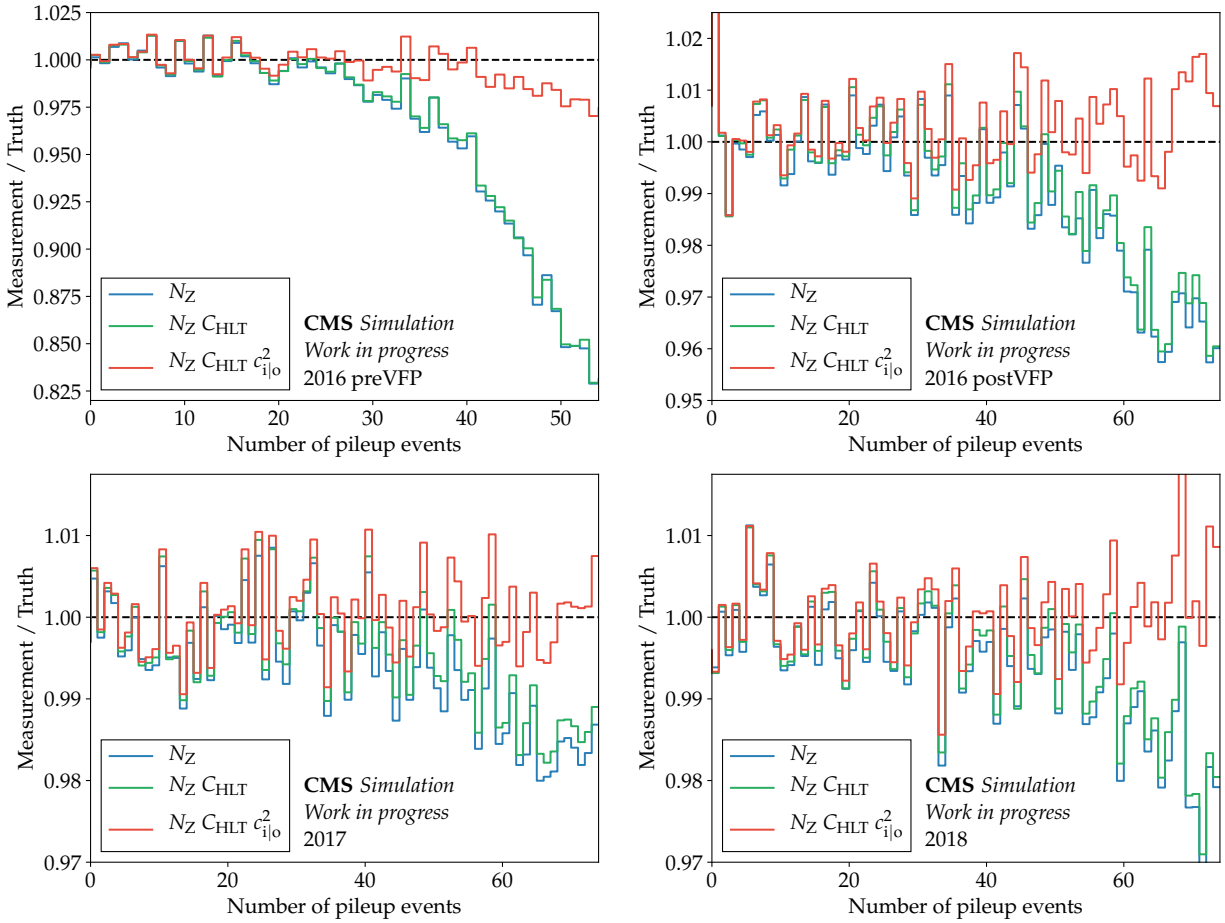

Fig. 3.12.: Results of the closure test performed in simulation for the 2016 preVFP (upper left), 2016 postVFP (upper right), 2017 (lower left), and 2018 (lower right) data-taking periods. The plot shows as a function of N_{PU} the ratio of N^Z as measured when treating simulation like data, divided by the true number of Z bosons multiplied with a constant acceptance factor of $A = 0.37$. The ratio is calculated neglecting the correlation factors C_{HLT} and $c_{i|o}$ (blue), taking into account C_{HLT} (green), and taking into account both C_{HLT} and $c_{i|o}$ (red).

3.6. Relative luminosity from Z boson rates

In Sections 3.5 and 3.4, the strategy of the Z boson rate extraction and calibration was outlined in detail. The measurement is performed almost completely independent of simulation. Only minor corrections are applied, leading to a good closure test. In this section, the Z boson rate measured in short time intervals is compared to the instantaneous luminosity measured by the conventional luminometer.

To account for changing detector conditions, the number of reconstructed Z bosons is measured separately for each run of data taking. Only runs with more than 20 luminosity blocks, i.e. corresponding to seven minutes of data taking, are considered to ensure

reliable fit results. During one run, the measurement is performed in slices of about $20\,\mathrm{pb}^{-1}$ of data measured with a reference luminometer. The size of the slices was chosen to obtain about 10 000 reconstructed Z candidates, which results in a statistical precision of 1% per slice. In case the remaining integrated reference luminosity at the end of a run is less than $30\,\mathrm{pb}^{-1}$, all remaining luminosity blocks are combined into one slice. Luminosity blocks in which no Z candidate is reconstructed are considered invalid and are removed if the recorded luminosity in this luminosity block is greater than $0.02\,\mathrm{pb}^{-1}$. Within $0.02\,\mathrm{pb}^{-1}$ of data, about ten Z bosons are expected while the probability to measure zero is lower than 0.01%.

To check the linearity of the method, i.e. the property that the Z boson rate scales linearly with the instantaneous luminosity, measured Z boson rates are compared to a reference luminosity. The reference luminosity is taken from a conventional luminometer, using the most up-to-date calibrations and corrections. The integral of the Z boson rates are normalized to the integral of the reference luminosity. For two example fills, the instantaneous luminosities are shown as a function of the fill time in Fig. 3.13. The integrated luminosities in the two fills shown are about $400\,\mathrm{pb}^{-1}$ and $540\,\mathrm{pb}^{-1}$, corresponding to 20 and 27 bins of $20\,\mathrm{pb}^{-1}$ each. The instantaneous luminosity in Fill 6255 decreased from initially $1.4 \cdot 10^{34}\,\mathrm{cm}^{-2}\,\mathrm{s}^{-1}$, corresponding to a PU of about 50, to about one-third of the initial value. It is observed that the shapes of the two independent measurements agree very well. The measured single muon efficiencies during those fills are also shown in Fig. 3.13. A significant dependence on time, and thus on PU, can be seen in particular for the HLT muon efficiency for which a rise by about 3% is measured.

The two LHC fills in 2017 were performed with different filling schemes. Up to fill 6167, the standard scheme was used while the later fills were done with the "8b4e" scheme. In the 8b4e filling scheme, eight filled bunches are followed by four empty bunches. In contrast, in the standard filling scheme, two batches of 48 filled bunches follow each other, spaced by 200 ns. While the Z boson rate is expected to be completely insensitive to the different filling schemes, the linearity of reference luminometers could well be affected. This highlights the relevance of the Z boson rate measurement as an independent and powerful cross-check. The agreement between the two independent results adds confidence that both methods are linear.

Combining all measurements of a data-taking period, more statistically significant results are obtained. The fiducial cross section $\sigma^{\mathrm{Z}}_{\mathrm{fid}} = N^{\mathrm{Z}}/\mathcal{L}^{\mathrm{Ref.}}$ is calculated as a function of the instantaneous luminosity using the reference luminometer. A nonconstant value could indicate incorrectly determined Z boson rates and is a good measure for the linearity of this method. As shown in Fig. 3.14 and 3.15, good linearity is observed in all data-taking periods. Even during the problematic data-taking period in 2016 preVFP, no significant slope is visible, which confirms the self-calibrating property of the method. The 2016 preVFP period can be considered as a stress test for the method and shows that the corrections, especially the correlation coefficient $c_{\mathrm{i|o}}$ between inner- and outer-track efficiency, which are significantly larger than in other periods, lead to a good agreement. The range of instantaneous luminosity goes from 1–$12\,\mathrm{nb}^{-1}\,\mathrm{s}^{-1}$ for 2016 and up to $18\,\mathrm{nb}^{-1}\,\mathrm{s}^{-1}$ in 2018 thus covering about one order of magnitude.

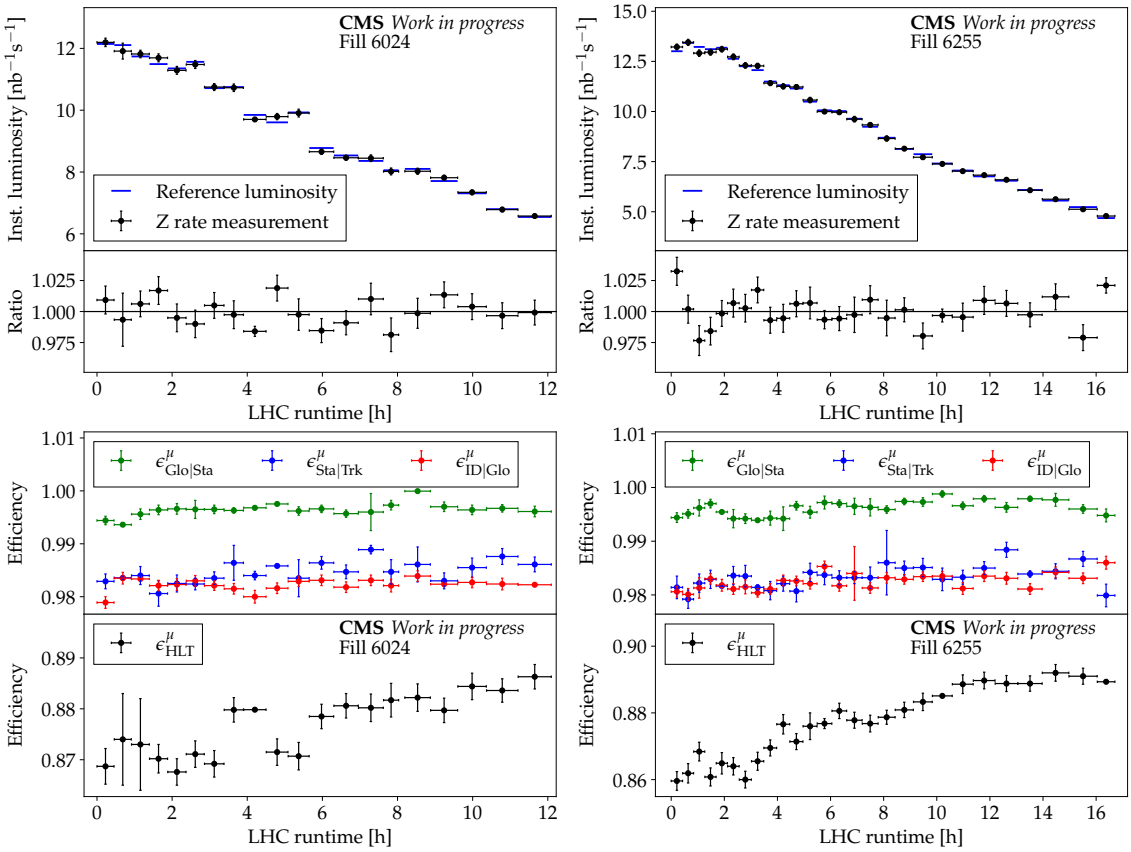

Fig. 3.13.: Upper: the Z boson rate, corrected for efficiency, compared to the reference luminosity in LHC fill 6024 (left) and 6255 (right) [148]. Each bin corresponds to about $20\,\mathrm{pb}^{-1}$, as determined by the reference measurement. For shape comparison, the Z boson rate is normalized to the reference integrated luminosity. The lower panels show the ratio of the two measurements. Lower: the measured single muon efficiencies used to calibrate the Z boson rate are shown as a function of time during the fills. The upper panel includes the muon reconstruction efficiencies $\epsilon^{\mu}_{\mathrm{Sta|Trk}}$ (blue) and $\epsilon^{\mu}_{\mathrm{Glo|Sta}}$ (green), and the identification efficiency $\epsilon^{\mu}_{\mathrm{ID|Glo}}$ (red). In the lower panel, the single muon trigger efficiency $\epsilon^{\mu}_{\mathrm{HLT}}$ is drawn.

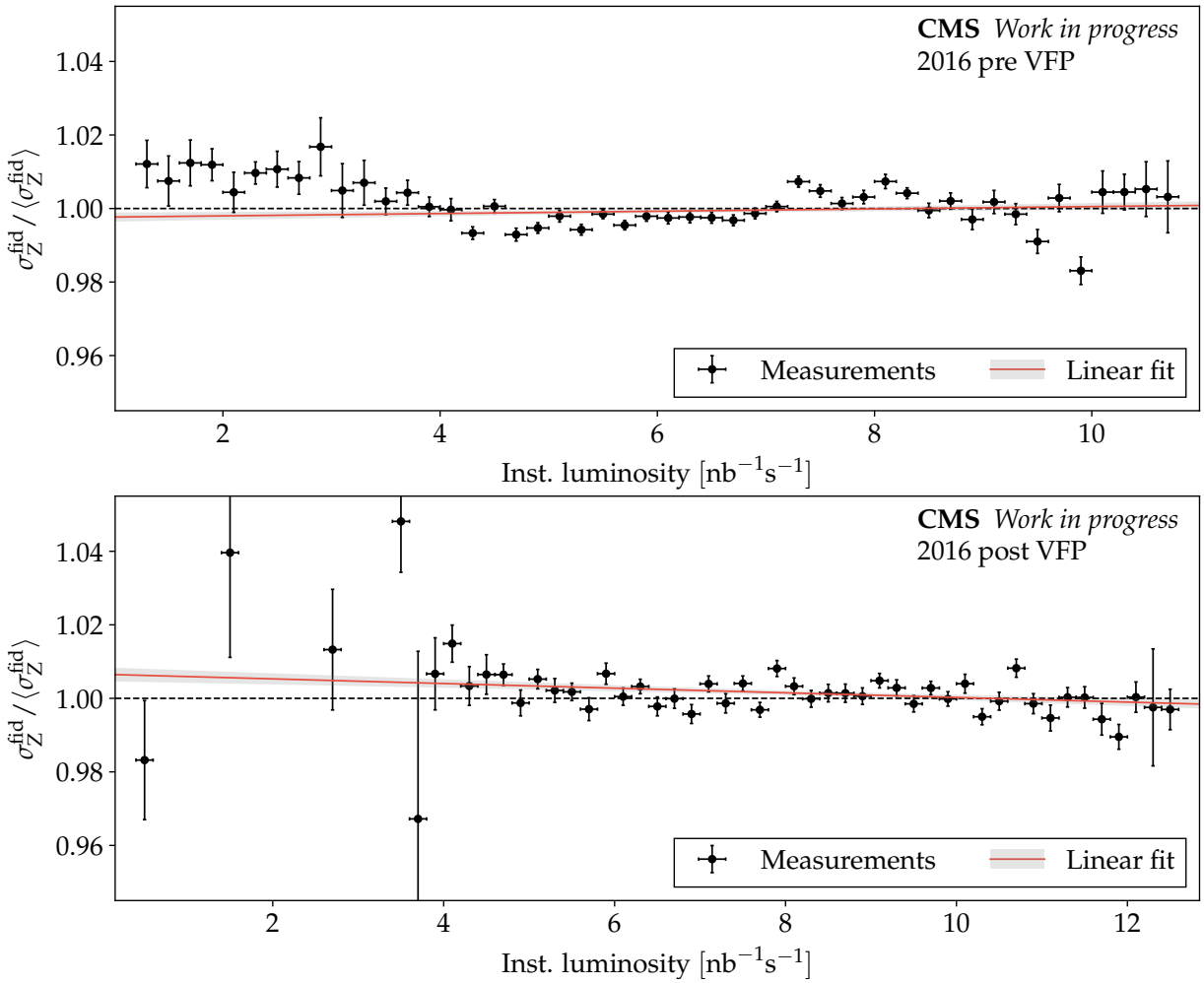

Fig. 3.14.: The fiducial Z boson cross section, normalized to the average, as a function of the instantaneous recorded luminosity. At each point, multiple measurements of the delivered Z boson rates are combined. The error bars correspond to the statistical uncertainties of the Z boson rates. A fit of a first-order polynomial is included (red line). Plots are generated from data taken in 2016 preVFP (upper) and 2016 postVFP (lower).

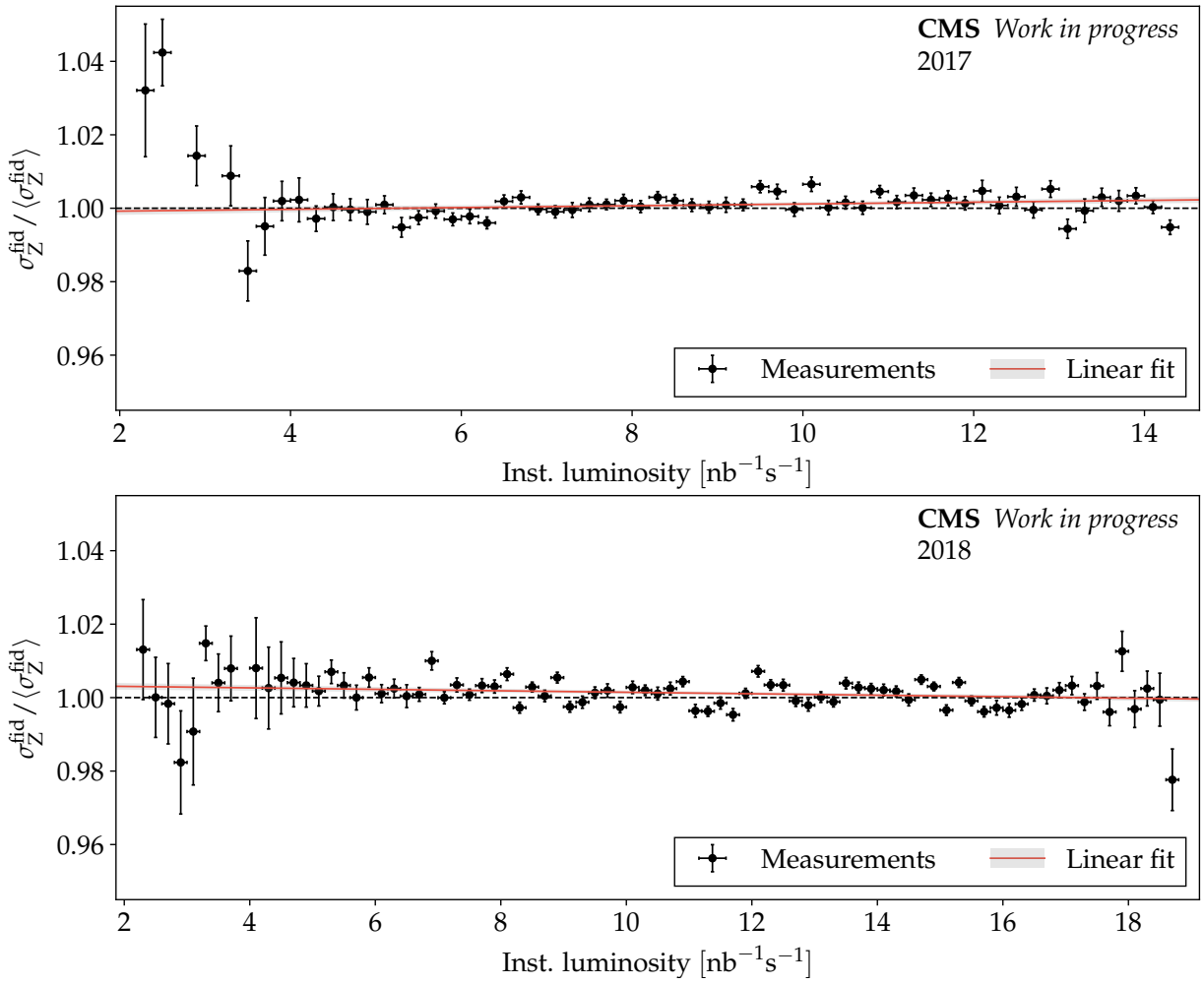

Fig. 3.15.: The fiducial Z boson cross section, normalized to the average, as a function of the instantaneous recorded luminosity. At each point, multiple measurements of the delivered Z boson rates are combined. The error bars correspond to the statistical uncertainties of the Z boson rates. A fit of a first-order polynomial is included (red line). Plots are generated from data taken in 2017 (upper) and 2018 (lower).

3.7. Absolute luminosity from Z boson rates

Using Eq. (3.3), the integrated luminosity in the high PU data referred to in the following as "Z luminosity" is determined from the integrated luminosity of the low PU data. In Fig. 3.16, the ratio between the Z luminosity and the reference luminosity measured using the conventional method [140, 142, 148] are shown. Each entry in the histogram corresponds to an interval of typically $20\,\mathrm{pb}^{-1}$ in the high PU data recorded in Run 2. The widths of the distributions of 1.3–1.5% are mainly caused by statistical fluctuations in the determination of the Z boson rate and efficiencies. This is consistent with the expectation for the statistical uncertainty from 10 000 Z bosons reconstructed in $20\,\mathrm{pb}^{-1}$ of data. A deviation from unity may be due to an inaccurate measurement of either the Z luminosity or the reference luminosity. Overall, a tension toward values below unity can be seen in all periods. In 2017, the Z luminosity is about 0.9% below the reference luminosity. The calibration of the reference luminosity in this year is the same as for the low PU period used to calculate the Z luminosity. Hence, the normalization uncertainty in 2017 cancels out in the ratio. On the reference luminosity, only the extrapolation uncertainty of 1.5% remains. This covers the observed difference between the two measurements. A stronger tension to lower values is observed in the other data-taking periods. Different calibrations for the reference luminosity were used in 2016 and 2018, and the uncertainty on the reference luminosity is larger and amounts to 1.8% and 2.3%, respectively. The tension in 2018 is between one and two standard deviations and indicates that the calibration in 2017 (used to normalize the Z luminosity in each year) may be overestimated with respect to the one in 2018. The tension in 2016 is more significant and could point to remaining unknown problems of the Z luminosity. As shown in the previous section, the linearity is well in agreement with the reference luminosity. However, there are substantial differences between 2016 and 2017, e.g., the silicon tracker was upgraded for 2017 with an additional layer. In other words, it is conceivable that there are PU independent effects in the transfer from one year to the other that are not yet considered.

To investigate the stability of the Z luminosity over time, the ratio of Z luminosity and reference luminosity as a function of the accumulated integrated luminosity is shown in Fig. 3.17. The figure shows a good stability of the Z luminosity measurement in all years, where only small patterns in time are apparent. Signs of instability are visible in the beginning of 2018 when the Z luminosity shows a small drop. In addition, there is a brief dip in the ratio in the second half of the data from 2016, indicating an unknown systematic effect. In 2016, the Z boson rate measurement is more affected by systematic effects compared to the other years, for example, the L1 prefire corrections are the largest and change over the year. It is yet unknown if this is related to the Z luminosity or the reference luminosity measurement. Systematic uncertainties on the Z luminosity are studied as discussed in the following section.

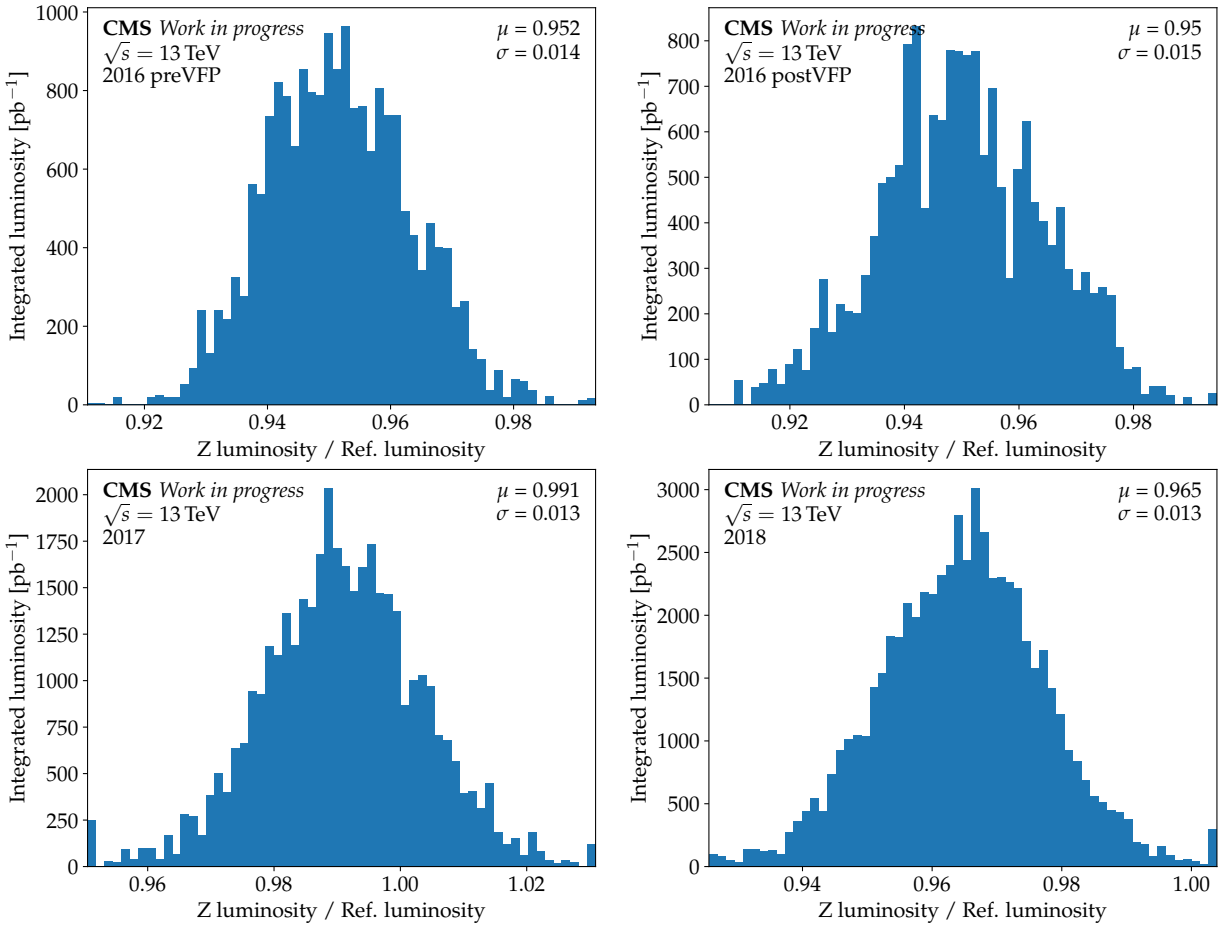

Fig. 3.16.: Histograms for the 2016 preVFP (upper left), 2016 postVFP (upper right), 2017 (lower left), and 2018 (lower right) data-taking periods. Each entry of the histogram represents the measurement of the luminosity from Z bosons in one interval of typically $20\,\mathrm{pb}^{-1}$ of the high PU data, divided by the integrated luminosity of the reference luminometer in the same interval. The first and last bins include the underflow and overflow contributions.

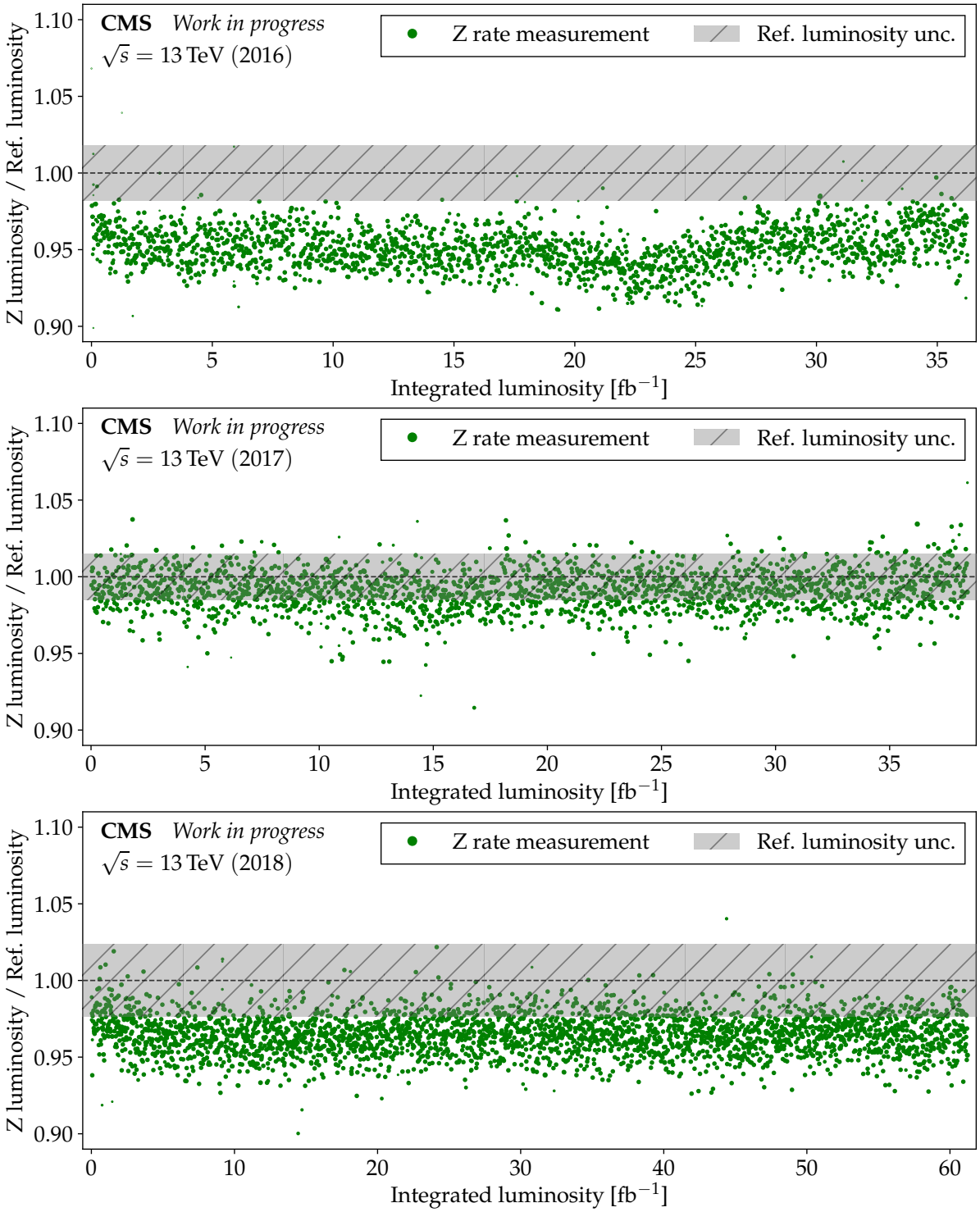

Fig. 3.17.: The luminosity as measured from Z bosons divided by the reference luminosity as a function of the integrated luminosity for the year 2016 (upper), 2017 (middle), and 2018 (lower). Each point represents the Z luminosity values measured in one interval of typically $20\,\text{pb}^{-1}$. The size of the point reflects the reference luminosity contained in each measurement. The grey band has a width of 1.8%, 1.5%, and 2.3% for each year, respectively. It corresponds to the uncertainty in the ratio of reference luminosities [140, 142, 148].

3.8. Study of systematic uncertainties

The uncertainties of the analysis were studied with the focus on the ratios $r = N^{Z}_{\text{highPU}} / N^{Z}_{\text{lowPU}}$ of the Z counts between high PU data sets in 2016 preVFP, 2016 postVFP, 2017, and 2018 and the low PU data set in 2017 as presented in Eq. (3.3). The full list of considered uncertainties for each period separately is given in Table 3.2 and the uncertainties on their ratios are summarized in Table 3.3. Their estimation is discussed in the following.

Table 3.2.: Summary of the efficiency-corrected number of Z bosons in each data-taking period. The impact of various sources of uncertainty are given in percentage. The numbers are given as relative uncertainty.

	$\delta N^{Z}_{\text{2016 preVFP}}$	$\delta N^{Z}_{\text{2016 postVFP}}$	$\delta N^{Z}_{\text{2017}}$	$\delta N^{Z}_{\text{lowPU}}$	$\delta N^{Z}_{\text{2018}}$
Correlation C_{HLT}	± 0.07	± 0.05	± 0.05	± 0.03	± 0.04
Correlation $c_{\text{i\|o}}$	± 1.56	± 0.23	± 0.26	± 0.03	± 0.24
Muon pref. up (stat.)	$+0.37$	$+0.22$	$+0.08$	$+0.08$	$+0.08$
Muon pref. down (stat.)	-0.36	-0.22	-0.08	-0.08	-0.08
Muon pref. up (syst.)	$+0.51$	$+0.4$	$+0.13$	$+0.13$	$+0.13$
Muon pref. down (syst.)	-0.5	-0.4	-0.13	-0.13	-0.13
ECAL pref. up	$+0.02$	$+0.04$	$+0.04$	$+0.14$	—
ECAL pref. down	-0.02	-0.04	-0.04	-0.14	—
Alt. sig. model	-2.84	-2.08	-1.95	-0.73	-1.6
Alt. bkg. model	-0.04	-0.13	-0.13	-0.17	-0.14
Lumi slice up	$+0.01$	-0.03	-0.03	-0.06	-0.01
Lumi slice down	-0.01	—	$+0.04$	$+0.07$	$+0.08$
Bin width up	$+0.06$	$+0.07$	$+0.04$	$+0.14$	$+0.02$
Bin width down	-0.02	$+0.03$	$+0.04$	$+0.05$	$+0.05$
Statistical	± 0.03	± 0.03	± 0.02	± 0.26	± 0.02
Systematic up	$+1.69$	$+0.52$	$+0.31$	$+0.27$	$+0.3$
Systematic down	-3.3	-2.15	-1.98	-0.78	-1.63
Total up	$+1.69$	$+0.52$	$+0.31$	$+0.37$	$+0.3$
Total down	-3.3	-2.15	-1.98	-0.82	-1.63

The statistical uncertainties are driven by the number of available Z bosons. They affect both the determination of the number of Z bosons itself and the efficiencies. The low PU data set, corresponding to an integrated luminosity of about $200\,\text{pb}^{-1}$, contributes a statistical uncertainty of about 0.26%. The statistical uncertainties for the full high PU data sets are negligibly small.

The uncertainty in the dimuon correlation factor at trigger level C_{HLT}, as discussed in Section 3.4.3, is estimated to be 50% of the correction. This estimate is supported by the good data-to-simulation agreement observed in the validation of data samples. The correlation is attributed to the isolation requirement of the single muon trigger. A slightly different trigger selection, with different isolation parameters, was used in 2016. However, the origin of the correlation is the same, thus the uncertainty is considered fully correlated among all data-taking periods.

No validation in data has been performed for the correlation between the inner and outer tracks, $c_{\text{i|o}}$, neither is the exact origin of this effect known. The uncertainty on

Table 3.3.: Summary of the ratio of the efficiency-corrected number of Z bosons in each period of high PU data taking to the ones in the low PU data of 2017. The impact of various sources of uncertainty are given in percentage. The numbers are given as relative uncertainty.

	$\delta\frac{N^{Z}_{2016\ preVFP}}{N^{Z}_{lowPU}}$	$\delta\frac{N^{Z}_{2016\ postVFP}}{N^{Z}_{lowPU}}$	$\delta\frac{N^{Z}_{2017}}{N^{Z}_{lowPU}}$	$\delta\frac{N^{Z}_{2018}}{N^{Z}_{lowPU}}$
Correlation C_{HLT}	±0.04	±0.02	±0.02	±0.01
Correlation $c_{i\|o}$	±1.53	±0.2	±0.22	±0.21
Muon pref. up (stat.)	$+0.52$	$+0.31$	—	$+0.11$
Muon pref. down (stat.)	-0.51	-0.31	—	-0.12
Muon pref. up (syst.)	$+0.38$	$+0.27$	—	—
Muon pref. down (syst.)	-0.37	-0.27	—	—
ECAL pref. up	-0.12	-0.11	-0.1	-0.14
ECAL pref. down	$+0.12$	$+0.11$	$+0.1$	$+0.14$
Alt. sig. model	-2.11	-1.35	-1.23	-0.87
Alt. bkg. model	$+0.13$	$+0.04$	$+0.04$	$+0.03$
Lumi slice up	$+0.07$	$+0.03$	$+0.04$	$+0.05$
Lumi slice down	-0.07	-0.07	-0.02	$+0.01$
Bin width up	-0.08	-0.07	-0.09	-0.12
Bin width down	-0.08	-0.02	-0.02	-0.01
Statistical	±0.26	±0.26	±0.26	±0.26
Systematic up	$+1.67$	$+0.47$	$+0.25$	$+0.28$
Systematic down	-2.69	-1.44	-1.25	-0.92
Total up	$+1.69$	$+0.54$	$+0.36$	$+0.38$
Total down	-2.7	-1.46	-1.28	-0.96

$1 - c_{\mathrm{i|o}}$ is thus estimated to be 100%. Since the same reconstruction algorithms were used in all data sets, the uncertainty is considered as fully correlated between the years.

The uncertainty in the prefiring corrections is split into statistical and systematic parts. The statistical uncertainty in the ECAL prefiring correction is negligible. The systematic uncertainty is estimated to be 20% of the nominal correction. Since the effects are caused by the same source between the years and derived using the same methods, the systematic uncertainty is treated as correlated. Different magnitudes between the data sets lead only to partial cancellations in r.

The robustness of the fit was studied by varying the bin size of the histograms by factors of 1/2–2. To check any dependence on the time intervals chosen for the measurements, the intervals of integrated luminosity were varied to 15 and 30 pb^{-1}. Both studies show negligible effects on the final result.

The extraction of the signal and background contributions was studied using alternative fit models as discussed in Sections 3.3.2 and 3.3.3. The alternative background model leads to a small reduction in N^{Z} for all data sets, indicating that the systematic uncertainty is strongly correlated between the data sets, and thus cancels largely in the ratio r between data sets. The alternative signal model leads to a much larger reduction in N^{Z} for all data sets. This reduction can be understood as arising from the different signal definition as discussed in Sec 3.3.2. Because the BW$\times$CB does not include the FSR and Z/γ^* interference effects, which are significant, especially in the lower tails of the distributions, the background model is pulled up and covers a larger portion of events. However, the different magnitude in reduction between the data sets is not expected and points to instability, which is particularly evident in the smaller low PU data set. An improved description of the signal modeling will be necessary to reach the full potential of the measurement. Since this uncertainty has been estimated to be much lower in other analyses [137, 167], it is expected that it will be possible for the final result of this analysis to reduce this uncertainty to a sub-dominant level. For the preliminary discussion in the following, it is thus not taken into account.

The total systematic uncertainty is obtained by adding the individual sources listed in Table 3.2 in quadrature. Together with the statistical uncertainty, the total uncertainty to transfer the luminosity from the low PU data to the high PU data in each period is

$$\delta r_{2016\ \mathrm{preVFP}} = \pm 1.67\%\,(\mathrm{syst}) \pm 0.26\%\,(\mathrm{stat}) = \pm 1.69\% \tag{3.18}$$

$$\delta r_{2016\ \mathrm{postVFP}} = \pm 0.48\%\,(\mathrm{syst}) \pm 0.26\%\,(\mathrm{stat}) = \pm 0.55\% \tag{3.19}$$

$$\delta r_{2017} = \pm 0.26\%\,(\mathrm{syst}) \pm 0.26\%\,(\mathrm{stat}) = \pm 0.37\% \tag{3.20}$$

$$\delta r_{2018} = \pm 0.29\%\,(\mathrm{syst}) \pm 0.26\%\,(\mathrm{stat}) = \pm 0.39\% \tag{3.21}$$

where the statistical uncertainty originates from the size of the low PU data set. An uncertainty of $<$2% is achieved for 2016 preVFP for which challenging data-taking conditions were present. A good linearity was observed in the period as shown in Fig. 3.14, but the strong tension observed in Fig. 3.16 indicate that additional corrections might be needed. In the other periods, the uncertainty is well below 1% and reaches the statistical precision of the low PU data set. The assumed uncertainty on $c_{\mathrm{i|o}}$ of 100% of its value above unity is rather conservative. Since the 2016 preVFP data shows good linearity when taking the correction into account, it indicates that $c_{\mathrm{i|o}}$ is well described

by simulation. A few more tests could be done to gain more confidence and reduce the assumed uncertainty. A possibility to measure $c_{\mathrm{i|o}}$ in data by using events with a single lepton was outlined at the end of Section 3.5.2. This way, the description of $c_{\mathrm{i|o}}$ from simulation could be assessed. On the other hand, it is conceivable that $c_{\mathrm{i|o}}$ itself can be reduced by a suitable choice of the inner- and outer-track definition. The exact origin of the correlation should therefore be studied and understood.

Overall, the method is very competitive with conventional luminosity measurements. Taking the current precision of 1.7% for the luminosity in the low PU data, the luminosity in the high PU 2017 data could potentially be determined to a precision of better than 1.8%. This is a significant improvement with respect to the current uncertainty of 2.3% [148].

3.9. Outlook

In this chapter, a detailed analysis of Z boson production for use in luminosity measurements has been presented. The strengths and weaknesses of Z boson rate measurements for luminosity determination have been characterized. The origin of the correlation between two muons from the Z boson decay were studied and minimized by appropriate selection criteria. Small remaining correlations coming from HLT selection at the level of 0.1% are understood. A correlation between the inner- and outer-track efficiencies was identified. Efforts were taken to mitigate this correlation, leading to a residual effect on the order of 0.1–0.2% per muon for the data in 2017 and 2018. However, the exact cause of this effect is not yet fully understood. A part of this effect is most likely related to muon-seeded tracks as discussed in Section 3.5.2. As a starting point, the muon reconstruction chain could be adapted such that no muon seeds are used when fitting the inner tracks. Simulated samples could be used to test whether this completely removes the correlation or whether there is some other unknown effect.

The linearity of the method was studied in simulation up to $N_{\mathrm{PU}} = 75$ and in data for instantaneous luminosity up to $1.8 \cdot 10^{34}\,\mathrm{cm}^{-2}\,\mathrm{s}^{-1}$ corresponding to $N_{\mathrm{PU}} \approx 50$. Good linearity was observed in all data-taking periods. The method is thus well applicable also in Run 3 data taking where on average a PU of 50 is expected. For the HL-LHC an average PU of 200 is foreseen [139]. More studies should be performed to validate the method in these extreme conditions. First and foremost the correlation between the inner and outer tracks but also the dimuon correlation from the HLT selection could increase to an uncontrollable level and require special attention.

Run 3 data taking has just begun and is expected to continue until end of 2025. As it was already done during Run 2, an initial measurement of the efficiency-corrected Z boson production rate will be performed within a few days after data taking. This provides a powerful comparison to the relative online luminosity and will be used to compare the luminosity between ATLAS and CMS as explained at the beginning of this chapter. With the updates done for the work presented in this thesis, also the data from the 2016 preVFP period is largely understood, which was not the case for the setup used during Run 2. This demonstrates the functionality and strength under more difficult conditions. With the gained understanding and the improved measurement strategy, the method will be much more reliable.

A precise measurement for the luminosity will not be available before 2023 as the

first vdM scan will take place in late 2022. A first estimate of the absolute luminosity from the Z boson rate can be obtained relatively easily using the fiducial cross section σ^{Z}_{fid} from theory. Taking the inclusive DY production cross section with perturbative N^3LO calculation in α_S and the acceptance factor from simulation, σ^{Z}_{fid} is known with a precision of about 3% [151]. Assuming that the signal modeling in the measurement will be better understood in the near future, a total uncertainty on the absolute luminosity using Z boson rates of about 3% could be achieved. This will be very competitive to the uncertainty of the online luminosity and an important input to early analyses. As the systematic uncertainties are uncorrelated, both measurements can be combined to reduce the overall uncertainty further.

As presented in this chapter, the method has excellent long-term stability. The efficiency-corrected Z boson rates in each year can be used to combine the luminosity from several years of data taking. The statistical procedure is described in detail in Appendix A. This way, it is expected that the overall uncertainty can be reduced. To perform the combination of the luminosity for Run 2, the remaining differences between years have to be fully understood and verified. The combination procedure will become more important in the future as several years of data taking at the same center-of-mass energy are forthcoming.

The Z boson rate measurement can also be extended to other decay channels, first of all, electrons. Even though not as clean as muons, electrons can be reconstructed and identified with good precision and in-situ measurements of the efficiencies can be performed. The measurement of $Z \to ee$ is affected by different systematic uncertainties, such as the prefiring or correlation factors. Thus, it provides additional cross-checks and the possibility for a combination.

The measured Z boson rates could also be used in a completely different context. An example would be the search for violation of the Lorentz invariance in the muon sector at the energy scale of m_Z. A similar search was performed for $t\bar{t}$ in Ref. [168]. Lorentz invariance violation would impact σ^{Z}_{fid} as the earth rotates. From the measured Z boson rates, σ^{Z}_{fid} can be obtained using the corresponding measured reference luminosity. As the Z boson rate in each slice of $20\,\text{pb}^{-1}$ is measured in a short time interval of about 30 min in a self-consistent way, it is perfectly suited for such an analysis. A typical analysis from CMS or ATLAS would be less suited for such a search as the efficiencies are calibrated by averaging over the full data-taking periods. And in the average, possible time dependencies are not taken into account.

4. Measurements of single top quark production in association with a Z boson

This chapter describes the most precise inclusive, and world's first differential measurement of the production cross section for single top quarks in association with Z bosons (tZq) in pp collisions at $\sqrt{s} = 13\,\text{TeV}$. From the measured inclusive cross section, the V_{tb} is determined. Observables for the differential measurements are chosen based on sensitivity to potential BSM physics, to assess the modeling, and to measure interesting properties. Among these properties is the top quark spin asymmetry which is proportional to the top quark polarization. A theoretical discussion about the value of a tZq analysis was outlined in Section 1.4. Results of this thesis were published by the CMS Collaboration in early 2022 in the Journal of High Energy Physics [169]. The paper was elaborated together with another institute within the CMS Collaboration. Both groups conducted two separate and independent analyses. The other group contributed to the paper with results on the inclusive cross section. I contributed to the paper with results on the differential cross sections and the spin asymmetry. The measured inclusive cross section documented in this thesis was used as an important cross-check and good agreement between the results has been found.

This chapter is structured as follows: first, an outline of the analysis strategy and an overview of previous tZq measurements from the ATLAS and CMS experiments is given in Section 4.1. Section 4.2 introduces the statistical approach used for the signal extraction. To measure properties of this rare process with good statistical precision, an efficient identification of all involved particles is vital. The selection of promising signal candidate events is described in Section 4.3. Background events passing the signal selection are studied and control regions (CRs) are defined as explained in Section 4.4. There, the contribution of events with at least one misidentified lepton is discussed in detail and estimated using control samples from data. Characteristic features of tZq events are used in a multiclass neural network (NN) to separate the signal from various background processes as explained in Section 4.5. Systematic uncertainties from theory predictions and experimental calibrations are discussed in Section 4.6. The measurement and results for the inclusive cross section are presented in Section 4.7. Section 4.8 presents the necessary ingredients for the differential measurements. These include the statistical framework which is based on multidimensional maximum likelihood fits, the definitions of detector-independent parton- and particle-levels objects, and the procedure followed to find a suitable binning for the unfolded distributions. Finally, the results are presented and compared to theory predictions using 4FS and 5FS assumptions. The measurement and result of the top quark spin asymmetry are described in Section 4.9. Concluding

remarks and an outlook at future opportunities are given in Section 4.10.

4.1. Introduction

The analysis is performed for final states with three leptons (e or μ). This also includes a small fraction of τ leptons that decay leptonically into electrons or muons. Unless stated otherwise, from now on, the term lepton is used to refer exclusively to electrons and muons. Nonresonant lepton pairs and off-shell Z bosons having an invariant mass $m_{\ell\ell'} > 30\,\text{GeV}$ are included, but the final state with an on-shell Z boson is targeted. One Feynman diagram contributing this way is shown in Fig. 4.1. The distinctive signature of the signal process in this final state consists of

- three isolated leptons where two of them come from the Z boson, i.e. they have the same flavor, opposite electric charge, and an invariant mass close to m_Z,
- a light flavored (u, d, s, or c quark) jet that recoils against the top quark and is often found in the forward region of the detector, denoted as "recoiling" jet,
- one b quark jet originating from the top quark decay,
- and missing transverse energy arising from the undetected neutrino from the top quark decay.

Figure 4.2 shows an event display of a typical tZq candidate recorded by the CMS experiment in the trilepton final state.

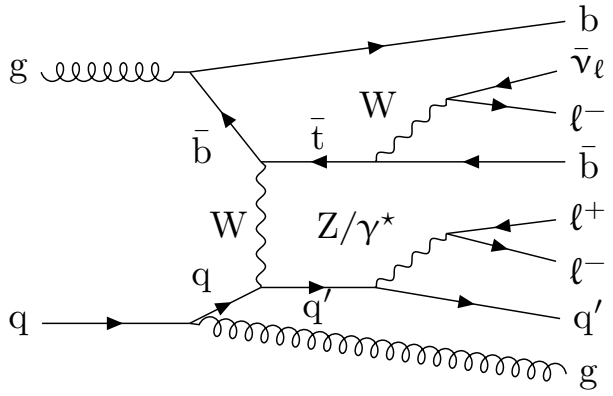

Fig. 4.1.: A Feynman diagram of tZq production including the leptonic decay of the Z/γ^* interference and the decay of the top quark into a b quark, lepton, and neutrino. On the analysis level, those give rise to three isolated leptons, a b quark jet, and missing transverse energy. The initial b quark that is required in the process originates from gluon splitting, giving rise to a second b quark jet with typically low p_T. A light flavor quark interacts via the space-like W boson, leading to a jet that recoils against the system with relatively high p_T and large $|\eta|$ values. A gluon from initial state radiation can lead to an additional jet in the final state.

As shown in Fig. 4.1, an additional b quark jet can arise from gluon splitting into a b quark-antiquark pair in the initial state. Such a jet typically has low p_T and is not always inside the acceptance of the detector. To a significant extent, events with additional light flavor quark- or gluon-jets coming from QCD radiations and gluon splitting are also expected. Because of these additional particles in the final state, the signature of tZq is more similar to that of $t\bar{t}Z$. On the other hand, some particles from $t\bar{t}Z$ events may escape detection through the limited detector acceptance and efficiency and $t\bar{t}Z$ events may appear more tZq-like in the detector. The separation of tZq from $t\bar{t}Z$ and other backgrounds is a challenge in the analysis. Final states with three prompt leptons offer the cleanest event signature for tZq, but they also have the smallest branching ratio as

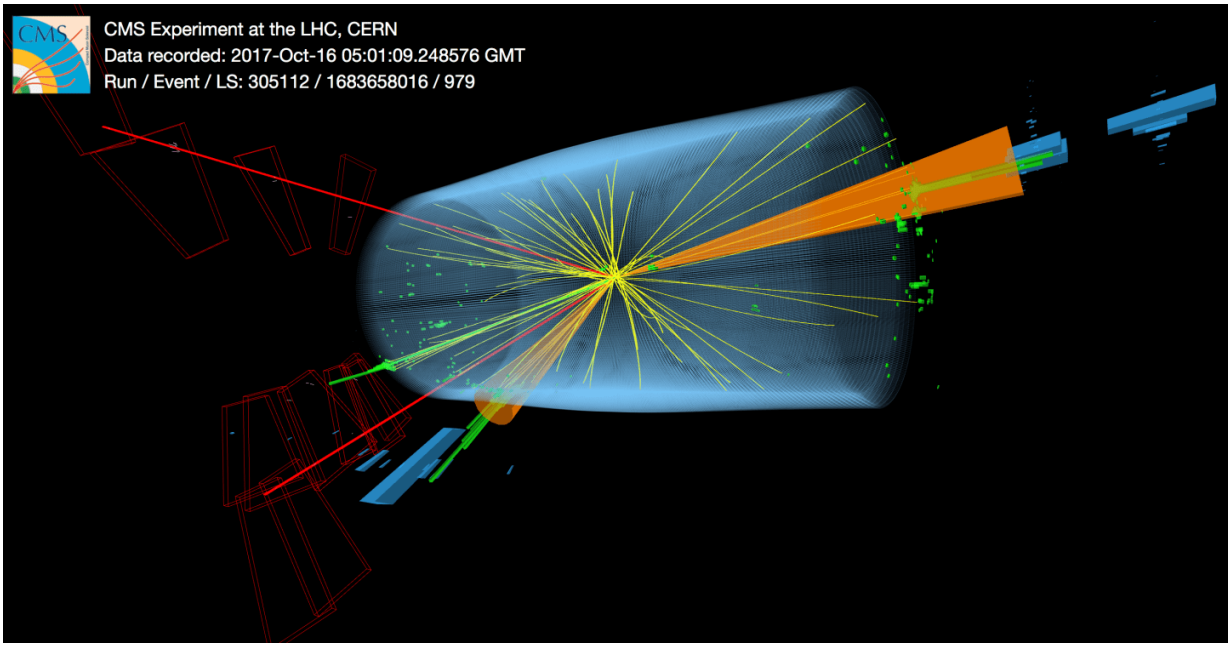

Fig. 4.2.: Event display of a typical tZq candidate in the final state with three leptons recorded by the CMS experiment in 2017. The two red lines indicate the presence of two muons, the isolated green line displays an isolated electron candidate. The two orange cones are jets with relatively high energy. While the jet to the left is more central, the jet to the right is radiated in the forward region of the detector and recoils against all other particles. Green and blue elements illustrate the energy deposits in the ECAL and HCAL systems. The yellow lines show particles identified as coming from pileup events.

shown in Fig. 4.3 on the left. Here prompt means that the leptons come from either the hard interaction, leptonic top quark decays, or from the decay of τ leptons, photons, or W, Z, or H bosons from the hard interaction. It is used opposed to nonprompt as discussed in Section 2.4.3. The $t\bar{t}Z$ production which has a slightly larger inclusive cross section also has a somewhat larger branching ratio to three leptons, since each of the two top quarks can decay leptonically. The branching ratios of $t\bar{t}Z$ are shown in Fig. 4.3 on the right.

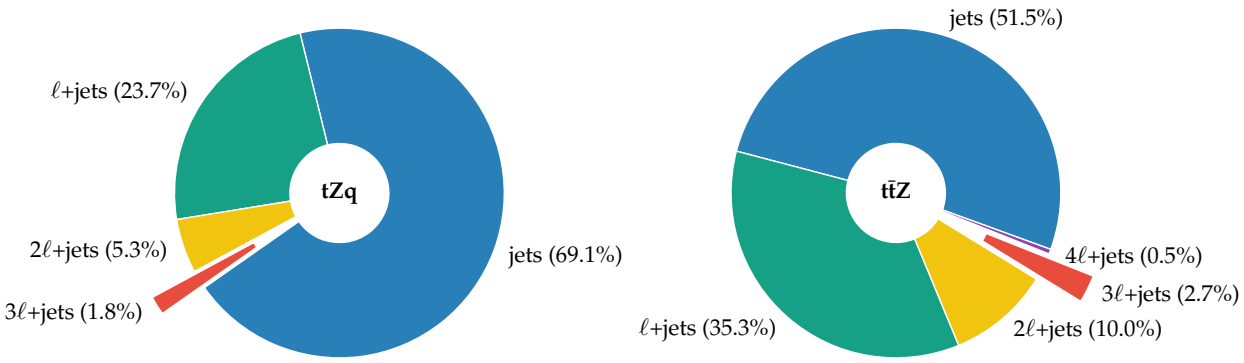

Fig. 4.3.: Frequency of the different final states of the tZq (left) and $t\bar{t}Z$ production. The lepton ℓ denotes electrons and muons and includes those from intermediate τ leptons

4.1.1. Previous measurements

The first measurement of tZq was performed using LHC Run 1 data at $\sqrt{s} = 8\,\text{TeV}$ recorded with the CMS experiment corresponding to an integrated luminosity of $\mathcal{L} = 19.7\,\text{fb}^{-1}$. A significance of 2.4 standard deviations was observed [170]. Later on, the first measurements at $\sqrt{s} = 13\,\text{TeV}$ using partial data from the LHC Run 2 corresponding to $\mathcal{L} = 36.1\,\text{fb}^{-1}$ and $\mathcal{L} = 35.9\,\text{fb}^{-1}$ led to the evidence by the CMS and ATLAS Collaborations with observed significances of 3.7 and 4.2 standard deviations, respectively [171, 172].

The tZq process was first observed by CMS in 2019 [136]. The measurement presented in this thesis follows in many parts the strategy used in this paper. Strengths were identified and weaknesses improved. In the observation, data corresponding to $\mathcal{L} = 77.4\,\text{fb}^{-1}$ was used. The tZq cross section was measured to be $111 \pm 13\,(\text{stat})^{+11}_{-9}\,(\text{syst})\,\text{fb}$ corresponding to a precision of about 15%. The analysis implemented a multivariate identifier to discriminate prompt from nonprompt leptons, following the strategy discussed in Section 2.4.3. Background processes with nonprompt leptons that are wrongly identified as prompt leptons are estimated using control samples in data. The so-called "fake factor" method is used where a weight is assigned to each event from this control sample. The weight is the probability that at least one of the leptons in the event is misidentified, given by the per lepton misidentification probabilities. Despite the improved estimation, the normalization of the background with nonprompt leptons was the dominant systematic uncertainty. Finally, a BDT was trained to discriminate tZq events from backgrounds in three different signal enriched regions (SRs), defined by the number of jets (N_j) and identified b jets (N_b) in the event. A binned maximum likelihood fit was then performed to extract the signal using multiple CRs enriched in events from background processes.

In 2020, the ATLAS Collaboration measured the tZq inclusive cross section as $97 \pm 13\,(\text{stat}) \pm 7\,(\text{syst})\,\text{fb}$ with a similar precision as that of Ref. [136] using the full Run 2 data of $\mathcal{L} = 139\,\text{fb}^{-1}$ [173]. Processes with nonprompt leptons are estimated from simulation while a dedicated method is exploited to enrich the simulated samples further with nonprompt leptons. A dedicated CR for processes with nonprompt leptons is constructed to constrain the normalization uncertainty related to this background. The tZq signal is separated from backgrounds using a NN classifier in two different SRs. The result is limited by the statistical uncertainty. Leading systematic uncertainties are related to the normalization of backgrounds with prompt leptons such as WZ, $\text{t}\bar{\text{t}}\text{Z}$, and ZZ.

A measurement of tZq in the final state with two leptons has recently been attempted [174]. The analysis is extremely challenging due to the overwhelming contributions from DY and $\text{t}\bar{\text{t}}$. Despite the application of complex machine learning algorithms, only low sensitivity was obtained compared to measurements in the trilepton channel.

4.2. Statistical model

The measurements in this analysis are performed using maximum likelihood fits of data to predictions binned in histograms. A similar procedure is used for the Z boson rate measurement discussed in Section 3.3. The predictions include efficiency and acceptance

effects and are modeled from simulated MC events or using control samples from data. Events from each simulated sample are normalized to their expected contribution by scaling them with weights

$$w_i = \frac{\mathcal{L}\sigma}{\sum_j^{N_{\text{Gen}}} w_j^{\text{Gen}}} w_i^{\text{Gen}} \sum_k^{N_{\text{Exp}}} w_{i,k}^{\text{Exp}} \,, \tag{4.1}$$

where $\mathcal{L}$ is the integrated luminosity of the data to which the sample is compared, and σ is the cross section from theory for the considered process. Each event is weighted with its generator weight w_i^{Gen}, which is 1 for samples generated at LO but can be different for other samples as discussed in Section 2.3.1. The generator weights are summed up where N_{Gen} is the total number of simulated events in the considered sample. To correct for differences between data and simulation, experimental calibrations are applied. Additional event weights $w_{i,k}^{\text{Exp}}$ are multiplied, where N_{Exp} is the number of such calibrations.

For the inclusive cross section measurement, the so-called signal strength is determined. It is defined as $\mu = \sigma_{\text{tZq}}/\sigma_{\text{tZq}}^{\text{SM}}$. To better constrain the signal contribution, the maximum likelihood fit is performed in several bins. The expected number of events in each bin, λ_i, is constructed from the signal and multiple (N) background processes,

$$\lambda_i\left(\mu, \boldsymbol{\Theta}\right) = \mu s_i(\boldsymbol{\Theta}) + \sum_j^N b_{i,j}(\boldsymbol{\Theta}) \,. \tag{4.2}$$

The contribution of tZq and various background processes in the i^{th} bin of the measurement are given by $s_i(\boldsymbol{\Theta})$ and $b_{i,j}(\boldsymbol{\Theta})$, respectively. A set of nuisance parameters $\boldsymbol{\Theta}$ are associated to the systematic uncertainties of the simulation. Each parameter Θ describes a shift in the prediction when varying it within the corresponding systematic uncertainty. The list of parameters comprises sources from the normalization of background processes, theory predictions, and experimentally determined quantities. For each source of uncertainty that affects the shape of a distribution, i.e. has a different effect on different bins, two alternative histograms are generated where the underlying source is varied by $\pm 1\sigma$, indicating the "up" and "down" variations. An interpolation between the nominal template and its variations is performed bin-by-bin to obtain a continuous dependency on $\boldsymbol{\Theta}$.

In the likelihood, the bin-by-bin Poisson probabilities are extended by Gaussian constraints taking into account prior knowledge about the nuisance parameters [175]:

$$L\left(\boldsymbol{k}; \mu, \boldsymbol{\Theta}\right) = \prod_{i=1}^{B} \frac{\lambda_i\left(\mu, \boldsymbol{\Theta}\right)^{k_i} \mathrm{e}^{-\lambda_i(\mu,\boldsymbol{\Theta})}}{k_i!} \prod_{j=1}^{P} e^{-\frac{1}{2}(\Theta_j - \Theta_{0j})^2/(\Delta\Theta)^2} \,, \tag{4.3}$$

where P is the number of nuisance parameters. The constant values Θ_{0j} and $\Delta\Theta_j$ are the initial estimate and prior uncertainty of the j^{th} nuisance parameter, respectively. The vector $\boldsymbol{k} = k_1, \ldots k_B$ contains again the numbers of observed entries in B bins.

The negative log likelihood (NLL) is minimized to obtain the signal strength $\hat{\mu}$ and nuisance parameters $\hat{\boldsymbol{\Theta}}$ that best describe the data. To estimate the uncertainties in $\hat{\mu}$, the

NLL is first made independent of the nuisance parameters in a process called "profiling". For different but fixed values of μ, the NLL is minimized by finding the best values of the nuisance parameters. Each nuisance parameter is then expressed as a function of the signal strength, $\hat{\boldsymbol{\Theta}}(\mu)$. Subtracting the value of the NLL at its global minimum and multiplying by two, yields the profile likelihood ratio

$$-2\Delta \ln L(\mu) = -2 \ln \frac{L\left(\mu; \hat{\boldsymbol{\Theta}}(\mu)\right)}{L\left(\hat{\mu}; \hat{\boldsymbol{\Theta}}\right)} \,. \tag{4.4}$$

This is a useful quantity since, according to the Wilks' theorem, for a sufficiently large data sample, the profile likelihood ratio is approximately χ^2 distributed [176]. Thus the 68% confidence interval can be obtained from the points where $-2\Delta \ln L(\mu) = 1$.

To test the method, an "Asimov" toy data set is used. This describes data generated as expected from the prediction by setting all parameters to their initial value. In each bin, exactly the expected number of events is generated. By construction, best fit values of the nuisance parameters and signal strength are at their initial values. Asimov toy data allows to check the validity of the model and to evaluate the expected uncertainties in the final result.

The measurements are performed using the HiggsCombine framework that was originally developed by the Higgs physics analysis group within the CMS Collaboration [177]. The framework is based on RooFit and performs the minimization of the NLL using the MINUIT package [161, 162].

4.3. Samples, event selection and reconstruction

For the measurements documented in this thesis, data from the LHC Run 2 recorded by the CMS experiment in the years 2016 to 2018 are used. The data corresponds to an integrated luminosity of $\mathcal{L} = 138\,\text{fb}^{-1}$ of pp collision data at $\sqrt{s} = 13\,\text{TeV}$. With an assumed cross section of 84.0 fb [69] in the final state with two leptons (including τ leptons) and a branching ratios into three prompt leptons of about 18% (including τ leptons only if they decay into electrons or muons), about 2 000 tZq events can be expected. Under the condition that the background contribution is understood well enough, this is a reasonable amount to perform first differential measurements. But the results will be dominated by the statistical uncertainty. For this reason, the analysis strategy is to maximize the identification efficiency of all involved objects, while keeping the misidentification rates at a manageable level.

4.3.1. Trigger selection and data sets

As described in Section 2.2.6, during data taking only events accepted by at least one of the active HLT paths are stored. To obtain a high efficiency in the HLT selection, a combination of single lepton, double lepton, and triple lepton as well as photon triggers is used. Besides HLT paths that require isolated leptons, also paths requiring nonisolated lepton and photon paths are included to improve the selection efficiency for leptons with high p_T. Since the running conditions have changed during data taking, there are

small differences in the HLT selections between the years. For each year, the HLT paths with the lowest p_T thresholds that are not prescaled are taken. The p_T thresholds for the isolated and nonisolated single muon HLT are at 24 GeV and 50 GeV for most of the data, respectively. For electrons, the thresholds are 25–32 GeV for a tight identification and 105–115 GeV for electrons triggered by the ECAL with a looser selection. Additional photon triggers are included to improve the efficiency for electrons with high p_T. Double-lepton HLTs have thresholds, depending on the lepton flavor and identification algorithm, of typically 17–23 GeV and 8–12 GeV for the leading and subleading lepton, respectively. Events are selected by triple-lepton HLT paths with even lower p_T thresholds of 9–16 GeV, 5–12 GeV, and 5–9 GeV for the three leptons. The complete set of trigger paths used in each year of data taking is summarized in Appendix B.

Depending on the accepted HLT paths of an event, a logic is implemented to select the event from either of the different primary data sets to avoid double counting. Only events for which the CMS detector was known to be fully operational are selected.

4.3.2. Simulated samples

Two sets of tZq signal samples are generated, one in the 4FS and one in the 5FS. Both are generated at NLO in the strong coupling constant α_S (with $\alpha_S = 0.118$) using the MadGraph5_aMC@NLO v5.2 matrix element generator [101, 104]. The top quark is treated as resonant particle assuming a mass of 172.5 GeV and its decay is modeled subsequently. Both, in the production and decay, the CKM-matrix element V_{tb} is assumed to be 1. This means that no W-t-s or W-t-d vertices appear in simulation. The emerging matrix-element particles are interfaced to pythia v8.2 [109] for the parton shower modeling as discussed in Section 2.3.1. Nonresonant dilepton pairs are included in the simulation as well as Z/γ^* interference. The parton shower also includes QED effects, i.e. ISR and FSR of photons. The predicted cross sections are

$$\sigma_{tZq}^{4FS} = 73.6 \pm 6.2 \pm 0.4\,\text{fb} \quad \text{and} \quad \sigma_{tZq}^{5FS} = 94.2^{+1.9}_{-1.8} \pm 2.5\,\text{fb}\,, \tag{4.5}$$

with the first and second uncertainty coming from QCD scale and PDF variations, respectively. In the simulation, the QCD scales were set to $\mu_R = \mu_F = H_T/2$. For this reason, the difference of the inclusive cross section between the 4FS and 5FS is larger than in the optimized settings used in Ref. [69] and presented in Table 1.2. For reasons mentioned in Section 1.4, events simulated in the 4FS sample are used in the following studies to describe the data and perform the measurements. However, the cross section in the 5FS is taken for the normalization of the sample.

The dominant background processes (WZ, ZZ, $t\bar{t}Z$, $Z\gamma$, etc.) are generated at NLO in α_S while for ZZ also gg initiated production is included that only appears at NNLO but has a significant contribution. Additional processes with small contributions are generated at LO. A summary of all simulated samples and their settings is given in Table 4.1.

4.3.3. Object selection

After trigger selection, further selection criteria for leptons and jets are applied to the offline reprocessed data.

Table 4.1.: Summary of configurations of simulated samples where V includes W and Z bosons. For samples where the settings are different between the years, the settings for 2016 are given first while the ones used in 2017/18 are given in brackets.

Process	Event generator	Perturbative QCD order	Tune	NNPDF version
tZq, $t\bar{t}Z$ $Z\gamma$, $t\bar{t}W$, $t\bar{t}t\bar{t}$	MadGraph5_aMC@NLO v2.4.2	NLO	CP5	3.1 NNLO
$t\bar{t}\gamma$	MadGraph	LO	CP5	3.1 NNLO
WZ, VVV, $t\gamma$, $W\gamma$	MadGraph5_aMC@NLO	NLO	CUETP8M1 (CP5)	3.0 NLO (3.1 NNLO)
$q\bar{q} \to ZZ$	powheg v2	NLO	CUETP8M1 (CP5)	3.0 NLO (3.1 NNLO)
$gg \to ZZ$	powheg v2 mcfm v7.0.1 [178] JHUGen v6 (v7.0.11) [179]	LO	CUETP8M1 (CP5)	3.0 LO (3.1 LO)
VH	minlo HVJ [180] JHUGen v7.0.9 (v7.0.11) [179]	NLO	CUETP8M1 (CP5)	3.0 NLO (3.1 NNLO)
$t\bar{t}H$	powheg v2	NLO	CP5	3.1 NLO
$t\bar{t}VH$, $t\bar{t}HH$, $t\bar{t}VV$	MadGraph	LO	CUETP8M2T4 (CP5)	3.0 LO (3.1 NNLO)
tHq, tHW, tWZ	MadGraph	LO	CUETP8M1 (CP5)	3.0 LO (3.1 NNLO)

Leptons

All the three prompt leptons from the tZq final state must be identified. At the same time, the rate to select nonprompt leptons should be at a manageable level. Nonprompt leptons can mimic prompt ones and constitute a challenging background. They are collectively attributed to hadrons or photons misidentified as leptons and leptons from hadron decays or from the conversion of nonprompt photons.

Leptons are selected based on the TOP LeptonMVA identification discussed in Section 2.4.3. The optimal working point for the analysis was studied by scanning different cut values of the TOP LeptonMVA and measuring quantities related to the sensitivity of the measurement. Among those quantities is $N^{\text{sig}}/\sqrt{N^{\text{bkg}}}$ where N^{sig} and N^{bkg} denote the expected yield of tZq and all other processes, respectively. The point where $N^{\text{sig}}/\sqrt{N^{\text{bkg}}}$ is maximum indicates a good choice for the cut value on the TOP LeptonMVA discriminator. Another figure of merit that indicates the optimal cut value at its maximum is the product of efficiency and purity. The purity is defined as $N^{\text{sig}}/(N^{\text{sig}} + N^{\text{bkg}})$ while the efficiency is defined as the fraction of selected tZq events from all tZq events in the final state with three leptons. Only events with $N_{\text{j}} \geq 2$, $N_{\text{b}} \geq 1$, and two leptons with opposite electric charge and same flavor, denoted as OSSF lepton pair, with an invariant mass of $|m_{\ell\ell'} - m_{\text{Z}}| < 15\,\text{GeV}$ are considered. These form the signal region as explained later.

The measured values for these quantities are summarized for electrons in Fig. 4.4. It shows that a looser selection with respect to the last tZq analysis from CMS [136] is preferable. Both, the $N^{\text{sig}}/\sqrt{N^{\text{bkg}}}$ and efficiency times purity have a flat optimum at about 0.14. However, the method to estimate the background processes with nonprompt

leptons is expected to become less reliable with such a loose cut value. Thus, a somewhat tighter cut value of 0.4 was chosen. It can be seen that the changes in the efficiency and purity of the signal between these two values are very small and the two figures of merit remain almost unchanged.

The choice results on average in a selection efficiency of about 95% per lepton. Leptons that pass a looser cut-based identification but fail the TOP LeptonMVA identification are likely to be nonprompt and denoted as "fakeable". These fakeable objects are used to construct a sideband region of data events and estimate the background contribution with nonprompt leptons as explained in more detail in the following section.

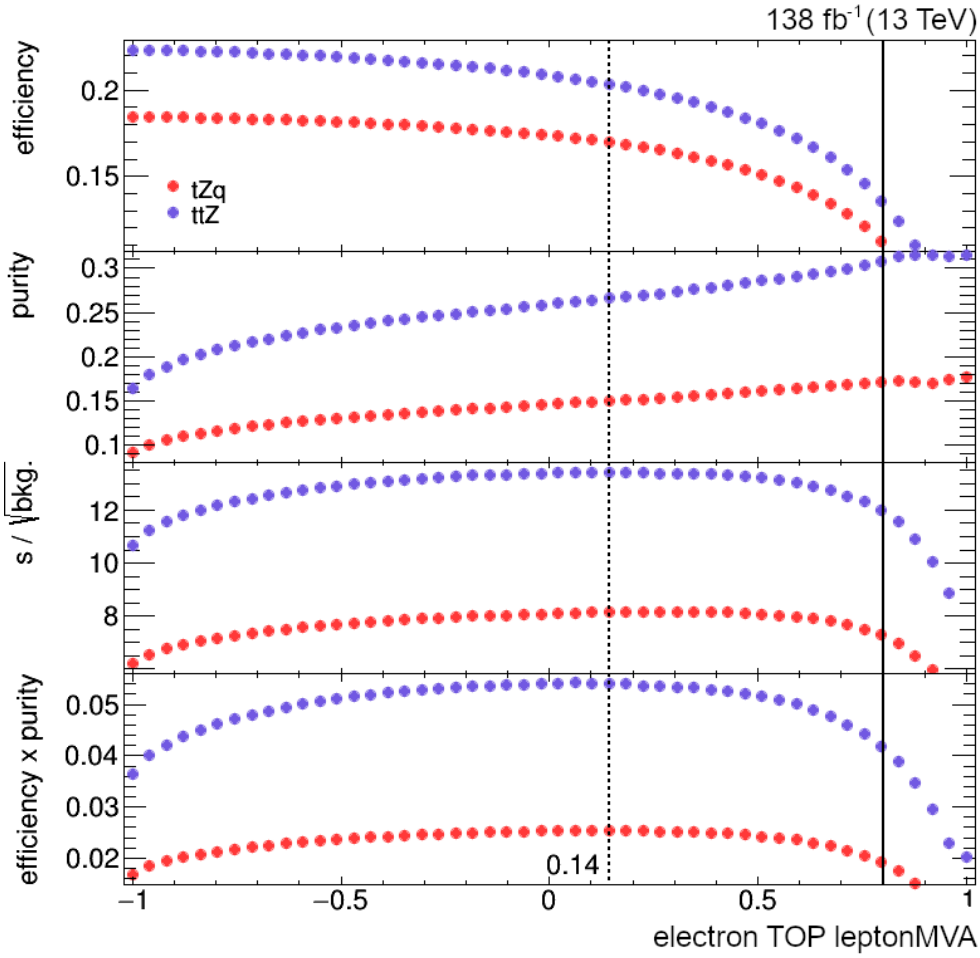

Fig. 4.4.: Event specific quantities for different cut values of the TOP LeptonMVA are shown while considering tZq (red) or $t\bar{t}Z$ (blue) as signal. The two figure of merits, $N^{sig}/\sqrt{N^{bkg}}$ and the product of efficiency and purity have an optimum at 0.14, indicated by the dashed black line. The solid black line at a TOP LeptonMVA value of 0.8 shows a cut value equivalent to the one used in the previous tZq analysis [136].

Jets

Jets are selected if they are reconstructed with the PF algorithm as discussed in Section 2.4.2. They are required to have $p_T > 25\,\text{GeV}$, $|\eta| < 5$, and fulfill loose quality

requirements to reject the majority of misidentified objects while keeping 98% of the jets arising from quarks produced in the main interactions. Jets are further required to be separated by $\Delta R > 0.4$ from the closest selected lepton to avoid counting the same object both as lepton and jet.

Jets with large $|\eta|$ are considered as candidates for the recoiling jet. During 2017, an increased level of noise was present in the ECAL barrel in the range of $2.65 < |\eta| < 3.139$. To mitigate the effect, jets falling in this region are required to have $p_{\mathrm{T}} > 50\,\mathrm{GeV}$. As discussed in Section 2.4.2, the forward region is more contaminated by jets coming from pileup (PU). The PU jet ID is applied for jets with $p_{\mathrm{T}} < 50\,\mathrm{GeV}$. For jets with $|\eta| > 2.5$, about 20% of the jets from PU are rejected while keeping 95% of the quark jets from the hard interaction [125]. The effect of applying the PU jet ID is shown for events with three leptons and at least one jet in Fig. 4.5. In the $|\eta|$ distribution of the most forward jet, it is visible that the PU jet ID also improves the consistency of data and simulation. Significant disagreement still remains in the tail of the distribution. However, further selection criteria are applied before the signal extraction is performed.

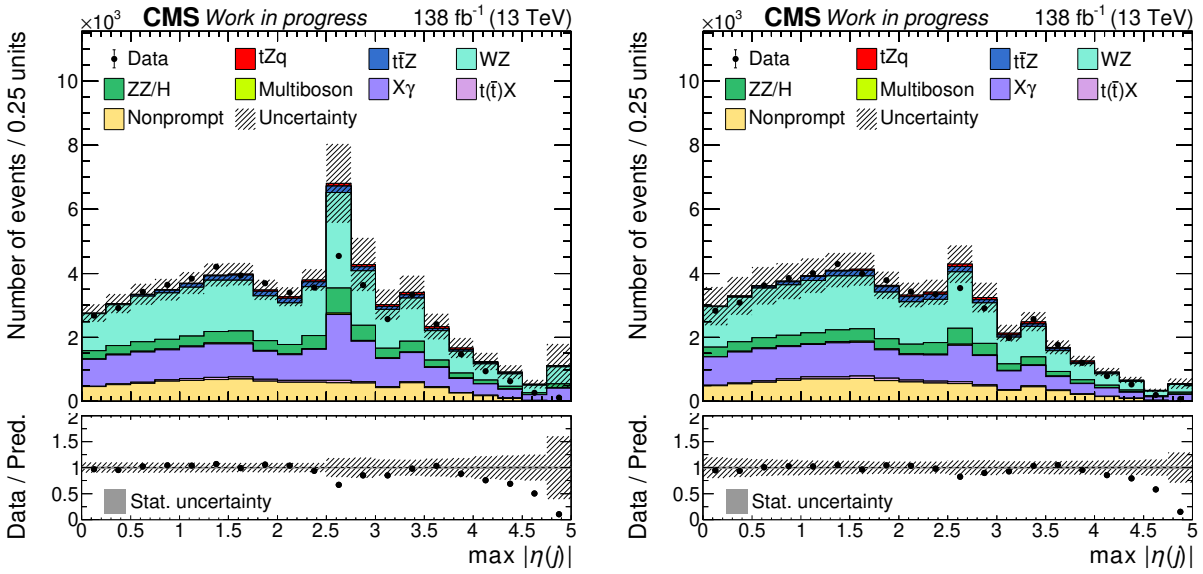

Fig. 4.5.: Number of events as a function of $|\eta|$ of the most forward jets in events with three leptons and at least one jet. Jets are included without (left) and with (right) applying the PU jet ID. The shaded area indicate the total uncertainty on the prediction, the grey area in the ratio indicats its statistical component.

Jets are denoted as "central" if they are reconstructed in the acceptance of the CMS pixel detector, which is within $\eta < 2.4$ for the data taken in 2016 and $\eta < 2.5$ for 2017 and 2018. Central jets are subjected to the DeepJet b-tagging algorithm to identify jets originating from the hadronization of b quarks [129, 130]. Jets from b quarks are selected with an efficiency of about 85%, while the misidentification rate is at the level of 1% for jets from u, d, or s quarks and gluons, and 15% for jets from c quarks.

4.3.4. Event reconstruction

The reconstruction of the Z boson and top quark, and the identification of the recoiling jet are essential at different stages of the analysis. Based on the presence of a Z boson candidate, events are separated in various regions to enrich either signal or background processes. From the reconstructed objects, characteristic features of tZq events can be exploited to calculate discriminant variables as input for the multivariate event classification. Finally, an accurate object reconstruction is needed for the differential cross section measurement of kinematic observables.

Z boson candidates

Two leptons with opposite electric charge and same flavor are denoted as OSSF lepton pair. An OSSF lepton pair is a Z boson candidate if it has an invariant mass with $|m_{\ell\ell'} - m_{\mathrm{Z}}| < 15\,\mathrm{GeV}$ with the mass of the Z boson of $m_{\mathrm{Z}} = 91.188\,\mathrm{GeV}$ [10]. In case of ambiguity, the OSSF lepton pair that minimizes $|m_{\ell\ell'} - m_{\mathrm{Z}}|$ is taken as the Z boson candidate. For events with four leptons, the presence of a second Z boson candidate is checked.

Neutrino

To reconstruct the neutrino momentum vector, a procedure is followed that is often used in single top quark analyses [58]. For events with three leptons and a Z boson candidate, the lepton that is not associated with the Z boson candidate is assigned to a leptonic W boson decay denoted as ℓ_W. The two measured components of the missing energy ($E_{\mathrm{T}}^{\mathrm{miss}}$ and ϕ^{miss}) are associated to those of the neutrino ν. Using the transverse components of ℓ_W and ν, the transverse W boson mass $m_{\mathrm{T}}^{\mathrm{W}}$ can be reconstructed which has a distinctive distribution for events containing a W boson. It is calculated as

$$m_{\mathrm{T}}^{\mathrm{W}} = \sqrt{2\; p_{\mathrm{T},\nu}\; p_{\mathrm{T},\ell_W}\left(1 - \cos\Delta\phi_{\ell_W,\nu}\right)}\,, \tag{4.6}$$

with $\Delta\phi_{\ell_W,\nu}$ being the difference in azimuthal angle between ℓ_W and ν.

In order to find the unknown neutrino $p_{\mathrm{z},\nu}$ component, the invariant mass of the ν-ℓ_W system is set to the W boson mass $m_{\mathrm{W}} = 80.379\,\mathrm{GeV}$ [10]. By neglecting the masses of ν and ℓ_W, this results in a quadratic equation with two solutions

$$p_{\mathrm{z},\nu}^{\pm} = \frac{\Lambda\; p_{\mathrm{z},\ell_W}}{p_{\mathrm{T},\ell_W}^2} \pm \sqrt{\frac{\Lambda^2\; p_{\mathrm{z},\ell_W}^2}{p_{\mathrm{T},\ell_W}^4} - \frac{E_{\ell_W}^2\; p_{\mathrm{T},\nu}^2 - \Lambda^2}{p_{\mathrm{T},\ell_W}^2}}\,, \tag{4.7}$$

where E_{ℓ_W} is the total energy of ℓ_W and

$$\Lambda = \frac{m_{\mathrm{W}}^2}{2} + p_{\mathrm{T},\ell_W}\; p_{\mathrm{T},\nu}\; \cos\left(\Delta\phi_{\ell_W,\nu}\right)\,. \tag{4.8}$$

Two cases can be considered separately for Eq. (4.7). In the first case the term under the square root is negative and no real solution exists. This happens when $m_{\mathrm{T}}^{\mathrm{W}}$ is larger than

m_W, which is unphysical for events that have a leptonically decaying W boson and no other neutrino. In this case one can assume that the E_T^{miss} is measured incorrectly since it is subject to large uncertainties. Hence the $p_{T,\nu}$ is modified as $p_{T,\nu} \to k \cdot p_{T,\nu}$ such that the product under the square root becomes zero. This is equivalent to the constraint $m_T^W = m_W$ and results in

$$k = \frac{m_W^2}{2\, p_{T,\ell_W}\, p_{T,\nu}\, \cos\left(1 - \Delta\phi_{\ell_W,\nu}\right)} \,. \tag{4.9}$$

With the modified $p_{T,\nu}$ exactly one $p_{z,\nu}$ solution exists. Equation (4.7) simplifies to

$$p_{z,\nu} = \frac{\Lambda\, p_{z,\ell_W}}{p_{T,\ell_W}^2} \,. \tag{4.10}$$

In the second case, the product under the square root in Eq. (4.7) is positive and two real solutions for $p_{z,\nu}$ exist.

Figure 4.6 shows a comparison of the reconstructed neutrino p_z component compared to the one of the generator-level neutrino from the top quark decay. Simulated tZq with three prompt leptons have been evaluated. In about one third of all events, exactly one neutrino solution exists. In the other two thirds, events have two solutions where the one with smaller $|p_z|$ usually agrees better with the true distribution. However, always picking the smaller $|p_z|$ solution would result in an underestimation. The choice is made based of the top quark reconstruction as explained next. As shown in Figure 4.6, this choice gives the best agreement with the true distribution.

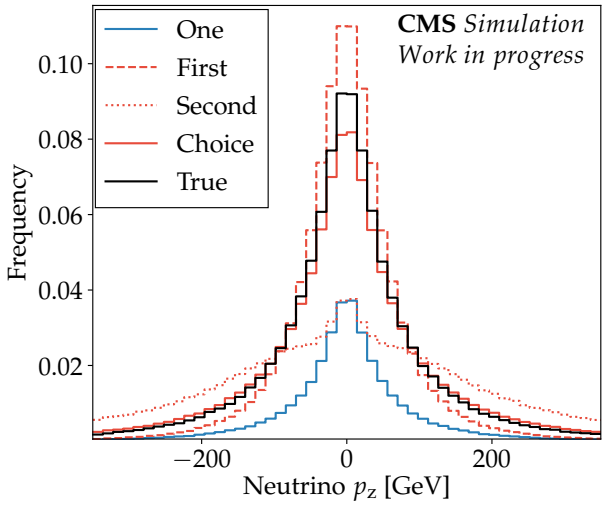

Fig. 4.6.: Distributions of the reconstructed neutrino p_z in simulated tZq events with three prompt leptons. Events with exactly one solution are drawn with a solid blue line. Added on top are those with two solutions. Plotted in dashed red for the solution with smaller $|p_z|$, in dotted red for the one with larger $|p_z|$, and in solid red for the solution chosen based on the top quark reconstruction. The true neutrino p_z distribution is shown with a solid black line.

Top quark candidate

The kinematics of the top quark are reconstructed for events with at least one identified (tagged) b jet. From the lepton and neutrino associated with the leptonically decaying W boson, and b jet, a top quark candidate is formed. If two neutrino solutions or multiple b tagged jets are available, the combination yielding the candidate mass closest to the

top quark mass used in the simulation of $m_t = 172.5\,\text{GeV}$ is taken. The properties of the obtained top quark candidates are investigated in simulated tZq events with three leptons, at least two reconstructed jets from which at least one is b tagged. The top quark candidate η and p_T is compared to the values of the generator-level top quark as shown in Fig. 4.7. Good agreement is obtained with little tension towards a more forward direction and a small underestimation of the p_T of the reconstructed top quark candidate.

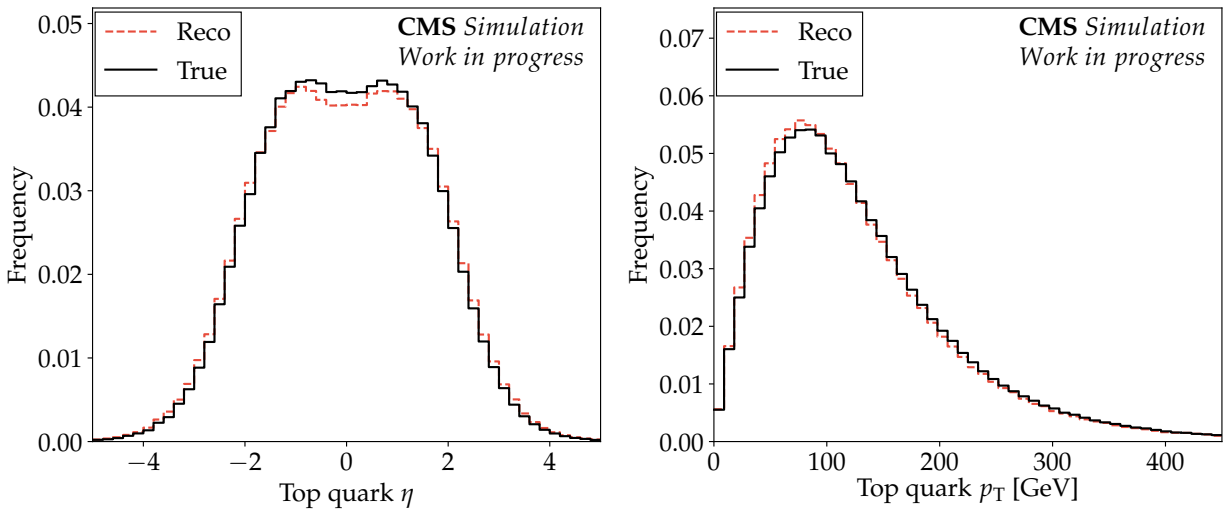

Fig. 4.7.: Distributions of the top quark η (left) and p_T (right) in simulated tZq events with three prompt leptons, at least two reconstructed jets from which at least one is b tagged. The generator-level distribution of the top quark is drawn in a solid black line, while the one obtained from the reconstruction is plotted with a dashed red line.

Recoiling jet

The recoiling jet originates from the spectator quark after emitting the time-like W boson, which leads to a jet with a relatively high p_T spectrum that peaks at about $1/2\,m_W \approx 40\,\text{GeV}$ [68]. From events with at least two jets of which at least one is b tagged, the jet from the recoiling quark is identified. The b jet that is assigned to the top quark candidate is not considered. In events with two jets, the recoiling jet is chosen to be the remaining jet in the event. This is true in about 76% of the cases as estimated from simulation. In the case of three or more jets, the recoiling jet is selected among those that are not b tagged, or, if all jets are b tagged, among all jets. Three approaches were tested to select the recoiling jet in case of ambiguity and the frequency for correct identification is measured in simulation for the jet with maximum p_T, the jet with maximum $|\eta|$, and the jet that maximizes the invariant mass of the system with the top quark candidate. The results are listed in Table 4.2 for different multiplicities of reconstructed jets in the event. For comparison, also the fraction of events in which the recoiling jet has been successfully reconstructed, which is the best possible fraction that can be achieved with either of the methods, is given. Based on this table, the jet with maximum p_T is chosen to assign the candidate for the recoiling jet.

Table 4.2.: Frequency for the correct identification of the recoiling jet based on three different methods. Values are given in bins of the number of reconstructed jets in the event and for the total number of events with at least two jets from which at least one is b tagged (labeled as inclusive). The number of events where the recoiling jet has been successfully reconstructed is given as a benchmark (labeled as reconstructed).

Method	2 jets	3 jets	4 jets	$\geq$5 jets	inclusive
p_{T}	76%	79%	78%	76%	78%
$\lvert\eta\rvert$	76%	64%	49%	35%	60%
invariant mass	76%	73%	68%	64%	71%
reconstructed	77%	91%	94%	95%	88%

4.3.5. Event selection

Events with at least three leptons are selected. To ensure a high trigger efficiency for selected events, the leptons are required to have $p_{\mathrm{T}} > 25/15/10\,\mathrm{GeV}$ for the leading, subleading, and trailing lepton, respectively. Events are rejected if the $E_{\mathrm{T}}^{\mathrm{miss}}$ is found to be incorrectly measured or reconstructed, caused for example by detector noise, poor calibration, or badly-reconstructed objects. Events are also required to have a primary vertex that fulfills basic quality requirements.

Signal selection

To further enrich the sample with tZq events and reject backgrounds, the presence of a Z boson candidate is required. Events satisfying these selection criteria are shown in a histogram binned in N_{j} and N_{b} on the left hand side of Fig. 4.8. Most reconstructed tZq events have at least two jets while in the phase space with zero or one jets, background processes are completely dominant. Also, events without identified b jets show a poor sensitivity to the signal. Hence, as illustrated in the figure, events are required to have at least two jets of which at least one is identified as b jet. The fraction of tZq events with three prompt leptons in this region is about 20% while the purity is less than 13%. To further increase the tZq purity in a signal region denoted as $\mathrm{SR}_{\mathrm{tZq}}$, the number of central jets ($N_{\mathrm{j}}^{\mathrm{central}}$) is required to be less than four. The region with $N_{\mathrm{j}}^{\mathrm{central}} \geq 4$ contains a significant amount of tZq events but is dominated by $\mathrm{t\bar{t}Z}$ events. This region is denoted as $\mathrm{CR}_{\mathrm{t\bar{t}Z}\,3\ell}$ and is used to control the $\mathrm{t\bar{t}Z}$ background. Figure 4.8 shows on the right hand side how well this requirements separates $\mathrm{t\bar{t}Z}$ from tZq events. In this Figure, a noticeable trend of an underprediction is visible for events with a large number of central jets. Expected event yields in the $\mathrm{SR}_{\mathrm{tZq}}$ and $\mathrm{CR}_{\mathrm{t\bar{t}Z}\,3\ell}$ from each process are listed in Table 4.3, with a comparison to the observed data. The fraction of the expected signal contribution in the $\mathrm{SR}_{\mathrm{tZq}}$ is about 16%. A deeper understanding of the individual processes and further isolation of the signal is necessary for a precise measurement of tZq. This will be addressed in upcoming sections.

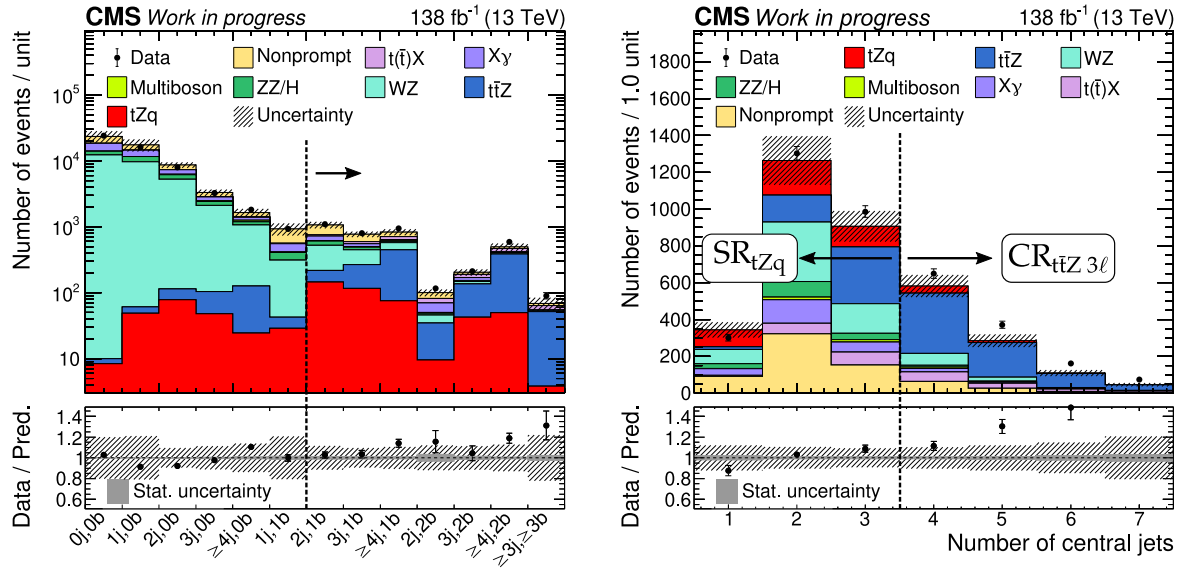

Fig. 4.8.: Left: Distributions of events with three selected leptons, a Z boson candidate in bins of the jet and b tagged jet multiplicities. Events that are further considered for the signal region are required to have at least two jets of which at least one is b tagged. This requirement is illustrated as a dashed line. Right: Events that enter the region SR_{tZq} and $CR_{t\bar{t}Z\,3\ell}$ as a function of the number of central jets. The requirement that defines the SR_{tZq} and $CR_{t\bar{t}Z\,3\ell}$ as illustrated with a dashed line.

Table 4.3.: Expected and observed events in the most signal enriched regions SR_{tZq} and $CR_{t\bar{t}Z\,3\ell}$. Statistical uncertainties in the simulated and observed data samples are given.

Process	SR_{tZq}	$CR_{t\bar{t}Z\,3\ell}$
tZq	391 ± 1	51 ± 1
$t\bar{t}Z$	469 ± 2	623 ± 2
WZ	561 ± 6	94 ± 2
ZZ	144 ± 1	15 ± 0
$X\gamma$	219 ± 8	25 ± 2
$t(\bar{t})X$	134 ± 1	98 ± 1
VVV	28 ± 1	11 ± 1
Nonprompt	566 ± 15	104 ± 7
Expected	2513 ± 18	1022 ± 8
Observed	2590 ± 51	1256 ± 35

4.4. Background processes

Since the SR_{tZq} has large background contributions, the study of various other processes is crucial for this analysis. Mutually exclusive CRs enriched in individual background processes are used to validate the modeling of each background component and constrain related uncertainties in the measurement. The definition of CRs is a tradeoff between two aspects. On one hand, they should be defined in a way that they enrich just one specific background source. On the other hand, the CR should be as similar as possible to the SR_{tZq} to mitigate differences in the respective background contribution between the regions. For instance, CRs can be defined without N_j requirements. However, since the modeling of jets is subject to large uncertainties, the measurement presented in this thesis is limited to events with at least two jets in all regions. The definitions of the SR and various CRs are listed in Table 4.4. Background processes are classified depending on the origin of the selected leptons, as discussed in the following.

Table 4.4.: Summary of the selection requirements that are applied for the SR and CRs used in the tZq measurements. A dash (—) indicates that no requirement is applied to the corresponding variable. Requirements that are given in brackets are imposed together in case the first requirement is not fulfilled.

Variable name	SR_{tZq}	$CR_{t\bar{t}Z\,3\ell}$	$CR_{t\bar{t}Z\,4\ell}$	CR_{WZ}	$CR_{Z\gamma}$	CR_{ZZ}	CR_{NP}
N_ℓ	3	3	4	3	3	4	3
N_b	$\geq$1	$\geq$1	—	0	—	—	1
N_j	$\geq$2	$\geq$2	$\geq$2	$\geq$2	$\geq$2	$\geq$2	2 or 3
N_j^{central}	$<$4	$\geq$4	—	—	—	—	—
E_T^{miss} / GeV	—	—	—	$>$50	—	—	—
$\lvert m(3\ell) - m_Z\rvert$ / GeV	—	—	—	—	$<$15	—	$>$15
OSSF lepton pairs	1	1	1(2)	1	1	2	0(1)
1. $\lvert m_{\ell\ell'} - m_Z\rvert$ / GeV	$<$15	$<$15	$<$15	$<$15	$>$15	$<$15	—($>$15)
1. $m_{\ell\ell'}$ / GeV	—	—	—	—	$>$35	—	—($>$35)
2. $\lvert m_{\ell\ell'} - m_Z\rvert$ / GeV	—	—	—($>$15)	—	—	$<$15	—

4.4.1. Irreducible background processes

Irreducible backgrounds are from processes that have partially identical final-state particles. They cannot be fully rejected by efficient identification of the leptons and jets and their contribution has to be estimated by other means. Irreducible backgrounds to tZq usually have a well understood signature and are properly modeled by MC event generators. They are usually selected with similar efficiency as for the signal process, hence it is feasible to generate a sufficient amount of events. Therefore, simulated samples are used to describe these processes.

Top quark pair production in association with a Z boson

As discussed earlier, one important source of irreducible background is $t\bar{t}Z$ production where examples of LO Feynman diagrams are:

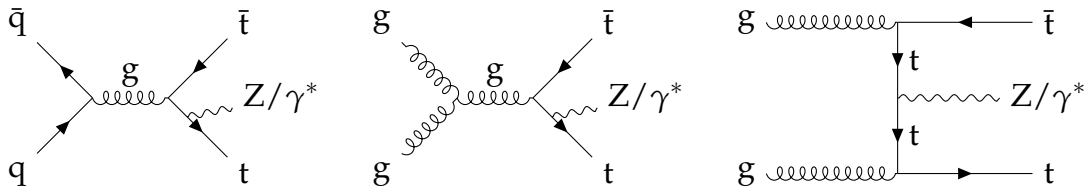

The process has a significant contribution to the three-lepton channel when the Z boson decays into leptons and one top quark decays leptonically while the other one hadronically. Due to the hadronically decaying top quark, $t\bar{t}Z$ events tend to have higher N_j and N_b where jets are primarily radiated in the central detector region. In addition to the $CR_{t\bar{t}Z\,3\ell}$, a second dedicated region is defined to check the modeling and constrain $t\bar{t}Z$ related uncertainties. Denoted as $CR_{t\bar{t}Z\,4\ell}$, this region is constructed from events with four leptons and one Z boson candidate. A veto on any second OSSF lepton pair is applied to reject ZZ events. In the signal extraction, events in this region are binned as a function of N_b where the bin with at least two b tagged jets is very pure in $t\bar{t}Z$ events as shown on the left side in Fig. 4.9. In the latest $t\bar{t}Z$ analysis by CMS, the cross section of this process was measured to a precision of ≈8% [181]. However, a tension towards a higher cross section was observed compared to the theoretical prediction. An underprediction is also visible in Fig. 4.8 for events in $CR_{t\bar{t}Z\,3\ell}$, and in the higher jet and b jet multiplicity bins of Fig. 4.9. In this analysis, the $t\bar{t}Z$ cross section is scaled to the theory prediction and a normalization uncertainty of 15% is assumed to cover a possible deviation.

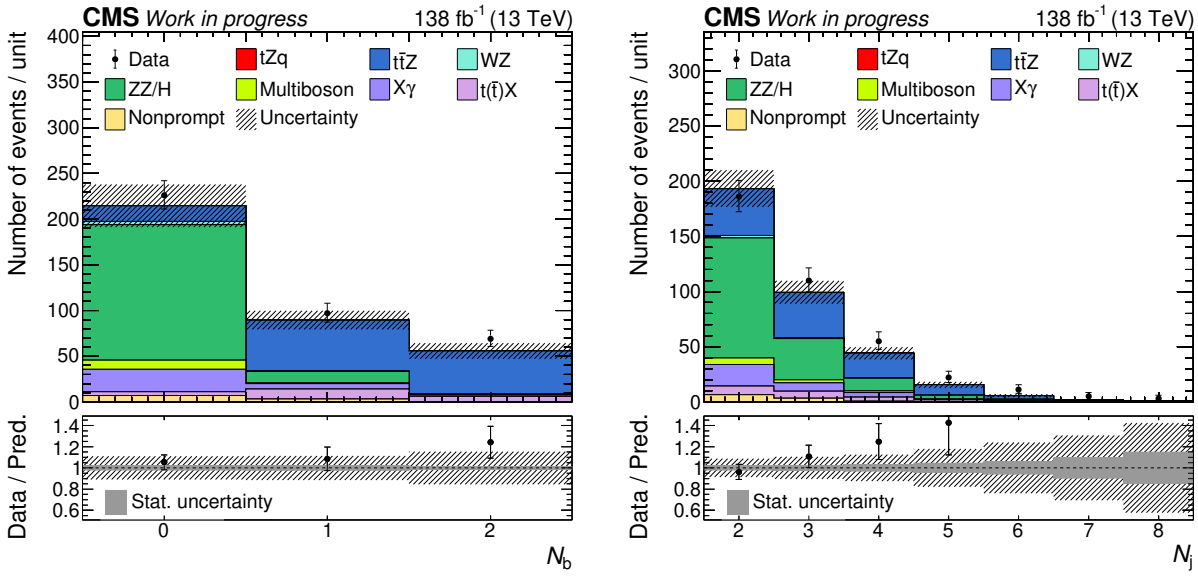

Fig. 4.9.: Events in the $CR_{t\bar{t}Z\,4\ell}$ as a function of the number of b tagged jets (left) and the number of jets (right).

Diboson production

The associated production of two heavy vector bosons, WZ and ZZ, is the dominant background contribution in the SR_{tZq}. It has a large cross section in the final state with three leptons compared to tZq and can mimic signal events via additional QCD radiation. Events can be largely rejected by an effective identification of b quark jets. However, jets from light flavor quarks or gluons can be misidentified as b jets. Moreover, the production with additional b quark jets, for example from gluon splitting, can lead to an irreducible background. Example Feynman diagrams for the WZ and ZZ processes with and without additional b quarks are:

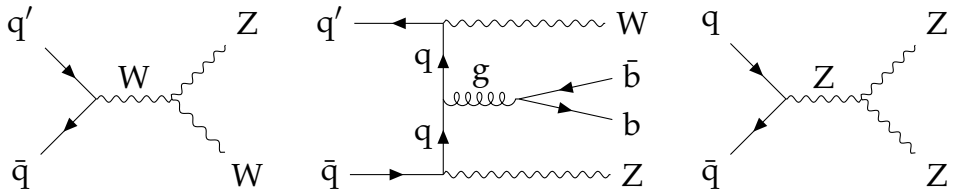

A CR_{WZ} is defined similar to the SR_{tZq} but vetoing any b tagged jet and without requirement on $N_j^{central}$. The purity of WZ events is enhanced by selecting events with $E_T^{miss} > 50\,GeV$. To get further sensitivity on the WZ process, events are binned in values of the m_T^W distribution whose shape is different from other processes, as shown in Fig. 4.10.

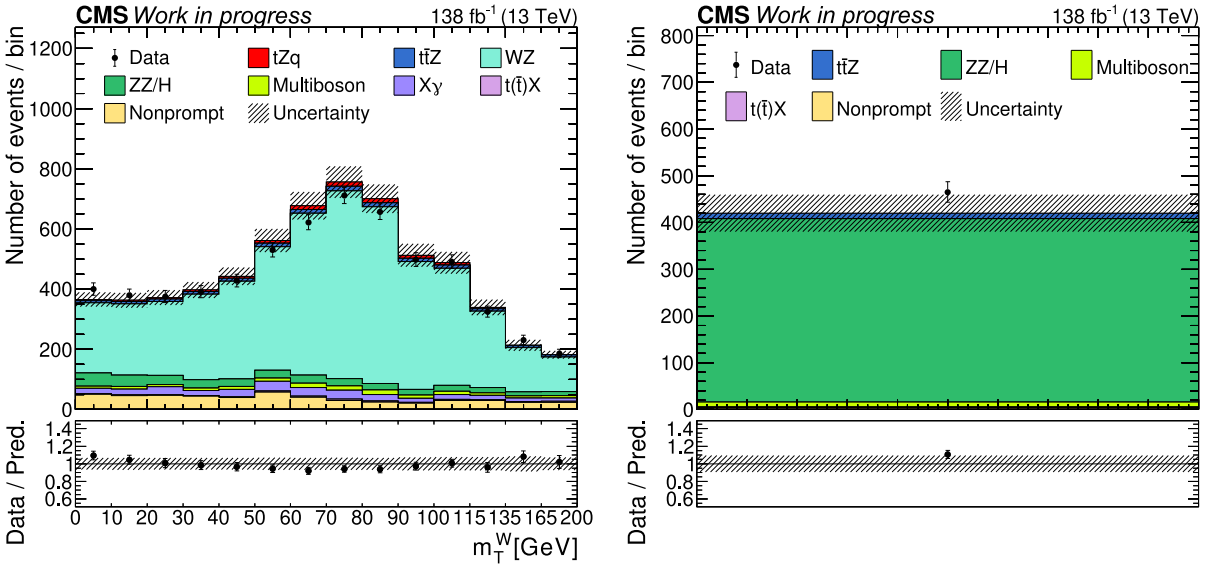

Fig. 4.10.: Events in the CR_{WZ} (left) binned in the m_T^W distribution and the total number of events in the CR_{ZZ} (right).

The simulation of additional b quarks is known to be prone to incorrect modeling. For instance, an underprediction of Z boson production in association with collinear b hadrons was observed during Run 1 [182]. During Run 2, a similar study was performed in the context of the tt̄Z measurement from CMS where no deviation from the prediction

was found within a 20% uncertainty [181]. For this analysis, the flavor content of the additional jets in the simulated WZ sample was measured and compared between SR_{tZq} and CR_{WZ}. In SR_{tZq}, the fraction of WZ events with at least one additional b quark is about 33%, while in CR_{WZ} this fraction is about 3%. Taking the 20% from Ref. [181] as uncertainty on the modeling of additional b quarks results in an extrapolation uncertainty of 6% for the overall WZ simulation in the signal region.

The simultaneous production of two Z bosons (ZZ) can contribute to SR_{tZq} if both Z bosons decay leptonically and one lepton fails the identification or is outside the detector acceptance. A CR_{ZZ} is obtained for events with four leptons and two Z boson candidates. This region was found to be very pure, as shown in Fig. 4.10. In the signal extraction, CR_{ZZ} is included with a single bin containing the total number of events in this region.

The high purity of the CRs allows to estimate the normalization of the WZ and ZZ backgrounds directly from the data. In the signal extraction, free-floating parameters are assigned to scale each contribution. This way, fewer assumptions are made and biases from possible limitations of the simulations in the phase space of the analysis are mitigated.

Rare processes

The production of three massive electroweak bosons (VVV) is a minor contribution and labeled in the plots as "Multiboson". Since this process was observed and agrees well with the prediction, a normalization uncertainty of 25% is assumed [183].

Further rare backgrounds containing top quarks but no photons are collectively denoted as $t(\bar{t})X$. Among them contributing the most is tWZ production followed by $t\bar{t}W$ and $t\bar{t}H$ production. Minor contribution from $t\bar{t}t\bar{t}$, tHq, tHW, $t\bar{t}WZ$, $t\bar{t}ZZ$, $t\bar{t}WW$, $t\bar{t}WH$, $t\bar{t}ZH$, and $t\bar{t}HH$ production are included as well. An uncertainty of 40% is assigned to the normalization of this group of backgrounds. This is comprised of a 25% uncertainty for $t\bar{t}W$ and $t\bar{t}H$ production, which has already been observed [184, 185], and a 50% uncertainty for the other processes in this category which are all yet undiscovered.

4.4.2. Processes with photons

Photons can convert into an electron-positron pair either solely by a virtual photon, or when photons interact with the detector material. The conversion can be very asymmetric in p_T such that one lepton has high enough p_T to pass the selection requirements, while the other one remains undetected. Processes contributing this way are mainly $Z\gamma$ with minor contributions from $t\bar{t}\gamma$, $W\gamma$, and $t\gamma$. They are summarized as $X\gamma$ and can be suppressed by a performant lepton identification. Nevertheless, significant contributions remain and need careful study.

Simulated samples are used to describe $X\gamma$ processes. To study the modeling of photon conversions, a $CR_{Z\gamma}$ is constructed by selecting events with three leptons and an OSSF lepton pair that is incompatible with a Z boson candidate. Instead, the invariant mass of the three leptons is required to be compatible with the Z boson mass within $\pm 15\,\text{GeV}$. This way, mainly $Z\gamma$ events with a photon coming from FSR are enriched. Since the prediction shows good agreement with the data in the $CR_{Z\gamma}$, the use of simulated samples is justified.

In the signal extraction, events in the $CR_{Z\gamma}$ are used in two bins, depending on whether or not they have an even number of muons as shown on the left in Fig. 4.11.

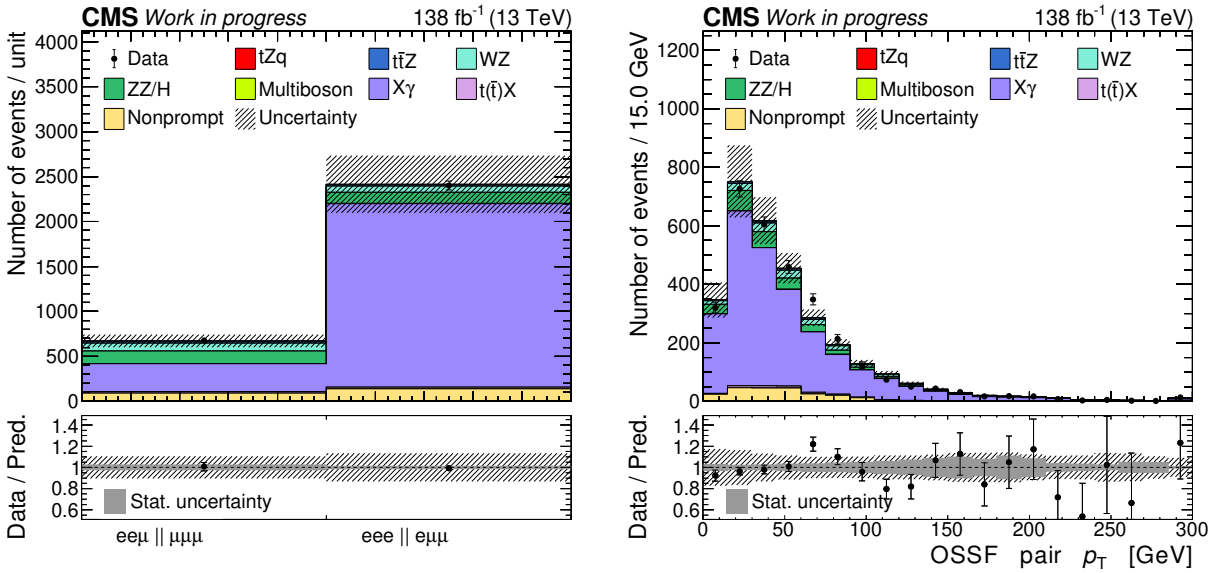

Fig. 4.11.: Events in the $CR_{Z\gamma}$ in two bins with even or odd number of muons (left) and as a function of the p_T of the OSSF lepton pair (right).

4.4.3. Processes with nonprompt leptons

A further class of backgrounds comes from processes with at least one nonprompt lepton and is shortly denoted as "nonprompt background". These can be well suppressed by the prompt lepton identification, hence they are termed reducible backgrounds. However, a finite likelihood to misidentify nonprompt leptons remains. Processes that contribute this way are mainly $t\bar{t}$ and DY, because of their large cross sections, which are orders of magnitude larger than tZq. Due to the looser working point of the TOP LeptonMVA, the nonprompt-background contribution is increased with respect to the earlier CMS analysis [136]. This makes it all the more important to understand and describe these processes precisely.

The fraction of $t\bar{t}$ and DY events passing the signal selection is overall very low. Modeling this background from simulation would hence require a unfeasible high number of events to achieve sufficient statistical precision. Moreover, because of imperfect simulation, the modeling of nonprompt leptons is unreliable. Instead, the nonprompt background is estimated using control samples from data with the fake factor method that has already been used in previous analyses in a similar way [186, 187].

Fake factor measurement

The nonprompt background is estimated by reweighting data events from a sideband region, the so-called application region (AR). The event weights depend on the fake factor f, which is the probability for a nonprompt lepton that passes the fakeable selection

criteria to also pass the TOP LeptonMVA identification. The values for f are extracted from data in a dedicated measurement region (MR) as explained later in this section. The method is illustrated in Fig. 4.12.

The AR is defined with identical cuts as the SR, but the leptons only have to fulfill the fakeable selection criteria instead of the TOP LeptonMVA identification. In addition, at least one of the leptons has to fail the TOP LeptonMVA identification to ensure that the AR does not overlap with the SR. The weights applied to the events in the AR depend on the number of leptons passing the fakeable selection criteria but failing the TOP LeptonMVA criteria as follows:

$$w(\ell_1^{\text{fake}}, \ell_2^{\text{fake}}, \dots \ell_n^{\text{fake}}) = (-1)^{n-1} \cdot \prod_{i=1}^{n} \frac{f(\ell_i^{\text{fake}})}{1 - f(\ell_i^{\text{fake}})} \,, \tag{4.11}$$

where ℓ_i^{fake} is the i^{th} lepton that fails the TOP LeptonMVA identification. While the nonprompt background corresponds to processes containing fewer prompt leptons than required, processes that have the required number of prompt leptons may still represent a small contribution to the AR due to the imperfect efficiency of the TOP LeptonMVA identification. These processes are estimated from simulation and subtracted from the data in the AR.

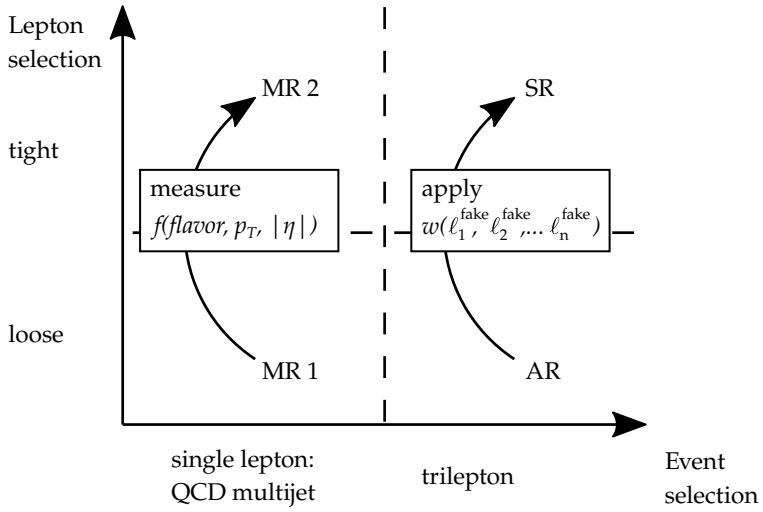

Fig. 4.12.: Illustration of the fake factor method. The fake factor f is measured as a function of p_{T} and $|\eta|$ for electrons and muons separately in a QCD multijet enriched measurement region (MR). It is given by the ratio of QCD events with exactly one lepton that passes the TOP LeptonMVA identification (tight) to the number of events with one fakeable lepton (loose), corresponding to MR2 and MR 1, respectively. The measured f is used to compute weights w to predict the events with nonprompt leptons in the signal region (SR) from the events in the application region (AR). The w depend on f of all leptons ℓ_i^{fake} in an event that pass the fakeable (loose) and fail the TOP LeptonMVA (tight) selection.

Cone correction

The object that fakes the lepton usually originates from a parton. Using the p_{T} of this parton instead of the one from the reconstructed lepton reduces the dependence on the object that fakes the lepton and improves the modeling of the nonprompt background. Therefore, a so-called transverse "cone" momentum, $p_{\text{T}}^{\text{cone}}$, is defined as:

$$p_{\text{T}}^{\text{cone}} = \begin{cases} p_{\text{T}} & \text{if lepton passes TOP LeptonMVA identification ,} \\ x \cdot p_{\text{T}}^{\text{Cl.Jet}} & \text{otherwise, if jet within } \Delta R < 0.4 \text{ ,} \\ x \cdot p_{\text{T}} \, (1 + I_{\text{PF}}) & \text{otherwise, if no jet within } \Delta R < 0.4 \text{ ,} \end{cases} \tag{4.12}$$

where $p_{\mathrm{T}}^{\mathrm{Cl.Jet}}$ is the p_{T} of the closest jet that is found within $\Delta R < 0.4$ to the lepton and I_{PF} is the PF isolation with $\Delta R = 0.4$. The value of $x = 0.67$ is chosen to ensure the continuity of $p_{\mathrm{T}}^{\mathrm{cone}}$ as a function of the TOP LeptonMVA discriminant. The fake factor is then parameterized in $p_{\mathrm{T}}^{\mathrm{cone}}$ and $|\eta|$ of the nonprompt lepton.

Closure test in simulation

The composition of the objects leading to nonprompt leptons in the AR and SR is usually different from that in the MR. In the AR and SR, the main processes that contribute to the nonprompt background are $\mathrm{t\bar{t}}$ and DY, which themselves have different parton contents. While in the $\mathrm{t\bar{t}}$ processes several b quarks lead to nonprompt leptons from heavy-flavor hadron decays, DY processes contribute more via light-flavor hadrons that are misidentified as leptons. To mitigate the dependence on the nature of the object that leads to the nonprompt lepton, the definition of the fakeable lepton is adjusted. Additional requirements for the fakeable lepton are studied in closure tests on simulated $\mathrm{t\bar{t}}$ and DY samples. The requirements are chosen such that the estimation of nonprompt backgrounds via the fake factor method in each simulated sample matches the event yields that are expected in the SR from the same simulated sample. These criteria comprise cuts on the DeepJet value of the closest jet and the p_{T} ratio of the lepton to the jet. Distributions from the closure tests for the $p_{\mathrm{T}}^{\mathrm{cone}}$ and $|\eta|$ of the trailing lepton and N_{j} are shown in Fig. 4.13. Good agreement between the predicted and expected contributions for $\mathrm{t\bar{t}}$ and DY simulation is found with the exception of DY simulation where the p_{T} of the trailing lepton is slightly overestimated. As DY contributes much fewer events in the $\mathrm{SR_{tZq}}$, this effect has a minor impact on the final measurement and is covered by the systematic uncertainties.

Measurement region

To measure f in bins of $p_{\mathrm{T}}^{\mathrm{cone}}$ and $|\eta|$, independently of the lepton flavors and each year, a large data sample pure in nonprompt leptons is needed. The MR is chosen to be enriched in QCD processes. Events with exactly one lepton that passes the fakeable selection criteria are selected. Additionally at least one jet is required with $p_{\mathrm{T}} > 25\,\mathrm{GeV}$, $|\eta| < 2.5$, and a separation to the lepton of $\Delta R > 0.7$. Events have to pass at least one of several single lepton+jet HLT paths. Only HLT paths without lepton-isolation requirements are chosen to mitigate any bias from the the trigger selection on the measurement. This is important because in the AR only one lepton has to pass the HLT selection and a bias in the trigger would overestimate the nonprompt background. In addition, requirements are applied on the reconstructed lepton and jet p_{T} individually for each HLT to ensure a plateau-level efficiency. A cut on the lepton $p_{\mathrm{T}}^{\mathrm{cone}}$ is applied to mitigate the bias of this selection on f.

Fake factor extraction

In addition to QCD events, the MR is contaminated with events containing prompt leptons from DY, W+jets, $\mathrm{t\bar{t}}$, WW, WZ, and ZZ production. To measure f for nonprompt

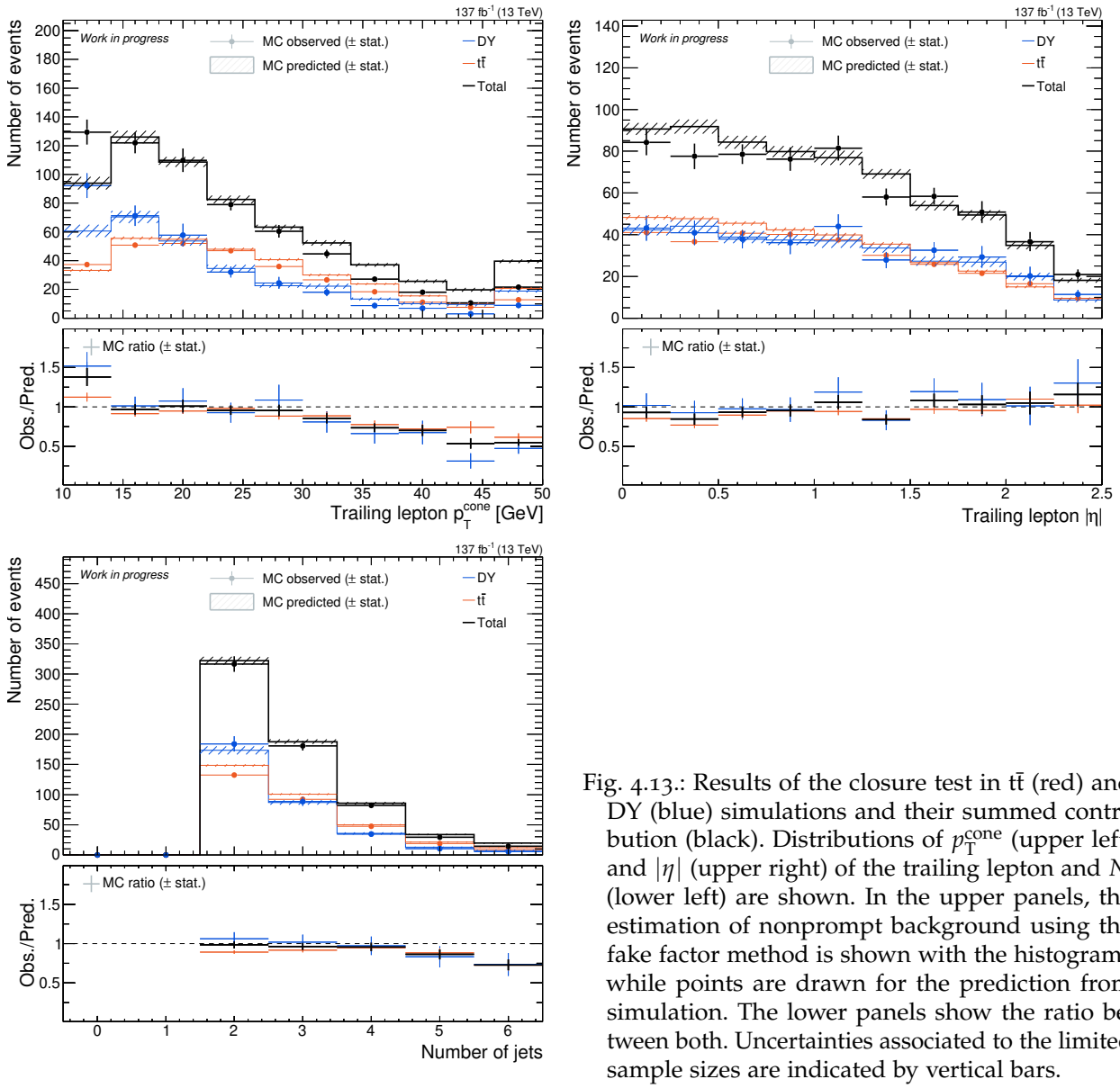

Fig. 4.13.: Results of the closure test in $t\bar{t}$ (red) and DY (blue) simulations and their summed contribution (black). Distributions of p_T^{cone} (upper left) and $|\eta|$ (upper right) of the trailing lepton and N_j (lower left) are shown. In the upper panels, the estimation of nonprompt background using the fake factor method is shown with the histograms while points are drawn for the prediction from simulation. The lower panels show the ratio between both. Uncertainties associated to the limited sample sizes are indicated by vertical bars.

leptons, these processes are taken into account. Data events in the MR are modeled with simulated samples.

In each bin of the measurement of f, events are separated into a pass and a fail category, depending on whether the lepton fulfills the TOP LeptonMVA identification or not. A maximum likelihood fit to templates from simulated samples for prompt and nonprompt contributions is performed simultaneously in both categories. In the fit, f is treated as free-floating parameter, scaling the nonprompt contribution in the fail category by $(1-f)$ and in the pass category by f. To separate prompt from nonprompt contributions, events are fit as function of

$$m_{\mathrm{T}}^{\mathrm{fix}} = \sqrt{2 p_{\mathrm{T}}^{\mathrm{fix}} E_{\mathrm{T}}^{\mathrm{miss}} \left(1 - \cos\Delta\phi\right)}\,, \tag{4.13}$$

which resembles $m_{\mathrm{T}}^{\mathrm{W}}$, but using a fixed value $p_{\mathrm{T}}^{\mathrm{fix}} = 35\,\mathrm{GeV}$ to mitigate the dependence on the lepton p_{T}. Examples of post-fit distributions are shown in Fig. 4.14.

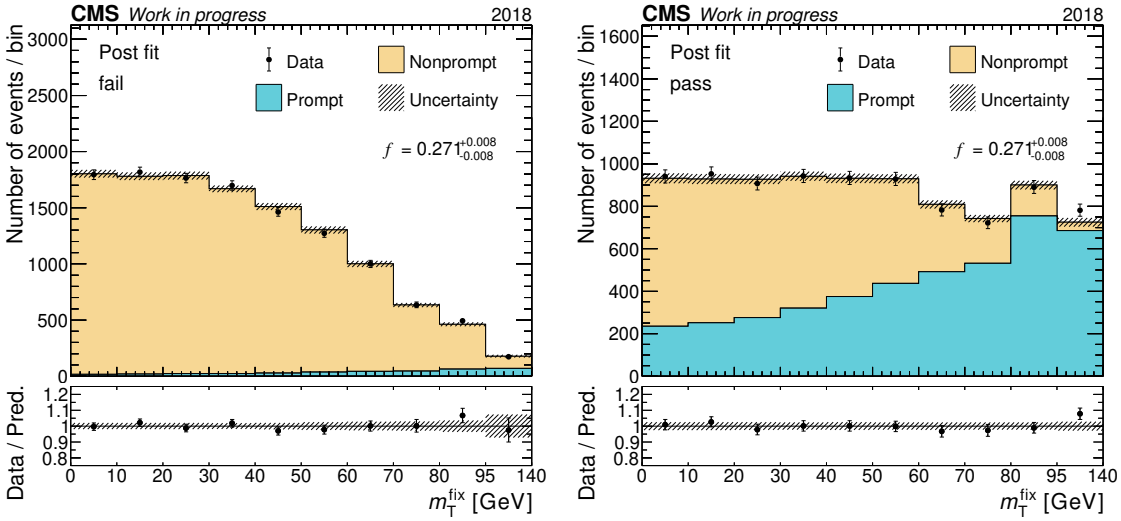

Fig. 4.14.: Post-fit distributions as function of $m_{\mathrm{T}}^{\mathrm{fix}}$ used to extract the fake factor for muons in the barrel region ($|\eta| < 1.2$) with $20\,\mathrm{GeV} < p_{\mathrm{T}}^{\mathrm{cone}} < 32\,\mathrm{GeV}$ for the year 2018. The fit is performed simultaneously for events where the muon passed (right) or failed (left) the TOP LeptonMVA identification.

Control region

To check the validity of the nonprompt background estimation in data, a $\mathrm{CR_{NP}}$ is defined for events with three leptons with the focus on dileptonic $\mathrm{t\bar{t}}$ events. Required are three leptons and two or three jets with at least one b tagged jet. Events with a Z boson candidate or OSSF pair with a low invariant mass are vetoed to ensure orthogonality to the signal region and reject data events not represented in the simulated samples, respectively. Distributions in the $\mathrm{CR_{NP}}$ shown in Fig. 4.15 have good agreement between data and prediction. Nevertheless a conservative normalization uncertainty of 30% is applied based on previous analyses.

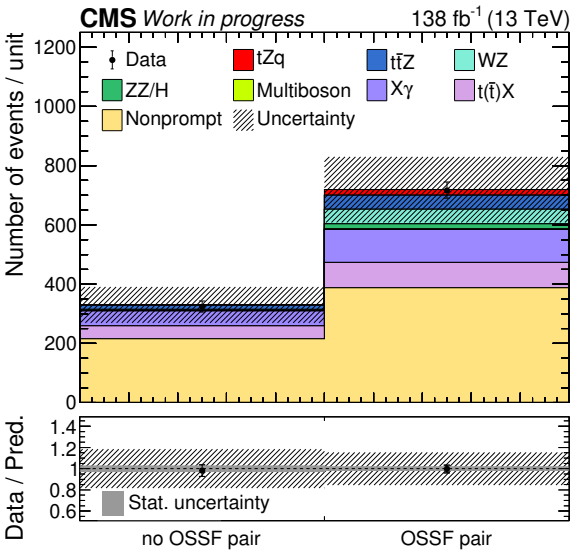

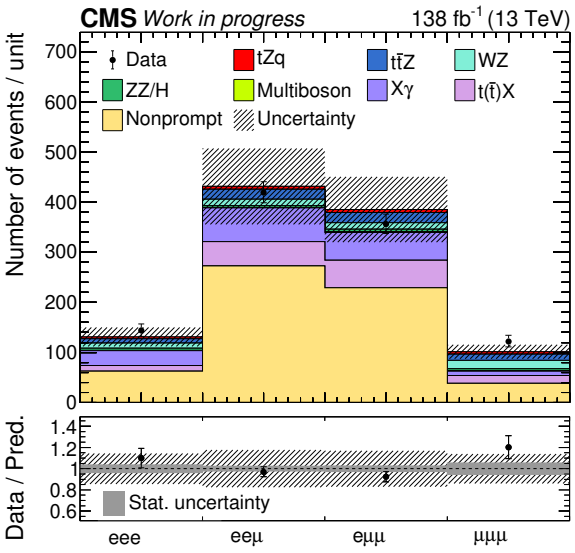

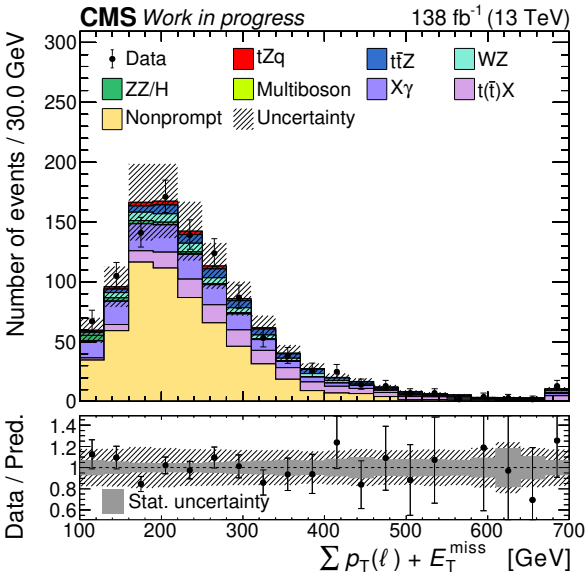

Fig. 4.15.: Events in the CR_{NP} shown in two bins with or without the presence of an OSSF lepton pair (upper left). This histogram is later used in the signal extraction to constrain the normalization uncertainty of the nonprompt background. Events in four bins depending on the number of electrons and muons in the event (upper right) and as a function of the scalar p_T sum of all leptons and E_T^{miss} (bottom left) are shown as cross-check.

4.5. Event classification with a multiclass neural network

To enhance the sensitivity to tZq production, an MVA is performed. Unlike the latest tZq measurement within CMS that was using a BDT [136], it was decided to use a more powerful multiclass neural network (NN) to separate tZq events from background contributions. This allows to achieve a better suppression of background events, which is particularly advantageous for the differential cross section measurements in which the signal has to be isolated in every bin of the measured observable. The algorithm was developed using the Keras [188] interface with the TensorFlow v2 [189] library as the backend.

4.5.1. Multiclass neural networks

In the multiclass NN, the information of various variables, so-called "features" are combined to construct output scores that optimally discriminate between different classes of events. As shown in Fig. 4.16, a NN consists of neurons arranged in layers. It has an input layer, where the values of the features are fed in, followed by intermediate (hidden) layers, and an output layer where the scores for different classes are provided. Each neuron after the input layer multiplies its input values $\boldsymbol{x} = x_1, \dots x_N$ from N neurons of the preceding layer by a set of weights $\boldsymbol{w} = w_1, \dots w_N$, and adds a bias factor b. A nonlinear function, the activation function a, is applied such that an output value is calculated as

$$y = a\left(\sum_i^N x_i w_i + b\right) , \tag{4.14}$$

and propagated to the neurons of the subsequent layer, until the output layer is reached.

The weights and biases are the free parameters of the network and have to be adjusted in a process called training. In the training, a set of samples is used where the class affiliation (label) of each event is known. For each event, the values for the input features are propagated through the NN to calculate the output scores. The output scores are then compared to the labels in a function known as loss function. The loss function gets minimized by computing the gradients of the weights and biases by means of backpropagation. The samples are fed into the NN and the weights and biases are updated in small batches. In this way, the loss function is subject to some statistical fluctuation and converges gradually to a more global minimum. If all batches of one samples are processed, one epoch of training is completed. The samples get shuffled for further epochs, until the loss function reaches its minimum. A more complete description of neural networks and other multivariate analysis techniques is given in Ref. [191, 192].

4.5.2. Choice of input features

To achieve a good classification of the NN, input features are chosen carefully as listed in Table 4.5. Features with a lower level of abstraction are $E_{\mathrm{T}}^{\mathrm{miss}}$, N_{j}, and N_{b}. Those are available without further computation and are found to provide already good separation power. They are supplemented by global event features, computed from jets, leptons, and

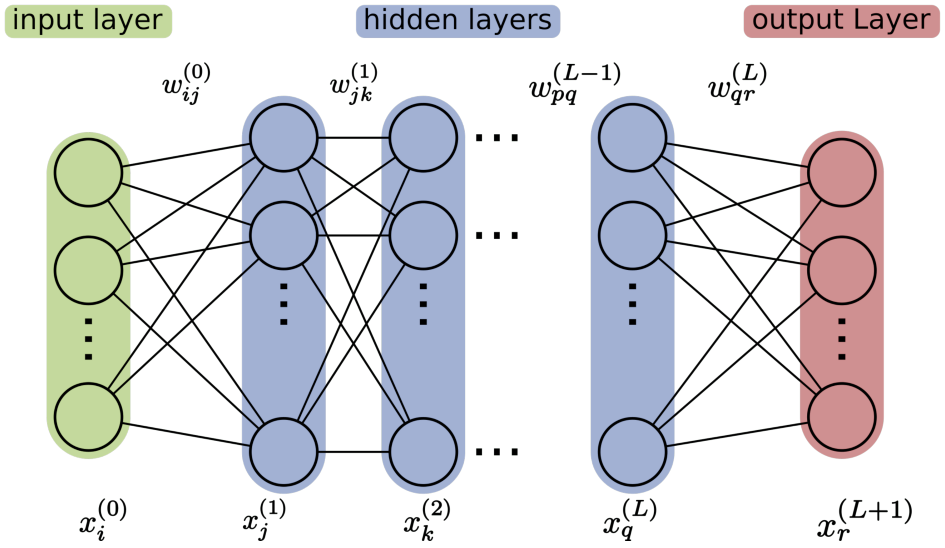

Fig. 4.16.: Illustration of a fully connected feed forward NN with an input layer (green), L hidden layers (purple), and an output layer (red). Neurons are represented by circles connected with lines. Each neuron passes a value x_i to the connected neurons of the next layer. The value gets multiplicated by a weight w_{ij}, where i and j indicate the origin and target neurons, respectively. Additionally, a bias is added (not shown). The weights and biases are the free parameters of the NN. From Ref. [190].

$E_{\mathrm{T}}^{\mathrm{miss}}$ like the scalar p_{T} sum of all jets, $\sum p_{\mathrm{T}}(j)$, or the scalar p_{T} sum of all leptons and $E_{\mathrm{T}}^{\mathrm{miss}}$, $\sum p_{\mathrm{T}}(\ell) + E_{\mathrm{T}}^{\mathrm{miss}}$. These give the strongest separation power as they are highly sensitive to the different event signatures without assuming any particular signature. Global features assuming a signal event signature are based on more physics insight and computed from reconstructed objects like the top quark candidate or the recoiling jet. Those are for example the $|\eta|$ of the recoiling jet, $|\eta(\mathrm{j}')|$, or the mass of the top quark, $m(\mathrm{t})$. They give complementary information and contribute significantly to the classification. The most important features are shown in Fig. 4.17, other features can be found in Figs. C.1 to C.3.

Validation of modeling of input features

The various features can only be used as input to the NN if the predictions describe the data within the uncertainties. Otherwise one would risk that the NN output distributions do not describe the data. To verify the modeling, goodness-of-fit tests are performed based on the profile likelihood ratio as explained in Section 4.2. The likelihood incorporates all systematic uncertainties that are later used in the signal extraction and will be elaborated in more detail in Section 4.7.

First, random data is generated using the predictions and assumed systematic uncertainties, denoted as toy data sample. The toy data is fit and divided by the fit result from the Asimov toy data set, resulting in the profile likelihood ratio χ^2_λ that serves as test statistic. In total, 10 000 toy data samples are generated and a histogram is filled as shown in Fig. 4.18. In analogy, the likelihood is evaluated for the observed data, and the $\chi^2_{\lambda,\mathrm{obs}}$ is calculated, again relative to the Asimov toy data set. The p-value of the test is defined as the number of toy data samples with $\chi^2_\lambda > \chi^2_{\lambda,\mathrm{obs}}$, divided by the total number of toy data samples. A p-value of 1% is chosen as threshold, any feature that yields a value below

Table 4.5.: List of features used in the multiclass NN training sorted by their importance.

Feature	Description
$\sum p_{\mathrm{T}}(j)$	Scalar sum of hadronic transverse momenta
$\max(m(j_1, j_2))$	Maximum invariant mass of any dijet system
$\max(\textsc{DeepJet}(j))$	Maximum DeepJet value of any jet
$\max(p_{\mathrm{T}}(j_1, j_2))$	Largest p_{T} of any dijet system
N_{j}	Number of jets
$\lvert\eta(\mathrm{j}')\rvert$	$\lvert\eta\rvert$ value of the recoiling jet
$\sum p_{\mathrm{T}}(\ell) + E_{\mathrm{T}}^{\mathrm{miss}}$	Scalar sum of leptonic momenta and missing transverse energy
$m(\mathrm{t})$	Top quark candidate mass
$m_{\ell\ell'}$	Z boson candidate mass
$m_{\mathrm{T}}^{\mathrm{W}}$	Transverse W boson mass
$\Delta\phi(\ell, \ell')$	Azimuthal angle between the two leptons from the Z boson candidate
N_{b}	Number of b tagged jets
$E_{\mathrm{T}}^{\mathrm{miss}}$	Missing transverse energy
$\Delta R\ (\mathrm{b_t}, \mathrm{j}')$	Angle between the b jet from the top quark candidate and the recoiling jet
$m(3\ell)$	Invariant mass of the three lepton system
Lepton asymmetry	$\lvert\eta\rvert$ of the lepton from the top quark candidate, multiplied by its charge
$\min(\Delta R(b, l))$	Smallest angle between any b jet and any lepton
$\max(\lvert\eta(j)\rvert)$	Maximum $\lvert\eta\rvert$ value of any jet
$\max(\Delta R(b, l))$	Largest angle between any b jet and any lepton in the event
$\Delta R\ (\mathrm{b_t}, \ell_W)$	Angle between the b jet and the lepton from the top quark candidate
$\cos(\theta^{\star}_{\mathrm{pol}})$	Cosine of the top quark polarization angle
$\max(\Delta\phi(j_1, j_2))$	Largest azimuthal angle between any pair of two jets

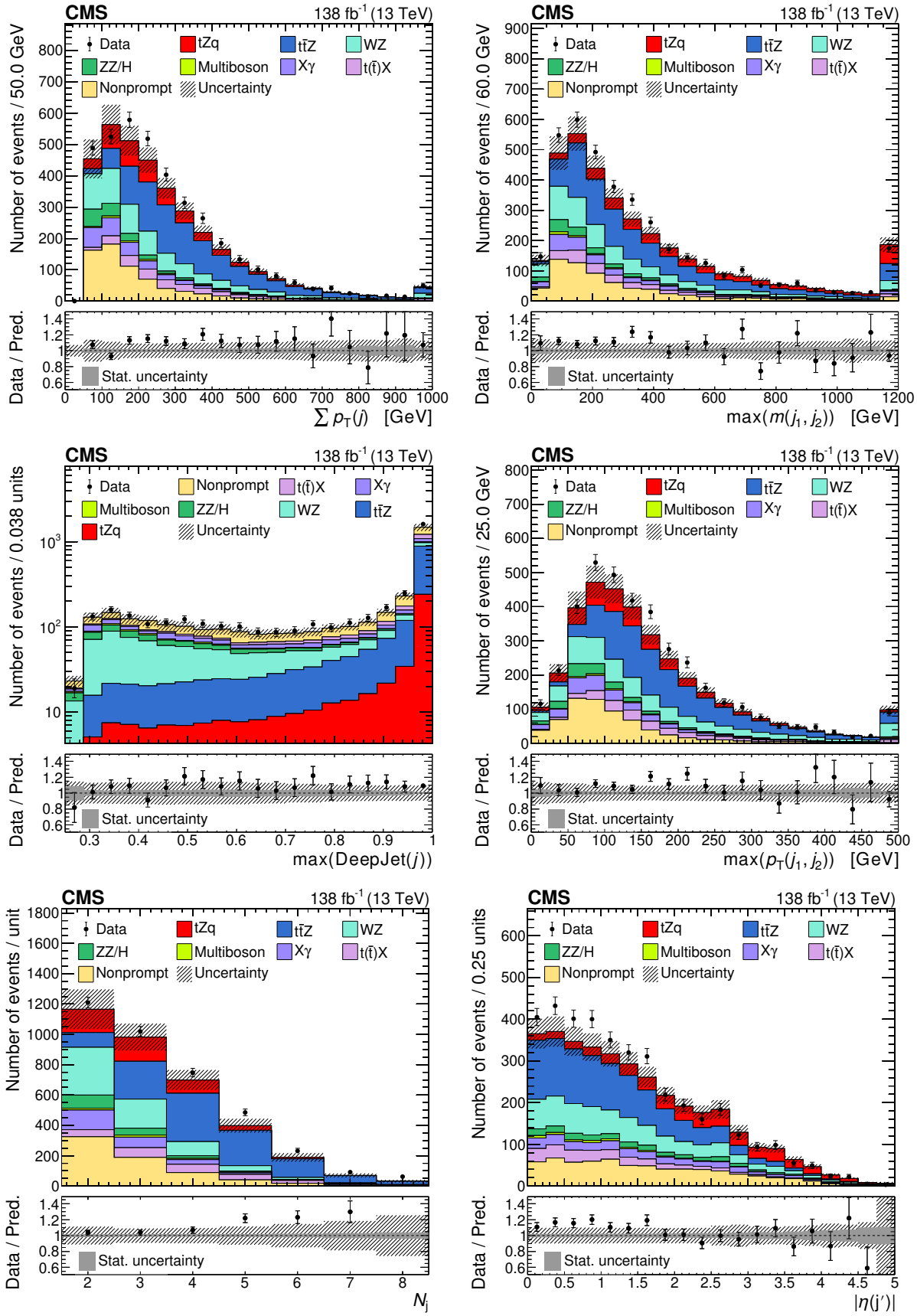

Fig. 4.17.: Distributions of events in the SR for the most powerful discriminating features including the scalar p_T sum of all jets (upper left), maximum invariant mass of any dijet system (upper right), maximum DeepJet score of any jet (middle left), maximum p_T value of any dijet system (middle right), jet multiplicity (lower left), and $|\eta|$ of the recoiling jet (lower right).

does not qualify and would be rejected.

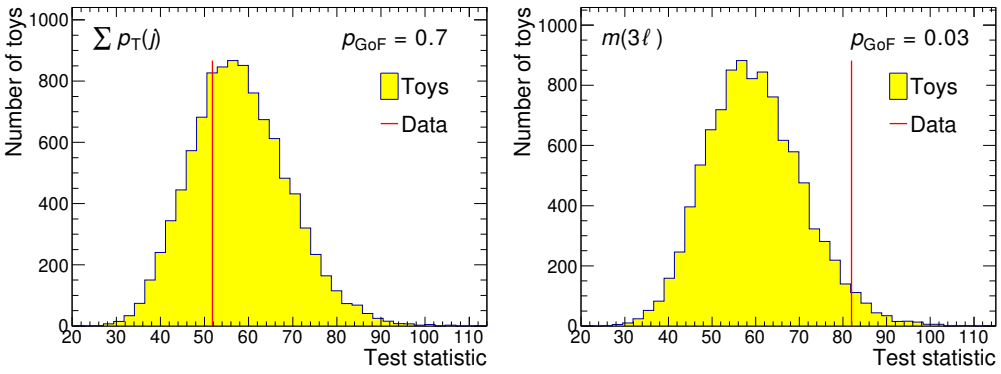

Fig. 4.18.: Goodness-of-fit test with the saturated model for the distribution of the scalar sum of hadronic transverse momenta (left) and the invariant mass of the three-lepton system (right). The test statistics of the toy data samples (yellow histogram) are compared to the one of the observed data (red line), leading to p-values of 70% and 3%, respectively.

In this way, p-values are calculated for each feature as shown in Section C.2. In general high p-values are found and show that the prediction can describe the data well. The lowest p-value of about 3% was obtained from the $m(3\ell)$ distribution. Since the observed data is randomly distributed and given the fact that in total 22 features are used, it is not unreasonable to find such a value in one case. As the threshold was set to 1% beforehand, no sign of inaccurate modeling is concluded.

4.5.3. Neural network architecture, training, and evaluation

To adapt the NN architecture to the different event topologies that are expected in the SR_{tZq}, a separation in multiple classes is performed. Five separate classes are defined to encapsulate the very different characteristics of each process. Those are: tZq, $t\bar{t}Z$, $t(\bar{t})X$, WZ, and all other processes including $X\gamma$, ZZ, VVV, and nonprompt backgrounds. Each process is weighted according to its cross section. This approach has proven to be superior in comparison with a binary classifier.

The NN has two hidden layers with 100 neurons each that use scaled exponential linear units (SeLu) as activation functions [193]. These SeLu functions have a self-normalizing effect on the output of each neuron and lead to a robust behavior of models with many free parameters. In contrast to the hyperbolic tangent, which was often used in the past, the SeLu avoids the problem of the vanishing gradient [194]. In this problem, the weights of neurons reach a value where they no longer get updated, and thus, no longer contribute to the optimization. A softmax activation function is used for the output layer with five neurons. This allows to interpret the output score of each neuron as the likelihood for the corresponding class. The use of batch normalization improves the minimization process and leads to a more generalizable model [195]. Dropout layers with a dropout rate of 0.4 are exploited to mitigate a possible overtraining [196].

Training procedure

The chosen model has in total 13 149 free parameters. Suitable values for those parameters have been found to achieve a good classification in the training procedure. For the training, simulated events selected in SR_{tZq} and $CR_{t\bar{t}Z\,3\ell}$ that represent data from all three years are taken. The benefit of the bigger sample size when training on all samples together outweighs the improvement when training each year separately to account for the small differences across the years.

To mitigate the risk of overtraining, events that are used in the optimization process of the NN are not used in the final signal extraction. Yet, a three-fold training approach is performed in order to use the full sample statistics. The sample is split into three data sets and three sessions of training are performed. In each training, two of the three data sets are used as training and validation sample, while the third data set is used to test the performance of the trained model. In the signal extraction, it is taken care that the model is always evaluated on those events that were not used in the respective training.

The training sessions are performed by minimizing the categorical cross entropy loss function with the Adam optimizer [197]. After each epoch of training the loss is calculated and the learning rate is reduced if a plateau is reached. The value of the loss as a function of the training epoch for one specific training is shown in Fig. 4.19. It is visible that the loss of the validation sample is lower than the loss of the training sample. This originates from the fact that during the calculation of the loss on the training sample, the dropout is enabled, which means some nodes of the NN are disabled. When evaluating the NN, the nodes is enabled, which leads to better classification and a lower value for the loss.

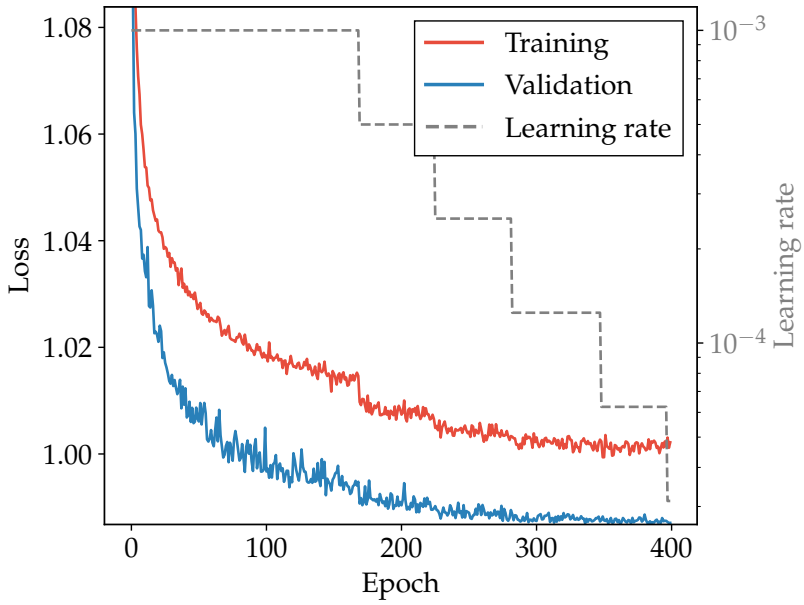

Fig. 4.19.: The categorical cross entropy loss as function of the training epochs for the training sample (red) and validation sample (blue). The learning rate is plot as dashed gray line with corresponding values on the right y axis.

Hyperparameter optimization

Aspects in the architecture of the NN, such as the number of layers, the number of neurons per layer, or the dropout rate, have to be chosen before the actual training.

Other examples of those so-called "hyperparameters" are the learning rate, batch size, or class weights used in the training. Depending on the problem, some choices work better or worse. One approach to find a set of hyperparameters that work well is to try different combinations for example by intuition or random choice. However, since the parameter space is high-dimensional, it is often not clear if there is another set of hyperparameters that works better. As a remedy, the Bayesian optimization procedure has been followed [198]. It is a sequential algorithm that starts with a few random guesses for sets of hyperparameters for which training sessions of the NN have been performed. From the figure of merit of each training, a prior function is estimated that describes the dependency on the hyperparameters. Taking into account the phase space that is less explored, a new set of hyperparameters is calculated which has the highest chance of being a better choice. A new training is performed and the prior is updated accordingly. This procedure can be repeated until the figure of merit converges to a minimum. As the figure of merit, the AUC score is taken, which is the area under the receiver operator characteristic (ROC) curve. Only little dependence on the number of layers and neurons per layer is observed. In the Bayesian optimization, the aspect of overtraining was not taken into account and the procedure preferred a complex model with a large number of layers and neurons. To reduce the risk of overtraining, a smaller number of neurons and layers is chosen with negligible loss in the performance.

Evaluation

The importance of each input feature is reflected in the ordering of Table 4.5 which is obtained by using a gradient-based method [199]. The output score of the events from each class is plotted in Fig. 4.20 for each node of the NN. A Kolmogorov–Smirnov test is performed between the training and test data sets. High p_{ks} values indicate good compatibility between the data sets and no sign of overtraining is observed.

The performance of the NN is evaluated by calculating the ROC which plots the efficiency to classify events from the tZq class correctly, against the efficiency to classify events from one of the background classes mistakenly as tZq. It is shown in Fig. 4.21 together with the AUC scores. A high AUC score indicates a good separation between tZq and the individual backgrounds. It is visible in the plots that the NN can isolate tZq very well against the different kinds of background. Small differences show that the separation of tZq from WZ works better than the average, while it works worse against the background from the category 'other', where backgrounds with nonprompt leptons contribute the most.

4.6. Corrections and systematic uncertainties

The imperfect theory prediction, simulation, reconstruction, and calibration of simulated samples leads to systematic deviations in the prediction of the data. To account for known differences, corrections are applied. Residual uncertainties and systematic deviations with unknown effects are estimated and reflected in the measurement. There are two types of uncertainties: normalization uncertainties like the normalization of background processes discussed in Section 4.4, and uncertainties that impact the event kinematics and thus lead

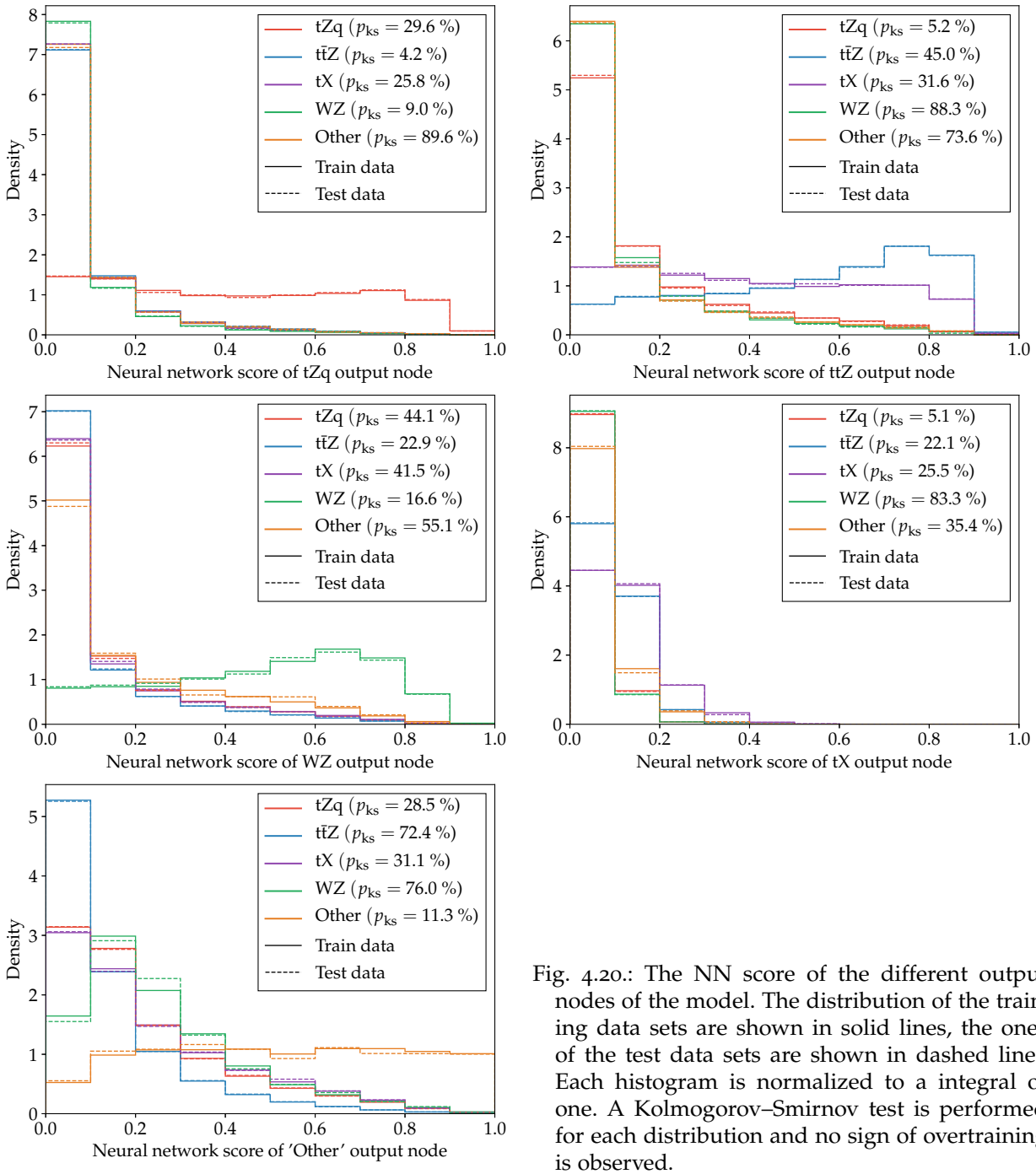

Fig. 4.20.: The NN score of the different output nodes of the model. The distribution of the training data sets are shown in solid lines, the ones of the test data sets are shown in dashed lines. Each histogram is normalized to a integral of one. A Kolmogorov–Smirnov test is performed for each distribution and no sign of overtraining is observed.

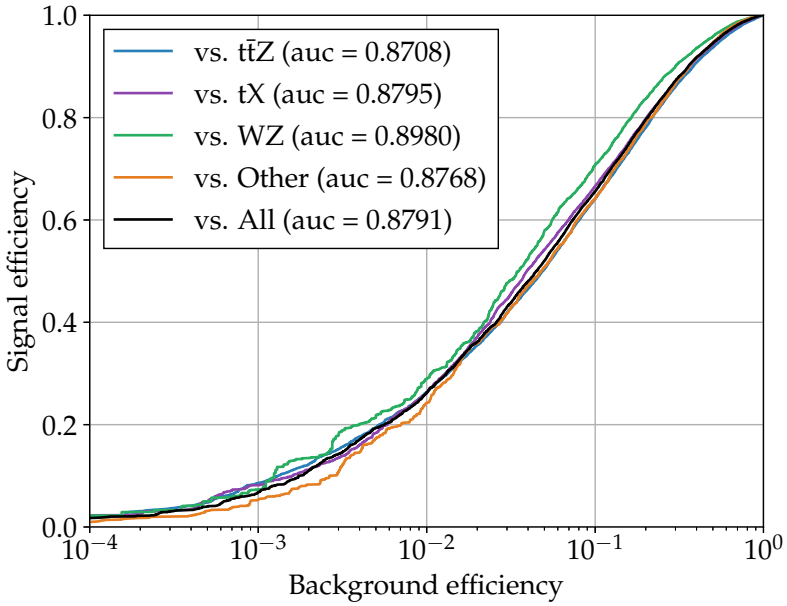

Fig. 4.21.: The ROC curve for the classification of tZq as signal and various backgrounds as background. The AUC score is shown for the separation against each individual background and against all backgrounds together. The classification performs better if the curve is closer to the lower right corner.

to a difference in the distribution used for the signal extraction. The latter are called shape uncertainties. For the shape uncertainties, two new histogram templates are generated by varying the underlying systematic source by $\pm 1\sigma$, indicating the "up" and "down" variation.

4.6.1. Theory uncertainties

In general, theory uncertainties affect the full simulation and impact not only the event kinematics but also the cross section of each process. Sources that impact the inclusive tZq cross section are not considered in the signal extraction. This is referred to as the "externalization" of normalization uncertainties. It can be done as σ_{tZq} is the subject of the measurement and is treated as free parameter in the fit. However, theory uncertainties can introduce differential normalization effects by the event selection, these are considered and denoted as "acceptance effects".

In this analysis, theory uncertainties in the tZq signal sample and the main background sample tt̄Z are considered. As the simulation settings for those samples were the same for data of all years of data-taking, all theory uncertainties are fully correlated between the years. The underlying origin of each uncertainty is discussed in more detail in Section 1.2.

PDF: The Hessian PDF set is used and the associated systematic uncertainty is decomposed into 100 eigenvectors and two variations of the strong coupling constant, α_S. This leads to 51 event-weight-based up and down variations [37]. The uncertainties are uncorrelated among themselves and considered fully correlated between the tZq and tt̄Z simulation.

Parton shower modeling: To account for the uncertainty in the parton shower from simulation, α_S is varied for the initial- and final-state radiation, ISR and FSR, independently by a factor of 1/2 and 2. The production mechanisms of QCD-induced and EW-induced

processes are different, hence the ISR is treated as uncorrelated between the tZq and $t\bar{t}Z$ samples. The FSR uncertainty is treated as fully correlated between tZq and $t\bar{t}Z$.

Matrix element factorization and renormalization scales: Uncertainties in the matrix element renormalization and factorization scales, μ_R and μ_F, are considered. The μ_R and μ_F are varied simultaneously by a factor of 1/2 and 2. As a cross-check, the fit was repeated by varying μ_R and μ_F independently. Treating them with two uncorrelated nuisance parameters in the fit, the corresponding uncertainty was found to be consistent. Since the production mechanisms of tZq (EW) and $t\bar{t}Z$ (QCD) are different, this uncertainty is treated as uncorrelated between tZq and $t\bar{t}Z$. Its effect on tZq events in the SR_{tZq} is shown in Fig. 4.22 where a clear shape effect is visible.

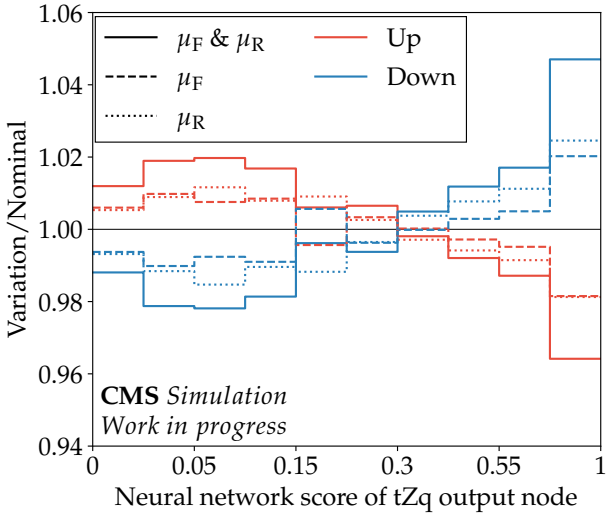

Fig. 4.22.: Relative effect of systematic up (red) and down (blue) variations of the matrix element μ_F and μ_R each one individually (dashed and dotted lines, respectively) and simultaneously (solid line). The plot is shown for simulated tZq events in the SR_{tZq} as function of the NN score of the tZq output node.

Underlying event tune and color reconnection: The uncertainties related to the parton shower and underlying event tune are estimated using alternative samples that represent the systematic uncertainties in the tunes [113]. For the color reconnection modeling, alternative samples generated with QCD-inspired and gluon-move models are analyzed [45, 47]. Uncertainties in the underlying event tune and color reconnection are uncorrelated with each other but each is correlated between tZq and $t\bar{t}Z$.

4.6.2. Calibration and experimental uncertainties

To calibrate differences between data and simulation, scale factors are applied to simulated samples either using event weights by modifying the kinematic properties of an object e.g. the jet energy. The different corrections are summarized in Fig. 4.23 and discussed in the following. To assess related uncertainties, each correction is varied by $\pm 1\sigma$, and events are reevaluated. Experimental uncertainties affect the event selection efficiency and shape of the distributions. They are applied to all simulated samples alike.

Luminosity: To reflect the uncertainty on the total luminosity recorded by CMS, a normalization uncertainty is applied to the total predicted event yields in each year ranging

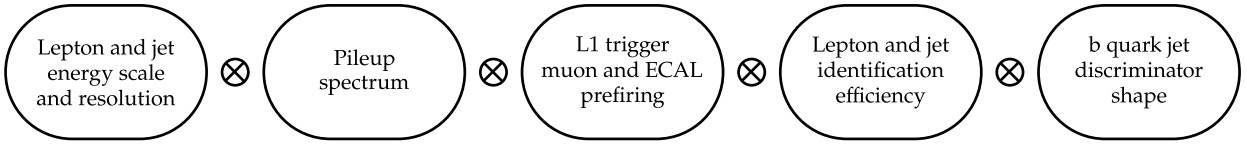

Fig. 4.23.: Different calibrations that are applied in the analysis. The lepton and jet energy and resolution are applied to both, data and simulation, while all other corrections are only applied on simulated samples.

between 1.2 and 2.5% [140, 142, 148]. Individual underlying sources are considered for the assessment of the correlations between the years.

Pileup spectrum: Event-based scale factors are applied to reweight the PU distribution in simulation to the one expected in the data. The uncertainty of this correction is dominated by the uncertainty on the total inelastic pp cross section and amounts to $\pm 4.6\%$ [200]. Using this uncertainty, the PU distribution for data is re-derived and the simulation is reweighted with varied scale factors as illustrated in Fig. 4.24 for data from 2017. This uncertainty is considered as fully correlated across the years.

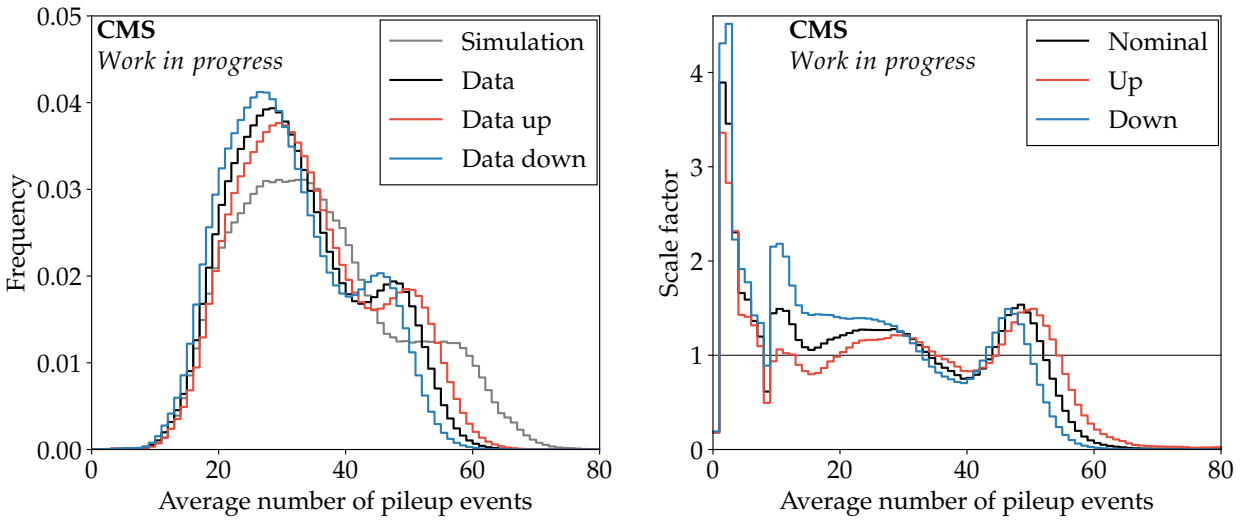

Fig. 4.24.: Left: Distributions of the number of PU interactions in each event in simulation (gray), compared to those in data using the central value of the total inelatis pp cross section (black), the up variation (orange), or down variation (blue) for data from 2017. Right: The scale factors that are applied on simulated samples to reweight the events according to the respective PU distribution in data.

Trigger efficiency: The trigger efficiency was studied in events selected by a set of reference triggers that are uncorrelated to the ones used for the cross section measurement. It was measured in data and simulation to be consistent with 100% in almost all phase space regions. Hence, no scale factor is applied. Due to the limited statistical precision of the trigger efficiency measurement in data, a normalization uncertainty of 2% is applied to account for possible differences between data and simulation. Since the trigger settings change during data taking, the uncertainty is considered uncorrelated across the years.

Lepton and jet identification efficiencies: The efficiency of the TOP LeptonMVA selection for prompt leptons in simulated events is corrected by scale factors measured in data with the tag-and-probe method using DY events. The measured scale factors are parameterized as a function of the lepton p_T and η. The main uncertainties are associated with the definition of the dilepton invariant mass region, the fit model used to extract the fraction of events containing leptons from the Z boson decay, and the statistical uncertainties in the considered simulation and data samples. An additional uncertainty accounts for the different event topology of events in the scale factor measurement with respect to selected events in this analysis. Similarly, events are corrected for differences between data and simulation in the PU jet ID selection efficiency and corresponding uncertainties are taken into account [125]. The statistical uncertainties are treated as uncorrelated across the years while the systematic uncertainties are treated as fully correlated.

Lepton and jet energy scale and resolution: Corrections for the leptons and jet energy scale and resolution are applied centrally within the CMS experiment [126, 201, 202]. Uncertainties related to these corrections are applied as a function of p_T and η of the respective object. Events are re-analyzed after the four-momenta of the objects have been varied by one standard deviation up and down for each uncertainty. For each variation on the jet energy scale, the correction on the b tag discriminant shape and $\vec{p}_T^{\,miss}$ are recomputed accordingly. The uncertainties are decomposed into individual sources, some of which are correlated between years, and others are uncorrelated.

Missing transverse energy: An additional uncertainty on the unclustered missing transverse energy is considered [203]. It affects the $\vec{p}_T^{\,miss}$ and is treated as uncorrelated between the years.

B quark jet discriminator shape: An event-by-event reweighting is performed to correct the DeepJet b tag discriminator distribution for differences between data and simulation [127]. This is necessary because the $\max(\text{DeepJet}(j))$ value is used as an input variable in the NN. Event weights depending on the p_T, η, and DeepJet discriminator value of each jet in the event are computed. In order to correct only the discriminator shape, but not the initial event yield prior to applying any requirement on b tagging, each event is corrected as a function of $N_j^{central}$. The event yield is allowed to change after b tag selection and uncertainties in the b tag scale factors, therefore, affect both the shapes and normalizations of distributions. Uncertainties are considered in their different sources to properly account for year-by-year correlations.

L1 trigger muon and ECAL prefiring: As already discussed in Section 3.5.3, because of a time shift in the response of L1 ECAL triggers, for a fraction of events the trigger decision was wrongly associated with the previous bunch crossing [98]. A similar effect was present in the muon system. As a consequence, uninteresting events were recorded while the subsequent interesting ones were rejected. Since these effects are not taken into account in the simulation, scale factors are applied as a function of p_T and η of jets,

photons, and muons in the event. Corresponding uncertainties are derived from varying the correction by ±20%.

HEM15/16 issue: In the late runs of 2018 data taking, the power supply of two HCAL modules broke down. This impacted the measured jet energy and $\vec{p}_{\mathrm{T}}^{\,\mathrm{miss}}$. As the effect is not well understood, no correction is applied but an uncertainty is assumed. In this uncertainty, the jet energy is modified for jets falling in the affected η-ϕ region of the detector and the $\vec{p}_{\mathrm{T}}^{\,\mathrm{miss}}$ is recomputed accordingly.

Limited sample size: The size of the simulated samples is limited and subject to statistical uncertainty. The same applies to the control samples in data used in the estimation of nonprompt backgrounds. To keep the number of independent uncertainty parameters at a minimum, the Barlow–Beeston-light approach is employed where one parameter is assigned to the total expected yield per histogram bin of the measurement [204].

4.7. Measurement of the inclusive cross section

The likelihood is constructed from events in the region $\mathrm{SR}_{\mathrm{tZq}}$ binned in the NN score of the tZq output node. The $\mathrm{t\bar{t}Z}$ output node is used for events in the region $\mathrm{CR}_{\mathrm{t\bar{t}Z\,3\ell}}$. Other CRs are included in the fit as well and binned as described in Section 4.4. The data and prediction for the three years are fitted in separate histograms to account for the correlation of uncertainties. One simultaneous fit is performed including all regions and all years. The pre-fit and post-fit distributions of the $\mathrm{SR}_{\mathrm{tZq}}$ are shown in Fig. 4.25. Good description of the data is achieved in all bins after the fit. Through profiling, a reduction of the uncertainties by the NLL fit to data is obtained. Post-fit plots of CRs are shown in Fig. 4.26. Again, good agreement of the simulation with data is visible in all bins.

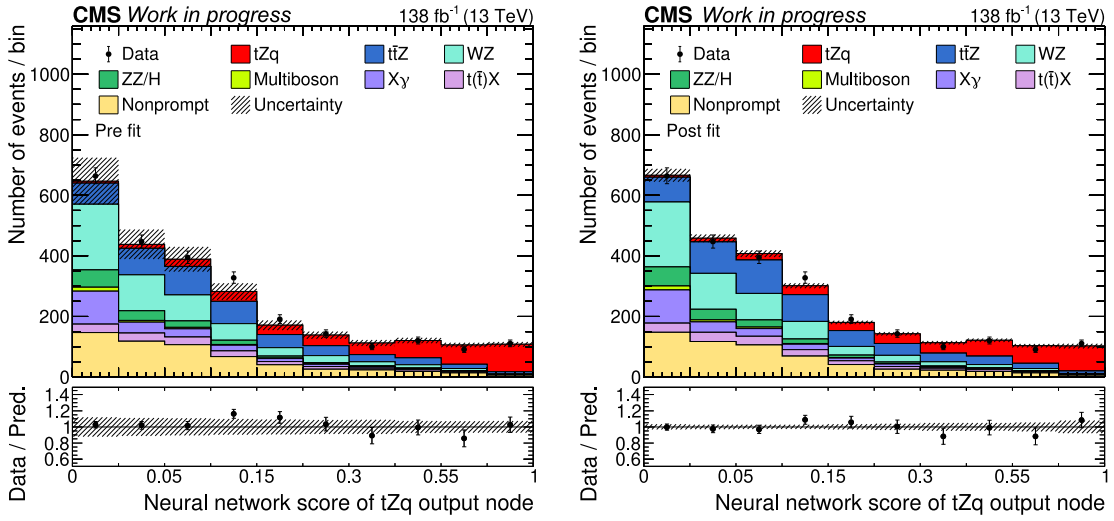

Fig. 4.25.: Pre-fit (left) and post-fit (right) distributions in the $\mathrm{SR}_{\mathrm{tZq}}$ from the measurement of the inclusive cross section. Through profiling the NLL, uncertainties can be visibly reduced.

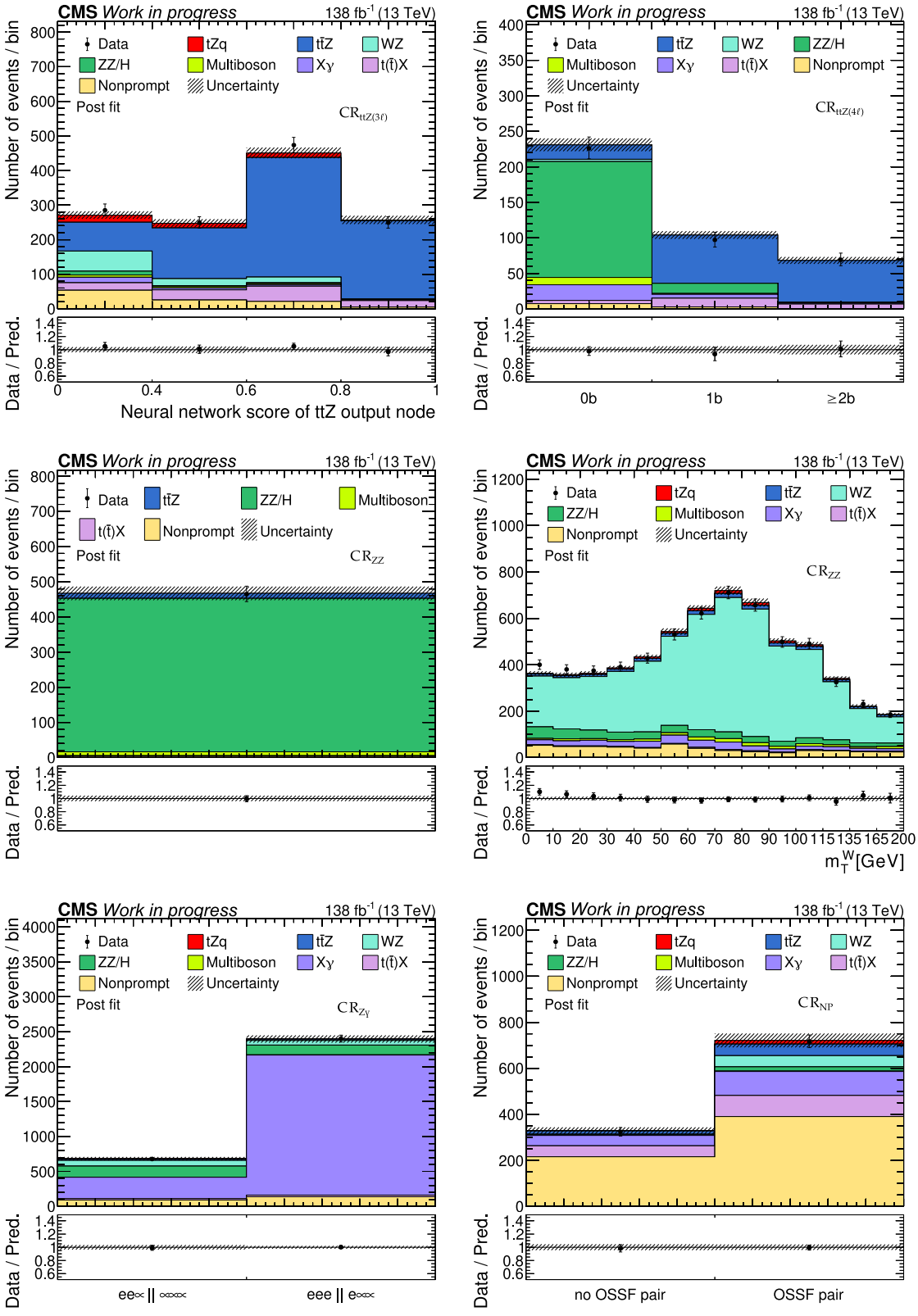

Fig. 4.26.: Post-fit distributions in the CRs from the measurement of the inclusive cross section.

4.7.1. Result

The extracted inclusive cross section yields

$$\sigma_{tZq} = 84.6\ ^{+6.9}_{-6.7}\ (\text{stat})\ ^{+6.4}_{-5.9}\ (\text{syst})\ \text{fb}\ , \tag{4.15}$$

with a relative precision of about 11%. This is the most precise measurement of the tZq cross section to date. The NLL was scanned fixing all nuisance parameters to their best fit values to assess the statistical component of the uncertainty and profiled to obtain the full uncertainty. The resulting profile likelihood ratio is shown as a function of the signal strength in Fig. 4.27.

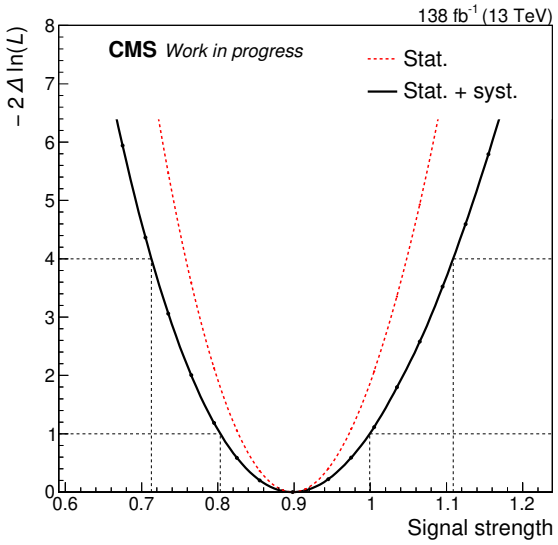

Fig. 4.27.: The profile likelihood ratio in the fit for the inclusive cross section measurement is shown when considering only the statistical uncertainties (dashed red line) or the combined statistical and systematic uncertainties (solid black line). The y-axis intersection points at 1 and 4 mark the 68% and 95% confidence intervals.

The statistical and combined systematic uncertainties are of similar order of magnitude. To study different systematic sources, the nuisance parameters are investigated with respect to their post-fit values. The likelihood is profiled for each nuisance parameter to find its associated 68% confidence interval. From this, it is estimated how much the $\pm 1\sigma$ variation of each nuisance parameter impacts the signal strength parameter. The procedure is first performed on the Asimov toy data set to see the expected precision and constraints on the nuisance parameters. It is repeated for the fit on data. The results are compared in Fig. 4.28. It can be seen that most of the nuisance parameters agree well with the expectation. The leading systematic uncertainties are related to the scale parameters μ_R and μ_F, the identification of b jets, and the background normalizations. By looking at the first column of Fig. 4.28 which shows the pulls of the nuisance parameters, $(\hat{\Theta} - \Theta_0)/\Delta\Theta$, it is apparent that some uncertainties are constrained in the fit. This applies in particular to the normalization of the nonprompt background which is halved. This behavior is understood and expected since a conservative uncertainty of 30% was initially assumed. A significant pull of the normalization of the $t\bar{t}Z$ background is observed. This is expected as also in previous measurements of $t\bar{t}Z$ a higher cross section than expected was measured [181]. To check if the prior uncertainty of 15% is appropriate, the fit is repeated by treating the $t\bar{t}Z$ normalization as a free-floating parameter. This way, a change of the measured inclusive cross section of about 1% is obtained. This is in agreement

within the systematic uncertainty in the $t\bar{t}Z$ normalization obtained in the nominal fit, as visible in Fig. 4.28.

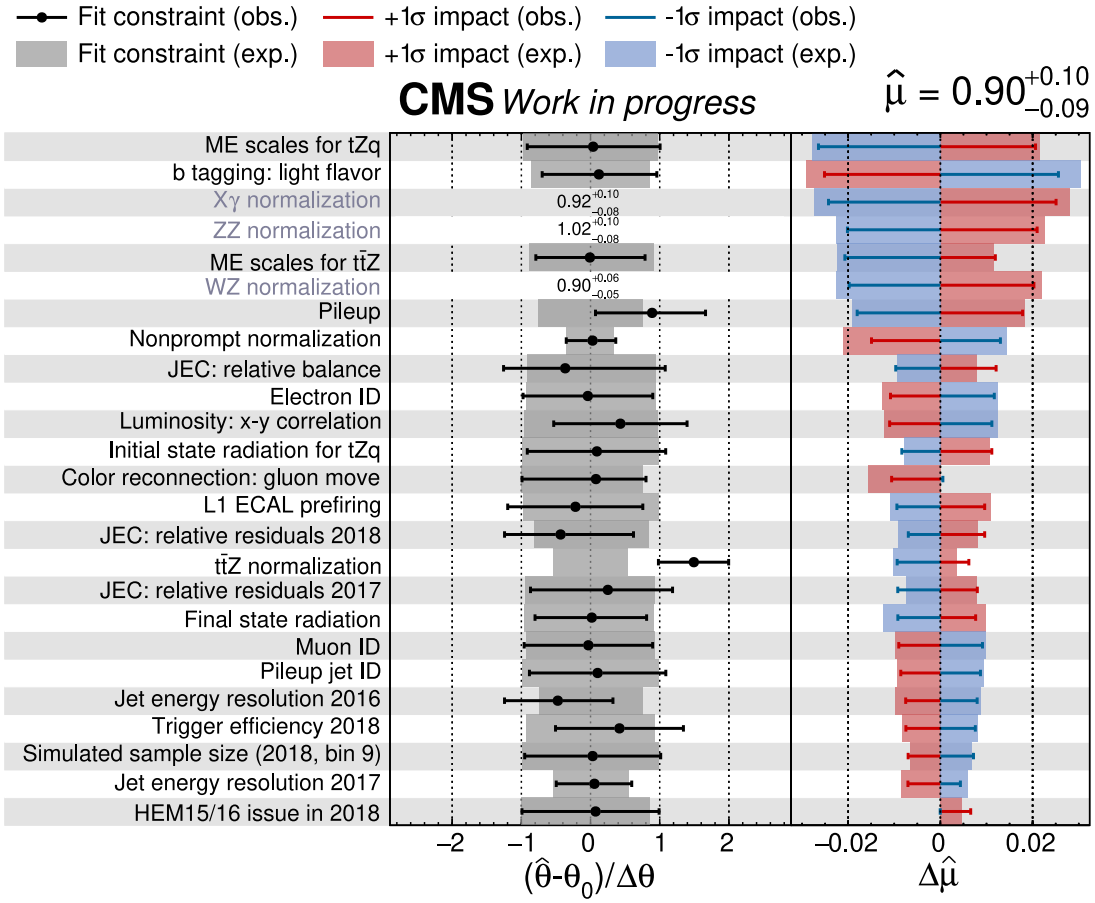

Fig. 4.28.: List of the dominant systematic uncertainties in the inclusive cross section measurement. Each uncertainty source is treated as a separate nuisance parameter in the fit. The black dots with the horizontal error bars in the first column show the difference of the nuisance parameter after the fit to data ($\hat{\Theta}$) to its prior value (Θ_0) divided by its prior uncertainty ($\Delta\Theta$). The dark gray bands show the same as it is expected from a fit to the prediction. The last column shows the impacts ($\Delta\hat{\mu}$) of each uncertainty source on the fitted signal strength parameter ($\hat{\mu}$) as it is observed in data (horizontal error bars) and expected (bands) for the up (red) and down (blue) variation of the nuisance parameter.

The improvements over the latest CMS analysis [136] are expected in part due to the larger data sample used in this analysis. Additional improvements come from the looser lepton identification which reduces the statistical uncertainty. Because of the looser lepton selection, it was also possible to include the CR_{NP}, which helped constrain the systematic uncertainty related to the nonprompt background. The improvement over the analysis from the ATLAS Collaboration [173] can be understood from the wider definition of the signal region. While in this analysis, also events with more than one b tagged jet are included, in the ATLAS analysis, they are not. Furthermore, the $CR_{t\bar{t}Z\,4\ell}$ region which was not included in the previous analyses, gives sensitivity to the normalization and systematic uncertainties related to $t\bar{t}Z$ production.

4.7.2. Determination of the V_{tb} CKM-matrix element

The measured tZq production cross section directly depends on the CKM-matrix element $|V_{tb}|$. As discussed in Section 1.3, $|V_{tb}|$ can be accessed without assuming unitarity of the CKM-matrix or the number of quark flavors. Under the assumption that $|V_{td}|$, $|V_{ts}| \ll |V_{tb}|$, the matrix element can be determined as

$$|f_{LV} V_{tb}| = \sqrt{\frac{\sigma_{tZq}}{\sigma_{tZq,\,theo}(V_{tb}=1)}}\,, \tag{4.16}$$

where f_{LV} is a real value to take into account possible BSM effects and is 1 under SM assumptions. The theory cross section $\sigma_{tZq,\,theo}$ is chosen from Ref. [69], calculated at NLO in α_S and predicted in the 5FS (also listed in Table 1.2). As recommended by the authors, the difference to the 4FS is considered as an additional uncertainty [69]. The uncertainty is thus inflated, resulting in a theory prediction of $\sigma_{tZq,\,theo} = 84.0^{+4.7}_{-3.9}$ fb. Together with the measured inclusive tZq cross section, this results in:

$$|f_{LV} V_{tb}| = 1.007\ ^{+0.056}_{-0.053}\ (\text{meas})\ ^{+0.028}_{-0.023}\ (\text{theo}) = 1.007\ ^{+0.063}_{-0.058}\,. \tag{4.17}$$

The result is in good agreement with $0.999172^{+0.000024}_{-0.000035}$, obtained from a global fit of measurements for all CKM-matrix elements under assumption of unitarity [10]. The result in this thesis has an uncertainty which is 2.5 times larger than a recent measurement of t-channel single top quark production, where a value of $V_{tb} = 0.988 \pm 0.024$ [58] is presented. Many of the uncertainties are expected to be uncorrelated between both measurements. With the measurement obtained here, a future combination can lead to improved results.

4.8. Measurements of differential cross sections

Differential measurements of the tZq cross section as a function of specific observables related to the top quark, Z boson, and recoiling jet, contain additional information. The observables measured in this analysis are:

- $p_T(t)$: the transverse momenta of the top quark,
- p_{T,ℓ_W}: the transverse momenta of the lepton of the top quark,
- $p_T(\ell,\ell')$: the transverse momenta of the Z boson,
- $\Delta\phi(\ell,\ell')$: the azimuthal angle between the leptons from the Z boson,
- $p_T(j')$: the transverse momentum of the recoiling jet,
- $|\eta(j')|$: the absolute pseudorapidity of the recoiling jet,
- $m(t,Z)$: the invariant mass of the top-Z system,
- $m(3\ell)$: the invariant mass of the three-lepton system,
- $\Delta R(t,Z)$: the ΔR between the top quark and the Z boson,
- $\Delta R(\ell_t,Z)$: the ΔR between the lepton from the top quark and the Z boson,
- $\cos(\theta^{\star}_{pol})$: and the cosine of the top quark polarization angle.

A variety of those variables are sensitive to BSM physics as outlined in Section 1.4. Possible BSM effects can be described in the framework of effective field theory (EFT) and in particular, the standard model EFT (SMEFT). In the SMEFT framework, the $p_{\mathrm{T}}(\mathrm{t})$, $m(\mathrm{t},\mathrm{Z})$, and $p_{\mathrm{T}}(\ell,\ell')$ variables are sensitive, for example to the $\mathcal{O}_{\mathrm{tW}}$ and $\mathcal{O}_{\phi\mathrm{tb}}$ operators that describe modified left-handed and right-handed W-t-b couplings [67, 71, 73]. Another example is the $\mathcal{O}_{\mathrm{tB}}$ operator that modifies the t-Z coupling. In case of new physics, an increased cross section can be expected, especially in the high energy regime. This would lead the leptons of the Z decay to be more collimated and an increase at low values of $\Delta\phi(\ell,\ell')$. The observables $p_{\mathrm{T},\ell_{\mathrm{W}}}$ and $m(3\ell)$ resemble $p_{\mathrm{T}}(\mathrm{t})$ and $m(\mathrm{t},\mathrm{Z})$, respectively, and are reconstructed only considering the leptonic decay products. Those contain less strong information but can be measured with higher precision. The variables $\Delta R(\mathrm{t},\mathrm{Z})$ and $\Delta R(\ell_{\mathrm{t}},\mathrm{Z})$ are sensitive to the modeling of the process and the top-Z coupling. The $p_{\mathrm{T}}(\mathrm{t})$ is also interesting since, during Run 1, the p_{T} spectrum of the top quarks in $\mathrm{t\bar{t}}$ production was found to be softer in data, compared to various MC simulations at LO and NLO calculations [205]. Partially, it can be explained by including higher-order calculations [206–208]. The question is if this effect also appears in the tZq production mechanism. The modeling of the recoiling jet ($p_{\mathrm{T}}(\mathrm{j}')$ and $|\eta(\mathrm{j}')|$) depends strongly on higher-order calculations and, to a lesser degree, on the PDFs of the simulation [69]. The $\cos(\theta^{\star}_{\mathrm{pol}})$ constitutes a powerful probe of the coupling structure of single top quark t-channel production [65] and is defined as in Section 1.3.2. Using $\cos(\theta^{\star}_{\mathrm{pol}})$, the top quark spin asymmetry is measured for the first time in tZq.

Reconstructed observables are impacted by hadronization effects and the imprecise measurement of event kinematics. Additionally, the number of measured events is reduced by the limited acceptance and imperfect reconstruction and identification efficiency of the detector. These effects impact the measured distributions and lead to a smeared and biased spectrum compared to generator-level distributions. To make comparisons of measured differential distributions with those from other experiments or alternative theory predictions, the detector effects, and optionally also hadronization effects, need to be reverted in a process called "unfolding".

The analysis presents a case with low statistical precision and large background contributions. For this, maximum likelihood-based unfolding is best suited. In this procedure, the unfolded distribution is extracted from the observed data in one single fit, taking into account statistical and all systematic uncertainties, background subtraction, and bin-to-bin migrations of the signal process. Essentially, a maximum likelihood fit is performed as discussed in Section 4.2, but in multiple dimensions to measure the cross section differentially as a function of some kinematic observables x at generator level. The tZq process is divided into different signal contributions, called generator-level bins:

$$\sigma_j = \int_{x_j^{\mathrm{low}}}^{x_j^{\mathrm{high}}} \frac{\mathrm{d}\sigma(x)}{\mathrm{d}x}\mathrm{d}x \,, \tag{4.18}$$

where x_j^{low} and x_j^{high} denote the lower and upper bounds of the j^{th} generator level bin, respectively. Each generator-level bin is represented by a separate signal template and scaled by a separate signal strength in the fit. The expected number of events in the i^{th}

bin is thus given by:

$$\lambda_i(\boldsymbol{\mu}, \boldsymbol{\Theta}) = \sum_j^S \mu_j s_{i,j}(\boldsymbol{\Theta}) + \sum_j^N b_{i,j}(\boldsymbol{\Theta}) \,, \tag{4.19}$$

where S is the number of signals, e.g. the number of generator-level bins, and $\boldsymbol{\mu} = \mu_1, \ldots \mu_S$ are the corresponding signal strengths.

4.8.1. Generator-level definitions

To extract experiment independent results that can be compared to other experiments or theory predictions, the signal extraction is performed using two different levels of definition: the "parton level" and the "particle level", collectively denoted as generator level. At the parton level, the measurement is performed in the full phase space of events with three prompt leptons. However, the definition strongly depends on the generator choice, and the extrapolation to the detector level is rather big. A particle-level definition aims to minimize the dependency on the generator choice and mitigates the extrapolation to the detector level.

Parton-level objects are defined based on outgoing particles generated in the hard interaction after ISR and FSR but before hadronization. As signal, tZq events with three prompt leptons are considered, including events with leptonic decaying τ leptons. The energy loss of matrix element particles due to gluon or photon radiation is not taken into account. This affects heavily the recoiling quark since it has a low mass, long lifetime, and interacts via the strong interaction. Thus, not all properties of the recoiling quark are well defined. The top quark on the other hand is heavy and has a short lifetime. Observables related to the top quark are well defined at the parton level and can be measured.

Particle-level objects are final-state particles from matrix element and parton shower and considered stable if they have a lifetime of more than 30 ps. Leptons can radiate photons, to take this into account a collection of "dressed" leptons is produced. Prompt electrons or muons are clustered with stable photons that are not arising from hadron decays with the anti-k_T algorithm [122, 123] and a cone size of $R = 0.1$. Jets are clustered with the anti-k_T algorithm and $R = 0.4$ from all stable particles excluding prompt leptons but including neutrinos from hadron decays. Using the "ghost" clustering method [134], non-stable b hadrons are scaled to a soft particle and included in the clustering process. The jet is labeled as b jet if such a ghost b hadron is clustered in the jet and the jet is in the region $|\eta| < 2.5$ of the detector. The missing transverse momentum $\vec{p}_\mathrm{T}^{\,\mathrm{miss}}$ is defined as the sum of the four vectors in the x-y plane of all neutrinos from W, Z, or prompt τ lepton decays. Based on the dressed leptons, the jets, and $\vec{p}_\mathrm{T}^{\,\mathrm{miss}}$, the event reconstruction and selection is performed analogue to detector-level objects as described in Sections 4.3.4 and 4.3.5. The measurements at particle level are performed in a fiducial phase space defined by tZq events that pass the requirements on the SR for particle-level objects. tZq events that enter the SR at detector level but do not pass the cuts at particle level are outside of the fiducial phase space and are considered as background.

Particle and parton-level distributions of the recoiling quark (jet) and $\cos(\theta^{\star}_{\text{pol}})$ are shown in Fig. 4.29. The figure illustrates that the particle-level distribution is much closer to the detector level. For the p_{T} of the recoiling quark (jet), values down to zero are included for the parton level where a measurement is unfeasible. Observables solely based on the recoiling quark (jet) are therefore only measured at particle level. The distribution of $\cos(\theta^{\star}_{\text{pol}})$, in contrast, is well described also at parton level. The advantage of the parton-level definition for this observable is that the relation in Eq. (1.45) is fulfilled, and the number of tZq events follows a linear function of $\cos(\theta^{\star}_{\text{pol}})$. This is not given at detector or particle level where the distribution drops at high values of $\cos(\theta^{\star}_{\text{pol}})$, caused by the acceptance cuts.

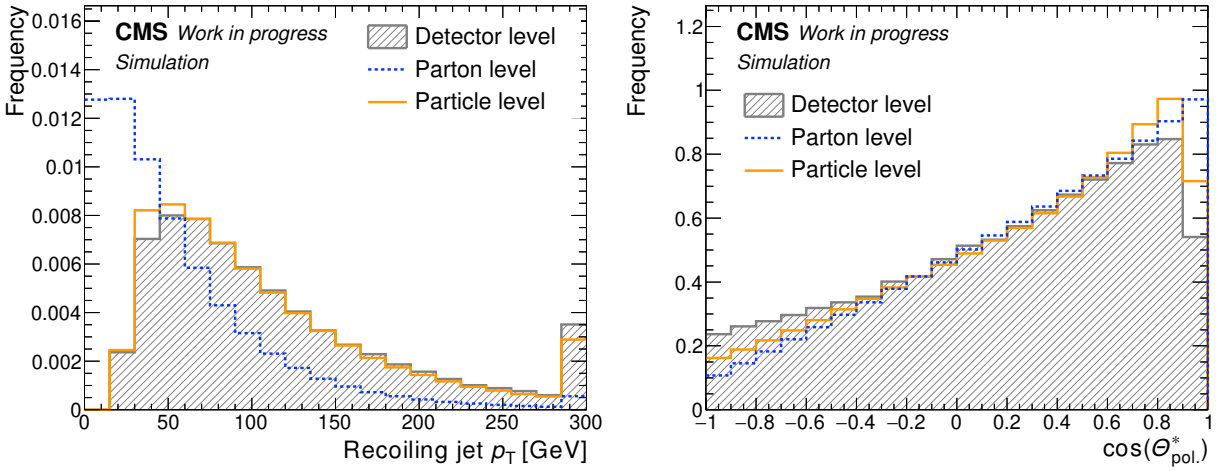

Fig. 4.29.: Distributions of the recoiling quark (jet) p_{T} (left) and $\cos(\theta^{\star}_{\text{pol}})$ (right) for simulated tZq events using the detector level (gray histograms), parton level (dotted blue line), and particle level (solid orange line) definition.

4.8.2. Choice of binning

To assess the extent to which a given reconstructed observable is smeared compared to the generator level, and to define a reasonable binning based on the available statistics, a response matrix is computed for simulated tZq events in the signal region. The response matrix relates the generator-level distributions to the detector-level distributions. Examples are shown for $p_{\text{T}}(\text{t})$ and $p_{\text{T}}(\ell, \ell')$ at parton and particle level in Figs. 4.30. The generator-level binning is optimized as a tradeoff between different quantities, namely: the expected number of tZq events in each detector-level bin, the bin width, the stability, and the purity. The stability is defined based on all reconstructed events as the fraction of events from a generator-level bin that are observed in the corresponding detector-level bin. The purity is defined based on all reconstructed events as the fraction of events from a detector-level bin, which belong to the corresponding generator-level bin.

The values of those quantities are found to be in a range that is suitable for the unfolding procedure. Observables that are defined solely on leptons have in general a very good resolution. Four bins is found to offer a reasonable compromise between granularity

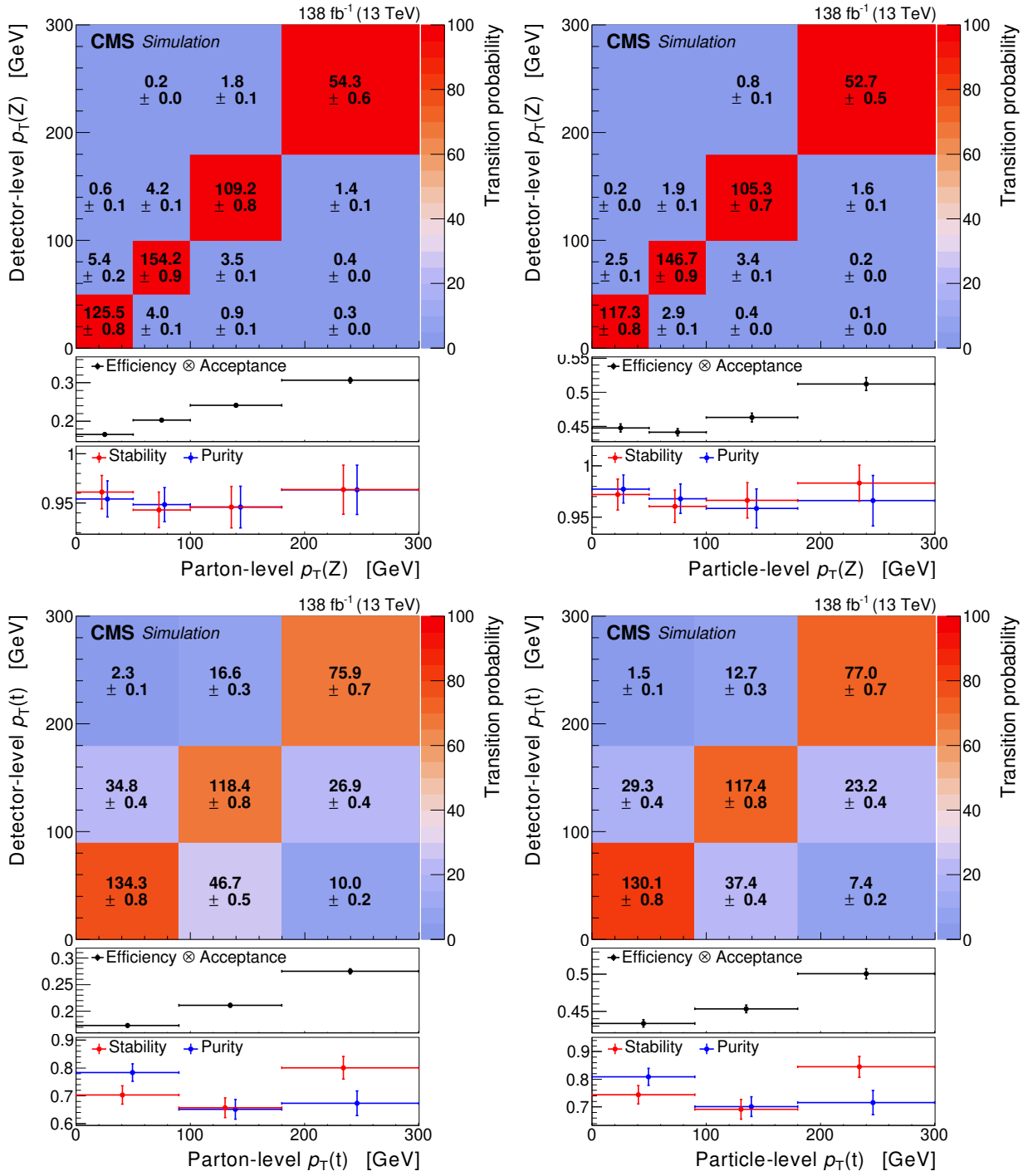

Fig. 4.30.: Response matrices for $p_T(\ell,\ell')$ (upper) and $p_T(t)$ (lower) at parton level (left) and particle level (right). In the 2D histograms, the number in each bin corresponds to the expected number of reconstructed tZq events and the associated uncertainty from the limited sample size in simulation. The color corresponds to the probability for an event belonging to a given generator-level bin to be reconstructed in a specific detector-level bin, hence, each column is normalized to unity. In the middle panels, efficiency times acceptance values for reconstructing tZq events are plotted. The lower panels show the stability and purity values as defined in the text.

and available sample size in each bin with purity and stability values above 95%. Poorer resolution is found for observables for which jets are included in the reconstruction. Therefore, the number of three bins is chosen to mitigate statistical fluctuations. The obtained purity and stability values are above 55%.

The condition number [209, 210] is another popular quality criterion and is used in many differential measurements. A low condition number usually indicates that an unregularized maximum likelihood estimation procedure is well suited for the task. It turns out that the condition number is low for all response matrices of this analysis, even if the number of bins is increased to four or five bins for observables for which jets are included in the reconstruction. An unregularized unfolding, however, is highly unstable in these cases and not feasible. Hence, the condition number turns out to be less useful in this analysis. The reason might come from the relatively low statistical precision.

4.8.3. Signal extraction

Events in the SR_{tZq} are partitioned in values of the observable to be measured, using the same intervals as for the binning at parton and particle level. In this way, the signal contributions of the different generator-level bins, i.e. the different signal templates, are well separated from each other. In each of those partition, events are binned in the NN score of the tZq output node to separate each tZq signal template from the various backgrounds. The resulting histograms are shown for the measurement of $p_T(j')$ and $m(3\ell)$ in Figs. 4.31 and 4.32, respectively. The upper panels display the pre-fit and the lower plots the post-fit histograms. It is well visible that the uncertainty can be reduced in the post-fit distributions in almost all bins. However, in the signal-enriched bins, the uncertainty increases. This is understood since the uncertainty in the signal normalizations is not taken into account in the pre-fit distributions. To constrain uncertainties in the backgrounds, all CRs are included in each fit as well. Due to the coarse binning of the measured observables, the use of regularization was found not to be necessary.

4.8.4. Results

The differential cross sections for the tZq process are measured as shown in Figs. 4.33 to 4.36. The precision is as low as 15% for observables that are reconstructed from leptonic objects only, and as low as 25% for observables that include jets.

Observables that are defined solely based on leptons have a more diagonal response matrix, as already visible in Fig. 4.30. As a consequence, each signal strength parameter can be constrained very well, which leads to smaller uncertainties in the final results. The observables that include jets are less diagonal in their response matrices, and hence larger uncertainties in the measured cross sections are observed. The measured distributions are plotted together with the theory prediction of tZq at NLO in the 4FS and 5FS. Theory uncertainties in these predictions include uncertainties in the matrix element scales μ_R and μ_F, the PDF, ISR, and FSR.

To quantify the agreement of the data with the theory, a χ^2 test is performed on the extracted data with respect to the tZq prediction in the 4FS and 5FS. The covariance matrices from the fit and theory predictions are used as shown for the $p_T(\ell, \ell')$ variable

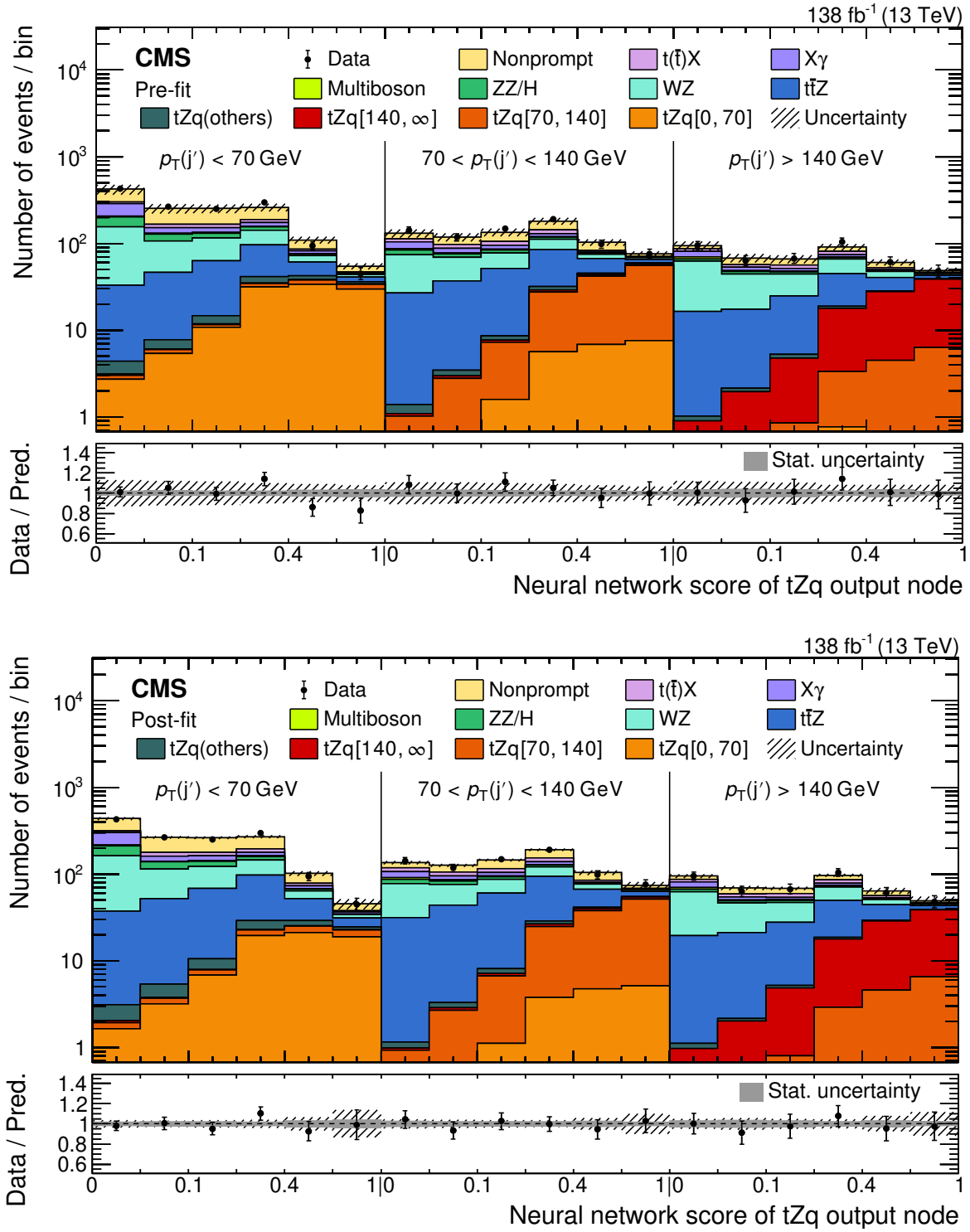

Fig. 4.31.: Pre-fit (upper) and post-fit (lower) distributions of the NN score of the tZq output node for events in the SR_{tZq}, used for the $p_T(j')$ differential cross section measurement at particle level. The data are shown by the points and the predictions by the colored histograms. The vertical lines on the points represent the statistical uncertainty in the data, and the hatched area is the total uncertainty in the prediction. The events are split into three subregions based on the value of $p_T(j')$ measured at the detector level. Three different tZq templates, defined by the same values of $p_T(j')$ at particle level and shown in different shades of orange and red, are used to model the contribution of each particle-level bin. Reconstructed tZq events that are outside of the fiducial phase space are labeled as "tZq (others)" and represent a minor contribution. The lower panels show the ratio of the data to the prediction, with the gray band indicating the uncertainty from the finite number of simulated events.

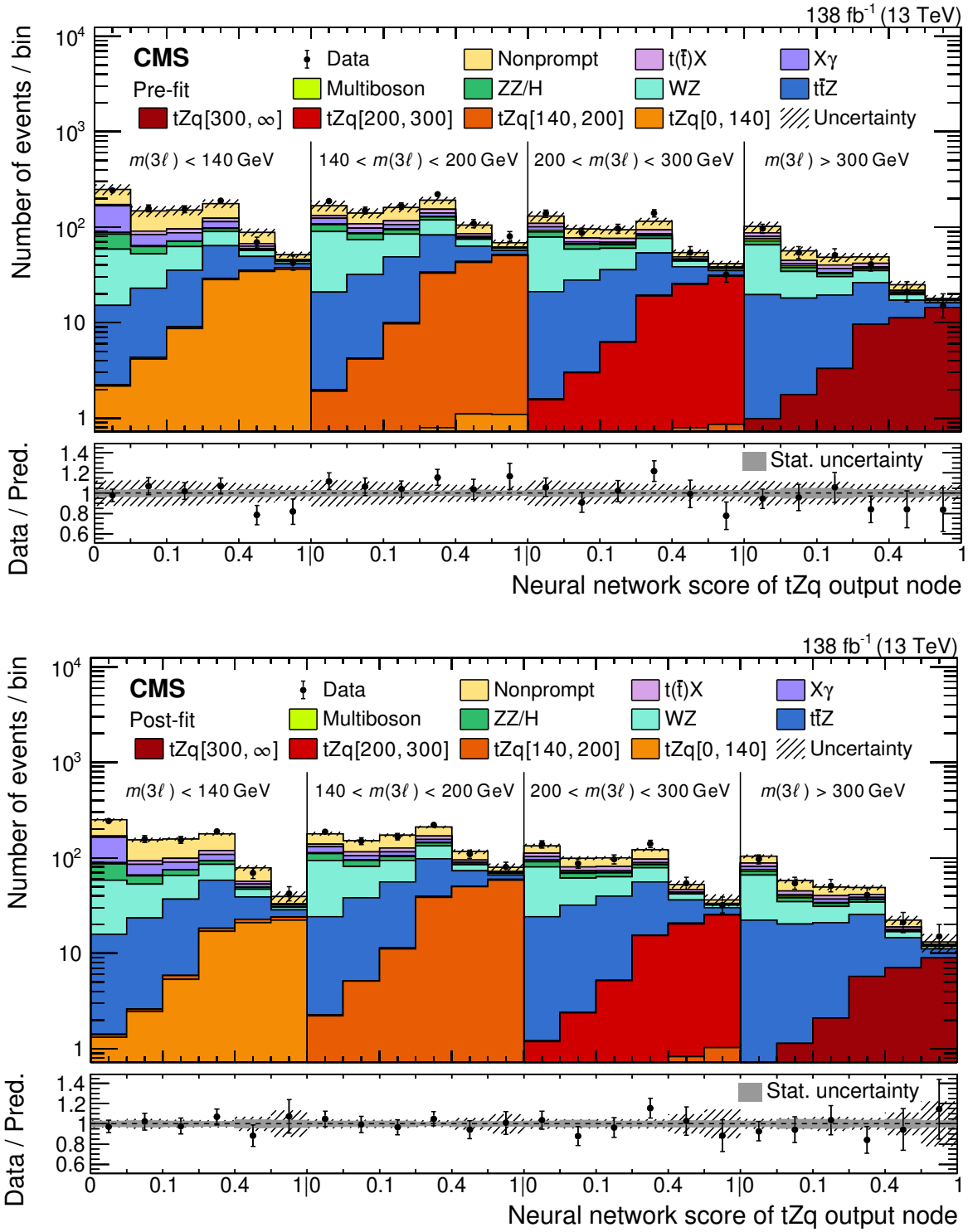

Fig. 4.32.: Pre-fit (upper) and post-fit (lower) distributions of the NN score of the tZq output node for events in the SR_{tZq}, used for the $m(3\ell)$ differential cross section measurement at the parton level. The data are shown by the points and the predictions by the colored histograms. The vertical lines on the points represent the statistical uncertainty in the data, and the hatched area is the total uncertainty in the prediction. The events are split into four subregions based on the value of $m(3\ell)$ measured at the detector level. Four different tZq templates, defined by the same values of $m(3\ell)$ at the parton level and shown in different shades of orange and red, are used to model the contribution of each parton-level bin. The lower panels show the ratio of the data to the prediction, with the gray band indicating the uncertainty from the finite number of simulated events.

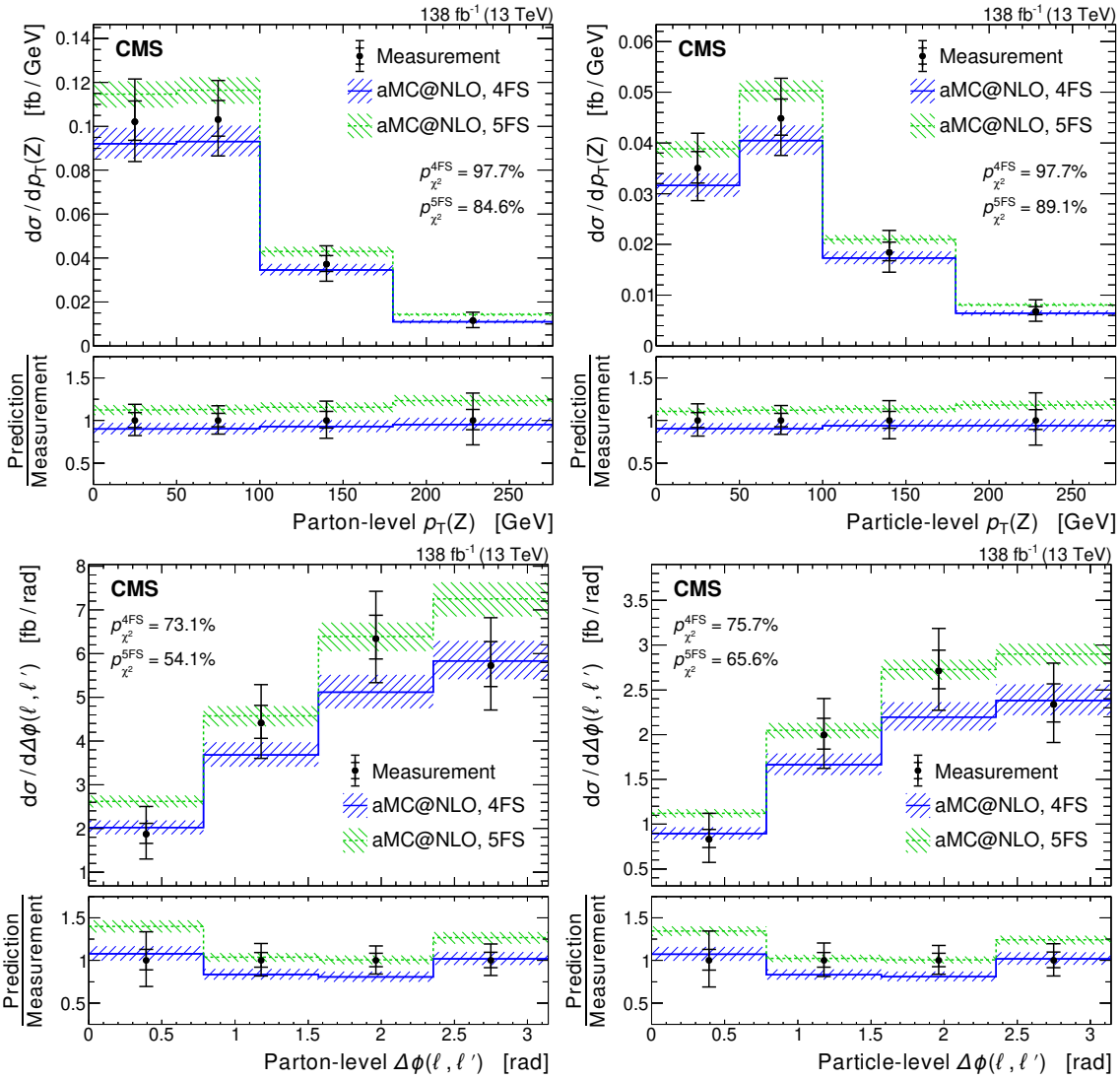

Fig. 4.33.: Absolute differential cross sections as a function of $p_T(\ell,\ell')$ measured at the parton (upper left) and particle levels (upper right), as well as a function of $p_T(j')$ (lower left) and $|\eta(j')|$ (lower right) at particle level. The observed values are shown as black points, with the inner and outer vertical bars giving the systematic and total uncertainties, respectively. The SM predictions for the tZq process are based on events simulated in the 5FS (green) and 4FS (blue). The p-values of the χ^2 tests are given to quantify their compatibility with the measurement. The lower panels show the ratio of the simulation to the measurement.

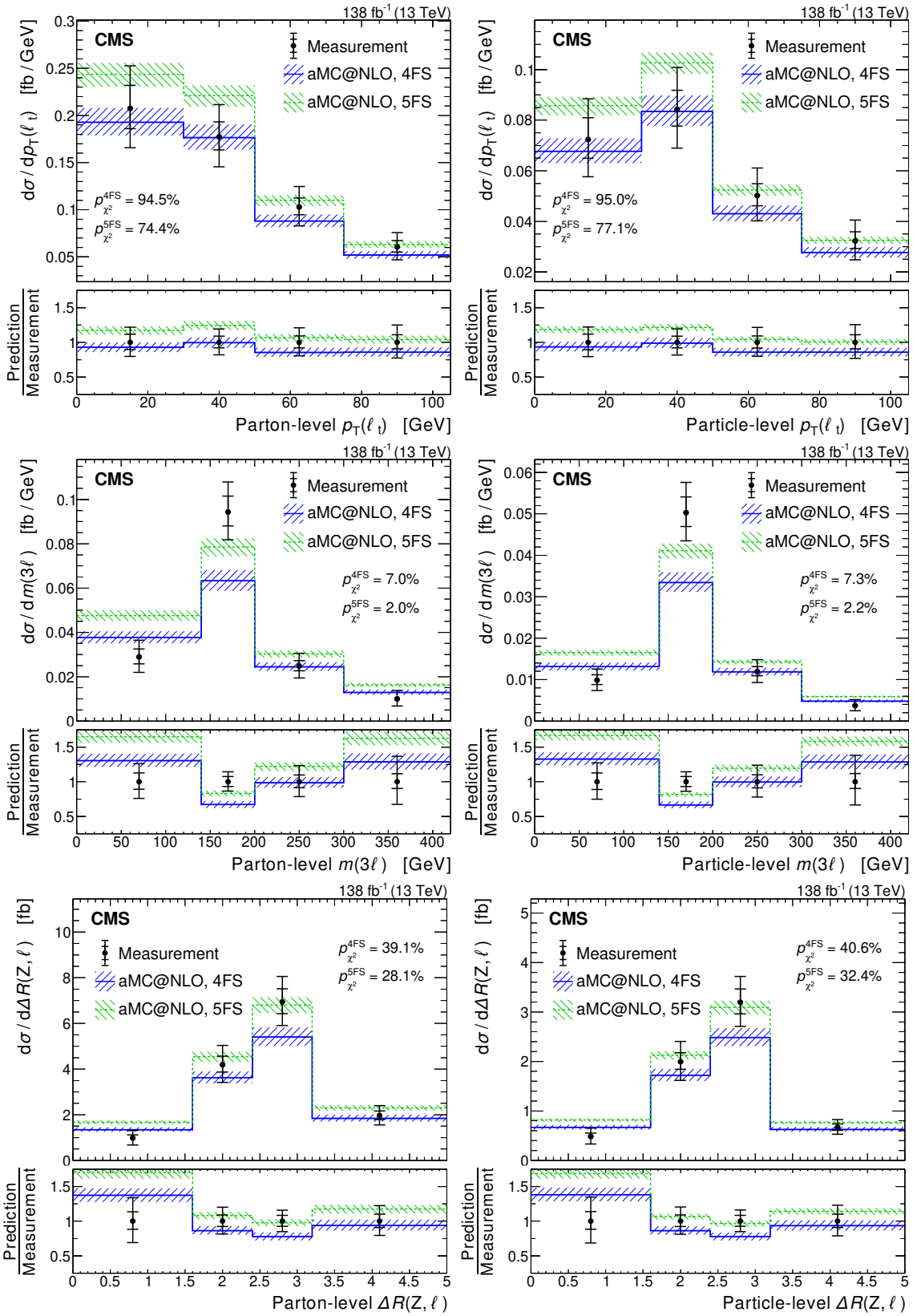

Fig. 4.34.: Absolute differential cross sections at the parton (left) and particle level (right) measured as a function of $\Delta\phi(\ell,\ell')$ (upper), p_{T,ℓ_W} (middle) and $m(3\ell)$ (lower). The observed values are shown as black points, with the inner and outer vertical bars giving the systematic and total uncertainties, respectively. The SM predictions for the tZq process are based on events simulated in the 5FS (green) and 4FS (blue). The p-values of the χ^2 tests are given to quantify their compatibility with the measurement. The lower panels show the ratio of the simulation to the measurement.

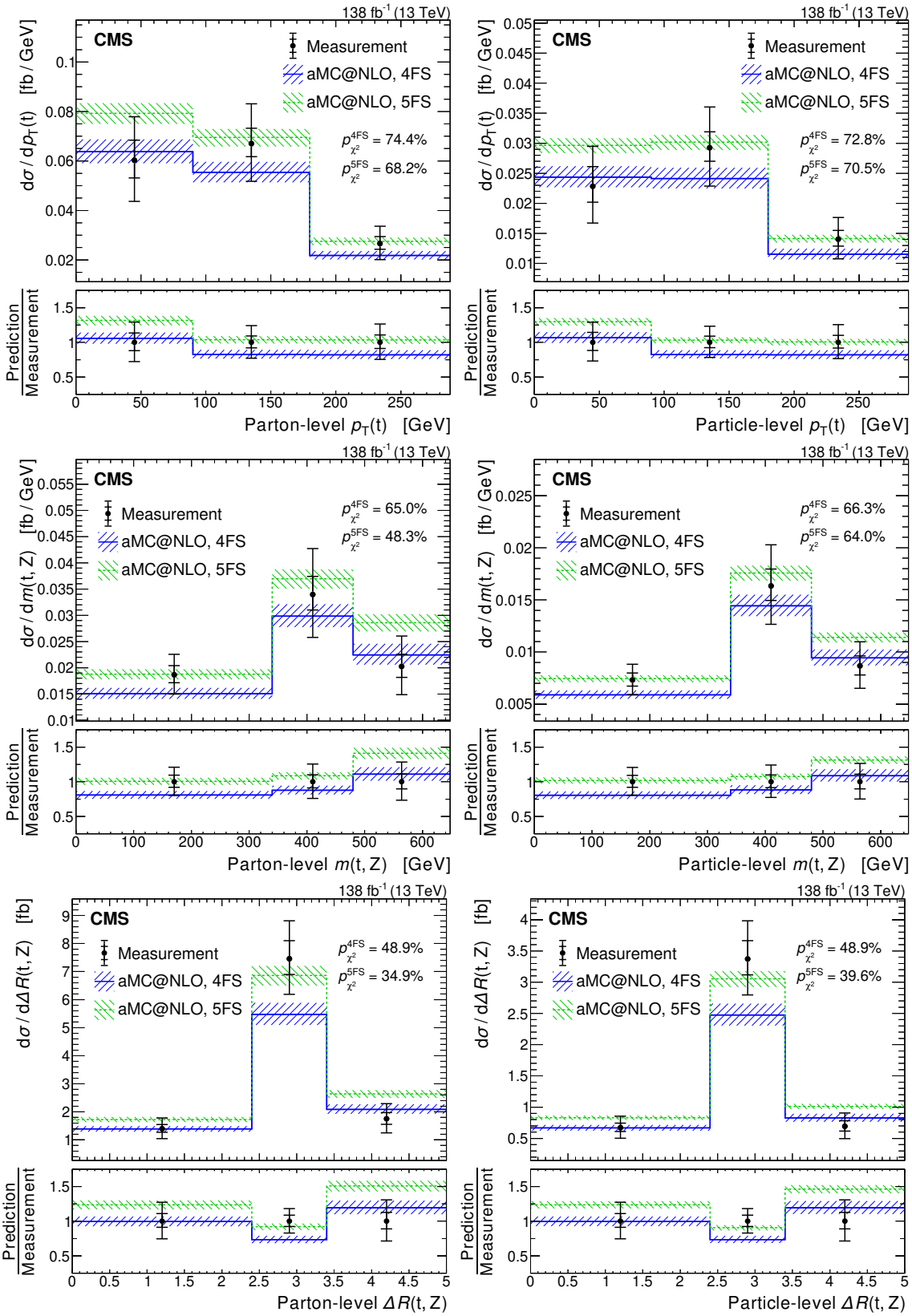

Fig. 4.35.: Absolute differential cross sections at the parton (left) and particle level (right) measured as a function of $p_T(t)$ (upper), $m(t, Z)$ (middle) and $\cos(\theta^{\star}_{pol})$ (lower). The observed values are shown as black points, with the inner and outer vertical bars giving the systematic and total uncertainties, respectively. The SM predictions for the tZq process are based on events simulated in the 5FS (green) and 4FS (blue). The p-values of the χ^2 tests are given to quantify their compatibility with the measurement. The lower panels show the ratio of the simulation to the measurement.

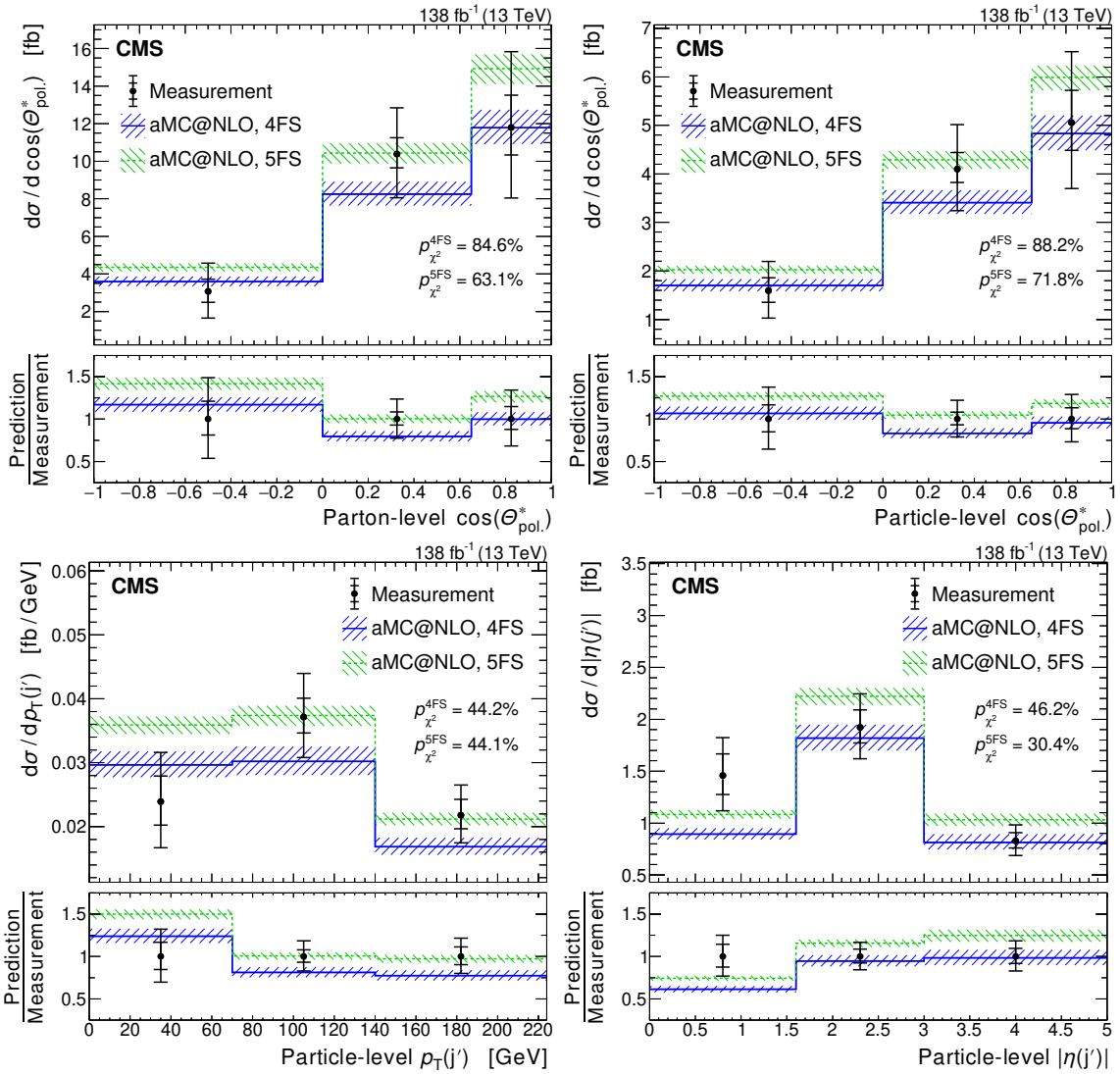

Fig. 4.36.: Absolute differential cross sections measured as a function of $\cos(\theta^{\star}_{\mathrm{pol}})$ at the parton (upper left) and particle level (upper right), as well as a function of $p_{\mathrm{T}}(\mathrm{j}')$ (lower left) and $|\eta(\mathrm{j}')|$ (lower right) at particle level. The observed values are shown as black points, with the inner and outer vertical bars giving the systematic and total uncertainties, respectively. The SM predictions for the tZq process are based on events simulated in the 5FS (green) and 4FS (blue). The p-values of the χ^2 tests are given to quantify their compatibility with the measurement. The lower panels show the ratio of the simulation to the measurement.

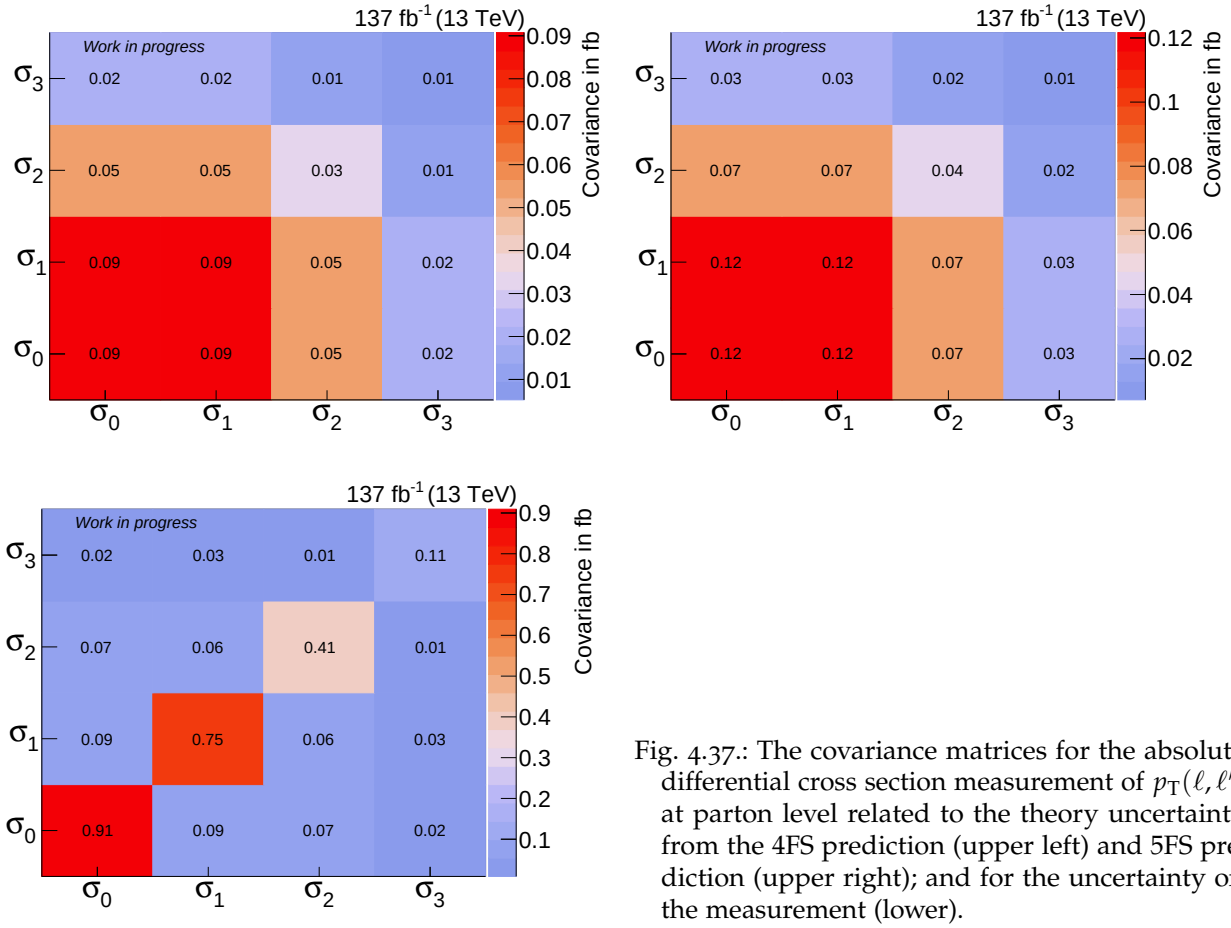

Fig. 4.37.: The covariance matrices for the absolute differential cross section measurement of $p_{\mathrm{T}}(\ell, \ell')$ at parton level related to the theory uncertainty from the 4FS prediction (upper left) and 5FS prediction (upper right); and for the uncertainty on the measurement (lower).

at the parton level in Fig. 4.37. The measurement dominates the diagonal elements of the covariance matrices but only shows small correlations between the different parton-level bins. Theory uncertainties are assumed to be fully correlated between the different parton-level bins. They contribute with off-diagonal elements with nonnegligible content.

The p-value of the χ^2 test is calculated and shows good agreement between data and theory in most of the distributions with one exception. The $m(3\ell)$ distribution has a p-value of about 7% (2%) at parton and particle level for the comparison with the 4FS (5FS) prediction as displayed in Fig. 4.34. It remains to be seen in future analyses with improved statistical precision if a significant disagreement in the modeling of the theoretical prediction in this distribution is present.

As the extrapolation from the detector level to the particle level is not so large, the systematic uncertainties at particle level are smaller than at parton level. The improvement in the uncertainty is, however, very small since all bins of the measurements are dominated by statistical uncertainties. The two different definitions are still useful as theorists may prefer one or the other for comparisons. Additionally, they serve as a cross-check. Distributions at particle level are closer to the data, e.g. in the upper plot in Fig. 4.34 the p_{T} cut on the lepton reduces visibly the contribution in the first bin.

Different sources of systematic uncertainties are studied by evaluating the impact and value of each nuisance parameter in the fit both using the expected distribution, and the measured result in the data. As illustrated in Fig. 4.38 for the measurement of the $m(3\ell)$

distribution at parton level, and $p_T(j')$ at particle level, the behavior are compatible with the inclusive fit. The leading systematic uncertainty now comes from the normalization of $X\gamma$ processes. This can be understood by its correlation with other nuisance parameters that are constrained when including events from the region $CR_{Z\gamma}$ in the fit.

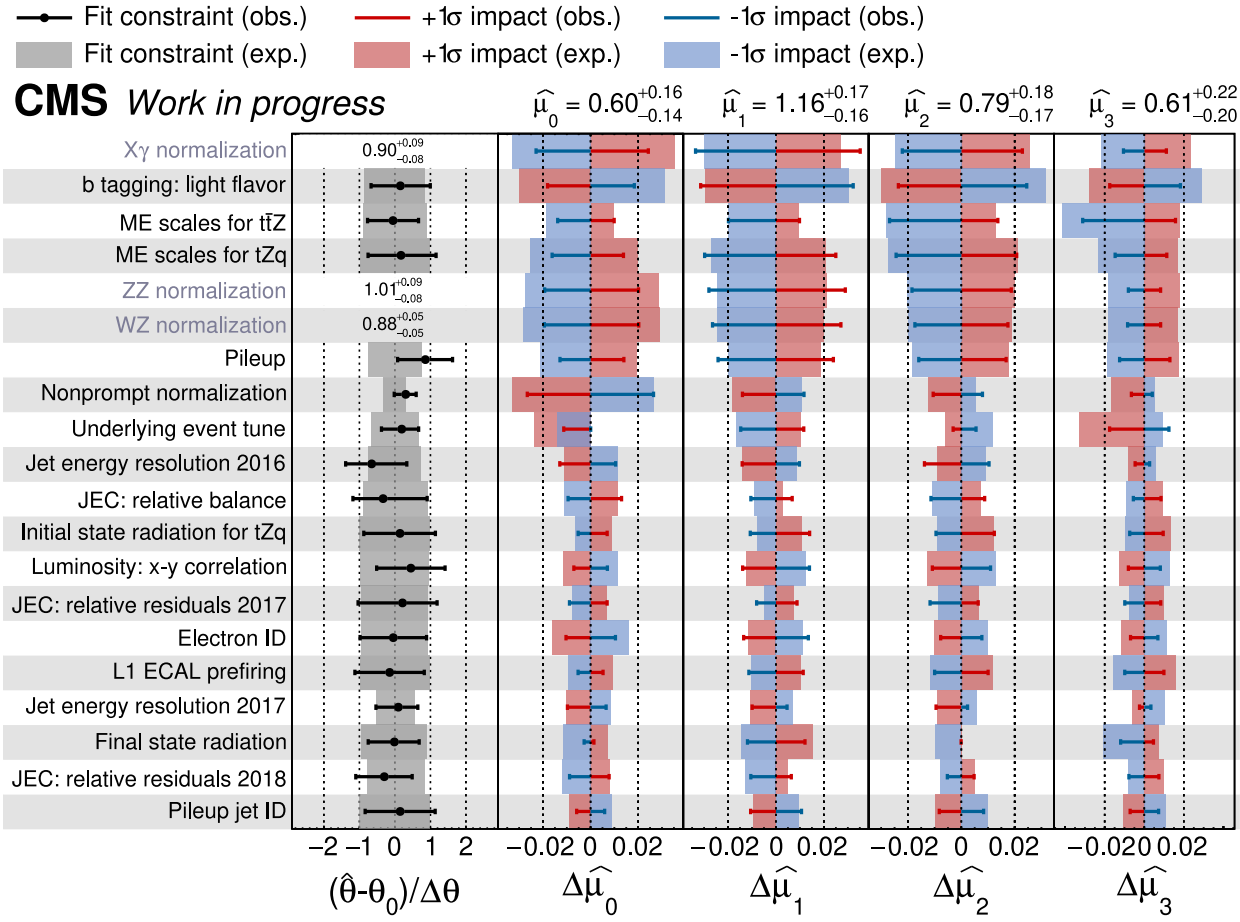

Fig. 4.38.: List of the leading systematic uncertainties in the differential cross section measurement for $m(3\ell)$ at parton level. Each uncertainty source is treated as a separate nuisance parameter in the fit. The black dots with the horizontal error bars in the first column show the difference of the nuisance parameter after the fit to data ($\hat{\Theta}$) to its assumed value (Θ_0) divided by its assumed uncertainty ($\Delta\Theta$). The dark gray bands show the same as it is expected from a fit to the prediction. The further columns show the impacts ($\Delta\hat{\mu}_i$) of each uncertainty source on the fitted signal strength parameter ($\hat{\mu}_i$) as it is observed in data (horizontal error bars) and expected (bands) for the up (red) and down (blue) variation of the nuisance parameter.

Normalized cross sections are calculated to increase the significance of the measurement on shape effects. By dividing through the total cross section, systematic uncertainties cancel out and are thus reduced. The covariance matrix from the fit is used to calculate the uncertainties in the normalized differential cross sections via Gaussian error propagation. It is observed that the statistical and systematic uncertainties have different correlation behavior. Statistical uncertainties are anticorrelated between two neighboring generator-level bins, while systematic uncertainties are correlated between all bins. For this reason, and due to nonlinearities in the ratio when computing the normalized differential cross

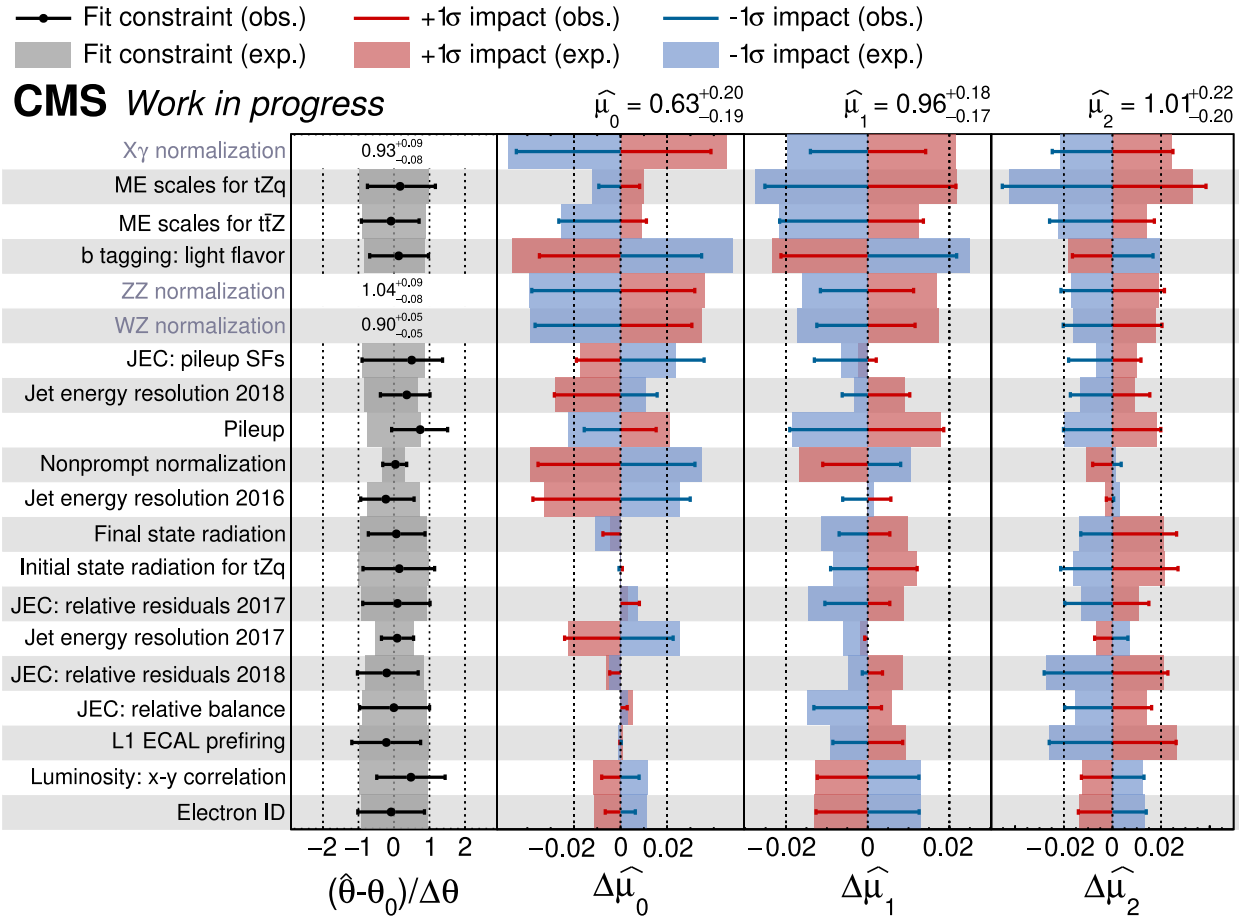

Fig. 4.39.: List of the leading systematic uncertainties in the differential cross section measurement for $p_T(j')$ at particle level. Each uncertainty source is treated as a separate nuisance parameter in the fit. The black dots with the horizontal error bars in the first column show the difference of the nuisance parameter after the fit to data ($\hat{\Theta}$) to its assumed value (Θ_0) divided by its assumed uncertainty ($\Delta\Theta$). The dark gray bands show the same as it is expected from a fit to the prediction. The further columns show the impacts ($\Delta\hat{\mu}_i$) of each uncertainty source on the fitted signal strength parameter (μ_i) as it is observed in data (horizontal error bars) and expected (bands) for the up (red) and down (blue) variation of the nuisance parameter.

sections, the result is expected to be more stable when propagating the statistical and systematic uncertainties independently and adding them in quadrature after propagation. Covariance matrices of the statistical and systematic uncertainty are shown for the $p_{\mathrm{T}}(\ell,\ell')$ at parton level in Fig. 4.40.

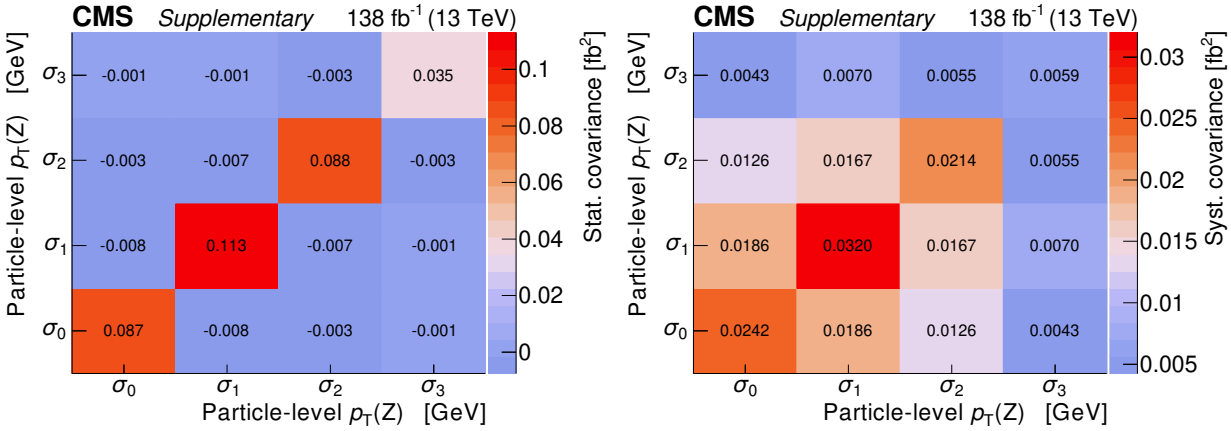

Fig. 4.40.: Covariance matrices of the measured absolute cross section from the differential measurement of the $p_{\mathrm{T}}(\ell,\ell')$ at parton level. The covariance matrix corresponding to the statistic uncertainty (left) and systematic uncertainty (right) are shown.

The normalized cross sections are presented in Figs. 4.41, 4.42 and 4.43. The uncertainties in the theory predictions are fully correlated and often not visible in the normalized case. The level of agreement is similar to the case of the absolute differential cross sections, however, shape effects are now more visible. The statistical precision is not yet good enough to judge which of the theoretical predictions is preferred by the data. This remains to be seen in future analyses with more data.

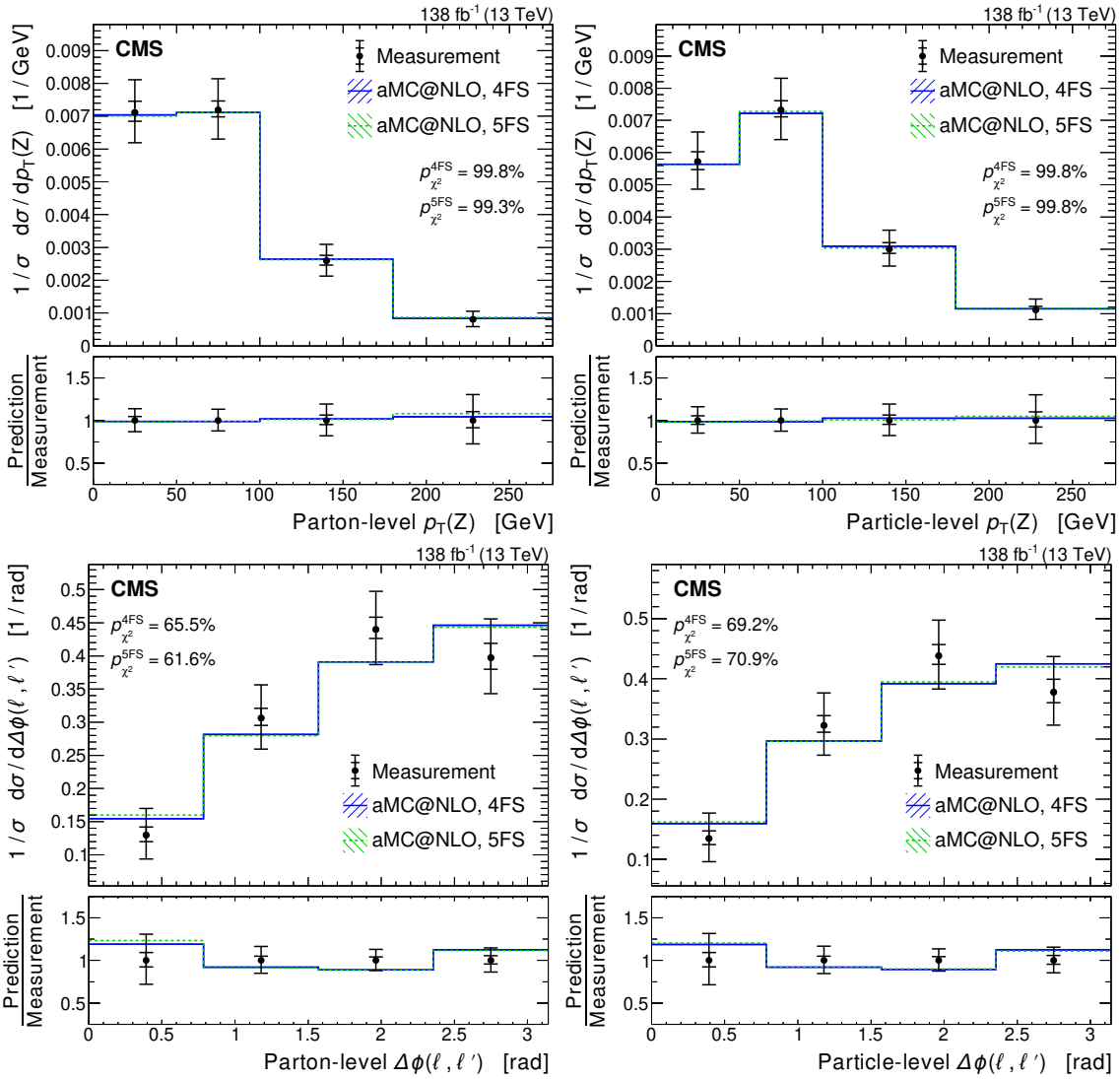

Fig. 4.41.: Normalized differential cross sections measured as a function of $p_T(\ell, \ell')$ at the parton (upper left) and particle level (upper right), as well as a function of $p_T(j')$ (lower left) and $|\eta(j')|$ (lower right) at particle level. The observed values are shown as black points, with the inner and outer vertical bars giving the systematic and total uncertainties, respectively. The SM predictions for the tZq process are based on events simulated in the 5FS (green) and 4FS (blue). The p-values of the χ^2 tests are given to quantify their compatibility with the measurement. The lower panels show the ratio of the simulation to the measurement.

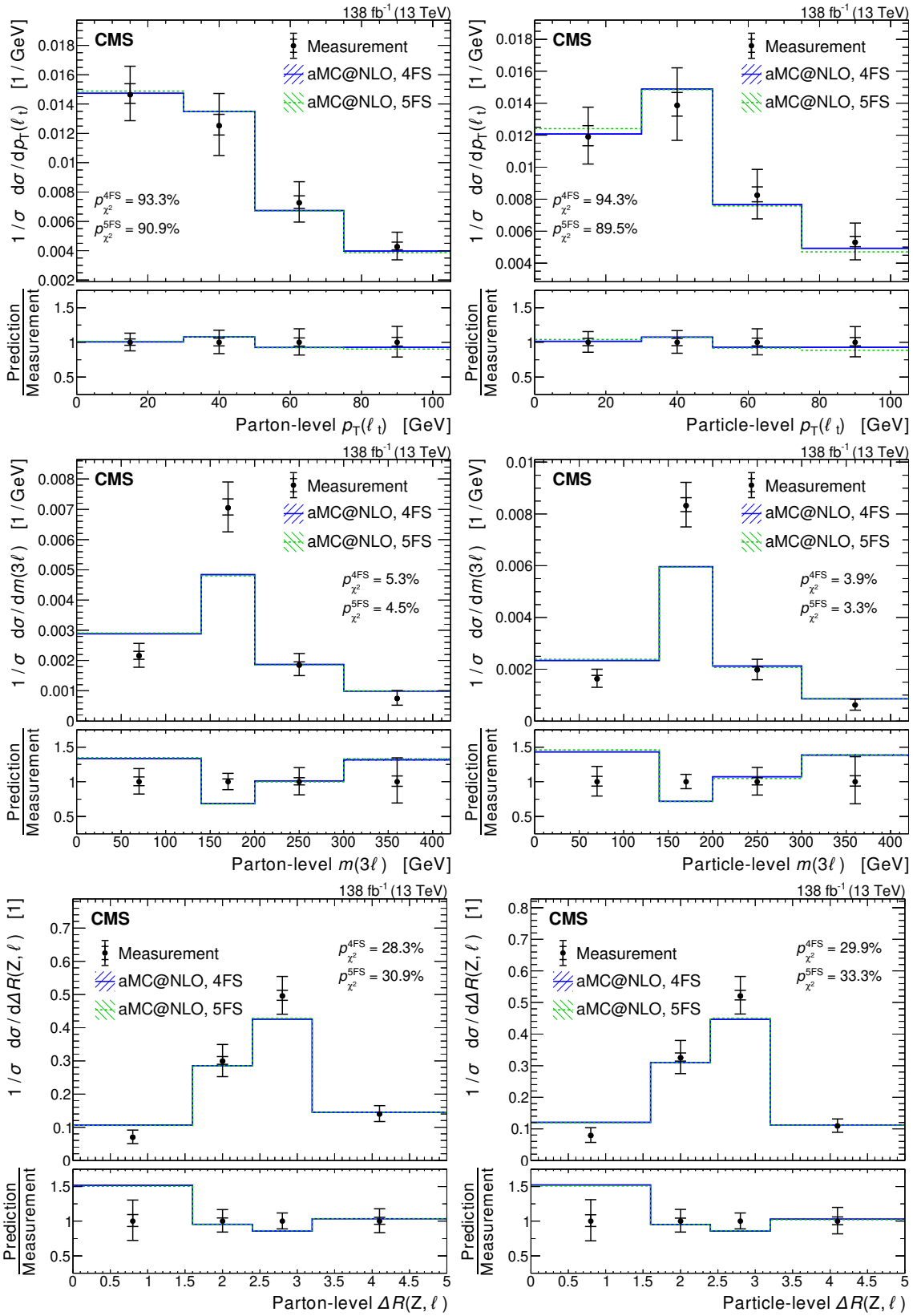

Fig. 4.42.: Normalized differential cross sections measured at the parton (left) and particle level (right) as a function of $\Delta\phi(\ell,\ell')$ (upper), p_{T,ℓ_W} (middle) and $m(3\ell)$ (lower). The observed values are shown as black points, with the inner and outer vertical bars giving the systematic and total uncertainties, respectively. The SM predictions for the tZq process are based on events simulated in the 5FS (green) and 4FS (blue). The p-values of the χ^2 tests are given to quantify their compatibility with the measurement. The lower panels show the ratio of the simulation to the measurement.

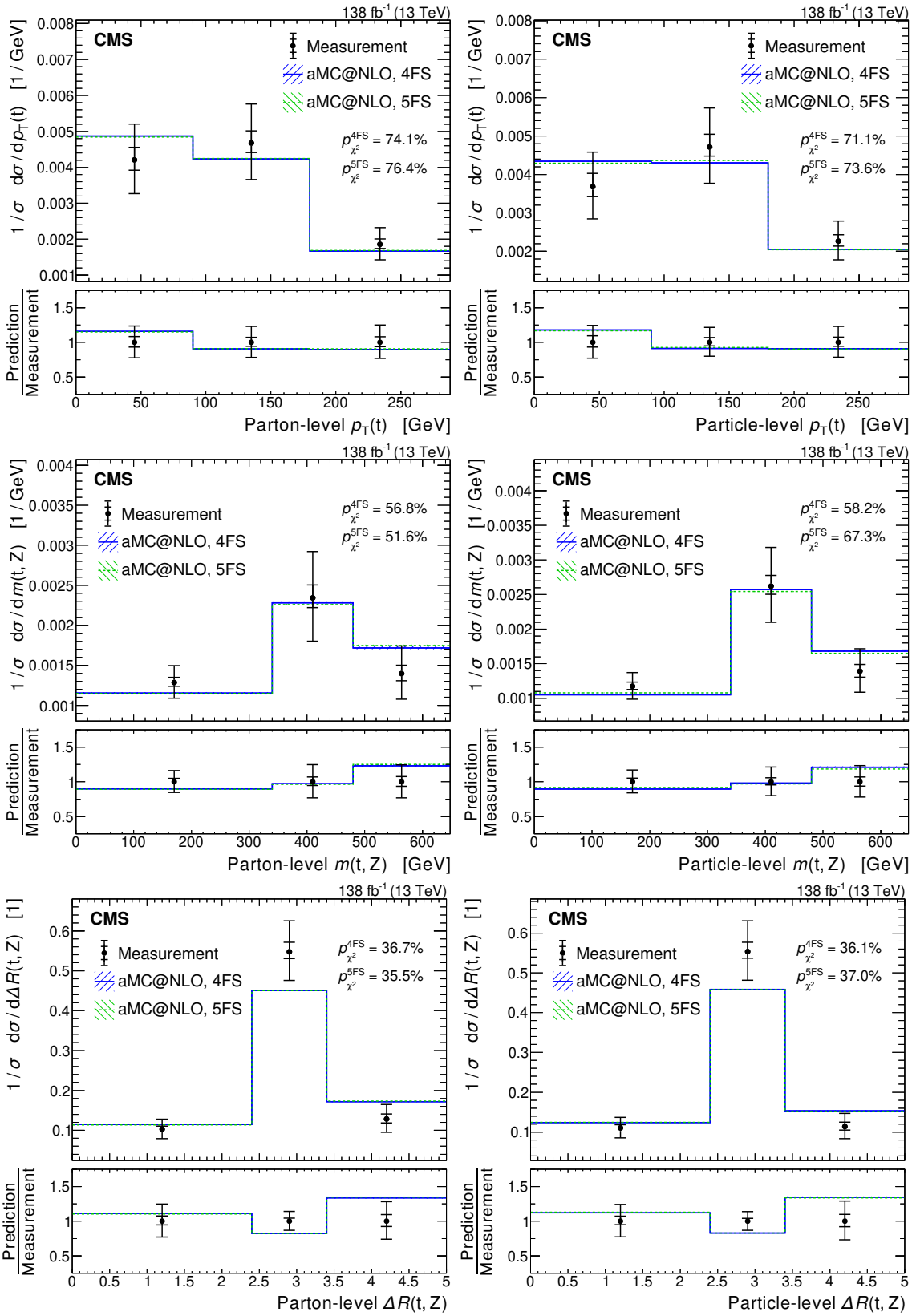

Fig. 4.43.: Normalized differential cross sections measured at the parton (left) and particle level (right) as a function of $p_T(t)$ (upper), $m(t,Z)$ (middle) and $\cos(\theta^{\star}_{pol})$ (lower). The observed values are shown as black points, with the inner and outer vertical bars giving the systematic and total uncertainties, respectively. The SM predictions for the tZq process are based on events simulated in the 5FS (green) and 4FS (blue). The p-values of the χ^2 tests are given to quantify their compatibility with the measurement. The lower panels show the ratio of the simulation to the measurement.

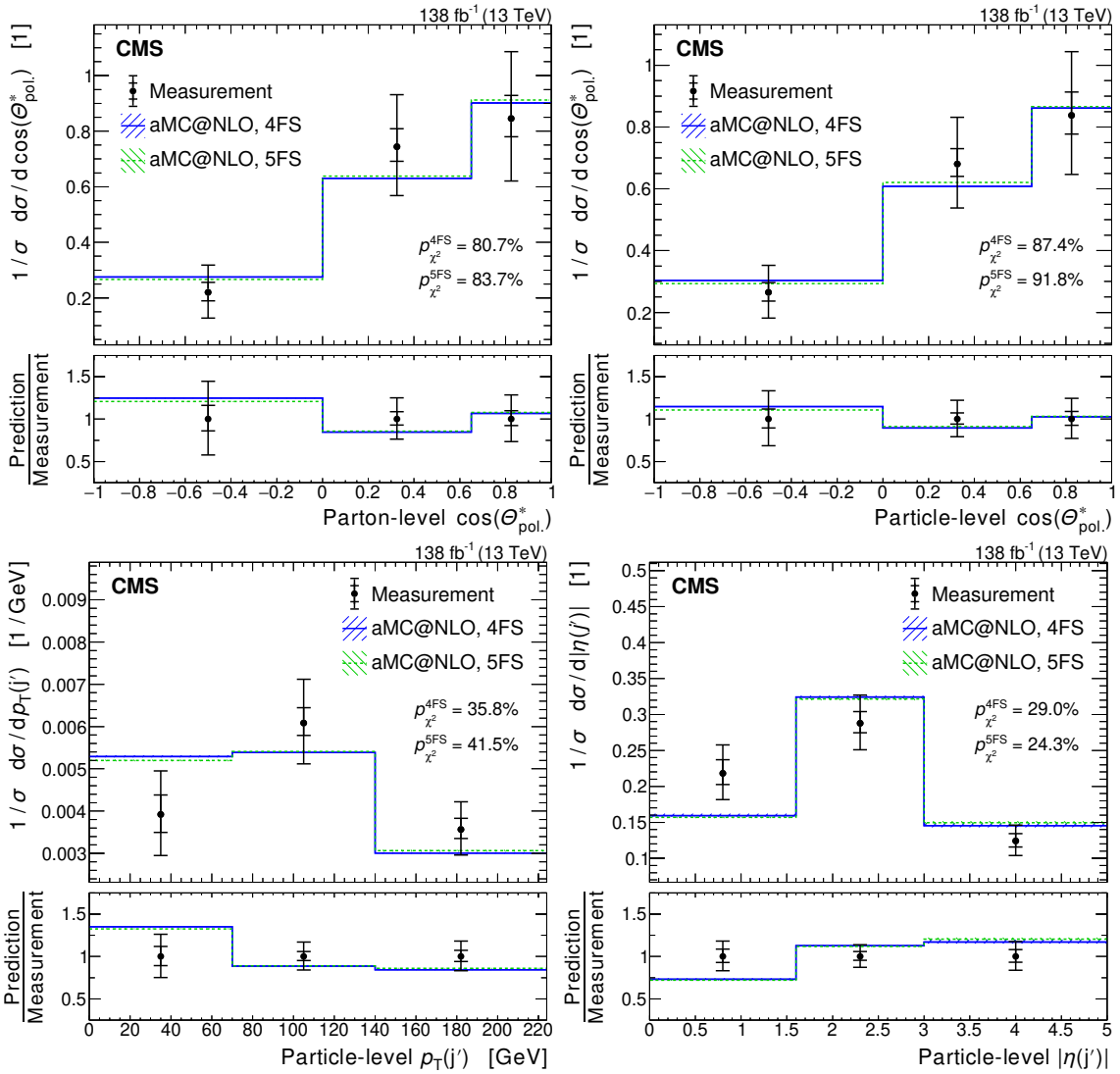

Fig. 4.44.: Normalized differential cross sections measured as a function of $\cos(\theta^{\star}_{\mathrm{pol}})$ at the parton (upper left) and particle level (upper right), as well as a function of $p_{\mathrm{T}}(\mathrm{j}')$ (lower left) and $|\eta(\mathrm{j}')|$ (lower right) at particle level. The observed values are shown as black points, with the inner and outer vertical bars giving the systematic and total uncertainties, respectively. The SM predictions for the tZq process are based on events simulated in the 5FS (green) and 4FS (blue). The p-values of the χ^2 tests are given to quantify their compatibility with the measurement. The lower panels show the ratio of the simulation to the measurement.

4.9. Measurement of the top quark spin asymmetry

As the top quark is so heavy and decays before it hadronizes, its spin influences the preferred direction of the decay lepton. The high degree of polarization in singly produced top quarks can be measured from angular distributions of the lepton with respect to some axis. A more detailed theoretical discussion is given in Section 1.3.2.

This section presents the first measurement of the spin asymmetry A_ℓ for the tZq production, which is proportional to the top quark polarization. The measurement is carried out in the optimized basis in a similar way as it was previously done in the t-channel single top quark analysis [65], via the differential cross section as a function of the polarization angle $\cos(\theta^\star_{\text{pol}})$,

$$\frac{\mathrm{d}\sigma_{\text{tZq}}}{\mathrm{d}\cos(\theta^\star_{\text{pol}})} = \sigma_{\text{tZq}} \left(\frac{1}{2} + A_\ell \cos(\theta^\star_{\text{pol}}) \right) . \tag{4.20}$$

This means the normalized differential cross section of $\cos(\theta^\star_{\text{pol}})$ is expected to follow a linear increase. At detector level and at particle level, the cross section differs from a linear behavior, as shown in Fig. 4.29, due to efficiency and acceptance effects in the event selection. The parton-level distribution is obtained in the full phase space by extrapolation from the detector level using efficiencies and acceptances from the simulation. Because all corrections are applied at parton level, a linear relation to Eq. (4.20) is obtained as visible in Fig. 4.29. The differential cross section at parton level, shown in Fig. 4.44, also exhibits a good agreement with a linear behavior. Thus, the measured parton-level distribution can directly be input in Eq. (4.20) to determine the spin asymmetry.

In previous analyses, a χ^2 fit of a linear function was performed on the measured $\mathrm{d}\sigma_{\text{tZq}}/\mathrm{d}\cos(\theta^\star_{\text{pol}})$ distribution to extract A_ℓ [65]. However, this assumes Gaussian limits and is only valid for large sample sizes. In this analysis, an approach without those approximations is performed by a maximum likelihood fit directly to data. The spin asymmetry is used as a free parameter together with a signal strength associated with the total tZq cross section. As before, three parton-level bins are chosen, using the same intervals. But this time, each parton-level contribution is scaled according to Eq. (4.20). The parameterization allows to have the full likelihood associated to A_ℓ and the uncertainty is directly obtained from the profiled likelihood ratio. The spin asymmetry is measured to be

$$A_\ell = 0.54 \pm 0.16\ (\text{stat}) \pm 0.06\ (\text{syst}) , \tag{4.21}$$

where A_ℓ is dominated by the statistical uncertainty. The theoretical prediction of the spin asymmetry is extracted from the 4FS and 5FS tZq simulation as 0.44 and 0.45, respectively, with negligible uncertainties in comparison to those of the measurement. Good agreement between the data and the predictions has been found. The simultaneously measured total tZq cross section is

$$\sigma_{\text{tZq}} = 81.1\ ^{+9.6}_{-9.0}\ (\text{stat})\ ^{+7.1}_{-6.9}\ (\text{syst})\ \text{fb} , \tag{4.22}$$

which is in agreement within the systematic uncertainties but not as precise as when measuring σ_{tZq} alone. This is expected since the fit has more freedom and the binning

has been chosen to gain sensitivity to A_ℓ. The pre-fit and post-fit distributions in bins of $\cos(\theta^\star_{\text{pol}})$ and the NN score of the tZq output node are shown in Fig. 4.45. The extracted differential cross section and the profile likelihood ratio as a function of A_ℓ are provided in Fig. 4.46.

A value of $A_\ell > 0.5$ implies a polarization greater than one, which is unphysical. The result is, however, unproblematic since the area with $A_\ell < 0.5$ is well within the obtained uncertainties.

The simultaneous measurement of A_ℓ and σ_{tZq} allows the use of both values consistently. For example, it can be used to test BSM scenarios with anomalous couplings of W-t-b interactions with right chirality. Further, it could be used to constrain Wilson coefficients that are sensitive to these interactions. Care has to be taken as the background is subtracted under SM assumptions. The confidence intervals of the fit in the 2D space of A_ℓ and σ_{tZq} compared to SM predictions of tZq in the 4FS and 5FS are shown in Fig. 4.47. It can be seen that the 4FS prediction has a slightly better agreement with the data.

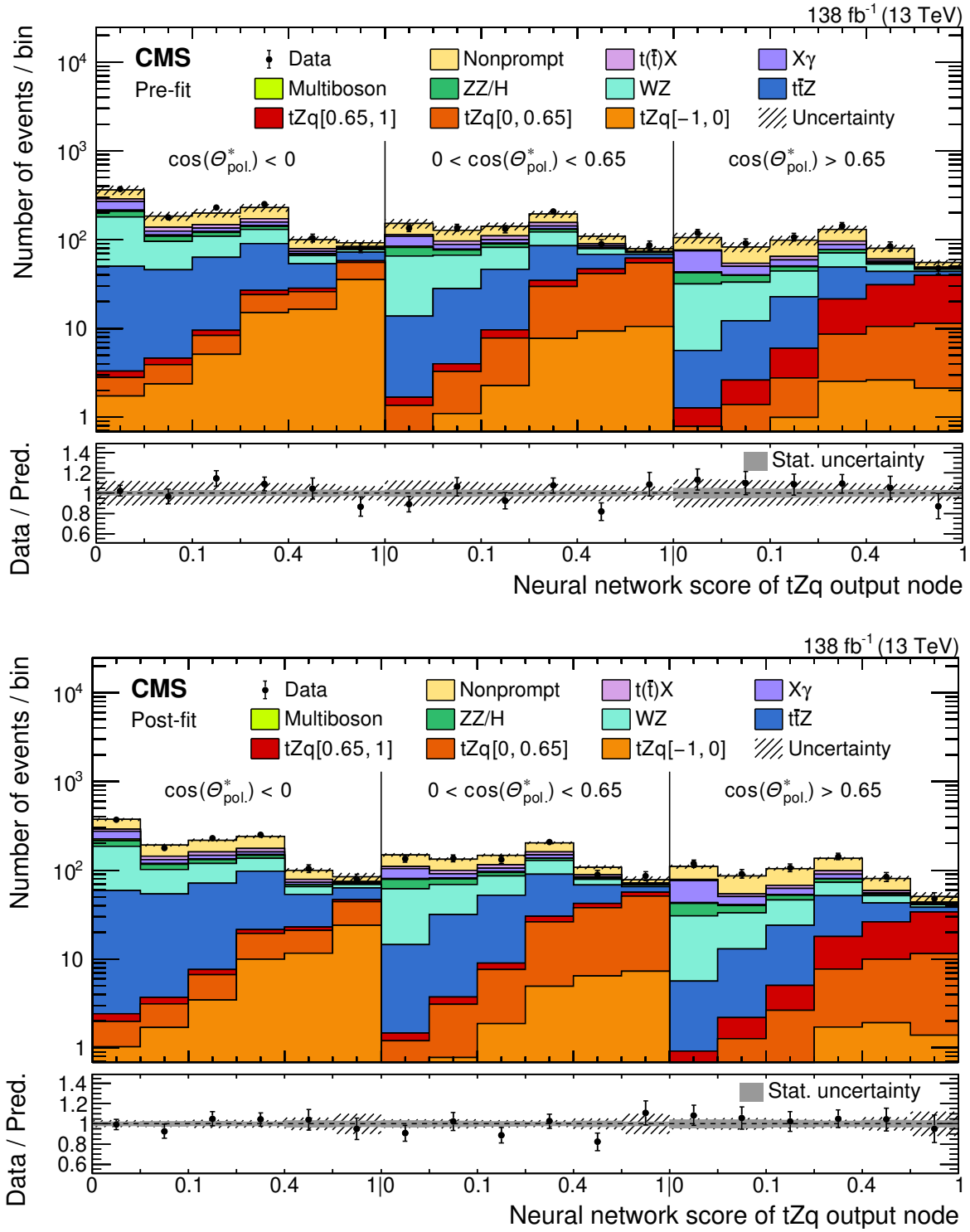

Fig. 4.45.: Pre-fit (upper) and post-fit (lower) distributions of the NN score of the tZq output node for events in the SR_{tZq}, used for the measurement of the spin asymmetry from the $\cos(\theta^{\star}_{pol})$ distribution at the parton level. The data are shown by the points and the predictions by the colored histograms. The vertical lines on the points represent the statistical uncertainty in the data, and the hatched area is the total uncertainty in the prediction. The events are split into three subregions based on the value of $\cos(\theta^{\star}_{pol})$ measured at the detector level. Three different tZq templates, defined by the same values of $\cos(\theta^{\star}_{pol})$ at parton level and shown in different shades of orange and red, are used to model the contribution of each parton-level bin. The lower panels show the ratio of the data to the prediction, with the gray band indicating the uncertainty from the finite number of MC events.

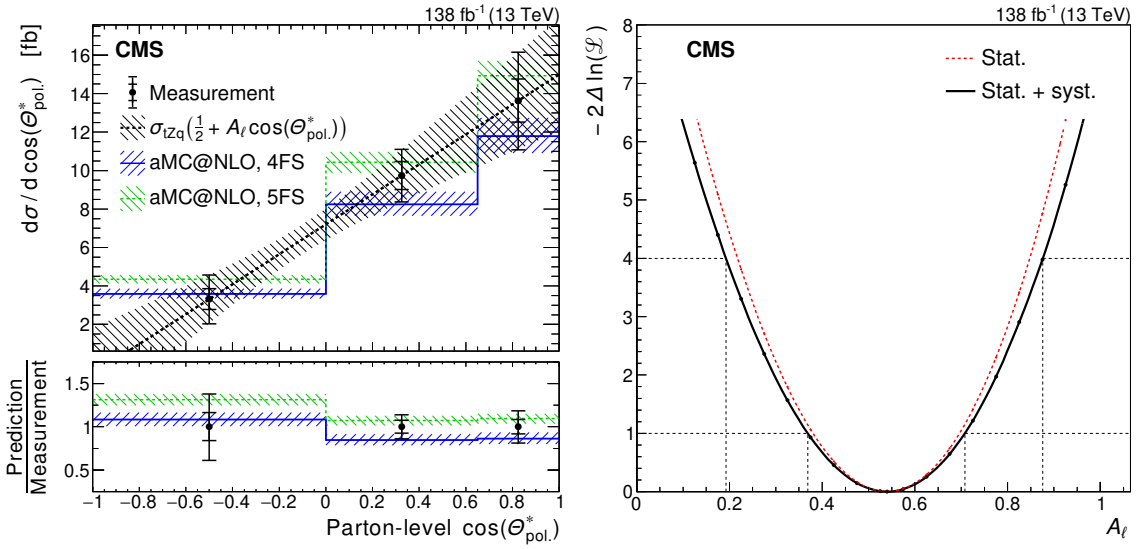

Fig. 4.46.: The left plot shows the measured absolute $\cos(\theta^{\star}_{\text{pol}})$ differential cross section at the parton level used in the extraction of the top quark spin asymmetry. The generator-level bins are parameterized according to Eq. (1.45), shown as a dashed line in the plot, such that the spin asymmetry is directly used as a free parameter in the fit. The observed values of the generator-level bins are shown as black points with the inner and outer vertical bars giving the systematic and total uncertainties, respectively. The SM predictions for events simulated in the 5FS (green) and 4FS (blue) are plotted as well. The lower panel displays the ratio of the MC prediction to the measurement. On the right, the negative log-likelihood in the fit for the spin asymmetry A_ℓ is shown when considering only the statistical uncertainties (dashed red line) or the combined statistical and systematic uncertainties (solid black line).

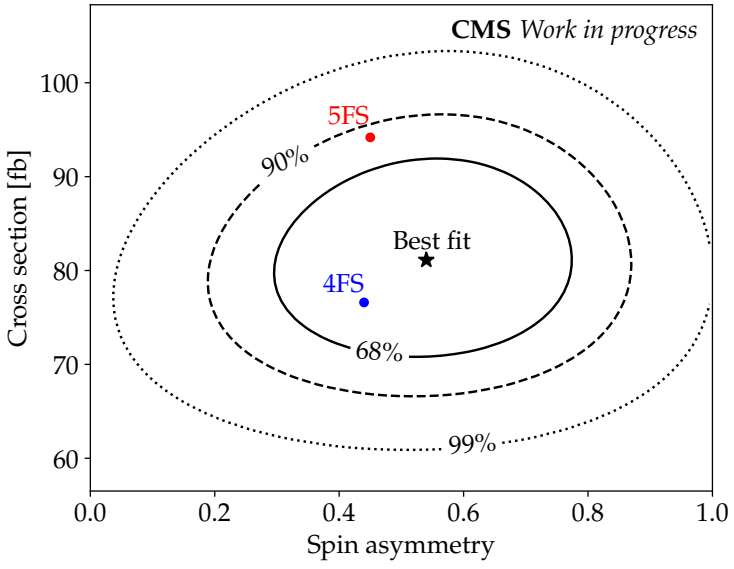

Fig. 4.47.: The value of the best fit for the measurement of the spin asymmetry as a function of A_ℓ and σ_{tZq} is shown as the black asterisk. The dots show the SM prediction for the 4FS (blue) and 5FS (red). The solid, dashed, and dotted lines show the 68%, 90%, and 99% confidence intervals, respectively.

4.10. Outlook

More data from future LHC runs will be highly beneficial for almost all measurements presented in this thesis. At the upcoming Run 3, about $300\,\mathrm{fb}^{-1}$ and at the HL-LHC about $3\,000\,\mathrm{fb}^{-1}$ of pp collision data will be collected. Neglecting the change in center-of-mass energy and the planned upgrade of the CMS experiment in 2026, the statistical uncertainties will be reduced by one over the square root of the increased luminosity. The statistical uncertainty on the inclusive tZq production cross section will be at the level of 4–5% and thus be subdominant already with the Run 3 data. At this stage, constraints on the CKM-matrix element V_{tb} from the production cross section of tZq become more relevant in a combination with those from single top quark t-channel measurements. Beyond that, but especially with the data from the HL-LHC, differential cross section measurements can be performed with higher accuracy and granularity. Measurements in events with top quarks and antiquarks separately can be performed to gain sensitivity to the proton PDFs. The measurement of the spin asymmetry will profit even more from the enlarged data sample and is projected to have a statistical precision of about 6% uncertainty in the HL-LHC. More data will also help to improve the systematic uncertainties. Thus, a precision of smaller than 8% in not unrealistic. With the available data, a measurement of the polarization in three dimensions might be possible as well. This will give additional sensitivity to effects from BSM physics. For the HL-LHC, the silicon tracker and muon system will be replaced to cover a wider pseudorapidity range. This increases the acceptance of electrons, muons, and b jets, and also helps rejecting jets from pileup in the forward region. As a result, a further reduction of statistical and systematic uncertainties is expected.

The analysis presented in this thesis is sensitive to a variety of EFT operators. However, the measurements rely on SM predictions for the various background processes. Most EFT operators that affect tZq also impact some of the background processes, most notably $\mathrm{t\bar{t}Z}$ production. In the future, consistent measurements of multiple processes affected by a mutual set of EFT operators should be performed. For example, the simultaneous measurement of the inclusive tZq and $\mathrm{t\bar{t}Z}$ cross sections. With the setup used for the presented measurement, expected uncertainties on the tZq and $\mathrm{t\bar{t}Z}$ signal strengths are shown in Fig. 4.48. As can be seen from the figure, the cross sections from both processes are anticorrelated in the measurement. A common interpretation is thus highly advantageous. Additionally, the cross section of both processes can be fit differentially, for example as a function of $p_{\mathrm{T}}(\ell, \ell')$. This would allow to perform EFT interpretations on the unfolded results, gaining sensitivity from the shape information of both distributions. Another observable that would be of particular interest is the number of jets as this has not been measured differentially for either $\mathrm{t\bar{t}Z}$ or tZq and a suspicious discrepancy can be seen in some of the figures presented in this thesis.

In future measurements, it would also be favorable to include the s-channel production of single top quarks in association with Z bosons (tZ) in the signal definition as well as tWZ where the W boson decays hadronically (tWZ, $\mathrm{W} \to \mathrm{q\bar{q}'}$). The tWZ, $\mathrm{W} \to \mathrm{q\bar{q}'}$ production represents higher-order EW corrections and interferes with tZq at NLO in

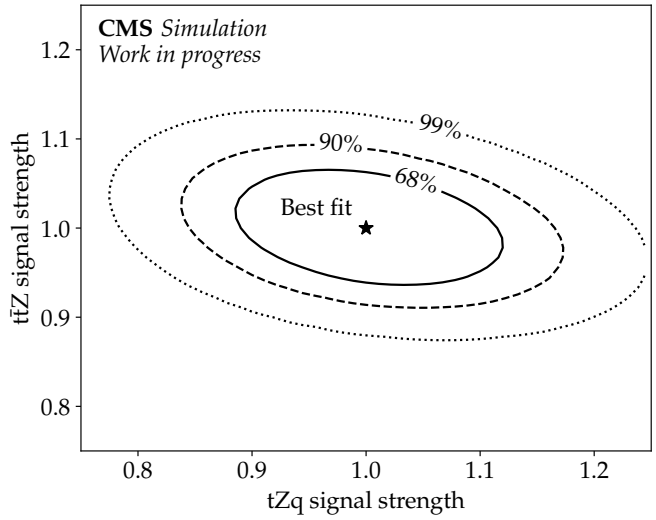

Fig. 4.48.: Expected tZq and tt̄Z signal strengths with the best fit result illustrated with the asterisk by construction at the point $(1, 1)$. The solid, dashed, and dotted lines show the 68%, 90%, and 99% confidence intervals, respectively.

the 5FS (or NNLO in 4FS). Including different production mechanisms would allow for comparisons with predictions at higher orders in perturbative EW calculations as discussed in Ref. [69]. Care has to be taken for tWZ at NLO in α_S for the Feynman diagrams with double-resonant top quarks as they overlap with those from the tt̄Z process. Ideal would be a sample generated without explicitly requiring the b quark and W boson from the decay of a top quark, similar to the simultaneous simulation of tt̄ and tW of Ref. [211].

Measurements of tZq and tt̄Z can be supplemented by selecting events with large-radius jets with high p_T, so-called "fat" jets. For this purpose, dileptonic or single leptonic final states can be targeted where either the top quark or the Z boson decay hadronically and has high enough p_T such that the decay products get collimated into one single fat jet. State-of-the-art machine learning, e.g. based algorithms based on graph neural networks can be employed to gain sensitivity in identifying fat jets with a substructure compatible with that of a top quark or a Z boson [212]. These events have a larger branching ratio and contain particularly valuable information as many EFT operators show strong deviations from SM predictions at high p_T as illustrated in Fig. 1.16. However, the reconstruction and identification of fat jets are often not well understood and prone to systematic effects both from experiment and simulation. From the experiment, the jet energy and identification algorithms of fat jets are usually not well known and calibrations can not be estimated as precisely since only few reference samples in this energy regime are available [213, 214]. On the theory side, the SM predictions in this energy regime are affected by higher-order effects like EW corrections. These are in the order of 10–30% for events where the lepton from the Z boson has a $p_T > 150\,\text{GeV}$ [69]. Electroweak corrections are currently not considered in the simulated samples. Further improvements of the experimental methods as well as the simulation are necessary to fully exploit the great potential of an analysis in this energy regime.

Summary and conclusions

A study is carried out of single top quark production in association with a Z boson (tZq) with the CMS experiment. Several new results are presented that constitute substantial experimental progress and important input to theory. Among the results are the first measurements of the tZq process of differential cross sections and the top quark spin asymmetry which were published by the CMS Collaboration in Ref. [169]. To achieve the results presented, the analysis was designed and built from the ground up. Proton-proton collision data recorded at a center-of-mass energy of 13 TeV are analyzed. The data was collected during the years 2016, 2017, and 2018, corresponding to an integrated luminosity of $138\,\text{fb}^{-1}$.

Final states with three leptons, either electrons or muons, are selected. As tZq production is a very rare process at the LHC, the selection criteria are optimized maximizing the number of selected tZq events while keeping background contributions that include misidentified leptons at a controllable level. Signal and control regions are defined to enrich individual processes, verify their modeling, and estimate background contributions. Background processes that contain nonprompt leptons are estimated from control samples in data, following the fake factor method [186, 187]. The probability of a nonprompt lepton to be selected is measured in multijet enriched regions. The fake factor method is verified and validated in simulation and control regions enriched in nonprompt leptons. To further improve the sensitivity of the measurement, a multivariate analysis is performed. A multiclass neural network is designed and optimized to distinguish tZq events from events of the various background processes, namely: top quark-antiquark pair production in association with a Z boson ($\text{t}\bar{\text{t}}\text{Z}$), other processes with top quarks, associated production of a W and Z boson, and associated production of two Z bosons, three massive gauge bosons, processes with photons, or backgrounds with misidentified leptons. The signal is extracted from a maximum likelihood fit to data, binned in the NN score of the tZq output node. Control regions are included to constrain the normalization of different background processes. Various systematic uncertainties from theoretical or experimental sources are studied and included in the fit as nuisance parameters. The inclusive tZq cross section is extracted with an unprecedented precision of about 11% as

$$\sigma_{\text{tZq}} = 84.6\ ^{+6.9}_{-6.7}\ (\text{stat})\ ^{+6.4}_{-5.9}\ (\text{syst})\ \text{fb}\ , \tag{4.23}$$

which is in agreement with standard model (SM) predictions. The leading systematic uncertainties are the signal modeling, b jet identification, and normalization of backgrounds. From the result, a direct determination of the CKM-matrix element V_{tb} is performed without assumptions on the number of quark flavors or unitarity of the CKM matrix. Although not the most precise direct measurement of V_{tb}, the estimate can be used in a combination to reduce the overall uncertainty.

For the first time, the tZq cross section is measured differentially as a function of 11 kinematic observables. These include observables that are sensitive to physics beyond the SM (BSM) and/or modeling aspects. The distributions are extracted at parton and particle levels to obtain experiment independent results. Response matrices are studied to optimize the binning of each distribution. Unregularized unfolding is performed where the differential cross sections are extracted by means of multidimensional binned maximum likelihood fits. Thereby, statistical and systematic uncertainties, background subtraction, and migrations of events between different bins of the observables are taken into account in a single step. Observables containing jets in the final state are measured with three bins and uncertainties down to 25% per bin. Those that are defined solely on leptons are measured to a precision as low as 15%. In all cases, the uncertainty is dominated by the limited size of the data sample. The results are compared to predictions obtained from simulation with and without considering the b quark as part of the proton sea. Overall a good agreement of the data with both predictions is observed, with neither prediction being favored over the other.

The top quark spin asymmetry, proportional to the top quark polarization, is accurately predicted by theory and is particularly well suited for testing the chiral structure of the weak interaction. Anomalous couplings, for example, flavor-changing currents with right chirality could modify the degree of polarization [57, 61]. A deviation from the SM prediction would thus be a strong hint to BSM physics. It is measured in the optimized basis using the distribution of the angle between the lepton from the top quark decay and the additional jet of the event, in the top quark rest frame. In a binned maximum likelihood fit, the spin asymmetry is fit simultaneously with the inclusive cross section. The measured value is in agreement with theoretical predictions and amounts to

$$A_\ell = 0.54 \pm 0.16\ (\text{stat}) \pm 0.06\ (\text{syst})\ , \tag{4.24}$$

which is again dominated by the statistical uncertainty.

No significant deviation from the SM is seen in any of the results presented in this thesis. This confirms the validity of the theory and the accurate descriptions of the employed models in this energy regime within the obtained precision. Some of the results, such as the inclusive cross section and spin asymmetry, can further be used to constrain BSM effects. However, it must be taken into account that most backgrounds are subtracted under SM hypothesis. Many BSM theories not only affect the tZq, but also other processes that are present in the background of the measurement such as $t\bar{t}Z$. This is the case especially in the framework of effective field theory. To make more compelling limits on modifications to the SM, new techniques need to be developed to take into account effects in all involved processes.

The understanding of tZq production is of utmost importance also for direct searches for new physics where a similar event signature can be expected. In many of these cases, tZq production is an important background and confidence of its valid description in simulation can reduce its associated uncertainties and thus improve the sensitivity of such searches. This is the case, for example in models with vector-like quarks, or flavor-changing neutral currents [51, 70].

The results presented in this thesis mark the start of the precision era for tZq measurements. More data from LHC Run 2 will be highly beneficial and allow to measure

the properties of the process with higher accuracy and granularity. With data from the HL-LHC, most tZq measurements presented in this thesis will reach their systematic limits.

In a second project, a measurement of Z boson rates to determine luminosity is performed. Luminosity is an integral part of every analysis and its precise determination is crucial for every precision cross section measurement. The presented work thus benefits the entire CMS Collaboration. For the first time, the Z boson rate is measured in the context of precision luminosity determination. This requires a detailed understanding of systematic effects at the sub-percent level. The approach is fundamentally different and affected by different systematic uncertainties compared to conventional luminosity measurements. The measurement is performed in the final state of two muons, which particularly suits the precision goal as these events have a very clean signature. The Z boson rate is measured in short time intervals of about 30 min to a statistical precision of $\approx$1%. The invariant mass of the dimuon system is used to fit the peaking Z boson mass spectrum and subtract the nonresonant background from all reconstructed candidates. Unlike conventional luminometers, the Z bosons rate measurement is in-situ calibrated to account for changing detector conditions like pileup or other systematic effects that impact the reconstruction efficiency. Using the same events as for the extraction of the reconstructed number of Z bosons, the muon trigger, identification, and reconstruction efficiencies are determined via tag-and-probe procedures. As muons are detected in the inner silicon tracker and outer muon system independently, it is possible to perform an almost entirely data-driven calibration of the Z boson reconstruction efficiency. Residual effects to which the tag-and-probe method is not sensitive are studied and corrections are applied. These concern the too-early response of triggers, the correlation between the two muons, and the correlation between the outer and inner track of each muon.

The linear relation between the efficiency-corrected measured rate of Z bosons and the instantaneous luminosity estimated using a reference measurement is tested for single LHC fills separately and a good agreement is found between both measurements. Measured Z boson rates in multiple fills are combined and no sign of nonlinearity was found in the tested range of 1–18 $\mathrm{nb}^{-1}\,\mathrm{s}^{-1}$. An absolute scale for the Z boson rate is obtained using low-pileup data as a reference, following the approach proposed in Ref. [158]. The method shows good stability over time for each year. Some tensions to lower values of the integrated luminosity are observed. Systematic effects on the summed efficiency-corrected Z boson rate in each year and their correlations are studied. Uncertainties in transferring the luminosity calibration from low-pileup data to high-pileup data are estimated to be $<$0.5% for most data-taking periods.

The analysis demonstrates an alternative approach to determine the absolute integrated luminosity with a competitive uncertainty. A publication including the results from the 2017 data is currently in preparation and has been preapproved within the CMS Collaboration. The measurements provide a powerful cross-check and can be used in future luminosity combinations of several years. The method will become more important in future data-taking at the LHC as the pileup will be increased and the determination of luminosity under these extreme conditions will become more challenging.

Appendix A.

Combining luminosity and Z boson rates

The ratios of the Z boson counts are independent of the reference luminosity, while the reference luminosity has uncertainties that are correlated and uncorrelated between the years as summarized in Table 2.2. The information on the ratios of the Z boson counts can be combined with the reference luminosity to constrain the uncorrelated uncertainties.

The combination of the ratios of the N^{Z} and reference luminosity of the three years is done following the best linear unbiased estimate (BLUE) procedure [215, 216]. Given the covariance between different measurements, the result is a linear combination that is mathematically proven to minimize the variance. The result is further unbiased, which means that for a large number of estimates the result equals the true value of the observable.

The integrated reference luminosity of each year of data taking is given by

$$\vec{\mathcal{L}}^{\text{Ref.}} = \begin{pmatrix} \mathcal{L}^{\text{Ref.}}_{2016} \\ \mathcal{L}^{\text{Ref.}}_{2017} \\ \mathcal{L}^{\text{Ref.}}_{2018} \end{pmatrix} = \begin{pmatrix} 36.33 \pm 0.42\,\text{fb}^{-1} \\ 41.48 \pm 0.96\,\text{fb}^{-1} \\ 59.83 \pm 1.50\,\text{fb}^{-1} \end{pmatrix}. \tag{A.1}$$

Since at the point of writing this thesis the measurement of the Z luminosity and study of associated uncertainties is not finalized, the combination is performed blinded. For simplicity, the uncertainty on the Z boson rates of each year is assumed to be 1% and fully correlated. The values for the Z luminosity are set to the value of the reference luminosity. For the three years of data taking, three estimations for the Z luminosity are obtained

$$\vec{\mathcal{L}}^{\text{Z}} = \begin{pmatrix} \mathcal{L}^{\text{Z}}_{2016} \\ \mathcal{L}^{\text{Z}}_{2017} \\ \mathcal{L}^{\text{Z}}_{2018} \end{pmatrix} = \begin{pmatrix} 36.33 \pm 0.74\,\text{fb}^{-1} \\ 41.48 \pm 0.85\,\text{fb}^{-1} \\ 59.83 \pm 1.22\,\text{fb}^{-1} \end{pmatrix}. \tag{A.2}$$

The full correlation matrix is

$$\mathbf{C}\left(\vec{\mathcal{L}}^{\text{Ref.}}, \vec{\mathcal{L}}^{\text{Z}}\right) = \begin{pmatrix} 1.00 & & & & & \\ 0.20 & 1.00 & & & & \\ 0.41 & 0.33 & 1.00 & & & \\ 0.23 & 0.66 & 0.38 & 1.00 & & \\ 0.23 & 0.66 & 0.38 & 0.99 & 1.00 & \\ 0.23 & 0.66 & 0.38 & 0.99 & 0.99 & 1.00 \end{pmatrix}. \tag{A.3}$$

When combining those estimates, the correlation matrix of the resulting three estimates is

$$\mathbf{C}\left(\vec{\mathcal{L}}^{\text{Comb.}}\right) = \begin{pmatrix} 1.00 & & \\ 0.97 & 1.00 & \\ 0.97 & 0.97 & 1.00 \end{pmatrix} . \tag{A.4}$$

The resulting new estimates are

$$\vec{\mathcal{L}}^{\text{Comb.}} = \begin{pmatrix} \mathcal{L}^{\text{Comb.}}_{2016} \\ \mathcal{L}^{\text{Comb.}}_{2017} \\ \mathcal{L}^{\text{Comb.}}_{2018} \end{pmatrix} = \begin{pmatrix} 36.33 \pm 0.40\,\text{fb}^{-1} \\ 41.48 \pm 0.46\,\text{fb}^{-1} \\ 59.83 \pm 0.67\,\text{fb}^{-1} \end{pmatrix} , \tag{A.5}$$

and

$$\text{sum}\left(\vec{\mathcal{L}}^{\text{Comb.}}\right) = 137.64 \pm 1.52\,\text{fb}^{-1} . \tag{A.6}$$

By construction, the central values remain unchanged in the blinded combination. The estimates before and after the combination are illustrated in Fig. A.1. By combining the information of the Z boson counts and the reference luminosity, a reduction of the uncertainty of the integrated luminosity for each year, and for the total integrated luminosity is achieved. The total Run 2 luminosity uncertainty, as well as the uncertainty on the luminosity of each year, are reduced to 1.1%. The results of the different years are almost 100% correlated. This is because the Z luminosity is assumed almost fully correlated to the reference luminosity in low PU, while the latter one is used to transfer the luminosity calibration to the different years.

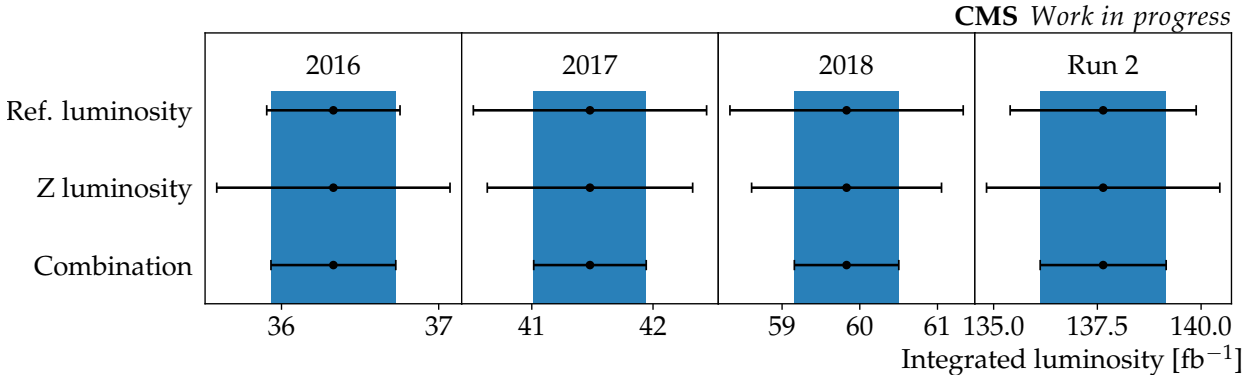

Fig. A.1.: Summary of luminosity estimations of the reference luminosity, the Z luminosity and the combination of both for the years 2016 (left panel), 2017 (second panel from left) and 2018 (third panel from left), as well as for the full Run 2 (right panel). The blue band shows the uncertainty on the combined results.

Appendix B.

List of trigger paths used in the tZq analysis

The complete set of trigger paths which is used for data collected in the years 2016, 2017, and 2018 is listed in Tables B.1, B.2 and B.3, respectively. The trigger paths are sorted by their corresponding data set.

Table B.1.: Selected trigger paths used to record events during data taking in 2016.

data set	trigger path
Single muon	HLT_IsoMu22
	HLT_IsoTkMu22
	HLT_IsoMu22_eta2p1
	HLT_IsoTkMu22_eta2p1
	HLT_IsoMu24
	HLT_IsoTkMu24
	HLT_Mu50
	HLT_TkMu50
	HLT_Mu45_eta2p1
Single electron	HLT_Ele25_eta2p1_WPTight_Gsf
	HLT_Ele27_WPTight_Gsf
	HLT_Ele105_CaloIdVT_GsfTrkIdT
	HLT_Ele115_CaloIdVT_GsfTrkIdT
Single photon	HLT_Photon175
Double muon	HLT_Mu17_TrkIsoVVL_Mu8_TrkIsoVVL
	HLT_Mu17_TrkIsoVVL_TkMu8_TrkIsoVVL
	HLT_TkMu17_TrkIsoVVL_TkMu8_TrkIsoVVL
	HLT_Mu17_TrkIsoVVL_Mu8_TrkIsoVVL_DZ
	HLT_Mu17_TrkIsoVVL_TkMu8_TrkIsoVVL_DZ
	HLT_TkMu17_TrkIsoVVL_TkMu8_TrkIsoVVL_DZ
	HLT_Mu30_TkMu11
	HLT_TripleMu_12_10_5
Double electron / photon	HLT_Ele23_Ele12_CaloIdL_TrackIdL_IsoVL_DZ
	HLT_Ele16_Ele12_Ele8_CaloIdL_TrackIdL
	HLT_DoubleEle33_CaloIdL_MW
	HLT_DoubleEle33_CaloIdL_GsfTrkIdVL
	HLT_DoubleEle33_CaloIdL_GsfTrkIdVL_MW
	HLT_DoublePhoton60
Muon + electron / photon	HLT_Mu23_TrkIsoVVL_Ele8_CaloIdL_TrackIdL_IsoVL
	HLT_Mu23_TrkIsoVVL_Ele8_CaloIdL_TrackIdL_IsoVL_DZ
	HLT_Mu8_TrkIsoVVL_Ele23_CaloIdL_TrackIdL_IsoVL
	HLT_Mu8_TrkIsoVVL_Ele23_CaloIdL_TrackIdL_IsoVL_DZ
	HLT_Mu30_Ele30_CaloIdL_GsfTrkIdVL
	HLT_Mu33_Ele33_CaloIdL_GsfTrkIdVL
	HLT_DiMu9_Ele9_CaloIdL_TrackIdL
	HLT_Mu8_DiEle12_CaloIdL_TrackIdL

Table B.2.: Selected trigger paths used to record events during data taking in 2017.

data set	trigger path
Single muon	HLT_IsoMu24
	HLT_IsoMu24_eta2p1
	HLT_IsoMu27
	HLT_Mu50
	HLT_OldMu100
	HLT_TkMu100
Single electron	HLT_Ele27_WPTight_Gsf
	HLT_Ele32_WPTight_Gsf
	HLT_Ele32_WPTight_Gsf_L1DoubleEG
	HLT_Ele35_WPTight_Gsf
	HLT_Ele115_CaloIdVT_GsfTrkIdT
Single photon	HLT_Photon200
Double muon	HLT_Mu17_TrkIsoVVL_Mu8_TrkIsoVVL
	HLT_Mu17_TrkIsoVVL_Mu8_TrkIsoVVL_DZ
	HLT_Mu17_TrkIsoVVL_Mu8_TrkIsoVVL_DZ_Mass8
	HLT_Mu17_TrkIsoVVL_Mu8_TrkIsoVVL_DZ_Mass3p8
	HLT_Mu19_TrkIsoVVL_Mu9_TrkIsoVVL_DZ_Mass3p8
	HLT_Mu37_TkMu27
	HLT_TripleMu_12_10_5
	HLT_TripleMu_10_5_5_DZ
	HLT_TripleMu_5_3_3_Mass3p8to60_DZ
Double electron / photon	HLT_Ele23_Ele12_CaloIdL_TrackIdL_IsoVL
	HLT_Ele16_Ele12_Ele8_CaloIdL_TrackIdL
	HLT_DoubleEle25_CaloIdL_MW
	HLT_DoubleEle33_CaloIdL_MW
	HLT_DiEle27_WPTightCaloOnly_L1DoubleEG
	HLT_DoublePhoton70
Muon + electron / photon	HLT_Mu23_TrkIsoVVL_Ele12_CaloIdL_TrackIdL_IsoVL
	HLT_Mu23_TrkIsoVVL_Ele12_CaloIdL_TrackIdL_IsoVL_DZ
	HLT_Mu8_TrkIsoVVL_Ele23_CaloIdL_TrackIdL_IsoVL_DZ
	HLT_Mu12_TrkIsoVVL_Ele23_CaloIdL_TrackIdL_IsoVL_DZ
	HLT_Mu27_Ele37_CaloIdL_MV
	HLT_Mu37_Ele27_CaloIdL_MV
	HLT_DiMu9_Ele9_CaloIdL_TrackIdL
	HLT_DiMu9_Ele9_CaloIdL_TrackIdL_DZ
	HLT_Mu8_DiEle12_CaloIdL_TrackIdL

Table B.3.: Selected trigger paths used to record events during data taking in 2018.

data set	trigger path
Single muon	HLT_IsoMu24
	HLT_IsoMu27
	HLT_Mu50
	HLT_OldMu100
	HLT_TkMu100
electron / photon	HLT_Ele32_WPTight_Gsf
	HLT_Ele115_CaloIdVT_GsfTrkIdT
	HLT_Photon200
	HLT_Ele23_Ele12_CaloIdL_TrackIdL_IsoVL
	HLT_Ele16_Ele12_Ele8_CaloIdL_TrackIdL
	HLT_DoubleEle25_CaloIdL_MW
	HLT_DiEle27_WPTightCaloOnly_L1DoubleEG
	HLT_DoublePhoton70
Double muon	HLT_Mu17_TrkIsoVVL_Mu8_TrkIsoVVL_DZ_Mass3p8
	HLT_Mu37_TkMu27
	HLT_TripleMu_12_10_5
	HLT_TripleMu_10_5_5_DZ
	HLT_TripleMu_5_3_3_Mass3p8to60_DZ
Muon + electron / photon	HLT_Mu23_TrkIsoVVL_Ele12_CaloIdL_TrackIdL_IsoVL
	HLT_Mu23_TrkIsoVVL_Ele12_CaloIdL_TrackIdL_IsoVL_DZ
	HLT_Mu8_TrkIsoVVL_Ele23_CaloIdL_TrackIdL_IsoVL_DZ
	HLT_Mu12_TrkIsoVVL_Ele23_CaloIdL_TrackIdL_IsoVL_DZ
	HLT_Mu27_Ele37_CaloIdL_MV
	HLT_Mu37_Ele27_CaloIdL_MV
	HLT_Mu8_DiEle12_CaloIdL_TrackIdL
	HLT_DiMu9_Ele9_CaloIdL_TrackIdL_DZ

Appendix C.

Input variables for the neural network classifier in the tZq analysis

C.1. Distributions of input variables

Additional distributions of the variables used as input to the neural network classifier in the tZq analysis shown in Figs. C.1 to C.3.

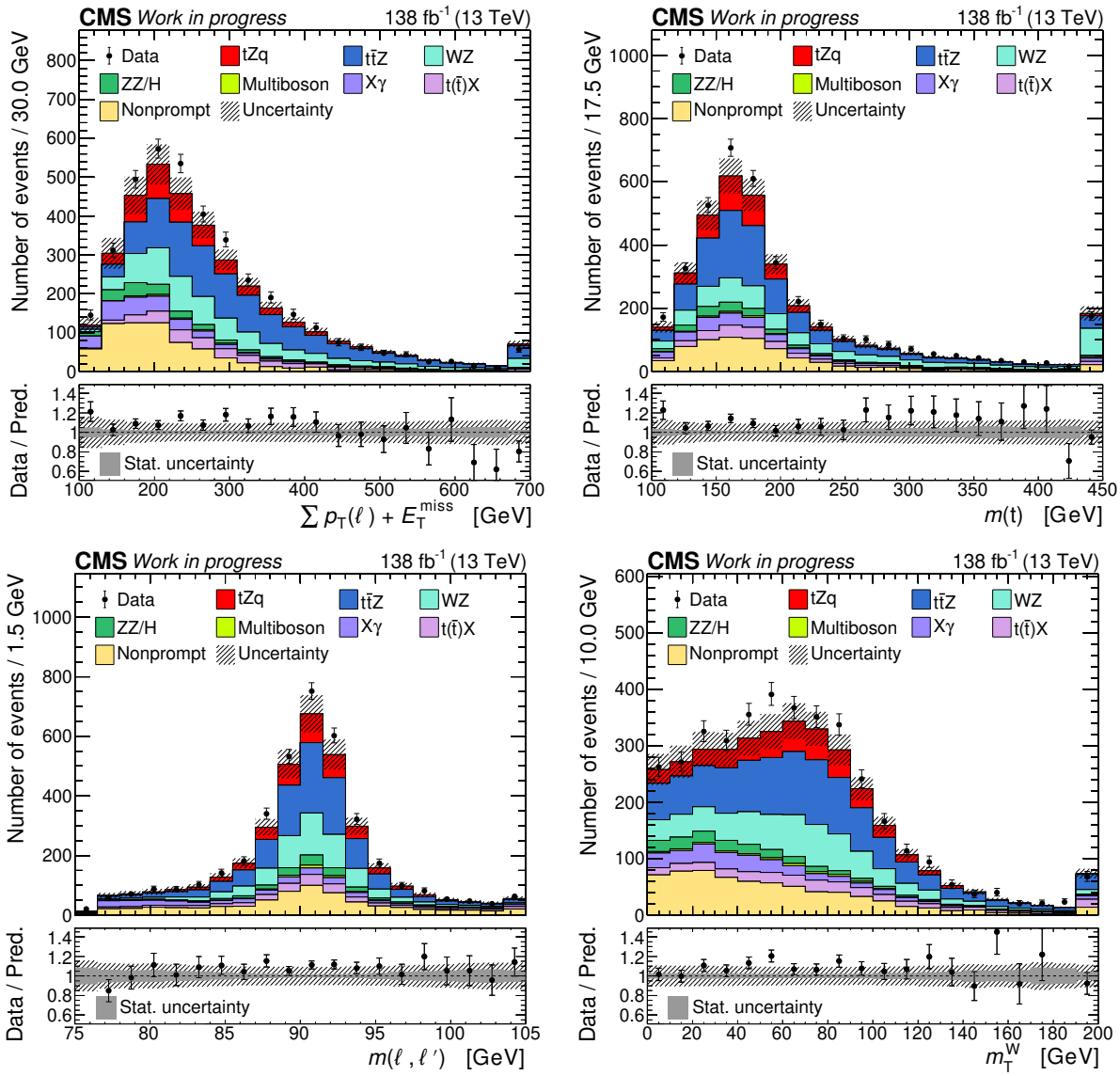

Fig. C.1.: Distributions of events in the SR for variables used in the NN classification including the scalar sum leptonic momenta and missing transverse energy (upper left), top quark candidate mass (upper right), Z boson candidate mass (lower left), and the transverse W boson mass (lower right).

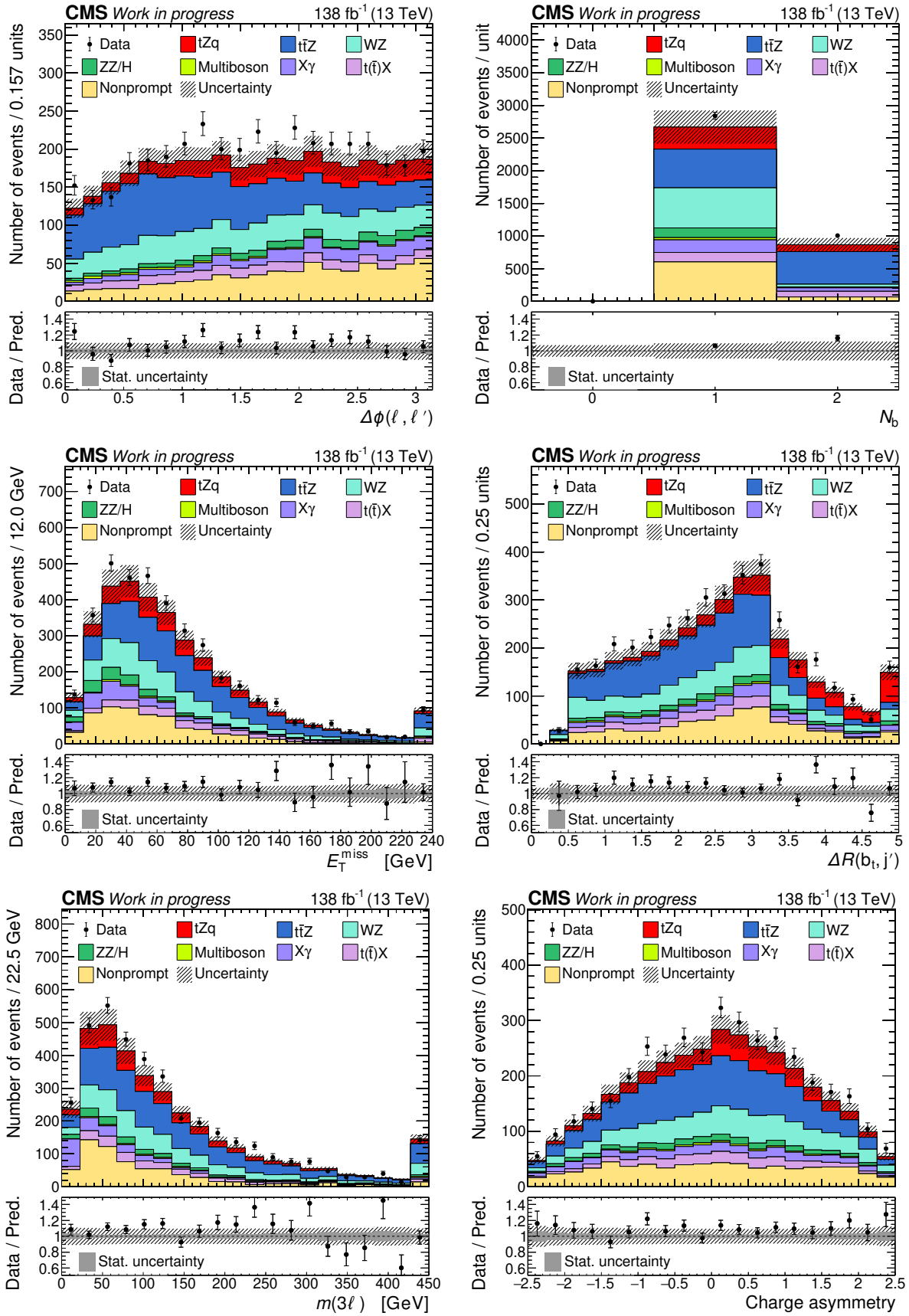

Fig. C.2.: Distributions of events in the SR for variables used in the NN classification including azimuthal angle between the leptons from the Z boson candidate (upper left), the multiplicity of b tagged jets (upper right), missing transverse energy (middle left), angle between the b jet from the top candidate and recoiling jet (middle right), invariant mass of the three lepton system (lower left), and $|\eta|$ of the lepton from the top, multiplied by its charge (lower right).

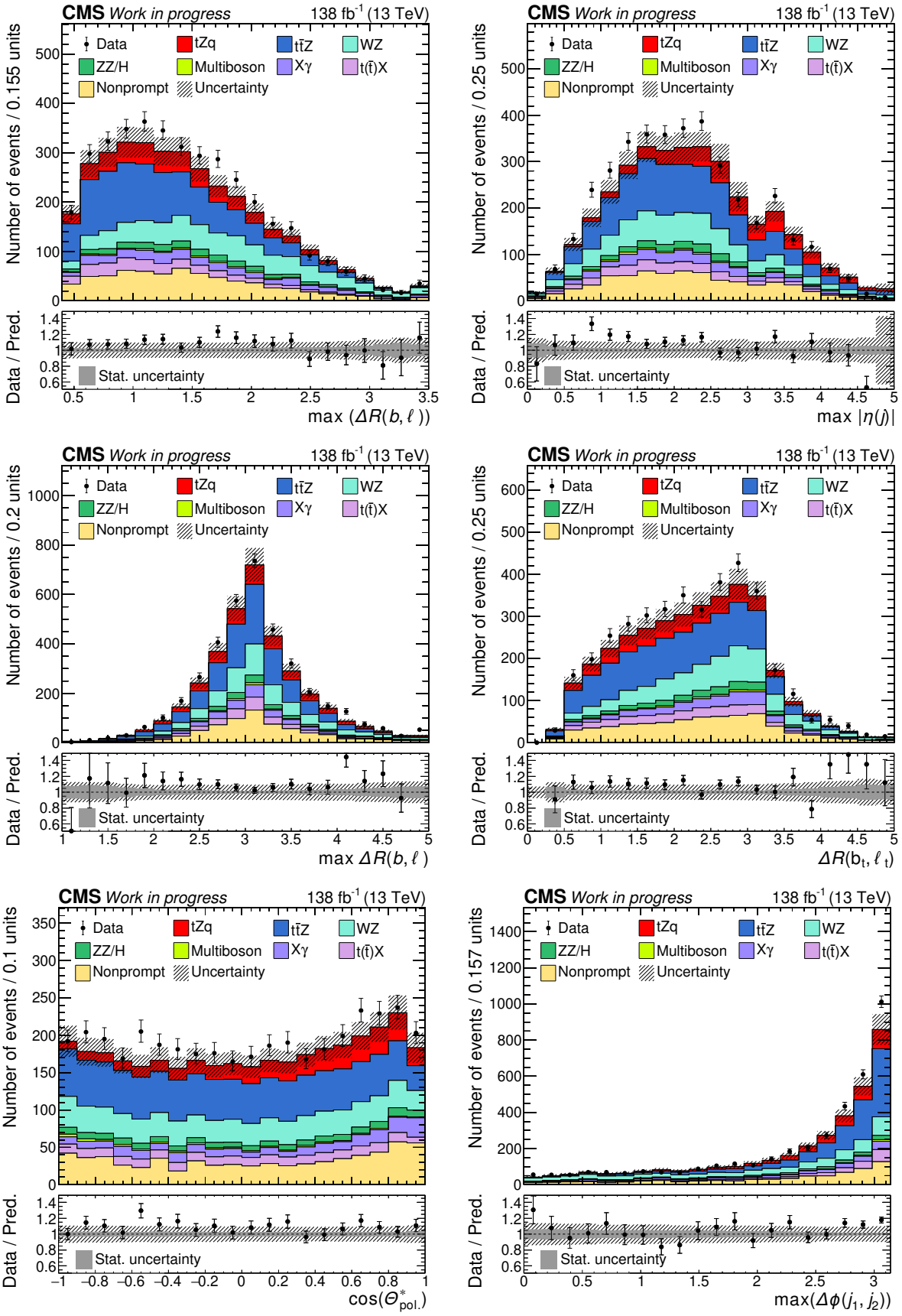

Fig. C.3.: Distributions of events in the SR for variables used in the NN classification including the smallest angle between any b jet and any lepton (upper left), maximum $|\eta|$ value of any jet (upper right). largest angle between any b jet and any lepton of event (middle left), angle between the b jet and the lepton from the top quark candidate (middle right), cosine of the top quark polarization angle (lower left), and largest azimuthal angle between any pair of two jets (lower right).

C.2. Goodness of fit tests

Results on the goodness-of-fit tests performed to validate the modeling of the input variables used for the neural network classifier in the tZq measurements are shown in Figs. C.4 and C.5.

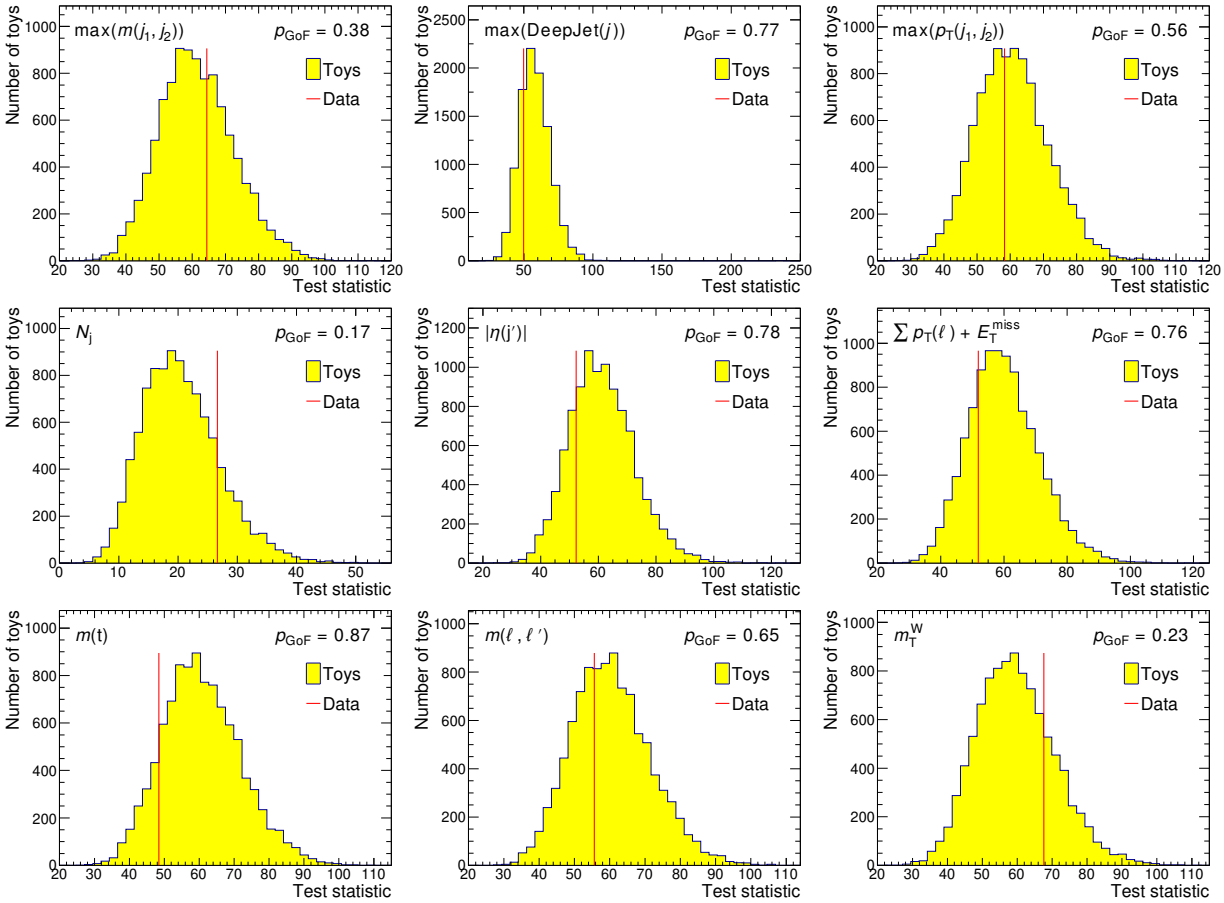

Fig. C.4.: Goodness-of-fit test with the saturated model for distributions used in the NN of the tZq analysis. The test statistics of the toy data samples (yellow histogram) is compared to the one of the observed data (red line).

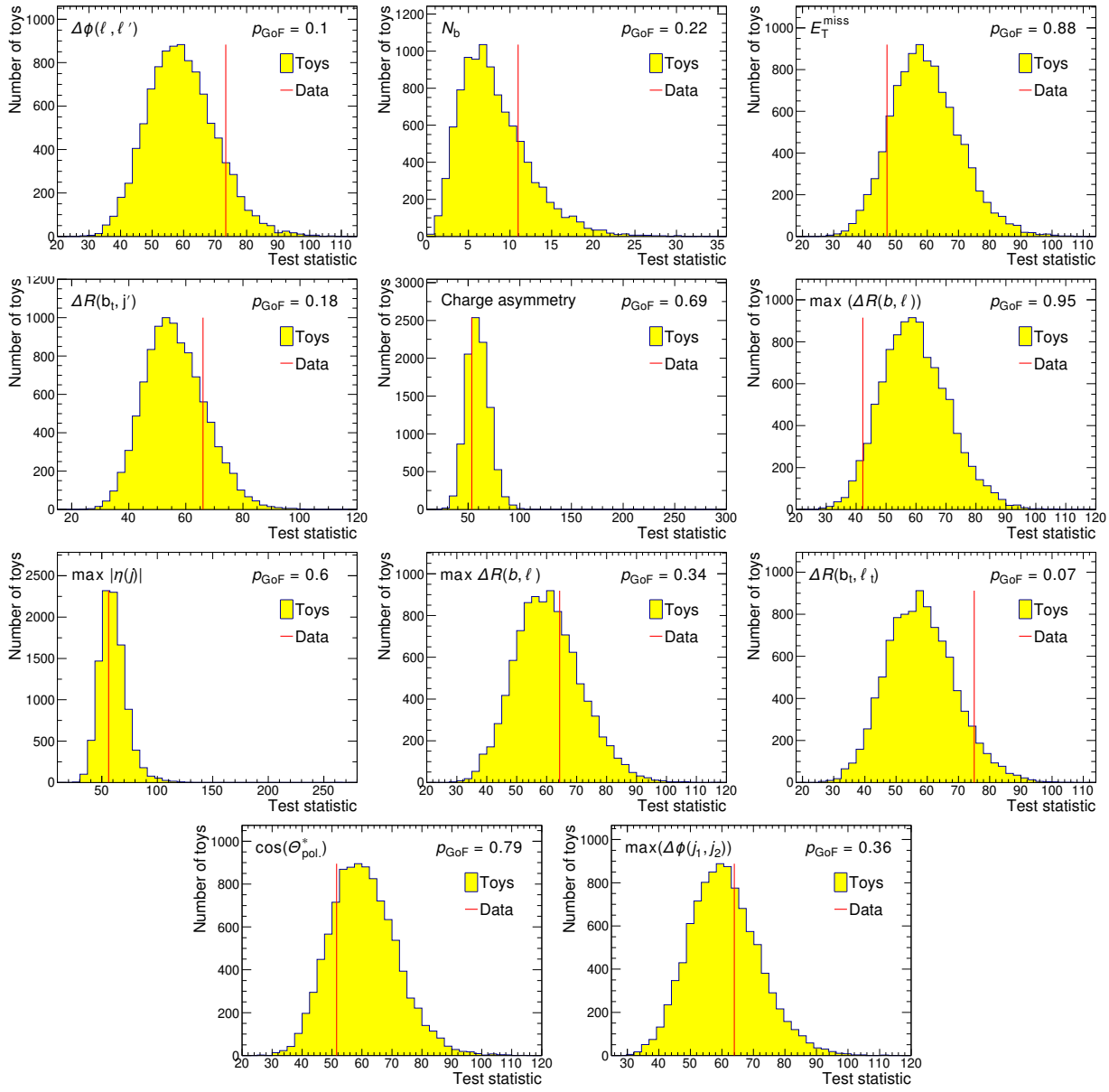

Fig. C.5.: Goodness-of-fit test with the saturated model for distributions used in the NN of the tZq analysis. The test statistics of the toy data samples (yellow histogram) is compared to the one of the observed data (red line).

Bibliography

[1] Muon g-2 Collaboration. "Measurement of the positive muon anomalous magnetic moment to 0.46 ppm." Phys. Rev. Lett. **126** (2021) 14 [arXiv: 2104.03281].

[2] LHCb Collaboration. "Test of lepton universality in beauty-quark decays "(2021) [arXiv: 2103.11769].

[3] CDF Collaboration. "High-precision measurement of the W boson mass with the CDF II detector." *Science*. **376** (2022) 6589.

[4] J. Schwichtenberg. *Physics from symmetry*. Springer, 2018.

[5] A. Zee. *Quantum field theory in a nutshell*. Princeton University Press, 2003.

[6] M. E. Peskin and D. V. Schroeder. *An introduction to quantum field theory*. Westview Press, 1995.

[7] ScienceTerms.net Editors. *Subatomic particle*. https://scienceterms.net/physics/subatomic-particle/. Accessed: May 2022. 2022.

[8] LEP Electroweak Working Group. "Precision electroweak measurements on the Z resonance." Phys. Rep. **427** (2006) 5-6 [arXiv: hep-ex/0509008].

[9] E. Noether. "Invariante variationsprobleme." ger. *Nachr. d. König. Gesellsch. d. Wiss. zu Göttingen, Math.-Phys. Klasse*. **1918** (1918).

[10] Particle Data Group. "Review of Particle Physics." PTEP. **2020** (2020) 8.

[11] A. Deur, S.J. Brodsky, and G.F. de Téramond. "The QCD running coupling." Prog. Part. Nucl. Phys. **90** (2016) [arXiv: 1604.08082].

[12] K.G. Wilson. "Confinement of quarks." Phys. Rev. *D*. **10** (1974) 8.

[13] C. S. Wu et al. "Experimental test of parity conservation in beta decay." Phys. Rev. **105** (1957) 4.

[14] S.L. Glashow. "The renormalizability of vector meson interactions." Nucl. Phys. **10** (1959).

[15] A. Salam and J.C. Ward. "Electromagnetic and weak interactions." Phys. Lett. **13** (1964) 2.

[16] S. Weinberg. "A model of leptons." Phys. Rev. Lett. **19** (1967) 21.

[17] T. Nakano and K. Nishijima. "Charge independence for V-particles*." Prog. theor. phys. **10** (1953) 5.

[18] M. Gell-Mann. "The interpretation of the new particles as displaced charge multiplets." Nuovo Cimento. **4** (1956) 2.

[19] F. Englert and R. Brout. "Broken symmetry and the mass of gauge vector mesons." Phys. Rev. Lett. **13** (1964) 9.

[20] P.W. Higgs. "Broken symmetries and the masses of gauge bosons." Phys. Rev. Lett. **13** (1964) 16.

[21] ATLAS Collaboration. "Observation of a new particle in the search for the Standard Model Higgs boson with the ATLAS detector at the LHC." English. Phys. Lett. *B*. **716** (2012) 1 [arXiv: 1207.7214].

[22] CMS Collaboration. "Observation of a new boson at a mass of 125 GeV with the CMS experiment at the LHC." Phys. Lett. *B*. **716** (2012) 1 [arXiv: 1207.7235].

[23] G. Degrassi et al. "Higgs mass and vacuum stability in the Standard Model at NNLO." JHEP. **08** (2012) 098 [arXiv: 1205.6497].

[24] J. H. Christenson et al. "Evidence for the 2π Decay of the K_2^0 Meson." Phys. Rev. Lett. **13** (1964) 4.

[25] N. Cabibbo. "Unitary Symmetry and Leptonic Decays." Phys. Rev. Lett. **10** (1963) 12.

[26] M. Kobayashi and T. Maskawa. "CP-Violation in the renormalizable theory of weak interaction." Prog. theor. phys. **49** (1973) 2.

[27] Super-Kamiokande Collaboration. "Evidence for oscillation of atmospheric neutrinos." Phys. Rev. Lett. **81** (1998) 8 [arXiv: hep-ex/9807003].

[28] Super-Kamiokande Collaboration. "Determination of solar neutrino oscillation parameters using 1496 days of Super-Kamiokande-I data." Phys. Lett. *B*. **539** (2002) 3-4 [arXiv: hep-ex/0205075].

[29] SNO Collaboration. "Direct evidence for neutrino flavor transformation from neutral-current interactions in the Sudbury neutrino observatory." Phys. Rev. Lett. **89** (2002) 1 [arXiv: nucl-ex/0204008].

[30] B.M. Pontecorvo. "Inverse beta processes and non-conservation of lepton charge." JETP. **7** (1958) 172.

[31] Z. Maki, M. Nakagawa, and S. Sakata. "Remarks on the unified model of elementary particles." Prog. theor. phys. **28** (1962) 5 [eprint: https://academic.oup.com/ptp/article-pdf/28/5/870/5258750/28-5-870.pdf].

[32] KATRIN Collaboration. "Direct neutrino-mass measurement with sub-electronvolt sensitivity." Nature Phys. **18** (2022) 2.

[33] E. Rutherford. "LXXIX. The scattering of α and β particles by matter and the structure of the atom." Lond. Edinb. Dubl. Phil. Mag. **21** (1911) 125.

[34] S. Mandelstam. "Determination of the pion-nucleon scattering amplitude from dispersion relations and unitarity. General theory." Phys. Rev. **112** (1958) 4.

[35] S. Moch, J.A.M. Vermaseren, and A. Vogt. "The three-loop splitting functions in QCD: the non-singlet case." Nucl. Phys. *B*. **688** (2004) 1 [arXiv: hep-ph/0403192].

[36] A. Vogt, S. Moch, and J.A.M. Vermaseren. "The three-loop splitting functions in QCD: the singlet case." Nucl. Phys. *B*. **691** (2004) 1-2 [arXiv: hep-ph/0404111].

[37] NNPDF Collaboration. "Parton distributions from high-precision collider data." Eur. Phys. J. *C*. **77** (2017) 663 [arXiv: 1706.00428].

[38] Y.L. Dokshitser. "Calculation of structure functions of deep-inelastic scattering and e^+e^- annihilation by perturbation theory in quantum chromodynamics." JETP. **46** (1977).

[39] V.N. Gribov and L.N. Lipatov. "Deep inelastic electron scattering in perturbation theory." Phys. Lett. *B*. **37** (1971) 1.

[40] G. Altarelli and G. Parisi. "Asymptotic freedom in parton language." Nucl. Phys. *B*. **126** (1977) 2.

[41] S. Dulat et al. "New parton distribution functions from a global analysis of quantum chromodynamics." Phys. Rev. *D*. **93** (2016) [arXiv: 1506.07443].

[42] NNPDF Collaboration. "Parton distributions for the LHC Run II." JHEP. **04** (2015) 040 [arXiv: 1410.8849].

[43] B. Andersson et al. "Parton fragmentation and string dynamics." Phys. Rep. **97** (1983) 2.

[44] T. Sjöstrand and M. van Zijl. "A multiple-interaction model for the event structure in hadron collisions." Phys. Rev. *D*. **36** (1987) 7.

[45] CMS Collaboration. *A new set of CMS tunes for novel colour reconnection models in* PYTHIA *8 based on underlying-event data*. http://cds.cern.ch/record/2780467. 2021.

[46] J.R. Christiansen and P.Z. Skands. "String formation beyond leading colour." JHEP. **2015** (2015) [arXiv: 1505.01681].

[47] S. Argyropoulos and T. Sjöstrand. "Effects of color reconnection on $t\bar{t}$ final states at the LHC." JHEP. **11** (2014) 043 [arXiv: 1407.6653].

[48] CDF Collaboration. "Observation of top quark production in $\bar{p}p$ collisions with the collider detector at Fermilab." Phys. Rev. Lett. **74** (1995) 14.

[49] D0 Collaboration. "Observation of the top quark." Phys. Rev. Lett. **74** (1995) 14 [arXiv: hep-ex/9503003].

[50] "Experimental discrimination between charge 2e/3 top quark and charge 4e/3 exotic quark production scenarios." Phys. Rev. Lett. **98** (2007) [arXiv: hep-ex/0608044].

[51] CMS Collaboration. "Search for single production of a vector-like T quark decaying to a top quark and a Z boson in the final state with jets and missing transverse momentum at $\sqrt{s} = 13\,\text{TeV}$ "(2022) [arXiv: 2201.02227].

[52] M. Guzzi, K. Lipka, and S. Moch. "Top-quark pair production at hadron colliders: differential cross section and phenomenological applications with DiffTop." JHEP. **01** (2015) 082.

[53] D0 Collaboration. "Observation of single top-quark production." Phys. Rev. Lett. **103** (2009) 9 [arXiv: 0903.0850].

[54] CDF Collaboration. "Observation of electroweak single top-quark production." Phys. Rev. Lett. **103** (2009) 9 [arXiv: 0903.0885].

[55] CMS Collaboration. *CMS top quark physics summary figures*. https://twiki.cern.ch/twiki/bin/view/CMSPublic/PhysicsResultsTOPSummaryFigures. Accessed: May 2022. 2021.

[56] CMS Collaboration. "Measurement of the single top quark and antiquark production cross sections in the t channel and their ratio in proton-proton collisions at $\sqrt{s} = 13\,\text{TeV}$." Phys. Lett. *B*. **800** (2020) [arXiv: 1812.10514].

[57] J.A. Aguilar-Saavedra. "A minimal set of top anomalous couplings." Nucl. Phys. *B*. **812** (2009) 1-2 [arXiv: 0811.3842].

[58] "Measurement of CKM matrix elements in single top quark t-channel production in proton-proton collisions at $\sqrt{s} = 13\,\text{TeV}$." Phys. Lett. *B*. **808** (2020) [arXiv: 2004.12181].

[59] ATLAS and CMS Collaborations. *LHCTopWG summary plots*. https://twiki.cern.ch/twiki/bin/view/LHCPhysics/LHCTopWGSummaryPlots. Accessed: May 2022. 2020.

[60] CMS Collaboration. "Measurement of the top quark polarization and $\text{t}\bar{\text{t}}$ spin correlations using dilepton final states in proton-proton collisions at $\sqrt{s} = 13\,\text{TeV}$." Phys. Rev. *D*. **100** (2019) 7 [arXiv: 1907.03729].

[61] T.M.P. Tait and C.P. Yuan. "Single top quark production as a window to physics beyond the standard model." Phys. Rev. *D*. **63** (2000) 1 [arXiv: hep-ph/0007298].

[62] G. Mahlon and S. Parke. "Improved spin basis for angular correlation studies in single top quark production at the Fermilab Tevatron." Phys. Rev. *D*. **55** (1997) 11 [arXiv: hep-ph/9611367].

[63] M. Jeżabek and J. H. Kühn. "V-A tests through leptons from polarised top quarks." Phys. Lett. *B*. **329** (1994) [arXiv: hep-ph/9403366].

[64] J.A. Aguilar-Saavedra and J. Bernabéu. "W polarisation beyond helicity fractions in top quark decays." Nucl. Phys. *B*. **840** (2010) [arXiv: 1005.5382].

[65] CMS Collaboration. "Measurement of differential cross sections and charge ratios for t-channel single top quark production in proton-proton collisions at $\sqrt{s} = 13\,\text{TeV}$." Eur. Phys. J. *C*. **80** (2020) 370 [arXiv: 1907.08330].

[66] ATLAS Collaboration. "Measurement of the polarisation of single top quarks and antiquarks produced in the t channel at $\sqrt{s} = 13\,\text{TeV}$ and bounds on the tWb dipole operator from the ATLAS experiment "(2022) [arXiv: 2202.11382].

[67] CMS Collaboration. "Probing effective field theory operators in the associated production of top quarks with a Z boson in multilepton final states at $\sqrt{s} = 13\,\text{TeV}$." JHEP. **12** (2021) 083 [arXiv: 2107.13896].

[68] J. Campbell, R.K. Ellis, and R. Röntsch. "Single top production in association with a Z boson at the LHC." Phys. Rev. *D*. **87** (2013) 11 [arXiv: 1302.3856].

[69] Davide P., Ioannis T., and Eleni V. "NLO QCD+EW predictions for tHj and tZj production at the LHC." *JHEP*. **08** (2020) [arXiv: 2006.10086].

[70] J. Shen, Y. Li, and Y. Liu. "Searches for anomalous tqZ couplings from the trilepton signal of tZ associated production at the 14 TeV LHC." Phys. Lett. *B*. **776** (2018) [arXiv: 1712.03506].

[71] C. Degrande et al. "Single top associated production with a Z or H boson at the LHC: the SMEFT interpretation." JHEP. **10** (2018) 005 [arXiv: 1804.07773].

[72] F. Maltoni, L. Mantani, and K. Mimasu. "Top quark electroweak interactions at high energy." JHEP. **10** (2019) 004 [arXiv: 1904.05637].

[73] Q. Cao et al. "A general analysis of Wtb anomalous couplings." Chinese Phys. C. **41** (2017) 6 [arXiv: 1504.03785].

[74] Brüning, O.S. and others. *LHC Design Report*. CERN Yellow Reports: Monographs. CERN, 2004.

[75] E. Mobs. *The CERN accelerator complex*. https://cds.cern.ch/record/2684277. Accessed: May 2022. 2019.

[76] ALICE Collaboration. "The ALICE experiment at the CERN LHC." JINST. **3** (2008).

[77] ALICE Collaboration. "Enhanced production of multi-strange hadrons in high-multiplicity proton-proton collisions." Nature Phys. **13** (2017) [arXiv: 1606.07424].

[78] LHCb Collaboration. "The LHCb Detector at the LHC." JINST. **3** (2008).

[79] LHCb Collaboration. "Measurement of the W boson mass." JHEP. **01** (2022) 036 [arXiv: 2109.01113].

[80] ATLAS Collaboration. "The ATLAS experiment at the CERN Large Hadron Collider." JINST. **3** (2008).

[81] CMS Collaboration. "The CMS experiment at the CERN LHC." JINST. **3** (2008).

[82] CMS Collaboration. "A measurement of the Higgs boson mass in the diphoton decay channel." Phys. Lett. *B*. **805** (2020) [arXiv: 2002.06398].

[83] CMS Collaboration. "Measurements of $t\bar{t}H$ production and the *CP* structure of the Yukawa interaction between the Higgs boson and top quark in the diphoton decay channel." Phys. Rev. Lett. **125** (2020) 6 [arXiv: 2003.10866].

[84] CMS Collaboration. "Measurement of the Higgs boson production rate in association with top quarks in final states with electrons, muons, and hadronically decaying tau leptons at $\sqrt{s} = 13\,\text{TeV}$." Eur. Phys. J. *C*. **81** (2021) 378 [arXiv: 2011.03652].

[85] R. Bruce et al. *Review of LHC Run 2 machine configurations*. https://cds.cern.ch/record/2750415. 2019.

[86] CMS Collaboration. *CMS luminosity - public results*. https://twiki.cern.ch/twiki/bin/view/CMSPublic/LumiPublicResults. Accessed: May 2022. 2021.

[87] Apollinari G. et al. *High-Luminosity Large Hadron Collider (HL-LHC): Technical Design Report V. 0.1*. CERN Yellow Reports: Monographs. CERN, 2017.

[88] T. Sakuma and T. McCauley. "Detector and event visualization with sketch up at the CMS experiment." J. Phys. Conf. Ser. **513** (2014) [arXiv: 1311.4942].

[89] CMS Collaboration. *Detector overview - silicon pixels*. https://cms.cern/detector/identifying-tracks/silicon-pixels. Accessed: May 2022.

[90] CMS Collaboration. *The CMS tracker system project*. Technical design report. CMS. CERN, 1997.

[91] CMS Collaboration. "Status of the CMS Phase 1 pixel detector upgrade." Nucl. Instrum. Methods *A*. **831** (2016).

[92] CMS Collaboration. "Description and performance of track and primary-vertex reconstruction with the CMS tracker." JINST. **9** (2014) 10 [arXiv: 1405.6569].

[93] CMS Collaboration. "Phase 1 upgrade of the CMS pixel detector." JINST. **12** (2017) 2 [arXiv: 2104.01927].

[94] CMS Collaboration. *The CMS electromagnetic calorimeter project: Technical Design Report*. https://cds.cern.ch/record/349375. 1997.

[95] CMS Collaboration. "Performance of the CMS hadron calorimeter with cosmic ray muons and LHC beam data." JINST. **5** (2010) 3.

[96] CMS Collaboration. "Performance of the CMS muon detector and muon reconstruction with proton-proton collisions at $\sqrt{s} = 13\,\text{TeV}$." JINST. **13** (2018) 6 [arXiv: 1804.04528].

[97] CMS Collaboration. *The Phase 2 upgrade of the CMS muon detectors*. https://cds.cern.ch/record/2283189. 2017.

[98] CMS Collaboration. "Performance of the CMS Level-1 trigger in proton-proton collisions at $\sqrt{s} = 13\,\text{TeV}$." *JINST*. **15** (2020) [arXiv: 2006.10165].

[99] CMS Collaboration. "The CMS trigger system." JINST. **12** (2017) 01 [arXiv: 1609.02366].

[100] K. Bos et al. *LHC computing grid*. Technical design report. LCG. CERN, 2005.

[101] J. Alwall et al. "The automated computation of tree-level and next-to-leading order differential cross sections, and their matching to parton shower simulations." JHEP. **07** (2014) 079 [arXiv: 1405.0301].

[102] F. Maltoni and T. Stelzer. "MadEvent: automatic event generation with MadGraph." JHEP. **02** (2003) 027 [arXiv: 0208156].

[103] N. Metropolis and S. Ulam. "The Monte Carlo method." J. Am. Stat. Assoc. **44** (1949) 247.

[104] R. Frederix and S. Frixione. "Merging meets matching in MC@NLO." JHEP. **12** (2012) 061 [arXiv: 1209.6215].

[105] M.L. Mangano et al. "Matching matrix elements and shower evolution for top-pair production in hadronic collisions." JHEP. **01** (2007) 013 [arXiv: hep-ph/0611129].

[106] P. Nason. "A new method for combining NLO QCD with shower Monte Carlo algorithms." JHEP. **11** (2004) 040 [arXiv: hep-ph/0409146].

[107] S. Frixione, P. Nason, and C. Oleari. "Matching NLO QCD computations with parton shower simulations: the POWHEG method." JHEP. **11** (2007) 070 [arXiv: 0709.2092].

[108] S. Alioli et al. "A general framework for implementing NLO calculations in shower Monte Carlo programs: the POWHEG BOX." JHEP. **06** (2010) 043 [arXiv: 1002.2581].

[109] T. Sjöstrand and others. "An introduction to PYTHIA 8.2." Comput. Phys. Commun. **191** (2015) [arXiv: 1410.3012].

[110] P. Skands, S. Carrazza, and J. Rojo. "Tuning PYTHIA 8.1: the Monash 2013 tune." Eur. Phys. J. *C*. **74** (2014) 3024 [arXiv: 1404.5630].

[111] CMS Collaboration. "Event generator tunes obtained from underlying event and multiparton scattering measurements." Eur. Phys. J. *C*. **76** (2016) 155 [arXiv: 1512.00815].

[112] CMS Collaboration. *Investigations of the impact of the parton shower tuning in* PYTHIA *8 in the modelling of* $\mathrm{t\bar{t}}$ *at* $\sqrt{s} = 8$ *and* 13 *TeV*. http://cds.cern.ch/record/2235192. CMS Physics Analysis Summary. 2016.

[113] CMS Collaboration. "Extraction and validation of a new set of CMS PYTHIA 8 tunes from underlying-event measurements." Eur. Phys. J. *C*. **80** (2020) 4 [arXiv: 1903.12179].

[114] S. Agostinelli et al. "GEANT4 — a simulation toolkit." Nucl. Instrum. Methods *A*. **506** (2003).

[115] CMS Collaboration. "Particle-flow reconstruction and global event description with the CMS detector." JINST. **12** (2017) [arXiv: 1706.04965].

[116] CMS Collaboration. *CMS slice image view (transverse/longitudinal/3-D)*. https://cds.cern.ch/record/2204863. Accessed: May 2022.

[117] W. Adam et al. *Track reconstruction in the CMS tracker*. https://cds.cern.ch/record/934067. 2006.

[118] K. Rose. "Deterministic annealing for clustering, compression, classification, regression, and related optimization problems." IEEE. **86** (1998) 11.

[119] CMS Collaboration and T. Mc Cauley. *Collisions recorded by the CMS detector on 14 Oct 2016 during the high pile-up fill*. https://cds.cern.ch/record/2231915. 2016.

[120] W. Adam et al. "Reconstruction of electrons with the Gaussian-sum filter in the CMS tracker at the LHC." J. Phys. G: Nucl. Part. Phys. **31** (2005) 9 [arXiv: physics/0306087v1].

[121] J.R. Quinlan. "Simplifying decision trees." Int. J. Man-Mach. Stud. **27** (1987) 3.

[122] M. Cacciari, G.P. Salam, and G. Soyez. "The anti-k_{T} jet clustering algorithm." JHEP. **04** (2008) 063 [arXiv: 0802.1189].

[123] M. Cacciari, G.P. Salam, and G. Soyez. "FastJet user manual." Eur. Phys. J. *C*. **72** (2012) 1896 [arXiv: 1111.6097].

[124] CMS Collaboration. *Pileup removal algorithms*. https://cds.cern.ch/record/1751454. 2014.

[125] CMS Collaboration. *Performance of the pile up jet identification in CMS for Run 2*. https://cds.cern.ch/record/2715906. 2020.

[126] CMS Collaboration. "Jet energy scale and resolution in the CMS experiment in pp collisions at 8 TeV." JINST. **12** (2017) [arXiv: 1607.03663].

[127] CMS Collaboration. "Identification of heavy-flavour jets with the CMS detector in pp collisions at 13 TeV." JINST. **13** (2018) [arXiv: 1712.07158].

[128] T. Müller et al. *Inclusive secondary vertex reconstruction in jets*. https://cds.cern.ch/record/927383. 2006.

[129] E. Bols et al. "Jet flavour classification using DeepJet." JINST. **15** (2020) [arXiv: 2008.10519].

[130] CMS Collaboration. *Performance of the* DeepJet *b tagging algorithm using* 41.9 *fb of data from proton-proton collisions at* 13 *TeV with Phase 1 CMS detector*. http://cds.cern.ch/record/2646773. CMS Detector Performance Note. 2018.

[131] M. Matsugu et al. "Subject independent facial expression recognition with robust face detection using a convolutional neural network." Neural Networks. **16** (2003) 5.

[132] S. Hochreiter and J. Schmidhuber. "Long short-term memory." Neural Computation. **9** (1997).

[133] K. Rehermann and B. Tweedie. "Efficient identification of boosted semileptonic top quarks at the LHC." JHEP. **03** (2011) 059 [arXiv: 1007.2221].

[134] M. Cacciari, G.P. Salam, and G. Soyez. "The catchment area of jets." JHEP. **04** (2008) 005 [arXiv: 0802.1188].

[135] M. Cacciari and G.P. Salam. "Pileup subtraction using jet areas." Phys. Lett. *B*. **659** (2008) 1-2 [arXiv: 0707.1378].

[136] CMS Collaboration. "Observation of single top quark production in association with a Z boson in proton-proton collisions at $\sqrt{s} = 13$ TeV." Phys. Rev. Lett. **122** (2019) [arXiv: 1812.05900].

[137] CMS Collaboration. "Measurements of differential Z boson production cross sections in proton-proton collisions at $\sqrt{s} = 13$ TeV." JHEP. **12** (2019) 061 [arXiv: 1909.04133].

[138] CMS Collaboration. "Measurement of the $\mathrm{t\bar{t}}$ production cross section, the top quark mass, and the strong coupling constant using dilepton events in pp collisions at $\sqrt{s} = 13$ TeV." Eur. Phys. J. *C*. **79** (2019) 368 [arXiv: 1812.10505].

[139] ATLAS and CMS Collaborations. *Report on the physics at the HL-LHC and perspectives for the HE-LHC*. 2019 [arXiv: 1902.10229].

[140] CMS Collaboration. "Precision luminosity measurement in proton-proton collisions at $\sqrt{s} = 13$ TeV in 2015 and 2016 at CMS." Eur. Phys. J. *C*. **81** (2021) 800 [arXiv: 2104.01927].

[141] CMS Collaboration. *CMS luminosity based on pixel cluster counting - Summer 2012 Update*. https://cds.cern.ch/record/1482193. 2012.

[142] CMS Collaboration. *CMS luminosity measurement for the 2018 data-taking period at* $\sqrt{s} = 13$ *TeV*. https://cds.cern.ch/record/2676164. 2019.

[143] P. Lujan. "Performance of the pixel luminosity telescope for luminosity measurement at CMS during Run 2." PoS. **EPS-HEP2017** (2017).

[144] M. Hempel. "Development of a novel diamond based detector for machine induced background and luminosity measurements." Ph.D. thesis. Brandenburg University of Technology Cottbus-Senftenberg, 2017.

[145] S. van der Meer. *Calibration of the effective beam height in the ISR*. https://cds.cern.ch/record/296752. 1968.

[146] C. Rubbia. *Measurement of the luminosity of $p\bar{p}$ collider with a (generalized) Van der Meer Method*. https://cds.cern.ch/record/1025746. 1977.

[147] J. Knolle. "Measuring luminosity and the $t\bar{t}Z$ production cross section with the CMS experiment." Ph.D. thesis. Universität Hamburg, 2020.

[148] CMS Collaboration. *CMS luminosity measurement for the 2017 data-taking period at $\sqrt{s} = 13\,TeV$*. http://cds.cern.ch/record/2621960. CMS Physics Analysis Summary. 2018.

[149] I.C. Brock et al. "Luminosity measurement in the L3 detector at LEP." Nucl. Instrum. Methods *A*. **381** (1996) 2.

[150] Belle II Collaboration. "Measurement of the integrated luminosity of the Phase 2 data of the Belle II experiment." Chinese Phys. C. **44** (2020) 2 [arXiv: 1910.05365].

[151] C. Duhr and B. Mistlberger. "Lepton-pair production at hadron colliders at N^3LO in QCD "(2021) [arXiv: 2111.10379].

[152] CMS Collaboration. *Luminosity determination using Z boson production at the CMS experiment*. Unpublished.

[153] CMS Collaboration. "Electron and photon reconstruction and identification with the CMS experiment at the CERN LHC." JINST. **16** (2021) [arXiv: 2012.06888].

[154] M. Dittmar, F. Pauss, and D. Zurcher. "Towards a precise parton luminosity determination at the CERN LHC." Phys. Rev. *D*. **56** (1997) [arXiv: hep-ex/9705004].

[155] ATLAS Collaboration. "Measurement of $W^{\pm}$ and Z boson production cross sections in pp collisions at $\sqrt{s} = 13\,\text{TeV}$ with the ATLAS detector." Phys. Lett. *B*. **759** (2016) [arXiv: 1603.09222].

[156] S. Dubourg, M. Schaumann, and D. Walsh, eds. *Proceedings of the 2019 Evian workshop on LHC beam operations*. 2019.

[157] ATLAS Collaboration. *Luminosity determination using $Z \to \ell\ell$ events at $\sqrt{s} = 13\,TeV$ with the ATLAS detector*. https://cds.cern.ch/record/2752951. 2021.

[158] J. Salfeld-Nebgen and D. Marlow. "Data-driven precision luminosity measurements with Z bosons at the LHC and HL-LHC." *JINST*. **13** (2018) [arXiv: 1806.02184].

[159] CMS Collaboration. *Simulation of the silicon strip tracker pre-amplifier in early 2016 data*. https://cds.cern.ch/record/2740688. CMS Detector Performance Note. 2020.

[160] CMS Collaboration. *Operation and performance of the CMS silicon strip tracker with proton-proton collisions at the CERN LHC*. Unpublished.

[161] W. Verkerke and D.P. Kirkby. "The RooFit toolkit for data modelling." *Statistical problems in particle physics, astrophysics and cosmology (PHYSTAT 05)*. World Scientific Publishing, 2006.

[162] F. James and M. Roos. "Minuit: A system for function minimization and analysis of the parameter errors and correlations." *Comput. Phys. Commun.* **10** (1975).

[163] J.E. Gaiser. "Charmonium spectroscopy from radiative decays of the J/ψ and ψ'." Other thesis. 1982.

[164] S. Das. "A simple alternative to the Crystal Ball function "(2016) [arXiv: 1603.08591].

[165] CMS Collaboration. "Measurement of the inclusive W and Z production cross sections in pp collisions at $\sqrt{s} = 7$ TeV." JHEP. **10** (2011) 132 [arXiv: 1107.4789].

[166] ATLAS Collaboration. "Muon reconstruction performance of the ATLAS detector in proton-proton collision data at $\sqrt{s} = 13$ TeV." Eur. Phys. J. *C*. **76** (2016) 292 [arXiv: 1603.05598].

[167] CMS Collaboration. "Measurement of the differential Drell–Yan cross section in proton-proton collisions at $\sqrt{s} = 13$ TeV." JHEP. **12** (2019) 059 [arXiv: 1812.10529].

[168] D0 Collaboration. "Search for violation of lorentz invariance in top quark pair production and decay." Phys. Rev. Lett. **108** (2012) 26 [arXiv: 1203.6106].

[169] CMS Collaboration. "Inclusive and differential cross section measurements of single top quark production in association with a Z boson in proton-proton collisions at $\sqrt{s} = 13$ TeV." JHEP. **02** (2022) 107 [arXiv: 2111.02860].

[170] CMS Collaboration. "Search for associated production of a Z boson with a single top quark and for tZ flavour-changing interactions in pp collisions at $\sqrt{s} = 8$ TeV." JHEP. **07** (2017) 003 [arXiv: 1702.01404].

[171] CMS Collaboration. "Measurement of the associated production of a single top quark and a Z boson in pp collisions at $\sqrt{s} = 13$ TeV." Phys. Lett. *B*. **779** (2018) [arXiv: 1712.02825].

[172] ATLAS Collaboration. "Measurement of the production cross section of a single top quark in association with a Z boson in proton-proton collisions at 13 TeV with the ATLAS detector." Phys. Lett. *B*. **780** (2018) [arXiv: 1710.03659].

[173] ATLAS Collaboration. "Observation of the associated production of a top quark and a Z boson in pp collisions at $\sqrt{s} = 13$ TeV with the ATLAS detector." JHEP. **07** (2020) [arXiv: 2002.07546].

[174] F. Colombina. "Search for tZq in dilepton final states with machine learning techniques." Master thesis. Universit'a degli Studi di Milano - Bicocca, 2020.

[175] J.S. Conway. "Incorporating nuisance parameters in likelihoods for multisource Spectra "(2011) [arXiv: 1103.0354].

[176] S.S. Wilks. "The large-sample distribution of the likelihood ratio for testing composite hypotheses." AOMS. **9** (1938) 1.

[177] CMS Collaboration. *HiggsAnalysis-CombinedLimit*. https://github.com/cms-analysis/HiggsAnalysis-CombinedLimit. Accessed: May 2022. 2022.

[178] J.M. Campbell and R.K. Ellis. "MCFM for the Tevatron and the LHC." Nucl. Phys. *B*. **205-206** (2010).

[179] Y. Gao et al. "Spin determination of single-produced resonances at hadron colliders." Phys. Rev. *D*. **81** (2010) 7 [arXiv: 1001.3396].

[180] G. Luisoni et al. "HW $\pm$/HZ +0 and 1 jet at NLO with the POWHEG BOX interfaced to GoSam and their merging within MiNLO." JHEP. **10** (2013) 083 [arXiv: 1306.2542].

[181] CMS Collaboration. "Measurement of top quark pair production in association with a Z boson in proton-proton collisions at $\sqrt{s} = 13$ TeV." JHEP. **03** (2020) 056 [arXiv: 1907.11270].

[182] CMS Collaboration. "Measurement of the cross section and angular correlations for associated production of a Z boson with b hadrons in pp collisions at $\sqrt{s}$ = 7 TeV." JHEP. **12** (2013) 039.

[183] CMS Collaboration. "Observation of the production of three massive gauge bosons at $\sqrt{s} = 13$ TeV." Phys. Rev. Lett. **125** (2020) 15.

[184] CMS Collaboration. "Measurement of the cross section for top quark pair production in association with a W or Z boson in proton-proton collisions at $\sqrt{s} = 13$ TeV." JHEP. **08** (2018) 011 [arXiv: 1711.02547].

[185] CMS Collaboration. "Observation of $t\bar{t}H$ Production." Phys. Rev. Lett. **120** (2018) 23 [arXiv: 1804.02610].

[186] CMS Collaboration. "Search for new physics in same-sign dilepton events in proton-proton collisions at $\sqrt{s} = 13$ TeV." Eur. Phys. J. *C*. **76** (2016) 439 [arXiv: 1605.03171].

[187] CMS Collaboration. "Evidence for associated production of a Higgs boson with a top quark pair in final states with electrons, muons, and hadronically decaying τ leptons at $\sqrt{s} = 13$ TeV." JHEP. **08** (2018) 066 [arXiv: 1803.05485].

[188] Chollet, F. and others. *Keras*. https://keras.io. Accessed: May 2022. 2015.

[189] M. Abadi and others. *TensorFlow: Large-scale machine learning on heterogeneous systems*. https://www.tensorflow.org. Accessed: May 2022. 2015.

[190] D. Walter. "Domain adaptation studies in deep neural networks for heavy-flavor jet identification algorithms with the CMS experiment." MA thesis. Karlsruhe Institute of Technology (KIT), 2018.

[191] M. Bishop. *Pattern recognition and machine learning*. Springer, 2006.

[192] Y. Bengio I. Goodfellow and A. Courville. *Deep learning*. Springer, 2016.

[193] G. Klambauer et al. "Self-normalizing neural networks." *Proceedings of the 31st international conference on neural information processing systems*. 2017 [arXiv: 1706.02515].

[194] S. Hochreiter. "Untersuchungen zu dynamischen neuronalen Netzen." Diploma thesis. Technische Universität München, 1991.

[195] S. Ioffe and C. Szegedy. "Batch Normalization: Accelerating deep network training by reducing internal covariate shift." *Proceedings of the 32nd international conference on international conference on machine learning - Volume 37*. 2015 [arXiv: 1502.03167].

[196] N. Srivastava et al. "Dropout: A simple way to prevent neural networks from overfitting." J. Mach. Learn. Res. **15** (2014) 56.

[197] D.P. Kingma and J. Ba. "Adam: A method for stochastic optimization "(2017) [arXiv: 1412.6980].

[198] J. Močkus. *On bayesian methods for seeking the extremum*. Springer Berlin Heidelberg, 1975.

[199] M. Sundararajan, A. Taly, and Q. Yan. "Axiomatic attribution for deep networks "(2017) [arXiv: 1703.01365].

[200] CMS Collaboration. "Measurement of the inelastic proton-proton cross section at $\sqrt{s} = 13\,\text{TeV}$." JHEP. **07** (2018) 161 [arXiv: 1802.02613].

[201] CMS Collaboration. "Energy calibration and resolution of the CMS electromagnetic calorimeter in pp collisions at $\sqrt{s} = 7\,\text{TeV}$"." JINST. **8** (2013) 09 [arXiv: 1306.2016].

[202] A. Bodek et al. "Extracting muon momentum scale corrections for hadron collider experiments." Eur. Phys. J. *C*. **72** (2012) [arXiv: 1208.3710].

[203] CMS Collaboration. "Performance of missing transverse momentum reconstruction in proton-proton collisions at $\sqrt{s} = 13\,\text{TeV}$ using the CMS detector." JINST. **14** (2019) 07 [arXiv: 1903.06078].

[204] R.J. Barlow and C. Beeston. "Fitting using finite Monte Carlo samples." Comput. Phys. Commun. **77** (1993).

[205] CMS Collaboration. "Measurement of the differential cross section for top quark pair production in pp collisions at $\sqrt{s} = 8\,\text{TeV}$." Eur. Phys. J. *C*. **75** (2015) 542 [arXiv: 1505.04480].

[206] M. Czakon, D. Heymes, and A. Mitov. "High-precision differential predictions for top quark pairs at the LHC." Phys. Rev. Lett. **116** (2016) 8 [arXiv: 1511.00549].

[207] M. Czakon et al. "Top pair production at the LHC through NNLO QCD and NLO EW." JHEP. **10** (2017) 186 [arXiv: 1705.04105].

[208] S. Catani et al. "Top quark pair production at the LHC: Fully differential QCD predictions at NNLO." JHEP. **07** (2019) 100 [arXiv: 1906.06535].

[209] Edelman. "On the distribution of a scaled condition number." **58** (1992) 197.

[210] J. Shen. "On the singular values of Gaussian random matrices." Linear Algebra Appl. **326** (2001) 1.

[211] T. Ježo et al. "An NLO+PS generator for $\text{t}\bar{\text{t}}$ and Wt production and decay including non-resonant and interference effects." Eur. Phys. J. *C*. **76** (2016) 691 [arXiv: 1607.04538 (hep-ph)].

[212] H. Qu and L. Gouskos. "Jet tagging via particle clouds." Phys. Rev. *D*. **101** (2020) 5 [arXiv: 1902.08570].

[213] CMS Collaboration. "Identification of heavy, energetic, hadronically decaying particles using machine-learning techniques." JINST. **15** (2020) 06 [arXiv: 2004.08262].

[214] "Measurement of the jet mass distribution and top quark mass in hadronic decays of boosted top quarks in pp collisions at $\sqrt{s} = 13\,\text{TeV}$." Phys. Rev. Lett. **124** (2020) 20 [arXiv: 1911.03800].

[215] R. Nisius. "On the combination of correlated estimates of a physics observable." Eur. Phys. J. *C*. **74** (2014) 3004 [arXiv: 1402.4016].

[216] R. Nisius. "BLUE: Combining correlated estimates of physics observables within ROOT using the Best Linear Unbiased Estimate method." Softwarex. **11** (2020) [arXiv: 2001.10310].

List of publications

Key publication

CMS Collaboration, "Inclusive and differential cross section measurements of single top quark production in association with a Z boson in proton-proton collisions at $\sqrt{s} = 13\,\text{TeV}$", JHEP. **02** (2022) 107 [arXiv:2111.02860].

Conference proceedings

D. Walter, "Rare top quark production in CMS", (32nd Rencontres de Blois 2021, Blois, France) [arXiv:2202.06038].

D. Walter, "Measurement of top-quark electro-weak couplings in associated top quark production with vector bosons with ATLAS and CMS", PoS. **EPS-HEP2021** (2021) 488 [arXiv:2202.06035].

Poster

D. Walter, "Measurement of the Differential Cross Section and Spin Asymmetry of the Associated Production of a Single Top Quark and a Z Boson at the CMS Experiment", (EPS-HEP2021) [contribution:105252].

Contributions to other publications

CMS Collaboration, "Probing effective field theory operators in the associated production of top quarks with a Z boson in multilepton final states at $\sqrt{s} = 13\,\text{TeV}$", JHEP. **12** (2021) 083 [arXiv:2107.13896]. *(Co-development of analysis framework)*

CMS Collaboration, "The Phase-2 Upgrade of the CMS Beam Radiation Instrumentation and Luminosity Detectors", [CMS-TDR-023]. *(Appendix B.1.3.2)*

CMS Collaboration, "The Phase-2 Upgrade of the CMS Beam Radiation, Instrumentation, and Luminosity Detectors: Conceptual Design", [CMS-NOTE-2019-008]. *(Section 6.5)*

Acknowledgements

My biggest thanks go to Nadjieh for accepting me as her student and giving me the possibility to work on this deeply interesting project. She always supported and encouraged me with full energy. Many thanks go to my second supervisor, Elisabetta Gallo who was always kind and helpful with questions and made my work as comfortable as possible. I really enjoyed the cooperation with Andreas Meyer, who advised me from the first day on. As a coordinator for the luminosity effort at DESY he gave me the possibility to work on the Z boson counting. Together with Jakob Salfeld-Nebgen, who helped me in my early days, Andreas was always available to discuss and drive the progress. Finally, he dedicated a lot of time proofreading this thesis. I would also like to thank Maria Aldaya for sharing her experience in all different matters, Alexander Grosjean whenever I had some questions about simulation, and Olaf Behnke who helped me with his statistical expertise in constructing the analysis. I extend my thanks to Matthias Komm who provided a lot of material through his analysis. Matthias also proofread my analysis chapter giving lots of helpful suggestions leading to many improvements. I thank Evan Ranken for reviewing the theory part and his physics discussions.

For the publication, I also want to thank the group from the University of Ghent, Didar Dobur, Kirill Skovpen, and Luka Lambrecht. Although not always easy, everyone gave his best to make a pleasant atmosphere and uncomplicated cooperation.

I also want to thank the many bachelor's, master's, and Ph.D. students, and postdocs that have been at DESY during my time. Always a pleasure was the lunchtime, Friday coffee, afternoon breaks, or random meetings in front of the coffee machine. Because everyone has a different story of life and opinion it was never boring. With many, I also enjoyed recharging the batteries and spending time outside of work. From my early days Joscha Knolle, Andrej Saibel, and Mattheo Defranchis not only gave me lots of advice for work but were also available for taking dinner or some drinks. I want to thank Sebastian Wuchterl who was always listening to my thoughts about work and took a lot of time for helpful discussions. Over the years, Sebastian has become an expert for restaurants around Hamburg and it has been a great pleasure taking dinner with him. Further, I want to thank Angela Giraldi for being the best guide for activities, Rafael Sosa and Luis Ignacio for playing football, Henriette Pettersen, Jonas Rübenach, Federica Colombina, and Alessia Saggio for interesting discussions and creating a pleasant atmosphere. I also want to thank Valerie Scheurer, Beatriz Lopes, and Michele Mormile for the audible joy from the office of next door. Further, I want to thank Josry Metvalli who always created a good mood. I would like to thank Jindrich Lidrych and Mikel Mendizabal who have provided lots of entertainment in the cheerless days of corona. I want to thank Birgit Breetzke and Gabriele Kalhoefer, our secretaries for the perfect handling of administrative things and for providing order not only to ensure that the coffee never runs out.

My final thanks go to Nicolas Tonon. As an office mate, he was every time available for discussions and questions and helped with dedication. He always carried joy with him and passed it on to all of us.